

THÈSE

Pour l'obtention du titre de

Docteur de l'Université de Lille

Spécialité : Mécanique des milieux fluides

École doctorale ENGYSYS-632

**Comportement d'une hydrolienne carénée à double axe
vertical dans une diversité de conditions d'écoulement
en mer et en bassin d'essais**

**Behaviour of a ducted twin vertical axis tidal turbine in a
diversity of flow conditions at sea and in a flume tank**

Thèse préparée au sein du Laboratoire d'Hydrodynamique Marine
de l'Institut Français de Recherche pour l'Exploitation de la Mer (Ifremer)

Présentée et soutenue publiquement le 18 Octobre 2023 par

Martin MOREAU

Composition du jury :

Sandrine AUBRUN	Professeure, Ecole Centrale de Nantes	Rapportrice
Ludovic CHATELLIER	Maître de Conférences HDR, Université de Poitiers	Rapporteur
Anne-Claire BENNIS	Professeure, Université de Caen Normandie	Présidente
Nicolas MAZELLIER	Professeur, Université d'Orléans	Examinateur
Grégory GERMAIN	Chercheur Habilité à Diriger des Recherches, Ifremer	Directeur de thèse
Guillaume MAURICE	Docteur-Ingénieur R&D, HydroQuest	Encadrant industriel

Remerciements

Comme il est d'usage et surtout parce que je n'aurais pas mené l'ensemble de ces travaux sans eux, je tiens tout d'abord à remercier sincèrement mes encadrants ; Grégory Germain pour la confiance accordée depuis mon stage d'ingénieur jusqu'à ce jour, pour sa disponibilité et son soutien au quotidien, ainsi que pour son pragmatisme ; Guillaume Maurice pour sa confiance également, pour sa rigueur scientifique et ses conseils techniques avisés, ainsi que pour son accueil chaleureux lors de mes visites à Grenoble.

Plus largement, je souhaite remercier l'ensemble de l'équipe d'HydroQuest, bien que principalement à distance, pour les échanges instructifs et leur soutien au cours de ces trois ans. Je remercie particulièrement Cédric Derveaux pour la conception et le suivi de fabrication de la maquette, Aloïs Richard pour sa collaboration sur l'analyse des mesures en mer, Noé Marcon pour les échanges concernant les mesures d'effort sur l'embase gravitaire, Matthieu Guilbot pour les calculs numériques dont j'ai eu besoin, Marion Rafin pour son soutien administratif et Raphaël Coquet pour la supervision de mes travaux. Je les remercie tous également de m'avoir permis de travailler sur cette thèse sans interférence avec les besoins à court terme de l'entreprise.

Pour la bonne ambiance de travail (et des pauses café) au quotidien, j'adresse de chaleureux remerciements à toute l'équipe de l'Ifremer au bassin de Boulogne. J'ai aimé venir travailler à leurs côtés ces dernières années. Merci à Jean-Valéry Facq, Thomas Bacchetti, Benoît Gaurier et Benoît Gomez pour leur aide à la mise en place et à la conduite des essais, ainsi qu'à Christèle Requillard pour son soutien administratif. Merci aussi à Yanis Saouli et Robin Linant qui ont repris le flambeau des essais sur les maquettes d'HydroQuest et à qui je souhaite de la réussite dans leurs travaux respectifs. J'adresse des remerciements particuliers à Noam Bloch qui m'a aidé dans mes travaux lors de son stage d'ingénieur et avec qui j'ai eu plaisir d'échanger, bien au-delà du travail. De même, j'adresse des remerciements tout particuliers à Maëlys Magnier pour les riches interactions sur nos thèses respectives mais également, et surtout, pour tout ce que nous avons partagé ces dernières années. Je remercie aussi Peter Davies d'avoir pris le temps de relire et d'améliorer la qualité de l'anglais de plusieurs parties de ce mémoire.

Au-delà des trois ans de doctorat, la rédaction de ce mémoire marque la fin de vingt-trois années de scolarité. Je profite donc de cet espace pour remercier, bien qu'ils ne liront probablement jamais ces lignes – à quelques exceptions près, l'ensemble des enseignants qui ont su à la fois satisfaire et développer mon envie d'apprendre.

Enfin, hors du cadre professionnel, je suis reconnaissant envers toutes les personnes

qui m'ont accompagné et soutenu d'une manière ou d'une autre au cours de mes années boulonnaises. J'adresse plus spécifiquement ma gratitude à mes proches pour leur présence et la permanence de leur soutien, éléments indispensables à la réussite de ce travail et à mon épanouissement.

Je souhaite une bonne lecture à celles et ceux qui s'intéresseront à ce travail, tout en présentant mes excuses aux lecteur.ice.s francophones. L'anglais ayant pris le dessus dans la littérature scientifique, j'abandonnerai notre langue dans la suite de ce mémoire.

Limiter le réchauffement climatique nécessite, entre autres adaptations, une réduction substantielle de l'utilisation des énergies fossiles et une électrification généralisée basée sur des systèmes de production faiblement émetteurs de gaz à effet de serre. Dans ce contexte, l'exploitation de l'énergie des courants de marée et autres énergies marines renouvelables gagne en intérêt. Ainsi, la dernière décennie a vu les premiers essais en mer de plusieurs concepts d'hydroliennes. Parmi eux, la première hydrolienne carénée à double axe vertical de 1 mégawatt, développée par HydroQuest, a été testée au large de l'île de Bréhat, en Bretagne, de 2019 à 2021. Dans la perspective des prochaines générations de turbines, l'entreprise souhaite améliorer ses outils de conception expérimentaux et numériques afin de gagner en confiance dans sa capacité à prédire les performances et les chargements mécaniques à l'échelle réelle à partir des expériences à échelle réduite. Cela ne peut se faire qu'en comparant les résultats obtenus en mer à ceux obtenus en laboratoire afin d'évaluer les potentiels effets d'échelle. Par conséquent, nous commençons ce mémoire par l'analyse des mesures en mer pour caractériser le comportement du prototype in-situ. Ensuite, nous étudions la réponse d'une maquette à l'échelle 1/20 de ce prototype à partir d'essais réalisés dans le bassin à houle et courant de l'Ifremer à Boulogne-sur-mer. Nous considérons de nombreuses conditions d'écoulement, allant de conditions idéales vers des conditions plus complexes et réalistes. Au-delà de la comparaison des résultats entre échelle réduite et échelle réelle, les analyses présentées dans cette thèse visent également à mieux comprendre l'influence de chacune des caractéristiques de l'écoulement des courants de marée sur le comportement de l'hydrolienne carénée. À partir de mesures de puissance, d'efforts et de sillage, nous étudions les effets du cisaillement de l'écoulement incident, de sa direction relative, de la turbulence générée par des obstacles bathymétriques et des vagues en surface sur la réponse de la maquette. Les résultats montrent que la génération de puissance est, en moyenne, insensible aux conditions d'écoulement incidentes alors que les fluctuations de puissance et d'efforts peuvent être fortement affectées. Enfin, nous discutons des effets d'échelle, notamment de l'influence du nombre de Reynolds, en comparant les résultats en bassin d'essais à ceux obtenus sur le prototype en mer. Les résultats permettent d'affiner la correction qu'il convient d'appliquer aux mesures à échelle réduite pour prédire la génération de puissance à échelle réelle. Bien que les efforts et le sillage semblent moins affectés par les effets visqueux, une comparaison détaillée avec les résultats à échelle réelle nécessiterait des améliorations sur les mesures en mer afin de mieux quantifier les potentiels effets d'échelle. Ces améliorations pourront être mises en œuvre dans les années à venir avec le lancement de la prochaine génération d'hydroliennes à double axe vertical.

Mots-clefs : Hydrolienne à flux transverse, Essais expérimentaux, Mesures in-situ

Abstract

Limiting human-caused global warming requires, among other adaptations, a substantial reduction of fossil fuel use and a widespread electrification based on low greenhouse gas emission production systems. In this context, harnessing the tidal current energy and other marine renewable energy sources has gained interest for the last decade, which lead to the first offshore tests for several tidal energy converter concepts. Among them, the first 1 megawatt ducted twin vertical axis tidal turbine prototype, developed by HydroQuest, was tested off the northern coast of Brittany, France, from 2019 to 2021. In the prospect of the next turbine generations, the company wants to improve its experimental and numerical design tools to gain confidence in its capacity to predict the full-scale performance and loads from the experiments at reduced-scale. That can only be done by comparing the results obtained at sea to those obtained in the laboratories to assess the potential scale effects. Therefore, we first analyse the measurements at sea to characterise the behaviour of the prototype. Then, we study the response of a 1/20 scale model of that prototype tested in the Ifremer wave and current flume tank in Boulogne-sur-mer, France. We consider many flow conditions, increasing the complexity from idealised towards more realistic conditions. Beyond the comparison between reduced- and full-scale results, the analyses presented in that thesis also aim at better understanding the influence of each of the tidal current flow characteristics on the ducted turbine. In more details, from power performance, loads and wake measurements, we study the effects of the incident flow shear, of the relative flow direction, of the turbulence generated by bathymetry obstacles and of surface waves on the model response. The results show that the average power performance is rather insensitive to the incident flow conditions whereas the power and load fluctuations can be strongly affected. Finally, we discuss the scale effects on the results by comparing the power performance, the loads and the wake results in the tank with those obtained on the prototype at sea. The results allow to refine the evaluation of the correction needed at reduced-scale to predict the power performance at full-scale, mainly due to Reynolds number difference. Even if the loads and the wake results seem less affected by the viscous effects, a detailed comparison with the full-scale results would require improvements on the measurements at sea to better quantify the potential scale effects. Those improvements may be implemented in the coming years with the launch of the next generation of twin vertical axis tidal turbines.

Keywords: Cross-flow tidal turbine, Experimental tests, In-situ measurements

Contents

Remerciements	iii
Résumé	v
Abstract	vii
1 General introduction	1
2 Full-scale prototype behaviour at sea	13
2.1 Sea states influence on the prototype behaviour	13
2.1.1 Introduction	13
2.1.2 Material and method	15
2.1.3 Turbine performance and behaviour	20
2.1.4 Conclusions	30
2.2 Design method and hydrodynamic coefficients assessment	31
2.2.1 Design method and load assessment	31
2.2.2 Power coefficient and optimal tip speed ratio assessment	34
3 Reduced-scale model behaviour and scale effects assessment	39
3.1 Reduced-scale model behaviour and wake in idealised flow conditions	39
3.1.1 Introduction	39
3.1.2 Material and method	41
3.1.3 Flow direction effect on the behaviour of the ducted 2-VATT	46
3.1.4 Flow direction effect on the wake of the ducted 2-VATT	49
3.1.5 Discussion and conclusions	61
3.2 Scale effects discussion	62
3.2.1 Scale effects on the turbine performance and loads	63
3.2.2 Scale effects on the flow surrounding the turbine	68
4 Reduced-scale model response facing more realistic flow conditions	75
4.1 Turbine behaviour in a vertically sheared and misaligned current	76
4.1.1 Introduction	76
4.1.2 Material and method	76
4.1.3 Flow shear and misalignment effects	81
4.1.4 Discussion	85
4.1.5 Conclusion	89
4.2 Turbine behaviour in the turbulent wake of a bathymetry obstacle	89

4.2.1	Introduction	89
4.2.2	Material and method	90
4.2.3	Bathymetry effects on the ducted 2-VATT behaviour	98
4.2.4	Conclusion	105
4.3	Turbine behaviour in presence of surface waves	106
4.3.1	Introduction	106
4.3.2	Material and method	109
4.3.3	Effect of waves against current on the ducted 2-VATT behaviour .	116
4.3.4	Conclusion	123
4.3.5	Supplement: surface waves effect analysis extension	124
5	General discussion and prospects	127
5.1	Synthesis of the flow conditions influence	127
5.1.1	Tested flow conditions at reduced-scale	127
5.1.2	Flow condition influence on the turbine behaviour	130
5.1.3	Scale effects discussion extension	137
5.2	General conclusion	138
5.3	Prospects	141
A	Effect of different bathymetry obstacles on the ducted 2-VATT	143
B	Influence of the velocity measurement location on the performance assessment	157
	Bibliography	161

CHAPTER 1

General introduction

Global context

According to the sixth climate change assessment report of the Intergovernmental Panel on Climate Change (IPCC, 2023), human activities, principally through emissions of greenhouse gases, have unequivocally caused global warming. Today, global greenhouse gas emissions continue to increase, with unequal historical and ongoing contributions arising from unsustainable energy use, land use and land-use change, lifestyles and patterns of consumption and production. Still according to IPCC (2023), widespread and rapid changes in the atmosphere, ocean, cryosphere and biosphere have occurred and human-caused climate change is already affecting many weather and climate extremes in every region across the globe. This has led to widespread adverse impacts and related losses and damages to nature and people. Adaptation planning and implementation progress but gaps still exist and will continue to grow at current rates of implementation, the IPCC says. Limiting human-caused global warming requires at least net zero CO₂ emissions. Therefore, all global modelled pathways that limit warming to 1.5°C and 2°C compared to 1850-1900 involve rapid, deep and, in most cases, immediate greenhouse gas emissions reductions in all sectors and systems this decade (IPCC, 2023). Regarding energy systems, reaching net zero CO₂ emissions entail a substantial reduction in overall fossil fuel use, electricity systems that emit no net CO₂ and a widespread electrification, among other adaptations. In addition, the IPCC state that energy generation diversification and demand-side management can increase energy reliability and reduce vulnerabilities to climate change.

Today, most of the world energy system adaptation to generate electricity with low CO₂ emissions relies on the installation of new hydroelectric, wind and solar energy power plants. Indeed, the contribution of these energy sources to the world electrical production has kept increasing over the past decades (IEA, 2022). Seas and oceans also offer a big source of renewable energy. The kinetic and potential energy associated with the surface waves, the temperature gradient between the sea surface and the deepwater, the potential energy associated with the tidal range and the kinetic energy associated



(a) SIMEC Atlantis deployed at MeyGen
© SIMEC Atlantis



(b) Sabella D10 at the Fromveur passage
© Sabella



(c) O2 turbine at the Fall of Warness test site
© Orbital Marine Power



(d) OceanQuest at the Paimpol-Bréhat test site
© HydroQuest

Figure 1.1 – Examples of megawatt(s) rated power tidal turbine technologies installed in Europe.

with the tidal currents are as many significant sources of renewable energy that are barely harvested today (IEA-OES, 2022). Their exploitation could contribute to reduce the fossil fuel use and further diversify the electricity generation system, as recommended by the IPCC. Specifically, the tidal current energy is derived from the movement of ocean water volumes caused by the gravitational attraction of the moon, the sun, and other astronomical bodies. Therefore, by opposition to wind and solar energy, tidal energy is a highly predictable source of renewable energy. The tidal currents are stronger nearshore and particularly where there are constrictions, such as straits, islands and passes. For instance, the average velocity over the water depth in the Alderney race, the first French tidal current energy hotspot, off the coast of Normandy, was measured up to $3 \text{ m}\cdot\text{s}^{-1}$ (Furgerot et al., 2020). Thus, a large amount of kinetic energy can be harvested in these shallow waters using Tidal Energy Converters (TEC).

Over the past decade, tidal current energy developments led to the installation of the first TECs with rated powers between 1 and 2 MW in Europe (Fig. 1.1, IEA-OES (2023)). The MeyGen project piloted by SIMEC Atlantis Energy is established in the Pentland Firth, north of Scotland. The phase 1 of the project has been operational since

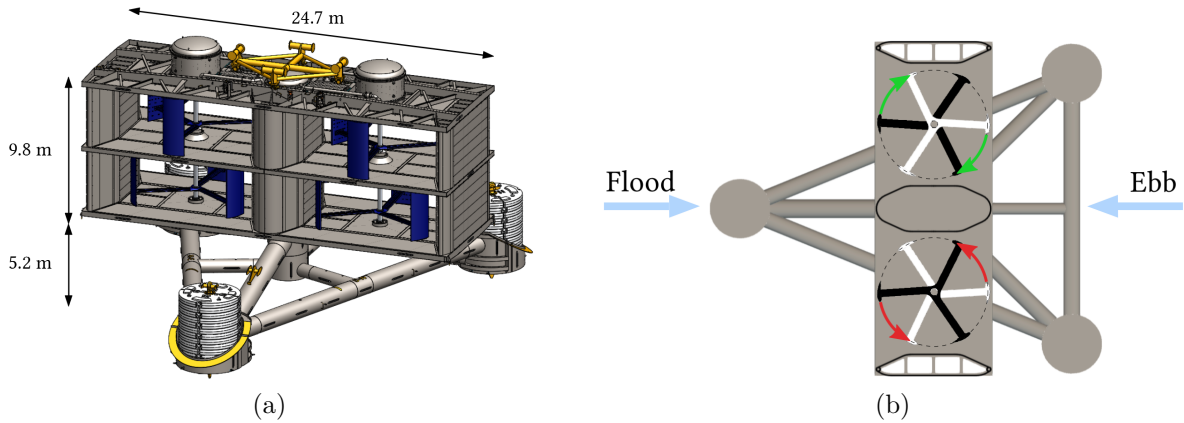


Figure 1.2 – (a) CAD view of the full-scale prototype. (b) Schematic top view of the ebb and flood tide configurations.

2018 and comprises four 1.5 MW-rated Horizontal Axis Tidal Turbines (HATT) installed on the seabed. They have generated over 50 GWh of renewable electricity, a world record for tidal current energy. Sabella D10 project is also based on a horizontal axis rotor technology installed on a gravity-based structure laying on the seabed. The project has been developed in the Fromveur Passage at Ushant Island, the second French hotspot for tidal resource off the western coast of Brittany. It became the first tidal turbine to supply electricity to the French grid, in November 2015. Still using HATTs, the O2 device developed by Orbital Marine Power is a 72 m long floating structure, supporting two 1 MW-rated turbines at either side. It has been tested at the European Marine Energy Center’s Fall of Warness tidal test site in Scotland since 2021. Finally, HydroQuest tested its ducted twin Vertical Axis Tidal Turbine (2-VATT) prototype (Fig. 1.2) called OceanQuest at the Paimpol-Bréhat test site, off the northern coast of Brittany, from 2019 to 2021. Two specific measurement campaigns enabled the certification of the 1 MW-rated ducted 2-VATT power curve following the International Electrotechnical Commission Technical Standards (IEC TS) 62600-200 (IEC, 2013). Along with the instantaneous power output measurement, that standard requires the use of two Acoustic Doppler Current Profilers (ADCP) placed in-line with the TEC, one upstream of the TEC extraction plane on the flood (rising) tide and the other upstream on the ebb (falling) tide. Those instruments have to be placed between 2 and 5 equivalent diameters from the TEC capture plane, and within 0.5 equivalent diameter of the principal ebb and flood direction streamlines coincident with the TEC extraction plane vertical centreline. Moreover, still according to the IEC TS 62600-200, the power curve is derived using the method of bins to calculate the mean values of the power output and of the tidal current velocity for each bin. The method of bins starts by computing the instantaneous cubic power weighted velocity averaged across the projected capture area. Then, we must calculate the temporal (10 minutes) cubic power weighted average value of these velocity data samples and the same temporal average of the power output data samples. The averaged velocity and power data points are binned according to their corresponding velocity bin value, with a maximal velocity increment of $0.10 \text{ m}\cdot\text{s}^{-1}$. Finally, we obtain the TEC power curve by calculating an average velocity and power data point using all of the data points in each velocity bin.

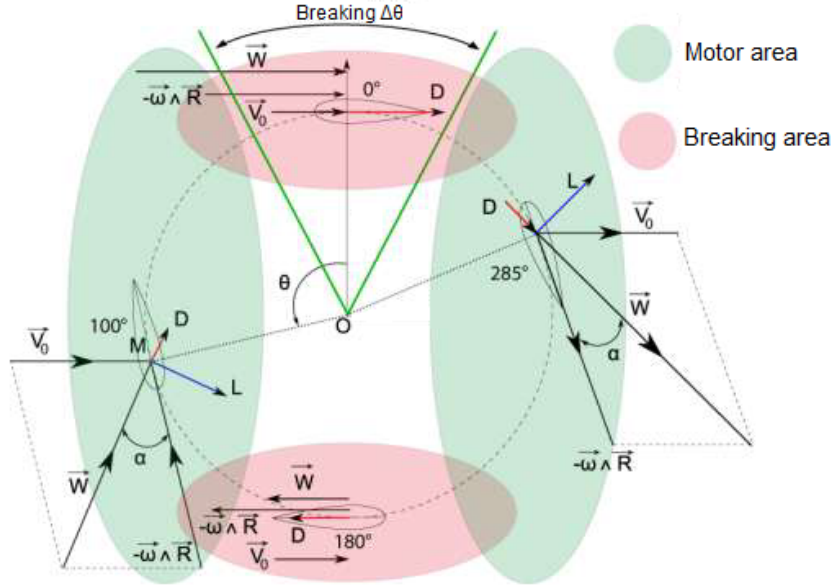


Figure 1.3 – Principle of operation of a vertical axis rotor, from Jaquier (2011). $W = V_0 + \omega R$ is the apparent velocity on the foil with V_0 the flow velocity, ω the rotational speed of the rotor with a radius R centred in O . D and L represent the drag and lift forces due to W on the foil at four angular positions θ .

Vertical axis turbines

HydroQuest’s TEC is inspired by Darrieus lift-based Vertical Axis Turbines (VAT) (Darrieus, 1931). The principle of operation of such rotors is described extensively in Beudet (2014). It is illustrated in Fig. 1.3 where a foil is displayed at four angular positions (θ) with the combination of the upstream flow and the rotational speed resulting in variable drag and lift forces on the foil. The projection of the lift and drag forces on the tangent to the circle swept by the blades generates a motor torque in the upstream and downstream areas and a braking torque in between, where the flow velocity and the rotational velocity directions are almost collinear (Jaquier, 2011). The angular range of the breaking areas, extended on the illustration for the sake of readability, vary with the rotor geometry. Therefore, the angular distribution of the torque generated by a single blade of a 3-bladed vertical axis rotor typically looks like in Fig. 1.4 with most of the motor torque generated in the upstream half, little braking torque around $\theta = 0^\circ$ and 180° , and motor torque generation in the downstream half of the circle. The downstream part of the rotation generates less torque than the upstream one due to the wake of the blades in the upstream half and to the one of the rotor shaft. Given this principle of operation, the torque fluctuation along the rotation makes the mechanical design more complex for a vertical than a horizontal axis turbine, and an isolated VAT may suffer from self-starting troubles depending on the random blades position at rest. Pairing two levels of vertical axis rotors on the same shaft with a phase difference between them, like in HydroQuest’s TEC, increases the self-starting capacity and smooths the torque fluctuation of the rotor column without affecting the rotor performance (Jaquier, 2011). Besides, isolated VATs have the significant advantage compared to HATTs to be insensitive to the flow direction. The rectangular capture area of a VAT and the faster wake recovery compared to the classic circular HATT are other advantages that can allow a

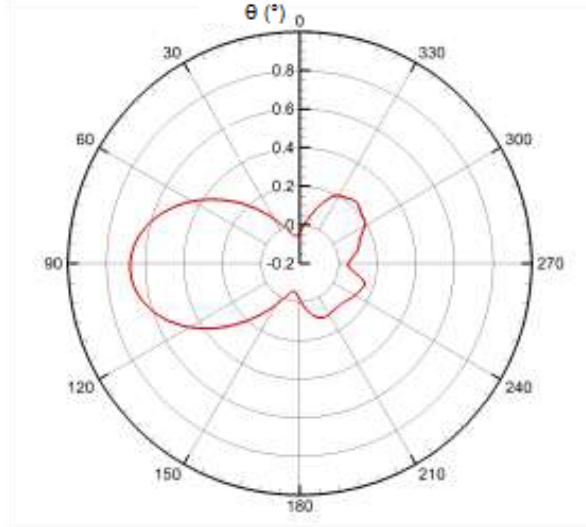


Figure 1.4 – Typical angular distribution of the torque generated by a single blade of a 3-bladed vertical axis rotor, from (Jaquier, 2011).

higher power density of TEC arrays (Mendoza et al., 2019; Ouro et al., 2022). Bachant et al. (2015) and Rolin et al. (2018) study the wake of such single vertical axis rotors and find that the average velocity deficit (and so kinetic energy) is asymmetrically distributed in the wake as the deficit is significantly stronger downstream of the rotor side where the blades move against the flow. In addition, the two studies reveal counter-rotating average swirling motions in the planes normal to the flow direction that are the main contributors to the streamwise momentum and average kinetic energy recovery, more importantly than the turbulence. The turbulence kinetic energy distributions are also asymmetrical but in an opposite way between the two studies as Bachant et al. (2015) find the maximal values behind the blades moving downstream whereas Rolin et al. (2018) find that maximum behind the blades moving upstream. That difference may be explained by differences of dynamic stall processes due to the rotor geometry differences (foil section, solidity...) and to the different Reynolds numbers.

Furthermore, several studies reveal that placing two counter-rotating vertical axis turbines side by side, like HydroQuest’s TEC, improves the power performance significantly compared to isolated VATs (Hill et al., 2014; Vergaerde et al., 2020a). It also reduces the vertical torque and the transverse loads on the turbine base (Vergaerde et al., 2020b), which is beneficial for the structural design. In addition, the wake past twin VATs is shorter compared to an isolated VAT and symmetrical (Müller et al., 2021). It was shown experimentally on non-ducted twin vertical axis wind turbines that the counter-rotational direction affects the turbine’s wake, without affecting significantly the mean power coefficient (Lam et al., 2017; Jiang et al., 2020; Müller et al., 2021; Vergaerde et al., 2020a). Müller et al. (2021) show that, when the blades move against the flow at the turbine centre, the wakes of the two rotors merge immediately downstream of the turbine and the merged wake expands mainly in the vertical direction; whereas, when the blades move with the flow at the centre, the wakes of the two rotors remain separated and the global wake mostly expands horizontally. Lam et al. (2017) find similar effects of the relative counter-rotation direction and observe pairs of stationary counter-rotating vortices at both sides of the twin rotors that contribute to the

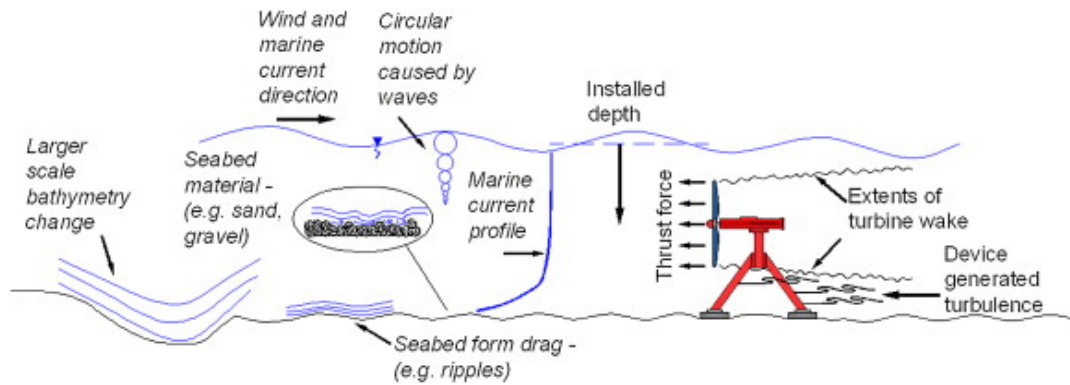


Figure 1.5 – Illustration of the flow conditions faced by a tidal energy converter, from Myers et al. (2012).

flow mixing. Furthermore, Grondeau et al. (2019) model numerically the HydroQuest’s ducted 2-VATT wake in 3D without the base during ebb tide, and Jégo et al. (2021) model it in 2D in both ebb and flood tide flow directions (Fig. 1.2). The relative direction of rotation of the two counter-rotating rotors is reversed between the two current directions as the blades move upstream at the 2-VATT centre during flood tides while they move downstream during ebb tides. The numerical results show that the power production is insensitive to the flow direction and that the rotor wakes merge faster with a stronger velocity deficit downstream of the central fairing in the flood tide configuration compared to the ebb. However, the numerical models were only validated by comparison to experimental results on a single non-ducted VATT since no results existed for a ducted 2-VATT.

Tidal current characteristics and implications

Despite the success of the previously mentioned industrial projects, further studies are still needed to improve the comprehension of the TECs response to the tidal current flow conditions. Indeed, the highly energetic tidal current flow conditions are complex, with high velocities and flow direction variability, vertically sheared velocity profiles, turbulent flows and surface waves, like illustrated by Myers et al. (2012) (Fig. 1.5). The influence of those flow characteristics on the typical HATTs is widely described in the literature, as presented next, but VATs, and even more so 2-VATTs, have been less studied overall.

First, the flow direction reverses between the flood and the ebb tides with varying velocity magnitudes. The relative angle between the two tide directions differs depending on the site considered. For instance, it is about 180° in the Alderney race (Furgerot et al., 2020; Sentchev et al., 2020) while it is closer to 160° at the Paimpol-Bréhat test site (EDF et al., 2022), where OceanQuest was tested. So, the TECs must be able to operate both during ebb and flood tides, potentially with significant misalignment angles between their heading and the flow direction. Bottom mounted HATTs usually deal with this direction change in two ways (Zhou et al., 2017). The first is to keep the rotor fixed, which implies that it is in the wake of the stanchion in one of the directions, leading to significant performance loss and load fluctuation (Frost et al., 2015). Besides, Frost et al. (2017) and Modali et al. (2021) find that the misalignment between the flow

direction and the HATT axis leads to a power reduction of 7 % and 9 % for a flow misalignment of 10° and 15°, respectively, by numerical and experimental approaches. The addition of a shroud around a HATT induces a reduction of the misalignment effect as only about 6 % of power loss is obtained for a shrouded turbine against 23 % for the free turbine with 25° misalignment (Shahsavari et al., 2020). The second way to deal with direction changes for HATTs is to equip the turbine with a yaw system that maintains the rotor facing the current. This way, the turbine performance remains optimal and constant whatever the flow direction (McNaughton, 2014) but it complicates the system, introducing additional risks of failure (Laws et al., 2016). Harrold et al. (2019) presents rotor loading characteristics of a HATT fixed on a triangular gravity-based foundation with a yaw system. They show a difference in mean rotor loading between ebb and flood tides, partly due to the influence of that asymmetric foundation. From this point of view, the insensitivity of isolated VATs to the flow direction appears to be a significant advantage compared to HATTs. The case of twin counter-rotating VATs is more complex, however, as the device loses the complete symmetry that characterises isolated VATs. Therefore, the effect of the flow misalignment on the behaviour of a ducted 2-VATT remains an open question. And, in the perspective of TEC farms, some devices may operate in the wake of others located upstream, depending on the flow direction and the spacing distance between the devices. So the wake interaction between TECs must also be considered in the development of such farms (Vennell et al., 2015; Gaurier et al., 2020b).

Furthermore, the seabed roughness slows the flow down in the boundary layer. The vertical velocity profiles measured at sea commonly follow power law fits across the whole water column (Furgerot et al., 2018; Cossu et al., 2021). Therefore, the TECs face sheared flows with a variable velocity magnitude over their capture height, depending on the installation depth. Magnier et al. (2022) and Vinod et al. (2021) study the response of a HATT in a sheared flow collinear with the rotor axis. Overall, they reveal an increase of about 30 % in torque and about 50 % in thrust fluctuation due to the flow asymmetry between the upper and the lower part of the rotor disc. Only a few studies consider single vertical axis wind turbines facing vertically sheared velocity profiles (Shamsoddin et al., 2016). Mendoza et al. (2019) studies the performance and the wake of such a wind turbine under varying surface roughness conditions, generating varying vertical shears and turbulence levels. They find minor influence of those conditions on the power coefficient and a faster wake recovery with the most sheared and turbulent velocity profile, rather explained by the turbulence mixing improvement than the vertical shear. However, to the author knowledge, the effect of a vertical velocity gradient has never been considered neither on twin vertical axis turbines nor on turbines combining several levels of out-of-phase VATs on a same shaft.

The seabed roughness is also responsible for turbulence and a high spatial variability of the tidal stream characteristics. (Mercier et al., 2022) reveal significant variability over distances of less than 100 m and over short time scales at the Paimpol-Bréhat test site. Besides, Mercier et al. (2021a) observe that large bathymetric singularities generate highly energetic coherent flow structures with a rising trajectory from the seabed to the free surface, generating boils in the Alderney Race, France. Coherent turbulent structures were also measured at the Fall of Warness, Scotland, by Naberezhnykh et al. (2023), and in the Menai Straits, Wales, by Lucas et al. (2022) where the most powerful coherent structures have a median length-scale of 13.2 m with a periodicity of about

105 s. Specific studies have been carried out in Ifremer’s wave and current flume tank to reproduce such flow configurations at a 1/20 scale and to better understand the flow physics induced by bathymetry obstacles (Ikhennicheu et al., 2019a; Magnier et al., 2021). Among the diversity of studied obstacles, a generic wide bottom mounted square cylinder was found to reproduce those highly energetic coherent flow structures with a rising trajectory (Ikhennicheu et al., 2019b; Mercier et al., 2020). The vortices are shed in the cylinder wake with a frequency around 0.25 Hz and their diameter was estimated to be about 0.6 m using Lamb-Osen vortex profiles. Thus, the coherent flow structures past the wide bottom mounted cylinder are of the same order of magnitude, both in time and space, as coherent structures measurement at sea according to Reynolds number similitude law (Lucas et al., 2022). Knowing the effect of such flow structures on tidal turbines located on their path is crucial for an appropriate structural design (Milne et al., 2010; Thiébaud et al., 2020).

Chamorro et al. (2015) first tested experimentally a HATT in the wake of vertically oriented cylinders. They find a strong interaction between the large-scale and broadband turbulence shed by the cylinders and the turbine power production. Then, Ouro et al. (2019) modelled the effect of sharp dunes on another HATT using Large Eddy Simulations (LES). Their results provide quantitative evidence of the effect of seabed-induced turbulence on the instantaneous performance and structural loadings of the turbine revealing how large-scale energetic turbulence structures affect the turbine performance. They also show that the turbine wake recovery is enhanced compared to the same turbine operating above a flat bathymetry due to the higher turbulence levels. Furthermore, Gaurier et al. (2020a) and Gaurier et al. (2020c) tested Ifremer’s generic HATT in the wake of the above mentioned wide bottom mounted square cylinder. They reveal large blade root force fluctuation due to the rotation through the sheared velocity field and show that the turbine load fluctuation directly responds to the vortex shedding low frequency. Based on the same database, Druault et al. (2022) explains that the typical turbine power frequency spectra decay in the inertial range (proportional to a $-11/3$ power law) is due to the spatial averaging of the velocity spectrum by the turbine blades. Regarding VATs, experiments were carried out to analyse the effect of the ambient turbulence intensity on H-rotor vertical axis wind turbines (Ahmadi-Baloutaki et al., 2015; Möllerström et al., 2016). The results show that the power performance only slightly increases with the turbulence intensity from 5 to more than 15 %, with variable results depending on the reference velocity computation method. In addition, coupled wind tunnel tests and LES on a straight-bladed vertical axis wind turbine shows that grid turbulence benefits both self-starting and wake recovery with a greater power production in turbulent flows (Peng et al., 2016). The previously mentioned LES study of OceanQuest’s wake by Grondeau et al. (2019), using lattice Boltzmann actuator-line approach, also analyses the influence of several upstream turbulence intensities. Their results show that the turbulence not only enhances the wake recovery but also modifies the wake shape evolution with the downstream distance. To the author knowledge, however, the effect of coherent flow structures on VATs have not been studied yet.

On top of those already complex flow characteristics, surface waves may propagate above the tidal currents, which adds more complexity and affects the tidal kinetic energy resource (Guillou et al., 2016). Zhang et al. (2022) presents a review of the state of research on wave-current interaction in nearshore areas. The waves generate velocity fluctuation, called orbital velocity, whose amplitude decrease exponentially with depth

in the whole water column (Molin, 2002). Their interaction with the current is affected by their relative direction of propagation with regard to the current direction (Bennis et al., 2022). The linear wave theory shows that the wave-current interaction increases the wave-length and reduces the wave height for waves following the current, and vice versa for opposing waves (Brevik et al., 1979). Numerous studies have considered the effect of waves on reduced-scale HATTs in towing tanks or flumes to better understand the wave-current-turbine interaction (Gaurier et al., 2020d) and to provide reliable assessment of the unsteady loads endured by the turbines. Among the first, Barltrop et al. (2006) find that the root bending moments of rotor blades fluctuate significantly due to the waves. Gaurier et al. (2013) reveal that the average power and thrust are unaffected by the presence of waves but their standard deviations increase as a peak appears at the wave frequency in the torque and drag spectra. Moreover, Martinez et al. (2018) show that the presence of waves propagating collinearly with the current are more detrimental than oblique ones and that they induce torque and thrust standard deviations that are almost double those associated with current only. Ordonez-Sanchez et al. (2019) analyse the performance of a HATT in the presence of both regular and irregular waves of similar characteristic heights and periods. They find no difference in the average power and thrust coefficients between the two wave cases but smaller fluctuation amplitudes with irregular waves than with regular ones. In addition, Martinez et al. (2020) observe a phase difference between the surface elevation and the thrust signals indicating that the turbine senses the waves before they reach the rotor plane. Such phase differences are also observed regarding the forces exerted by surface waves on piles and are explained by the added mass force, which is proportional to the accelerative force exerted on the mass of water displaced by the pile (Morison et al., 1950). Finally, Draycott et al. (2020) offer a new insight into the nature of wave loading on a HATT revealing the rotational sampling of wave-induced velocities, that oscillate at the frequency f_η , by the blades rotating at the frequency f_ω . As a result, they observe a high frequency loading pattern on the blades with dominant frequencies at $mf_\omega \pm kf_\eta$ of which the magnitude decreases with the integers m and k . Similarly, numerical models such as the one presented in Perez et al. (2022) find that when HATTs operate in large wave conditions at sea, the load cycle is governed by the periodic wave-induced velocity fluctuation while the average power and thrust are barely affected by the presence of waves.

As opposed to the plentiful studies considering waves effect on HATTs, only a few studies considers the waves influence on VATTs and none on 2-VATTs. Bachant et al. (2011) were the first to address the effect of waves on the average performance of a lift-based vertical axis tidal turbine. The experimental results show an increase in power coefficient as well as a shift towards higher tip speed ratios of the whole power curve with waves compared to current only conditions. They suggest that the wave-induced fluid velocity could increase the blade angle of attack beyond its stall angle. However, the study only considers regular waves with a constant height and focuses on the power coefficient on a limited tip speed ratio range, disregarding the low tip speed ratios. Secondly, combining viscous CFD method and linear wave theory, Zhang et al. (2014) find that the instantaneous tip speed ratio of a Darrieus-type rotor varies due to the presence of waves, which leads to torque and power fluctuation. However, the numerical model with waves lacks a proper comparison to some experimental data for validation before studying the wave effects. Finally, Lust et al. (2021) tested a 1 m diameter H-Darrieus rotor in a tow tank with three regular surface waves of different height and

period. They find that the presence of waves degrades the power production slightly when compared to the current only case, and that the power variation increases with the wave height between the two wave cases. In addition, their results show that the waves modify the cyclic signatures in the power measurement depending on the phase difference between the blade angular position and the wave phase. However, that study only focuses on theoretical regular waves and on the power coefficient, disregarding the load coefficients on the structure.

Scale effects

Experimental tests at reduced-scale and numerical simulations offer the opportunity to control the upstream flow characteristics to analyse both their physics and their influence on the TECs response (Gaurier et al., 2020d; Guillaud et al., 2020). Thus, they are also used to enhance the turbine designs (Guilbot, 2021) as well as to assess the performance and the loads of the TECs before their full-scale deployment. However, the results validity remains questionable when scaling up to full-scale prototypes operating at sea, whichever the TEC technology, since only few data from in-situ measurements on HATTS is publicly available (McNaughton, 2014; Harrold et al., 2019), and none for VATs, to the author knowledge. Reduced-scale model experiments can be representative of a full-scale prototype operation only if the model and the prototype obey the same physical laws. This is achieved if geometric, kinematic, and dynamic similarities are satisfied, leading to identical dimensionless loads and performance for the model and the prototype (Bertram, 2012). In the design of tidal turbine scale model tests, most of the attention is focused on force ratios (dynamic similarity) as geometric and kinematic scaling (length and velocity ratios) are more easily done (Doman et al., 2015). For the power performance assessment of such turbines, the Reynolds number scaling, representing the ratio of inertial to viscous forces, is the most relevant. Indeed, the stall angle of NACA0018 foils increases with the Reynolds number, so the drag and lift coefficients of the blade foils, that are directly related to the turbine power performance, are strongly dependent on that dimensionless parameter (Michna et al., 2022). However, the Reynolds number scaling is impossible to achieve at reduced-scale while keeping the same fluid as at full-scale. When Reynolds number matching is not possible, common practice in the industry is to use Froude number scaling (Doman et al., 2015). The later is not appropriate to determine the power output or the structural loads, but it is relevant when considering the influence of the gravity or the buoyancy, such as in presence of surface waves, on the turbine behaviour. Froude number values less than 0.5 generally ensure stable flows when there are no obstacles in the water column whereas Froude numbers close to 1 lead to critical flow conditions with possible standing waves and transient surface effects (Harrison et al., 2010). The blockage ratio between the turbine projected area and the cross-section of the tank must also be considered. It has to be kept low enough not to artificially increase the turbine performance compared to open water conditions as more flow is constrained to go through the turbine when the blockage ratio is high (Ross et al., 2020a).

Ross et al. (2022), extended in Ross (2020), presents the effect of the Reynolds number, the Froude number (either computed with the channel depth or the turbine submergence) and the blockage ratio on the performance and the drag of an isolated 2-bladed vertical axis tidal turbine (VATT). The turbine was first characterized at a

baseline operating condition before changing independently each of the four dimensionless parameters while the others were held roughly constant at baseline values. They find that increasing each parameter by approximately 30 % increases the drag coefficient by about 5 % in all the cases while the increase of the Reynolds number, the blockage ratio and the submergence depth Froude number leads to a maximal power coefficient increase by about 21 %, 14 % and 7 % respectively. On the other hand, the channel depth Froude number has a negligible effect. Thus, the Reynolds number appears to be the most impacting dimensionless number on the turbine performance whereas the Froude number is the least one (as long as it remains low enough). Bachant et al. (2016) focuses on the Reynolds number influence on the energy conversion and the near-wake dynamics of a high solidity 3-bladed VATT. They find that the maximal performance of the turbine becomes independent of the Reynolds number based on the blade chord ($Re_c = \omega Rc/\nu$, with ω the rotational speed, R the rotor radius, c the chord and ν the kinematic viscosity), when it reaches $Re_c \simeq 2.5 \times 10^5$. In addition, the mean velocity and turbulence measurements in the near-wake are barely affected over the investigated range of Reynolds numbers. However, a similar Reynolds number threshold is revealed when transport terms for the streamwise momentum and mean kinetic energy are calculated. Finally, Miller et al. (2018) analyses the experimental performance of a 1/22.5 scale vertical axis wind turbine compared to the commercial 5-bladed turbine. Utilizing highly compressed air as the working fluid, they reach high Reynolds numbers while still maintaining dynamic similarity by matching the tip speed ratio and Mach number. The results show that the turbine power performance becomes independent of the Reynolds number based on the rotor diameter when $Re_D = U_0 D/\nu \simeq 3.2 \times 10^6$, with U_0 the upstream flow velocity and $D = 2R$ the turbine diameter, which is beyond the commercial scale Reynolds number. In addition, they find that the evolution of the maximal power coefficient with Re_D can be nicely fitted by an error function from $Re_D = 0.6$ to 5×10^6 .

Thesis scope

Focusing on the ducted 2-VATT developed by HydroQuest, the first objective of the present work is therefore to compare experimental results at reduced-scale to those of the 1 MW-rated prototype to discuss the validity of the experimental results extrapolation for the design of the next full-scale devices. To that end, we developed a 1/20 scale model of the 1 MW-rated prototype that we tested in the Ifremer wave and current flume tank (Gaurier et al., 2018). Beyond the comparison between reduced- and full-scale results, our second objective is to better understand the response of the ducted 2-VATT to each of the flow condition characteristics individually. Therefore, we tested the model in many flow conditions, increasing the complexity from idealised towards more realistic conditions. In addition, an experimental characterisation of the turbine wake is also needed to contribute to the numerical models validation and to initiate the work on the future tidal turbine farms layout. Following these objectives, the manuscript is structured as follows, based on published or in-review scientific articles.

Chapter 2 focuses on the full-scale 1 MW-rated prototype tested by HydroQuest at the Paimpol-Bréhat test site. We start by describing the turbine geometry and the instrumentation used to measure both the flow conditions and the 2-VATT behaviour. The flow characteristics of that offshore test site are also described. We identify complex flow conditions, like at other tidal energy sites, including flow direction asymmetry

between ebb and flood tides, vertically sheared velocity profile and turbulence generated by the rough bathymetry, and severe sea states occasionally. Then, selecting specific instants in the two year-long measurement database, we provide an overview of the full-scale turbine performance as well as of the wake and the mechanical behaviour. We particularly focus on the influence of the sea state on the power and loads fluctuation.

Then, chapter 3 aims at qualifying the scale effects between reduced-scale experiments and full-scale operation. To that end, the first part (3.1) starts by describing the 1/20 scale model of the ducted 2-VATT and its instrumentation extensively. It continues with the analyse of the performance and the wake of the model in the typical idealised experimental flow conditions, namely with a uniform incident velocity profile and a flow direction aligned with the turbine heading, with a low turbulence level and the absence of surface waves. In that study, we focus on the effect of the relative flow direction, either coming from one or the other side of the turbine like during ebb and flood tides. Finally, putting together the measurements at sea and those in the flume tank, we assess the accuracy of the typical reduced-scale experiments to predict the full-scale results in the second part (3.2). Indeed, although the geometric similarity between the reduced- and the full-scale devices is respected, the dynamic similarity cannot be fully achieved and the rotor control laws are different. We consider the power performance, the structural loads and the flow surrounding the ducted 2-VATT one after the other. We also discuss the complementarity between experimental tests and numerical models to predict the full-scale results.

In chapter 4, we increase the inflow complexity at reduced-scale to bring the flow characteristics closer to the one of the tidal currents at sea. First (4.1), we analyse the effect of the vertical shear of the incident flow, still with a low turbulence level, on the ducted 2-VATT behaviour compared to the idealised uniform inflow. In addition, we examine the turbine model response when it operates facing a sheared flow with a misalignment angle up to $\pm 15^\circ$ between its heading and the flow direction. Then, the model response is studied facing unsteady flow conditions either due to the presence of bathymetry obstacles upstream or to the presence of surface waves. Regarding the bathymetry, we tested the model downstream two generic geometries of bathymetry obstacles with two relative distances between those obstacles and the ducted 2-VATT. The results in the four configurations are presented in the appendix A and we focus on the most detrimental configuration, in terms of average power loss and loads fluctuation increase, in the second part of the chapter (4.2). The last part (4.3) investigates the ducted 2-VATT model response when surface waves propagate on top of the current. We aim at qualifying the effect of the amplitude and the period of the wave as well as of their direction, either following the current or propagating against it. We also compare the effect of regular and irregular waves of similar period and height.

Finally, we summarise the experimental results at reduced-scale in all the flow conditions tested in the concluding chapter (5). Thus, we identify the critical conditions from a mechanical design point of view and we complete the discussion regarding the reduced-scale results validity to predict those at full-scale. The general conclusion recaps the main results and answers the initial objectives before enumerating numerous prospects that could complete the present study in a near future.

Full-scale prototype behaviour at sea

This chapter aims at establishing the state of the knowledge regarding the behaviour of the 1 MW-rated ducted twin vertical axis tidal turbine prototype tested at the Paimpol-Bréhat test site. We start in the first part (2.1) by describing the prototype geometry, the instrumentation setup and the flow characteristics at the test site. Then, selecting specific instants in the two year-long measurement database, we present the main power performance, wake and load measurement results with a focus on the sea state influence. That first part was originally published as Moreau et al. (2022b), “Sea states influence on the behaviour of a bottom mounted full-scale twin vertical axis tidal turbine”, in *Ocean Engineering*. Then, we make use of some works done by the HydroQuest team in the second section (2.2) to extend the state of the knowledge.

2.1 Sea states influence on the prototype behaviour

2.1.1 Introduction

In the past decade, a large amount of work has been performed on lab-scale tidal turbines, whether horizontal axis (HATT) (Mycek et al., 2014; Ebdon et al., 2021; Payne et al., 2018) or vertical axis (VATT) (Chatellier et al., 2018; Hoerner et al., 2020; Priegue et al., 2017). In particular, Gaurier et al. (2020d) showed that the flow fluctuation induced either by the presence of turbulence or waves increases torque and loads fluctuation of the lab-scale HATT, without shifting significantly the mean values compared to laminar current alone. Draycott et al. (2019) also demonstrated that loads and power fluctuation of a HATT strongly mimics both the temporal and spectral form of the generated focused wave condition at lab-scale and Druault et al. (2022) gives a physical interpretation of the power-law scaling in the inertial range of the turbine power spectra.

However, there is a lack of feedback on the validity of lab-scale results extrapolation to full-scale (Moreau et al., 2021) since few tidal turbine developers have achieved full-scale deployment (Harrold et al., 2019; Scarlett et al., 2019; Black & Veatch, 2020) even

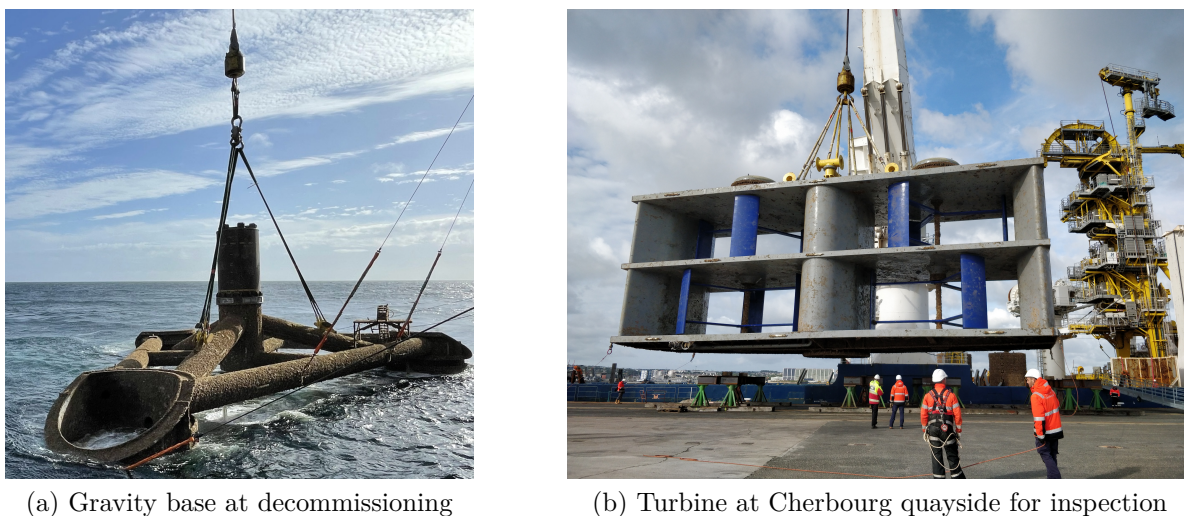
if there are currently some plans to expand to commercially sized projects with farms of turbines (Goss et al., 2021; Jeffcoate et al., 2015). Coles et al. (2021) reports that 18 MW of tidal stream capacity has been installed in the UK since 2008. The majority of the systems have been monitored and controlled in order to evaluate their performances.

The incident velocity measurement is an important input in the performance characterisation of TECs. The International Electrotechnical Commission Technical Standards (IEC TS) requires only a single bottom mounted Acoustic Doppler Current Profiler (ADCP) upstream to investigate the vertical distribution of the current velocities for resource and power performance assessment (IEC, 2013). The mean incident velocity is then computed under the assumption of flow homogeneity on the TEC width. However, mean incident velocity assessment from single ADCP measurements is sensitive to many sources of uncertainties associated mainly with the beams spreading, their misalignment as well as the tilt of the device and the turbulence intensity (Rathnayake et al., 2020). Five beam ADCP, including a vertical one, can also be used to measure surface waves and turbulence of the flow (Guerra et al., 2017). Boufferrouk et al. (2016) show that, except for peak period, spectral estimates of wave height, mean energy period and spectral bandwidth from an ADCP vertical beam agree well with estimates from co-located directional wave buoys. For turbulence kinetic energy measurement, methods for separation of wave and turbulence effects on the fluctuating part of the velocity needs to be used (Togneri et al., 2021; Filipot et al., 2015). In Mercier et al. (2021b), large-eddy simulation of a high Reynolds number flow over a rough sea bed is performed and used to assess the accuracy of two coupled 4-beam ADCPs system forming an 8-beam arrangement. The results are globally satisfying and confirm the relevance and efficiency of the tested 8-beam configuration for the turbulence characterisation. The quality of the results near the seabed is lower however, which questions the accuracy of ADCP measurements in the bottom of the water column, especially if only one 4-beam ADCP is used to characterise the incident flow.

Since 2008, EDF has developed a test site for Tidal Energy Converters (TEC) with on- and off-shore infrastructures off Bréhat island, near Paimpol, France (Terme et al., 2015; Pham et al., 2009; Pham et al., 2010). The first program was conducted by OpenHydro who tested three generations of its TEC, which should have led to the grid-connection of two 1 MW turbines. This program ended in 2017 leaving EDF's infrastructures available. In the spring of 2019, HydroQuest installed its own 1 MW capacity TEC demonstrator, *OceanQuest*, at the test site.

For this company, the installation at sea comes after a decade of development of twin counter-rotating vertical axis current energy converters, inspired by Darrieus and Achard turbines (Achard et al., 2006). Before 2019, numerical simulations (Grondeau et al., 2019; Guillaud et al., 2020), tank tests and installations in rivers provided knowledge and feedback to the developer. The installation of the turbine at sea was an important step forward in the development of the technology. Following this installation, a dedicated flow measurement campaign enabled the certification of *OceanQuest's* power curve by Bureau Veritas according to the TS 62600-200 (IEC, 2013). After two years of successful tests at sea, the demonstrator was retrieved to be inspected and dismantled in October 2021 (Fig. 2.1).

In this study, we first describe the design of the ducted twin vertical axis tidal turbine (2-VATT) and the environmental conditions present at the Paimpol-Bréhat test site (2.1.2). Then, the performance and the behaviour of the demonstrator are analysed



(a) Gravity base at decommissioning

(b) Turbine at Cherbourg quayside for inspection

Figure 2.1 – *OceanQuest* retrieval from Paimpol-Bréhat test site in October 2021.

in the temporal and spectral domains with regard to the sea states (2.1.3).

2.1.2 Material and method

The first part of this section presents the main parameters of *OceanQuest* and its embedded instrumentation for performance and mechanical behaviour measurements. Then, we detail the method used to characterise the flow using Acoustic Current Doppler Profilers (ADCP). Finally, we introduce the process implemented in this study to select relevant data among the 21 months of operation to study the waves effects on the 2-VATT behaviour.

2.1.2.1 Vertical axis tidal turbine demonstrator

OceanQuest is composed of two independent counter-rotative vertical axis rotor columns (Fig. 1.2 (a)). During flood tides, the rotors rotate against the flow at the inside, along the central fairing, whereas they rotate with the flow at the inside during ebb tides (Fig. 1.2 (b)). The columns are mounted in a $H = 9.8$ m high and $W = 24.7$ m wide mechanical structure made of fairings and plates. Each column is made of two levels of rotors fixed to the same shaft with a 60° phase difference between them, and each rotor is made of three 3.8 m high blades with a NACA 0018 profile projected on the swept cylinder. The rotors radius (R) is 4 m with blades chord (c) of 1.47 m which leads to a solidity (s , Eq. 2.1) of 1.1.

$$s = \frac{N \cdot c}{R} \quad (2.1)$$

Permanent Magnet Generators (PMG) are placed at the top of each column shaft on the mechanical structure. The PMG pilot the rotors by an open loop torque control based on the rotational speed measurement following the control law defined in Eq. 2.2 with Q the torque, ω the rotational speed, k the control parameter and D_0 a constant that depends on the turbine's specifications. The output power is limited to its nominal value P_{max} by limiting the torque, and so increasing the rotational speed (Eq. 2.3).

$$Q = k.D_0.\omega^2 \quad (2.2)$$

$$Q = \frac{P_{max}}{\omega} \quad (2.3)$$

The turbine structure is fixed on the vertical mast of a tripod gravity base. The electric conversion elements are installed in a watertight chamber, located inside the upper central fairing. The turbine is connected to shore with a 16 km long optical fibre for generators control and measurement signals, and the electric power is dissipated in power banks.

The electrical current and voltage at the generators output are both measured at 1 Hz to calculate the active power converted by the turbine. Knowing the electrical and mechanical parameters of the machine, the current measurement is also used to model the mechanical torque on the rotor shafts. The rotational speed is measured on each shaft by position encoders at 1 Hz. Besides, strain gauges are placed on the vertical mast of the base to measure deformations in flexion and torsion. A calibration process was carried out on the dock before the immersion of the demonstrator to estimate the shear load at the top of the base's mast (where the turbine is fixed) from the measured strains. Due to the base asymmetry with regard to the transverse axis, the transformation matrix for axial loads (F_x , in the turbine heading direction) is different according to whether the load is applied from one side or the other. A single transformation matrix is needed for transverse loads (F_y) since the base is symmetrical in that direction.

2.1.2.2 Flow measurements

For performance assessment following IEC standards (IEC, 2013), two dedicated ADCP Measurement Campaigns (MC1 and MC2) were held. To measure incident current velocities, two Nortek Signature 500 ADCP were installed on the seabed between 50 and 60 m off turbine on each side, aligned with the main flow directions (Fig. 2.2). 'ADCP1' and 'ADCP2' refer to the instruments used during the first and the second measurement campaigns respectively. ADCPs noted '-NW' are used as the flood tide profilers and those noted '-SE' as the ebb tide profilers. Four acoustic beams are used to measure the current at 1 Hz in 0.5 m high cells on the whole water depth (varying from approximately 36 to 48 m between the Lowest and the Highest Astronomical Tide, noted LAT and HAT respectively). A fifth vertical beam is used to measure waves at 2 Hz in altimeter mode. The reference incident velocity (U_{cap}) is computed as the cubic power weighted average in time over 10 minutes and in space over the capture area (from $z = 5.2$ m to 15.0 m above the seabed at the TEC position, assuming the velocity profile to be transversely homogeneous), as it is required in the TS 62600-200 (IEC, 2013).

In addition, another Nortek Signature 500 ADCP, referred to as 'ADCP-HQ', fixed on the top of the turbine, measured the velocity profile (with 1 m cell size at 1 Hz) and the waves (at 2 Hz) above the turbine all the time during the 21 months of operation. Outside performance assessment campaigns, the data acquired by this instrument is used to qualify the sea state and to estimate the incident U_{cap} .

Apart from the power curve assessment that follows TS 62600-200 (IEC, 2013), we study the data measured during the hour centred on the tidal velocity peak of each tidal cycle. The identification of this instant is not straightforward since the velocity does

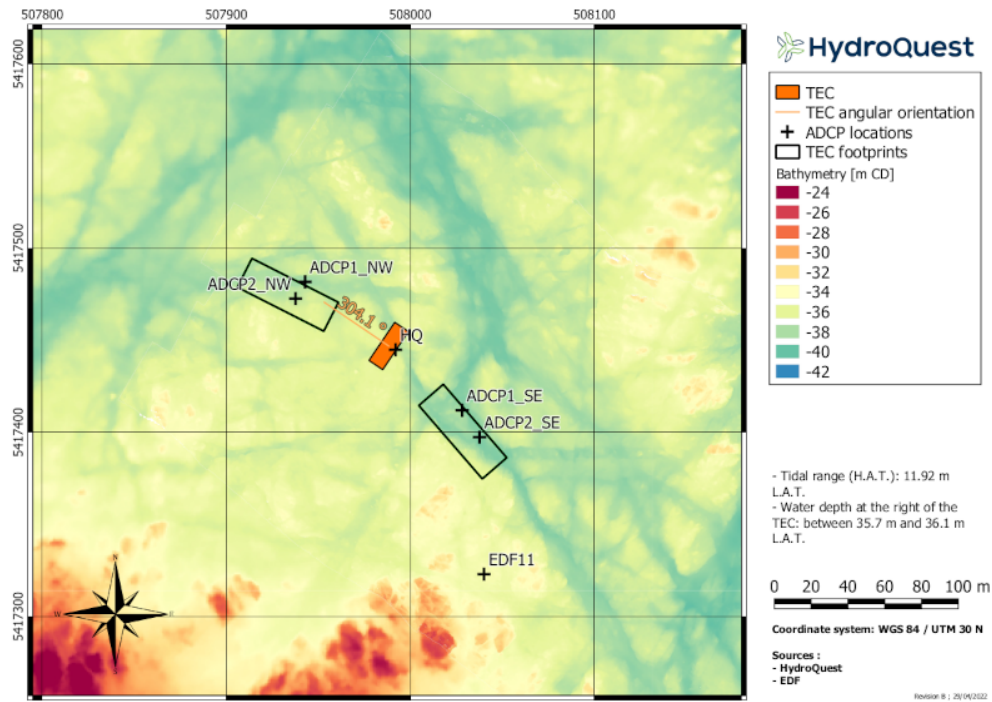


Figure 2.2 – Acoustic Doppler Current Profilers (ADCP) positions around the turbine displayed on a bathymetry map. 'ADCP1' and 'ADCP2' refer to the instruments used during MC1 and MC2 respectively. The TEC footprints represent the areas, aligned with the main ebb and flood tide directions, in which the ADCPs must be placed for performance assessment according to the TS 62600-200 (IEC, 2013).

not vary uniformly. To overcome this, we compute U_{cap} on the whole flood or ebb tidal cycle considered and fit the data with a third order polynomial which provides a single peak of velocity.

Finally, for spectral analysis, we compute the Fourier Transform (FT) of U_{HQ} which is the velocity measured by ADCP-HQ averaged in space over a surface equivalent to the capture area, approximately 5 meters above the turbine.

2.1.2.3 Flow characteristics

Fig. 2.3 illustrates the principal current directions relative to the TEC measured at the hub height during the first performance assessment campaign. The flood tide comes principally from the direction 297° and the principal ebb direction is 139° . Consequently, the misalignment between the TEC heading and the principal flood (resp. ebb) tide direction is equal to 7° (resp. 15°). The observed misalignments values are included in the domain defined by the design basis of the demonstrator. The flood tide current provides velocities with a maximum close to 3 m/s whereas the ebb current is lower, with a maximum around 2 m/s at the hub height.

10-minute averaged velocity profiles measured by the two ADCP1 in calm sea states are plotted on Fig. 2.4. We display the profiles measured within the two hours around the velocity peak, during three tidal cycles of range 6.2 m, 8.3 m and 10.5 m. The maximal tidal range between HAT and LAT being about 12 m, higher velocities can be expected during extreme tidal cycles. To have an idea of the average incident velocity

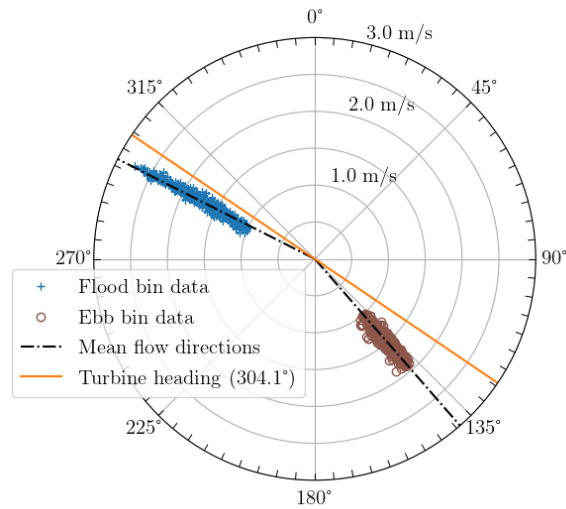


Figure 2.3 – Tidal current magnitudes and origin directions at the hub height during MC1. Bin data refer to the method described in TS 62600-200 (IEC, 2013).

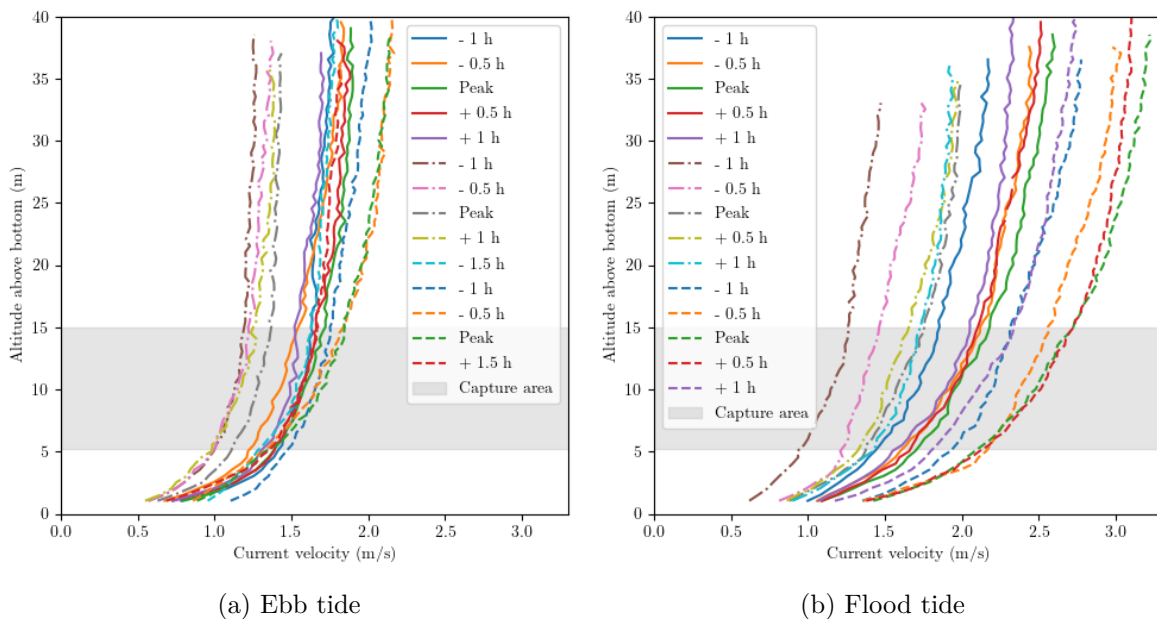


Figure 2.4 – Ebb and flood tide velocity profiles for three tidal ranges (-. 6.2 m, - 8.3 m, - - 10.5 m) at ± 1 h around the velocity peak, in calm sea conditions. The limit altitudes of the TEC’s capture area are represented by the grey zone.

profile, we first normalize each profile by its mean value over the capture area. Then, we plot the mean value of the normalized profiles at each altitude as well as the extreme values for ebb and flood tides on Fig. 2.5. The results show that the incident profile is almost self-similar between ebb and flood tides from the seabed to the top of the capture area of the turbine. Besides, we notice an important velocity shear at the altitude of the capture area with a 22 % (19 % resp.) velocity difference between the bottom and the top of the capture area for flood (ebb resp.) tide currents.

Concerning waves, the ADCP measurements reveal that the most important wave

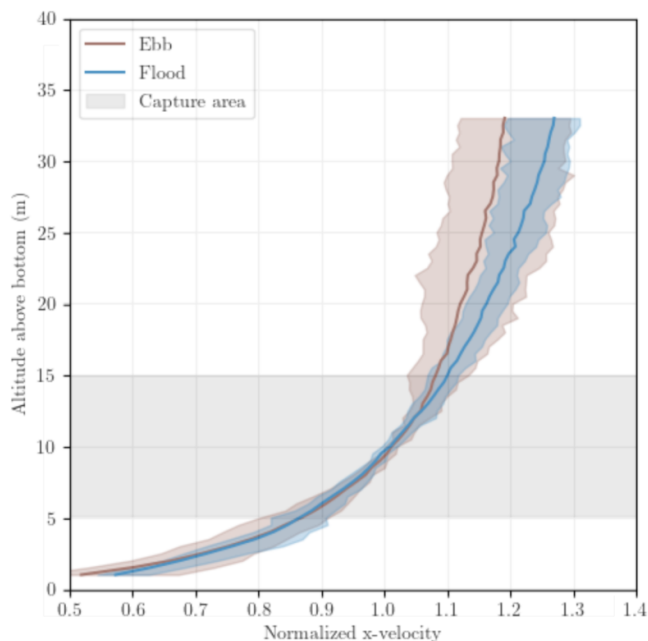


Figure 2.5 – Statistical current velocity profiles calculated from the profiles on Fig. 2.4. The solid lines stand for the mean profiles and the shades for the range between minimal and maximal velocity values along the height. The statistical profiles are cut at $z = 33$ m to compute the mean over a constant number of profiles even though the water level varies.

events over the test period are associated to swells coming from North-West (against ebb tide currents) with a peak period (T_p) of about 12 s (Fig. 2.6). The median significant wave height (H_s) computed on 30 minutes over this period is 1.15 m and the median T_p is 8.7 s. Besides, H_s remained below 1.7 m 75 % of the time. The most extreme wave event was measured in December 2019 with $H_s = 5.95$ m and $T_p = 11.9$ s but the TEC was parked to protect it from extreme loads.

Finally, EDF also performed an ADCP campaign at Paimpol-Bréhat test site in 2011. The ADCP was located at the position EDF11 on the Fig. 2.2. From this campaign, the turbulent intensity at the turbine’s height is evaluated around 15 % for current velocities over $1 \text{ m}\cdot\text{s}^{-1}$ (Filipot et al., 2015). It is also showed that the turbulence decreases with the elevation in the water column and that it is higher during ebb tides than flood tides, probably due to the local bathymetry downstream and upstream the measurement point.

2.1.2.4 Data selection process

For the power curve assessment, according to the TS 62600-200 (IEC, 2013), all the data acquired during the ADCP campaigns are considered, without sea state conditions discrimination.

For the wake consideration, the mechanical behaviour and loads analyses, we need to select specific instants representing the overall conditions to which the turbine was subjected among the 21 months of full time 1 Hz acquisition. As such, we developed an algorithm that helps identifying instants in specific conditions defined with criteria on the turbine status, the incident velocity and the wave conditions. In this study, we

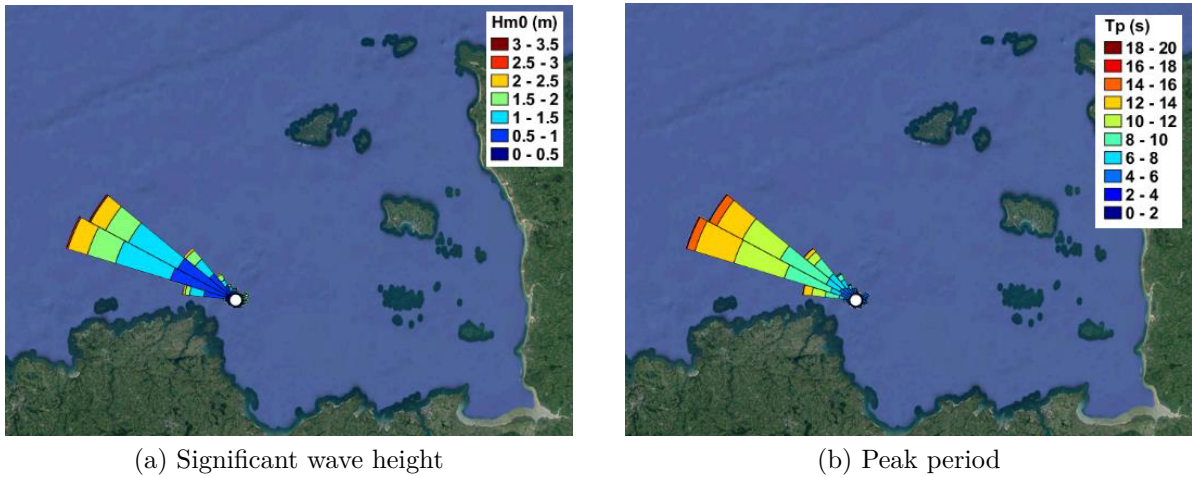


Figure 2.6 – 30-minute wave statistics at Paimpol-Bréhat test site based on ADCP-IEC measurements from July to October 2019. NortekMED production.

focus on the instant at which the two columns of the turbine are in production mode during the hour centred on the tidal current velocity peak, both in flood and ebb tides, for a wide range of incident velocities. The wave conditions are differentiated into two categories: either *calm sea* with a significant wave height lower than 1.3 m and a peak period lower than 7 s or *rough sea* with H_s higher than 2 m and T_p higher than 10 s. With such criteria, the maximal orbital velocity expected at the top of the device according to Airy wave theory is less than 0.01 m/s in calm sea conditions and more than 0.30 m/s in rough sea.

For the two categories, the wave conditions are established in terms of direction and peak period. Specifically, we select instants at which the waves direction varies less than 60° and the peak period less than 3 s during the 3 hours centred on those instants. An example of this algorithm’s output is displayed in Fig. 2.7. Following this process, we identified about 40 moments matching the requested conditions on which the following mechanical behaviour and turbine wake studies are based.

2.1.3 Turbine performance and behaviour

In the following part, we analyse the performance and the behaviour of the turbine in the different sea states described above. The first section addresses an overview of the 2-VATT power performance and wake. Then, the TEC behaviour is analysed in the temporal domain in terms of operating points and thrust, and in the spectral domain to highlight the periodic impact of waves on the machine. Finally, we discuss the impact of the flow fluctuation on the mean and the standard deviation of the TEC loads.

2.1.3.1 Overall analysis

Power curve assessment

Two measurement campaigns were held to assess the sensitivity of the power performance to the control parameter k . The 10-minute averaged active power generated by the TEC is plotted versus the mean power weighted tidal current velocity on Fig. 2.8

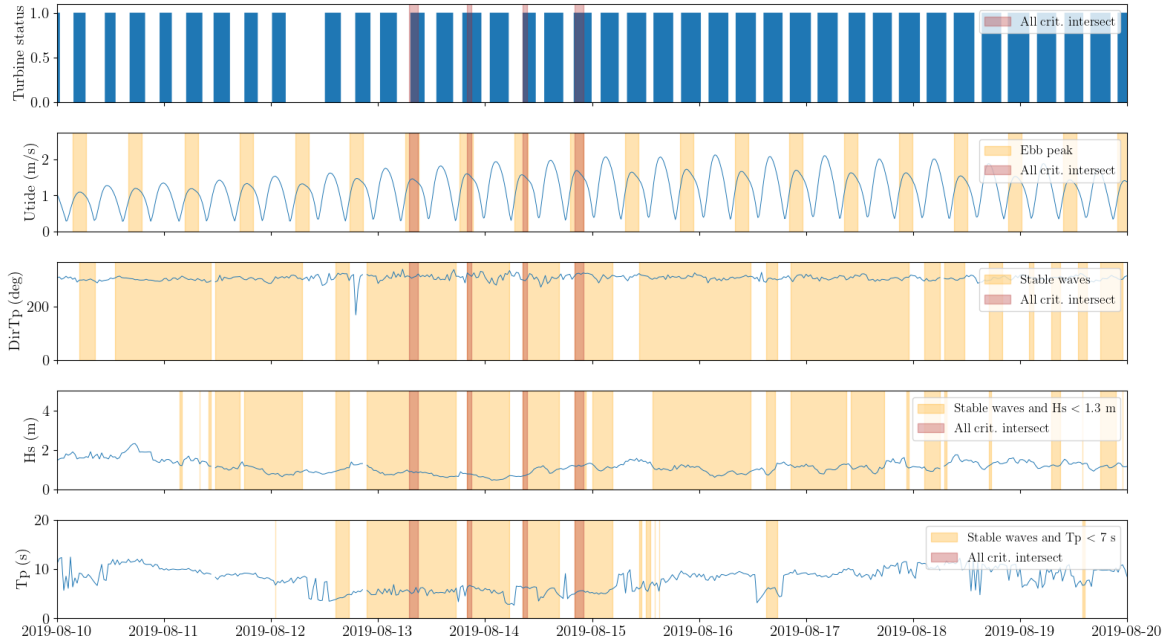


Figure 2.7 – Illustration of the algorithm output for the selection of instants matching specific operating conditions and sea states. In this example, the conditions required are: turbine in production mode during ebb tide with calm wave conditions ($H_s < 1.3$ m and $T_p < 7$ s).

(a), following the TS 62600-200 (IEC, 2013). The results show that the ebb and flood tide power curves from MC1, when $k = 1.0$, are superimposed. This suggests that the turbine’s performance is equivalent whether the flow comes from one side or the other of the machine and that the 2-VATT is insensitive to flow misalignments with regard to its heading up to $\pm 15^\circ$ (Fig. 2.3). However, this superimposition is no longer observed during MC2, when $k = 1.5$, as the ebb power curve is lower than the flood power curve. Besides, it appears that the overall performance of the 2-VATT is higher when $k = 1.5$ compared to $k = 1.0$ as the mean active power is 11 % and 36 % higher during the ebb and the flood tides, respectively, over the whole velocity range.

This performance improvement was expected since the control parameter value $k = 1.5$ had been adjusted to optimise the operating point of the turbine, but the flood performance increase exceeds the expectations. Beyond the tuning of k , the difference between MC1 and MC2 curves are also probably due, in part, to the change in the ADCP locations between the two campaigns, even if the IEC standards are respected (Fig. 2.2). Indeed, the measured flow characteristics, such as turbulence and velocity profile, depend strongly on the instruments position downstream of bathymetric variations (Ikhennicheu et al., 2019a). Fig. 2.8 (b) presents the mean tidal current velocity vertical shear profiles during MC1 and MC2 when the mean velocity at the hub height is 1.5 ± 0.05 m/s, as defined in the TS 62600-200 (IEC, 2013). The flood profiles (ADCPs -NW) are significantly different between the two campaigns, showing the spatial variability of the flow. Since the computation of U_{cap} is based on the assumption that the velocity profile is homogeneous over the turbine width, there is an uncertainty on its value that can explain part of the difference between MC1 and MC2 power curves. The TEC footprints where the ADCP can be installed, as defined in the IEC standards and represented in

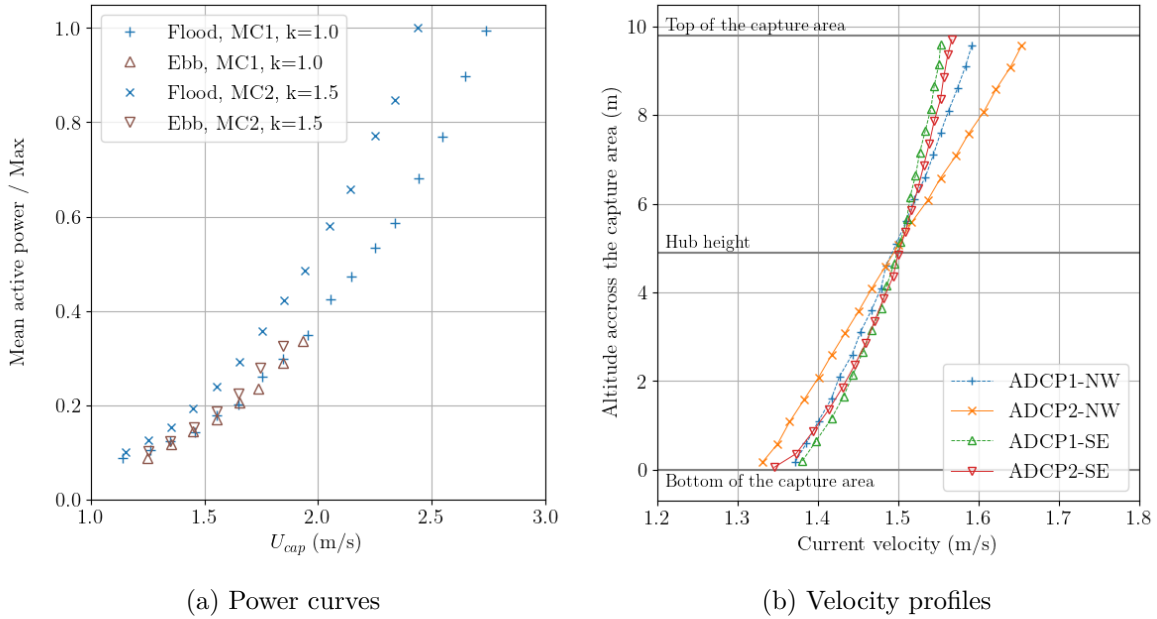


Figure 2.8 – (a) Power curves and (b) mean tidal current velocity vertical shear profiles when the mean velocity at the hub height is 1.5 ± 0.05 m/s, both established from MC1 and MC2 following the TS 62600-200 method (IEC, 2013).

Fig. 2.2, should be narrowed to make the flow measurements, and thus the performance assessments, more comparable between different measurement campaigns.

Wake consideration

For power curve assessment, only the upstream ADCP is considered in the process. Hereafter, we propose to analyse the downstream ADCP measurements to study the TEC wake characteristics in calm sea states. The velocity deficit observed during ebb tides by the ADCP2-NW (Fig. 2.10 (a & b)) extends from the bottom of the capture area of the turbine up to 5 meters above it and represent 15 to 20 % of the incident velocity at its maximum, in the top half of the capture area. We can also observe an over-speed between the seabed and the bottom of the turbine indicating that the incident flow tries to bypass the obstacle. This velocity profile shape is similar to the one computed numerically by Grondeau et al. (2019).

As shown in Fig. 2.9, the instruments are placed approximately 55 m on each side of the turbine, being about 2.2 times the TEC width (W). However, the downstream ADCPs are not properly aligned with the main incident flow direction and the TEC due to the asymmetry between flood and ebb tides (Fig. 2.3). Fig. 2.9 displays the ADCP locations with regard to the TEC boundaries projections along the main ebb and flood tide directions. It shows that the two ADCP1 are located on the edge of the projections downstream of the TEC and that the two ADCP2 are outside these projections.

Numerically, the wake almost hardly expands laterally and remains within the TEC projection along the flow direction at $2W$ downstream distance (Grondeau et al., 2019; Jégo et al., 2021). Consequently, it is not surprising to observe that the ADCP2-SE does not measure any velocity deficit at flood tide (Fig. 2.10 (c)), which shows that it

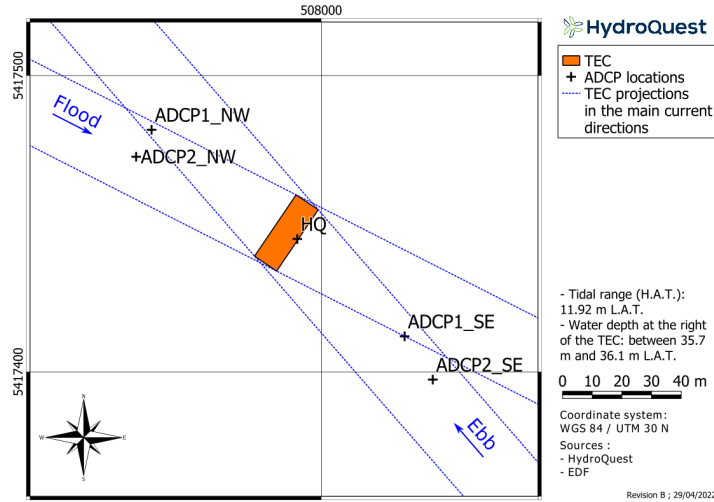


Figure 2.9 – ADCP locations with regard to the TEC boundaries projections along the main ebb and flood tide directions.

is outside the wake region. However, even though the upstream profile data is lacking for a proper comparison, we can clearly see a velocity deficit at the turbine height in the ADCP1-SE measurement, located downstream at flood tides (Fig. 2.10 (d)). These observations suggest that the wake lateral boundary is located between the two instrument positions, which is coherent with the numerical simulation results (Grondeau et al., 2019; Jégo et al., 2021).

During ebb tides (Fig. 2.10 (a and b)), the ADCP2-NW measures a clear velocity deficit even though it is located outside the TEC projection, unlike the ADCP2-SE at flood tide. The difference of wake behaviour between ebb and flood tides can be explained by different hypotheses. Firstly, the 2D numerical simulation of *OceanQuest* presented by Jégo et al. (2021) shows that the wake expands a bit more laterally when the turbine operates in the ebb tide counter-rotating configuration, with the flow at the inside, than in the flood tide configuration, against the flow at the inside. Secondly, the lateral fairings of the turbine probably guide the flow along its own heading, diverting the wake from the flow's incident direction (Fig. 1.2). We assume that the wake remains diverted from the incident direction further downstream at ebb tide than at flood tide as the incident velocity magnitude is lower at ebb tide. This flow behaviour was not predicted numerically by Jégo et al. (2021) but the numerical model had been validated by comparison to a single vertical axis rotor, without surrounding fairing. Consequently, it appears that a more complete characterisation of the TEC wake, either in-situ or at least experimentally, is required both to better understand its physics and to validate numerical models.

2.1.3.2 Mechanical behaviour investigation

To go into the demonstrator characterisation in depth, specific developments are carried out to analyse the 1 Hz signals in the temporal and spectral domains as well as their statistics. To focus on the influence of sea states on the 2-VATT and avoid discussions on the control law effects, we consider only the data points corresponding to a single control parameter value ($k = 1.0$).

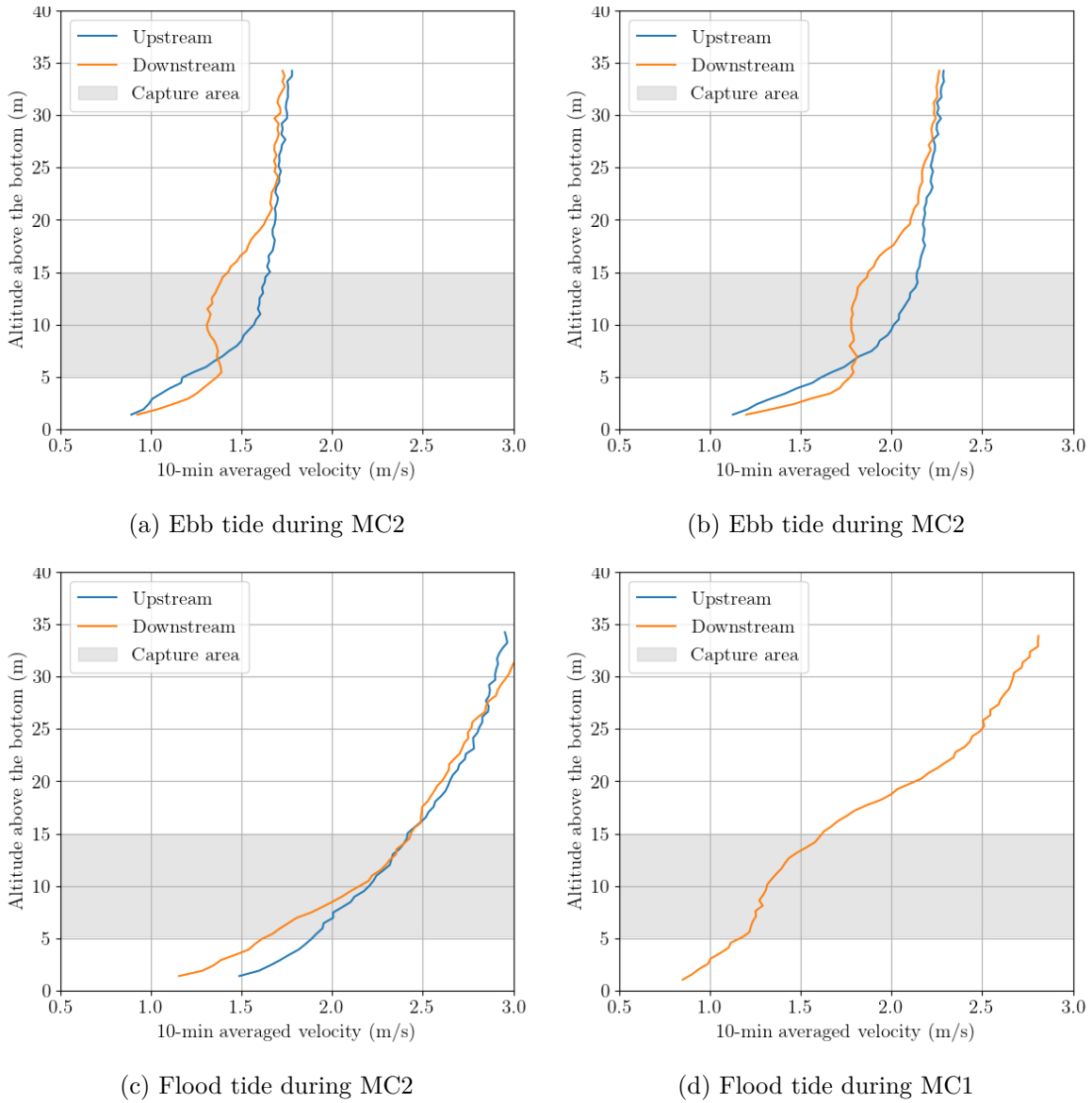


Figure 2.10 – Upstream and downstream 10-minutes averaged velocity profiles at the tidal velocity peak measured by bottom mounted ADCP placed as shown in Fig. 2.2, with the turbine is in production mode.

Temporal domain

Fig. 2.11 presents a time series at 1 Hz of the axial load on the turbine during the hour centred on the tidal velocity peak. Fig. 2.11 (a and b) are at flood tide with a similar incident velocity of approximately 2.1 m/s, in calm and rough sea conditions respectively, and Fig. 2.11 (c and d) are at ebb tide with a similar incident velocity of approximately 1.5 m/s, in calm and rough sea conditions respectively too. As explained in the section 2.1.2.1, two transformation matrices, using different strain gauges, are needed to assess axial loads in the two directions (positive or negative) due to the base asymmetry. For equivalence between flood and ebb tide, Fig. 2.11 displays the absolute value of the axial load in the main direction (Fx) and its opposite ($Fx - opp$) in negative. From these plots, it is obvious that the presence of harsh waves generates significantly

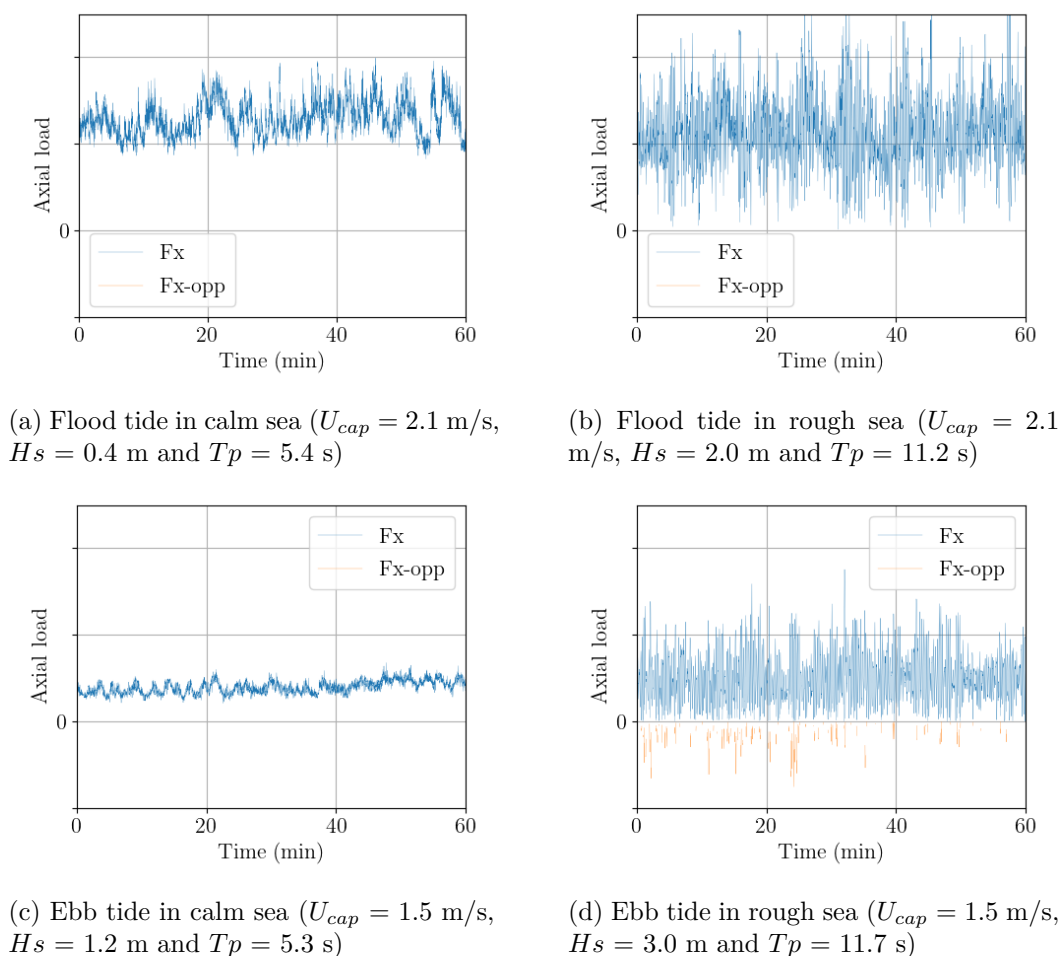


Figure 2.11 – Time series of the axial load on the turbine during the hour centred on the peak tidal velocity of each tidal cycle. Fx is the axial load computed from the strain gauges with the transformation matrix defined for loads in the current direction considered and $Fx - opp$ is the measurement using the transformation matrix defined for the opposite direction. The vertical axis scale is the same for the four plots but the values are not communicated.

stronger fluctuation in the axial load, without shifting significantly the mean value for similar incident velocity. Besides, one can notice on Fig. 2.11 (d) that when the mean velocity is low, and so the mean Fx load too, the waves generate loads in the direction opposed to the current flow direction. However, given the instrumentation used, we cannot fully recompose the time series of the loads when its sign changes. Consequently, for the analysis of the turbine’s behaviour that follows, only the Fx signals are considered.

To complete the mechanical behaviour analysis of the demonstrator, Fig. 2.12 displays the operating points of the two generators at 1 Hz during the hour centred on the tidal velocity peak in six different situations. The control law of the generators, displayed in black lines, is based on two curves: one that applies a torque (Q) proportional to the rotational speed (ω) to the square (Eq. 2.2) and one limiting the output power to a maximal value by speeding (Eq. 2.3). Consequently, when the incident velocity increases in calm sea conditions (Fig. 2.12 a, b and c), the mean operating point (indi-

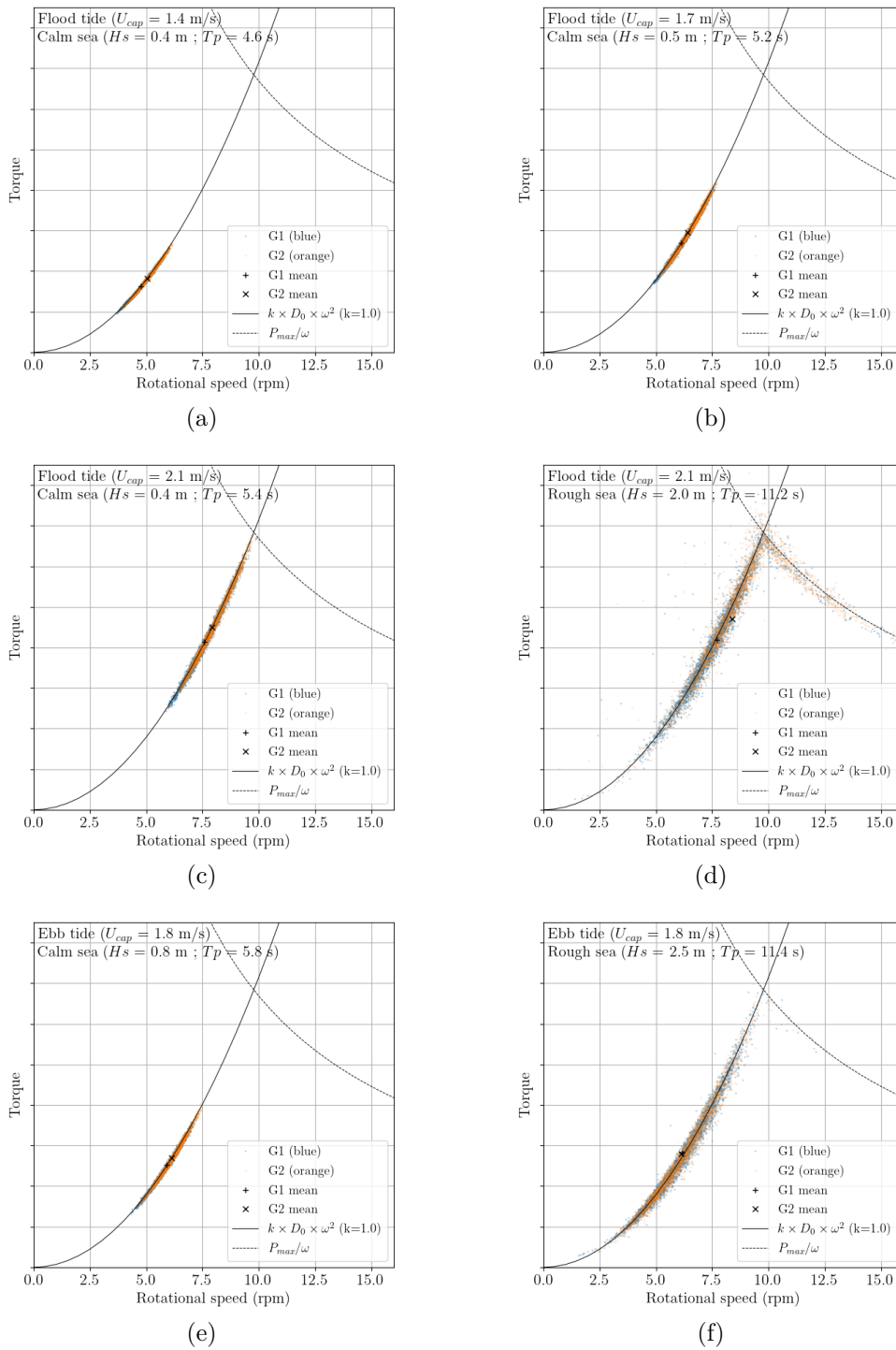


Figure 2.12 – Operating point of the two generators (G1 in blue, G2 in orange) at 1 Hz over the hour centred on the tidal velocity peak. (a, b & c) are at flood tide in calm sea conditions with $U_{cap} = \{1.4, 1.7, 2.1\}$ m/s respectively. (c & d) are at flood tide with $U_{cap} = 2.1$ m/s in calm and rough sea states respectively. (e & f) are at ebb tide with $U_{cap} = 1.8$ m/s in calm and rough sea states respectively. The black crosses represent the mean operating point and the black lines the control laws. The vertical axis scale is the same for the six plots but the values are not communicated.

cated by the black crosses) shifts to higher Q and ω . In addition, it appears that the spreading of the operating points along the control law curve increases with the mean operating point. Furthermore, by comparing Fig. 2.12 c and e to d and f respectively, one can see that the presence of important surface waves increases the operating point fluctuation significantly even if the mean incident velocity U_{cap} is constant. When the latter is high, the presence of waves can even lead the generators to operate following the power limiting control law while this is not the case in calm sea conditions (Fig. 2.12 c and d). Conversely, the mean operating point over the hour are unchanged between rough and calm sea conditions, given the uncertainty on the mean incident velocity assessment, when the power limit is not reached.

Spectral domain

For spectral analysis of the mechanical behaviour we focus on two pairs of cases with high incident current velocity, corresponding to the cases presented in Fig. 2.12 (c to f), to avoid uncertainties due to sign changes in the axial load for the spectral analysis (Section 2.1.3.2). Fig. 2.13 compares the spectral response of the demonstrator at flood (a and b) and ebb tides (c and d), in calm (a and c) and rough sea states (b and d). Each sub-figure presents the Fourier Transform (FT) of the velocity measured above the turbine and averaged on a surface equal to the capture area (U_{HQ}), the FT of the torque of the two generators (Q_{G1} and Q_{G2}) and of the axial and transverse loads. In addition, the bottom subplot displays the coherence function between the velocity and the torque as well as between the velocity and the axial load spectra.

On one hand, in the case of calm sea states, the frequency content of the turbine response and of the flow is poor with most of the response contained mainly in the low frequencies, below 0.06 Hz, and without any peaks at higher frequencies. Consequently, the coherence function of the velocity with the torque and with the axial load is below 0.5 at all the frequencies meaning that the turbine response is not related to the flow fluctuation. Besides, a peak related to the blade passing frequency is expected (Harrold et al., 2019) but the Nyquist frequency of these 1 Hz measurement is too low to observe it.

On the other hand, in rough sea states, the velocity FT shows the contribution of the waves to the flow fluctuation, between 0.05 and 0.2 Hz. The pattern observed on the velocity FT is easily recognisable on the torque and loads FT, which is confirmed by the high levels of coherence between the spectra. One can also notice that the coherence level is at its maximum for the lowest frequency waves and decreases as the frequency increases. This shows that the demonstrator responds more strongly to long period waves. Overall, this result reveals the high sensitivity of the bottom mounted 2-VATT to the periodic loads induced by surface waves.

2.1.3.3 Loads statistics

This last section aims at summarising the sea states influence on the 2-VATT response by studying most of the instants identified using the algorithm described in the Section 2.1.2.4 from a statistical point of view. Given the fact that the two rotor columns behave similarly both in the temporal and spectral domain, the following analysis focuses on the generator 1.

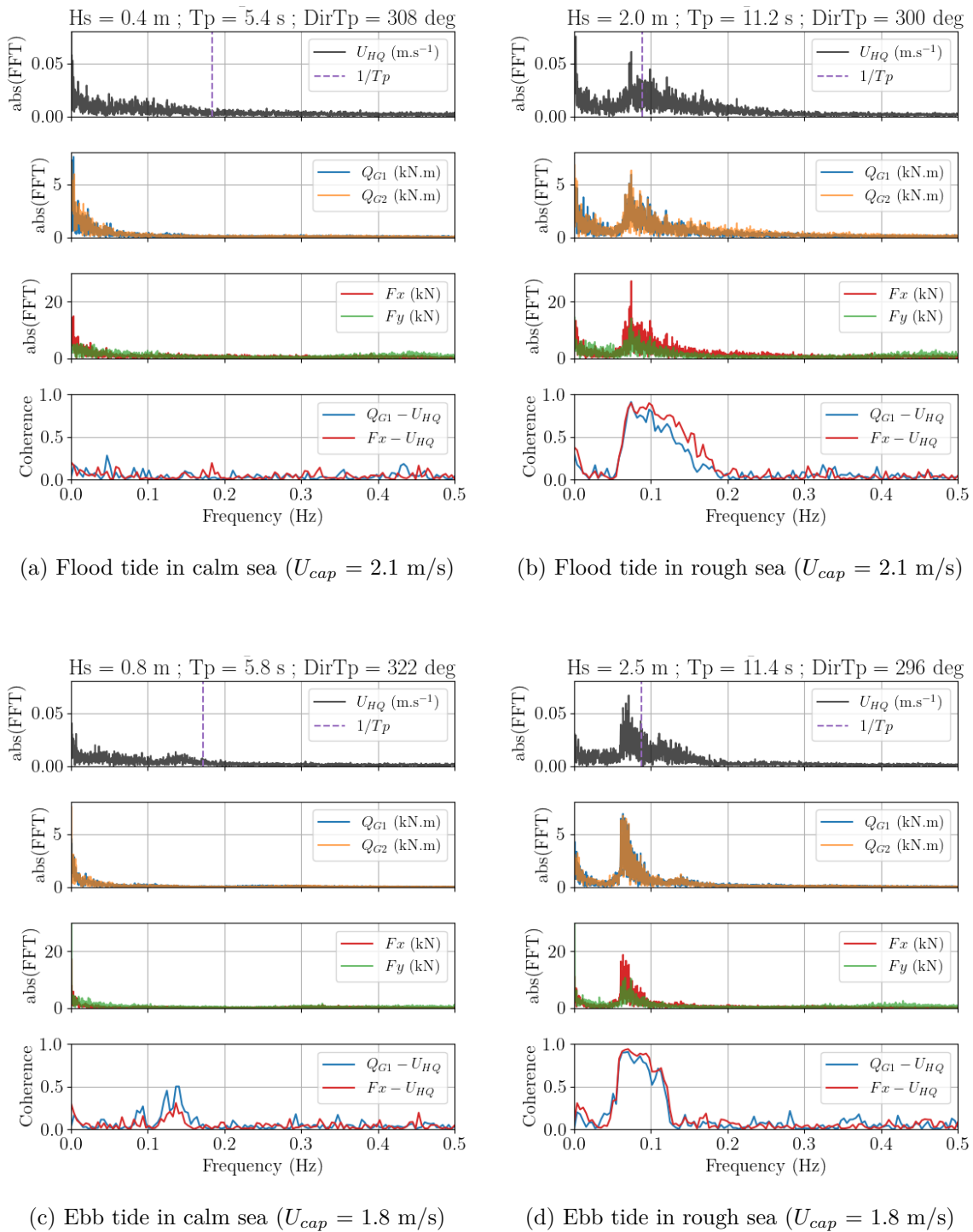


Figure 2.13 – Each sub-figure presents the Fourier Transform of the torques of each generator (Q_{G1} and Q_{G2}), of the axial and transverse loads and of the vertically averaged velocity measured above the turbine (U_{HQ}) as well as the coherence function between $Q_{G1} - U_{HQ}$ and $Fx - U_{HQ}$. Cases on the left are in calm sea states and in rough sea states on the right, at flood tide at the top and ebb tide at the bottom. The data analysed is the hour centred on the peak velocity.

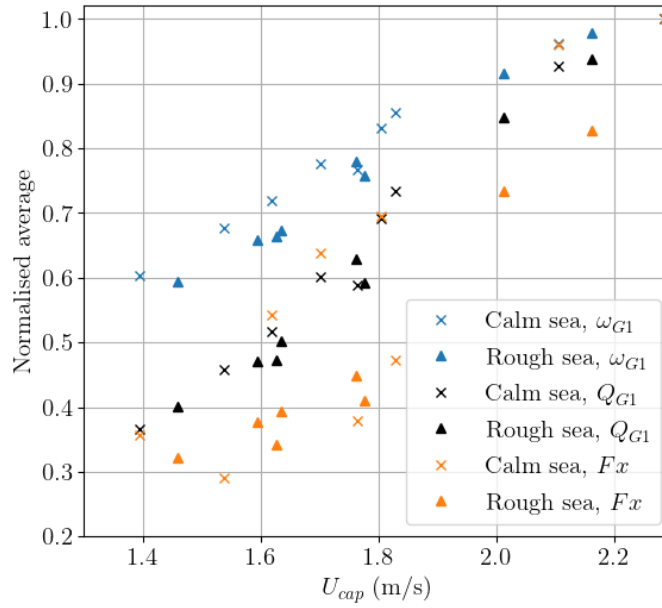


Figure 2.14 – Normalised average over the hour centred on the tidal velocity peak of the torque (C_{G1}) and the rotational speed (ω_{G1}) of the generator 1, and of the axial load (Fx) with regard to U_{cap} . Each quantity is normalised by its maximal value.

Fig. 2.14 displays the normalised average over the hour centred on the tidal velocity peak of the rotational speed, the torque and the axial load for the calm and rough sea states, with regard to the incident velocity. The three quantities increase along the same trend whether in calm or rough sea states when U_{cap} increases, showing the insensitivity of the 2-VATT to the sea states in average. The torque and thrust averages increase faster with U_{cap} as they depend on the flow velocity to the power two while the rotational speed depends on the velocity to the power one.

Besides, to quantify the load fluctuation induced by the flow, Fig. 2.15 presents the Fluctuation Intensity (FI , standard deviation divided by mean) of the rotational speed, the torque and the axial load for the calm and rough sea states. It appears that in calm sea state, the FI of the rotational speed, the torque and the axial load are insensitive to the incident velocity magnitude. In average over the points in calm sea, FI is 9.0 % for ω_{G1} , 17.9 % for C_{G1} and 16.1 % for Fx . This trend with regard to the velocity magnitude is like the turbulence intensity, which is the FI of the velocity. For a constant tip speed ratio ($\omega R/U$), the rotational speed is proportional to the incident velocity. However, the turbulence intensity is assessed between 15 and 20 % at Paimpol-Bréhat test site (Filipot et al., 2015), which is about two times $FI(\omega_{G1})$. Consequently, it means that the 2-VATT is not sensitive to all the flow fluctuation induced by turbulence. The blades are very likely not sensitive to turbulent structures of a small length scale compared to their own geometry. We assume that the turbine behaves as a low-pass filter between the flow fluctuation and the rotational speed (and so the torque) fluctuation as it is observed at lab-scale. Indeed, Deskos et al. (2020) show that the power spectra of a lab-scale horizontal axis tidal turbine follows the velocity spectra behaviour in the large turbulent scales region but has a steeper slope behaviour over the inertial frequency sub-range, illustrating the low-pass filtering of the turbine.

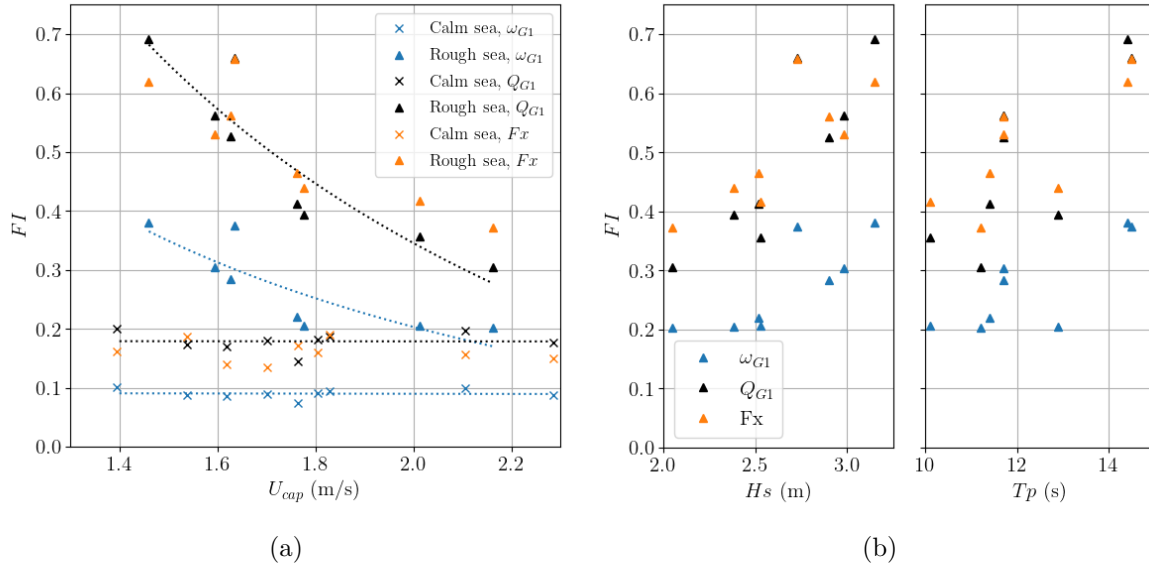


Figure 2.15 – (a) Fluctuation intensities (FI) over the hour centred on the tidal velocity peak of C_{G1} , ω_{G1} and Fx with regard to U_{cap} . (b) Fluctuation intensities of Fx and ω_{G1} in rough sea states with regard to the wave parameters H_s and T_p .

Furthermore, the average FI in rough sea states over the whole velocity range appear to be 3.0 times higher for ω_{G1} , 2.7 for C_{G1} and 3.1 for Fx compared to the calm sea state. The torque and thrust FI exceed 50 % when H_s is higher than 2.8 m, reaching almost 70 % for the largest waves ($H_s ; T_p$) \simeq (3.1 m ; 14 s). One can also notice that the machine loads FI in rough sea states decrease with U_{cap} . The first explanation for this result is the definition of FI itself, which is the division of the standard deviation by the average of the signal. A given wave induces a given periodic solicitation and so a given standard deviation of the loads. Besides, the average of the three quantities considered increases with U_{cap} (Fig. 2.14). Consequently, for a given wave, the ratio of the loads standard deviation to the average decreases when the velocity increases. A second explanation, due to a database bias, intensifies this trend. Indeed, Fig. 2.15 (b) shows that the FI increases with H_s and T_p . But, by putting Fig. 2.15 (a) and (b) together, it appears that the cases at high H_s are also those at low U_{cap} , and vice versa. Thus, even though the database is made of 21 months of measurements, it does not allow us to decorrelate clearly the influence of the incident velocity and the waves height on the evolution of FI in rough sea states.

2.1.4 Conclusions

HydroQuest achieved full scale deployment in spring 2019 when it immersed its first 1 MW capacity tidal turbine at EDF's Paimpol-Bréhat test site. More than two years after its immersion, the machine was retrieved, although still fully operational, showing the reliability of such bottom mounted twin vertical axis turbines. The demonstrator was equipped with instrumentation to measure electrical power generation, rotors rotational speed and turbine loads. Acoustic Doppler Current Profilers were also placed around the turbine to qualify the incident flow velocity profiles and the surface waves characteristics.

The characterisation of the environmental conditions present at Paimpol-Bréhat show that the ebb and flood tide directions are not symmetrical, leading to a turbine misalignment of about 7° at flood and 15° at ebb tide, and that the velocity profile is strongly sheared at the turbine height. Surface waves appear to propagate mainly in the same direction as flood tide and are, therefore, mainly against ebb tide currents.

The mechanical behaviour analysis shows that the presence of surface waves multiplies the fluctuation intensities of rotational speed, torque and thrust by almost 3 compared to cases in calm sea state. The latter exceeds 50 % for thrust and torque when Hs is higher than 2.8 m and reaches 70 % for the largest waves ($Hs ; Tp$) \simeq (3.1 m ; 14 s), without shifting significantly the average values. This fluctuation increase appears to be directly linked to the periodic solicitations of the waves in the spectral domain, even though the demonstrator is installed more than 35 m below the surface. We also observed that the fluctuation intensity of the rotational speed is about 2 times lower than the turbulence intensity, which shows that the turbine behaves as a low-pass filter, whatever the control parameter.

To complete this study, a better characterisation of the spatial variability of the flow and of the influence of the ADCP position on the mean incident velocity assessment would help explaining the power curve differences. In addition, proper wake measurement campaigns would be needed to complete its characterisation and to explain why the turbine wake behaves differently between ebb and flood tides. Finally, in a near future, these results will be compared to those obtained at lab-scale to characterise scale effects and define proper extrapolation laws from reduced-scale results to full-scale.

2.2 Design method and hydrodynamic coefficients assessment

To complete the state of the knowledge regarding the full-scale prototype for the comparison between reduced- and full-scale results, we make use of some works done by HydroQuest before and/or simultaneously with the preparation of this thesis. We first describe the method followed to design the ducted 2-VATT structure and to assess the extreme loadings (2.2.1), before discussing the actual load measurements on the demonstrator. We finally present the method to get the power coefficient evolution with the tip speed ratio of the prototype and the results (2.2.2).

2.2.1 Design method and load assessment

The method followed by HydroQuest for the mechanical design of the 1 MW-rated demonstrator is thoroughly described in internal reports (HydroQuest, 2018b; HydroQuest, 2018c; HydroQuest, 2018a). Overall, the goal is to design a structure able to withstand the worst turbine situation in the worst environmental conditions it would face during its lifetime. These are called the ultimate limit states. Three turbine situations are identified as critical for the structural design:

- normal operating with the rotors rotating at the nominal rotational speed and the device producing power;
- runaway of the two rotor columns, which generates the maximal thrust among all the possible situations;

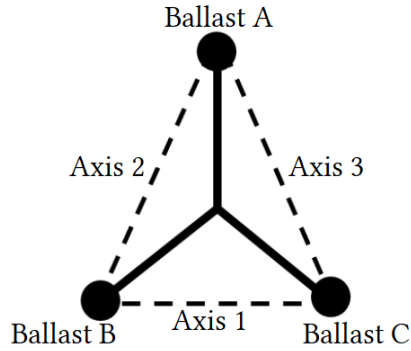


Figure 2.16 – Top view scheme of the gravity base overturning axes.

Table 2.1 – Design criteria to which the Paimpol-Bréhat prototype mechanical design has to resist.

Index	Definition
1	Maximal force in the turbine heading direction F_x
2	Maximal force in the transverse direction F_y
3	Maximal force in the vertical direction F_z
4	Maximal sliding force $\sqrt{F_x^2 + F_y^2} + f_c \times F_z$
5	Maximal overturning moment around the axis 1
6	Maximal overturning moment around the axis 2
7	Maximal overturning moment around the axis 3

— runaway of one column while the other is parked, which generates the maximal torsion on the gravity base.

In addition, the environmental conditions at the test site are assessed by a large omnidirectional meteocean data analysis. The worst conditions are considered as a combination of the maximal current speed with a 50 Years Return Period (YRP) and the largest wave conditions with a 5 YRP, and vice versa (5 YRP current with 50 YRP wave), for several current and wave directions. Facing those situations, the final device has to satisfy seven design criteria, summarised in Tab. 2.1. First, the turbine and the base designs has to resist to the maximal force in the turbine heading direction (F_x), in the transverse direction (F_y) and in the vertical direction (F_z). In addition, the device stability also has to be guaranteed. To ensure no-sliding, the structure must resist to the maximal sliding force defined as $\sqrt{F_x^2 + F_y^2} + f_c \times F_z$ with $f_c = 1.1$ the seabed friction coefficient. Finally, the device has to remain stable facing the maximal overturning moments around the three base axes (Fig. 2.16).

The first step is to identify the most detrimental directional current and wave conditions among the meteocean database regarding each design criteria. To this aim, the maximal loads in each condition is computed based on the hydrodynamic load coefficients measured on a 1/20 scale static model of the turbine, tested in the Ifremer wave and current flume tank; and on an estimation of the maximal instantaneous velocity at the turbine height at sea, considering the maximal current velocity and the maximal

Table 2.2 – Most detrimental wave and current conditions regarding the whole design criteria. Directions are relative to the turbine heading and the velocity magnitude is at the turbine height.

Index	Wave			Current	
	Dir (°)	Hs (m)	Tp (s)	Dir (°)	Vel (m/s)
54	15	7.6	15.0	5	2.9
83	-15	10.4	15.0	-5	2.1
87	0	10.4	15.0	0	2.1
100	15	10.0	15.0	25	2.3

orbital velocity due to the waves according to Airy’s linear wave theory. The additional contribution of the turbulence to the maximal loads is considered empirically from the tank experiments and assessed as a ratio of the loads in steady current alone. It turns out that four specific wave and current conditions cover the critical situations for the seven design criteria (Tab. 2.2). Finally, in each of these conditions, the instantaneous loads are computed with the turbine operating in the three critical situations (normal operating, runaway of the two columns, one runaway and one parked rotor column) at the maximal instantaneous velocity. These loads are computed by numerical simulations in a horizontal cross-section of the turbine based on the unsteady Reynolds-averaged Navier-Stokes equations with corrections to add the loads applied to the horizontal plates and the generator shelters.

Furthermore, beyond the ultimate limit states, the prototype design also aim at ensuring that the structure resists to the fatigue stress. The fatigue lifetime of the turbine is designed for 5 years (anticipating a possible reuse) and that of the foundation for 2 years. The load cycle considered is based on the annual distribution of the environmental parameters considering the 2 years return period wave and current conditions. Given the short lifetime, the fatigue design criteria are easily covered by the ultimate limit state covering.

To monitor the loads endured by the structure during the tests at sea and so to get feedback on the load assessment used for the structural design, strain gauges were fixed inside the vertical mast of the base. The goal was to measure the horizontal forces (streamwise and crosswise) and the torsion torque applied at the top of the base mast by the turbine. Due to some delay in the time schedule, the strain-to-load relationships could not be correctly defined before the launching of the device. Therefore, the calibration of the horizontal loads was done after the tests at sea, when the base was brought back to the dock in Cherbourg in 2021. The calibration process and the results are described in details in an internal report (HydroQuest, 2022b). Using a crane and a specific slings setup, horizontal loads between 0 and 120 kN were applied at the top of the base mast (Fig. 2.17), where the turbine is fixed to the base. The loads applied by the crane and the gauge strains were measured simultaneously. We find that a linear combination of two gauge strains, diametrically opposed in the load direction, allows to track the load applied with 20 to 30 % error for the loads in the turbine heading direction. Those linear combination can then be used to compute the horizontal loads applied to the demonstrator in operation but the torsion measurements were abandoned.



Figure 2.17 – Setup used to calibrate the strain of the gauges with regard to the horizontal load applied at the top of the base mast.

In the previous part (2.1), we presented the MC1 and MC2 Measurement Campaign results in the scope of the power performance assessment. Following an analogous methodology, the drag coefficient of the ducted 2-VATT demonstrator is assessed using the simultaneous strain gauge and ADCP measurements (HydroQuest, 2022a). During the tests at sea, the strain gauge signals drifted with time. Those drifts are corrected assuming no hydrodynamic loads at each slack tide. While the cubic power weighted average of the velocity is computed over the capture area and over 10 minutes for the power assessment according to the TS 62600-200 (IEC, 2013), the square power weighted average velocity (U_{cap2}) is computed over the same area and time for the drag coefficient assessment. Fig. 2.18 displays the evolution of the force in the turbine heading direction (F_x) with regard to the square power weighted velocity. It appears that the loads measured can be more than 5 times higher than the loads applied in the calibration process, which may add error in the results compared to the calibration results. That being, we can compute the drag coefficient (C_x) of the demonstrator using a second order polynomial fit of the bin values like $F_x = 0.5\rho S_{rot}C_xU_{cap2}^2$, with ρ the water density and $S_{rot} = 4DH_{blade}$ the projected area of the four rotors. We find that the overall average drag coefficient of the ducted 2-VATT is 1.5 during MC1 and 1.7 during MC2 when the flow velocity exceeds $1.2 \text{ m}\cdot\text{s}^{-1}$. Finally, Fig. 2.19 displays the distribution of the 10-minute averaged drag coefficient of the prototype in operation during flood tides of the measurement campaigns. We observe that 98 % of the C_x values are contained in the interval $[1.2; 2.0]$ during MC1 and in $[1.4; 2.1]$ during MC2. Therefore, the 10-minute averaged highest drag coefficient measured are more than 30 % higher than the overall average over the whole measurement campaigns. Similarly to the power curve differences, we assume the difference of drag coefficient between MC1 and MC2 to be most probably due to the difference of ADCP positions which gives different reference upstream velocities.

2.2.2 Power coefficient and optimal tip speed ratio assessment

Besides, HydroQuest carried out specific tests between MC1 and MC2 to define the evolution of the power coefficient (C_{Pcol} , Eq. 2.4 with H_{blade} the blade height) with the tip speed ratio (λ , Eq. 2.5) of each rotor column. The method used and the results are presented in an internal report (HydroQuest, 2021) and summarised below.

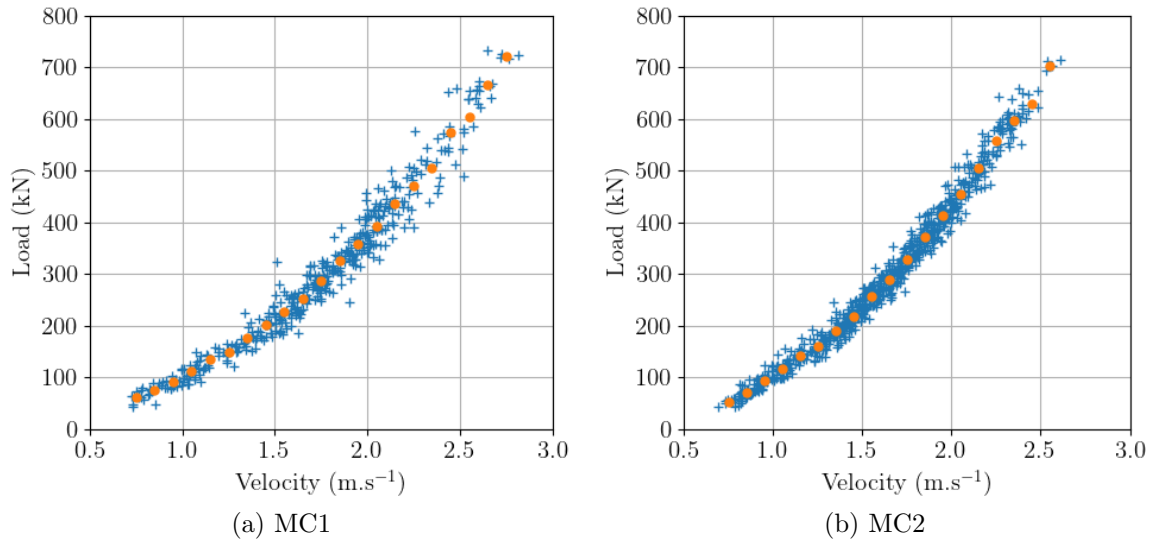


Figure 2.18 – Evolution of the force in the turbine heading direction with regard to the square power weighted velocity during the flood tides of the two measurement campaigns. The crosses are the 10-minute average values and the dots are the 0.1 m.s^{-1} bin values, from (HydroQuest, 2022a).

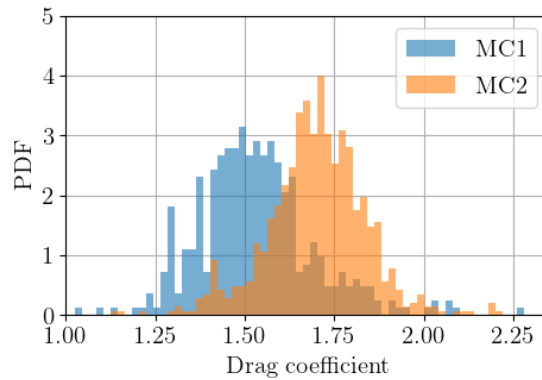


Figure 2.19 – Probability density function (PDF) of the 10-minute-averaged drag coefficient measured during flood tides on the demonstrator in operation during the two measurement campaigns, from HydroQuest (2022a).

$$C_{Pcol} = \frac{\omega Q}{\rho D H_{blade} U_{cap}^3} \quad (2.4)$$

$$\lambda = \frac{\omega R}{U_{cap}} \quad (2.5)$$

Out of MC1 and MC2, we did not measure the far upstream velocity needed for the computation of both C_{Pcol} and λ . The only flow velocity measurement available is that of the ADCP-HQ measuring the velocity profile above the turbine. During MC1, the three ADCPs (ADCP1-NW, ADCP1-SE and ADCP-HQ, see Fig. 2.2) measured simultaneously the velocity profile above them. Therefore, we can establish a relationship between the velocity measured by the ADCP-HQ above the turbine and the far upstream

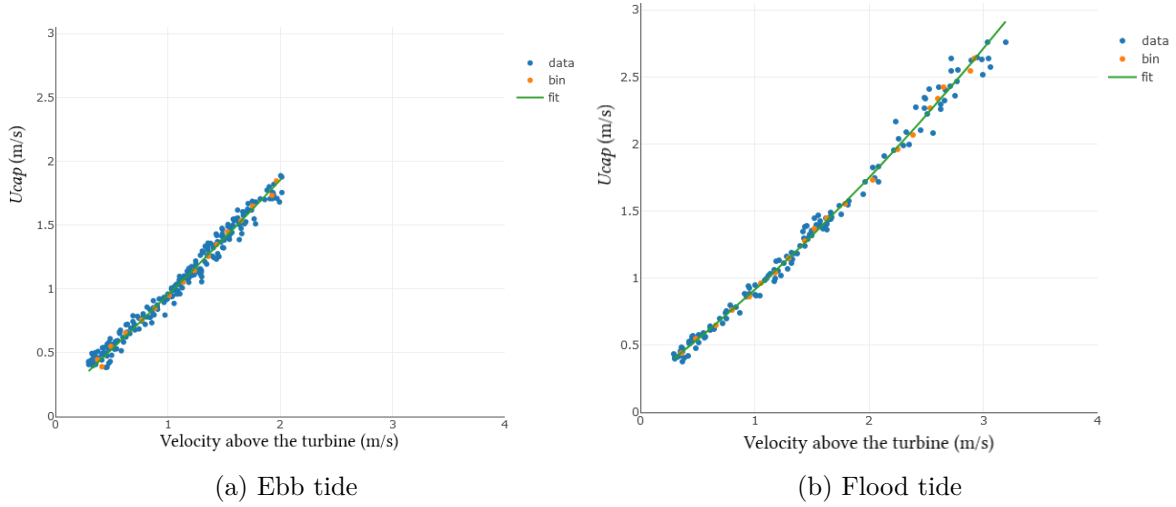


Figure 2.20 – Cubic power weighted average upstream velocity (U_{cap}) versus the velocity measured above the turbine by the ADCP-HQ, from (HydroQuest, 2021).

velocity measured at the turbine height by either the ADCP1-NW for the flood tides or the ADCP1-SE for the ebb tides. To this end, we consider the ADCP cells covering the turbine capture height for the bottom mounted ADCP and the cells covering that same height above the ADCP-HQ head. Then, we compute the cubic power weighted time and space average of the velocity following the IEC (2013) Technical Standard 62600-200. The averaged velocities are binned, still according to that standard, and fitted with a second order polynomial (Fig. 2.20). Thus, we obtain the relationships 2.6 and 2.7 to estimate the far upstream reference velocity measured during MC1 from the velocity measured by the ADCP-HQ above the turbine.

$$U_{cap,flood} = 0.064U_{ADCP-HQ}^2 + 0.645U_{ADCP-HQ} + 0.204 \quad (2.6)$$

$$U_{cap,ebb} = 0.034U_{ADCP-HQ}^2 + 0.800U_{ADCP-HQ} + 0.118 \quad (2.7)$$

First, during the spring tides of spring 2020, the rotors tip speed ratio was changed manually by setting different values of the control parameter k (Eq. 2.2), from one tidal cycle to the other. The output power and rotational speed measurements were carried out on a single rotor column (G1), with the other one (G2) parked, with $k = \{0.35; 1.00; 1.52; 1.75; 2.00; 2.30; 3.00\}$. Fig. 2.21 displays the results showing the 10-minute averaged power coefficient with regard to the tip speed ratio during flood tides, when the output power exceeded a given threshold. Each symbol corresponds to a k value and the symbols colour represents the value of the estimated upstream reference velocity. The pink dots are the averages of the C_{Pcol} and λ for each k value while the error bars (and the pink shade) represent the uncertainty on the C_{Pcol} and λ values due to the estimation of the upstream velocity instead of the actual velocity measurement. The pink curve is a third order polynomial fit of the average points. The results show that the tip speed ratio providing the maximal power coefficient is about $\lambda_{opt} \simeq 1.35$ when $k \simeq 1.5$. The same method was applied during the summer 2020 while the two rotor columns were in operation. Fewer k values were tested, mostly focused around the optimal value, as presented in Fig. 2.22. The optimal tip speed ratio and the maximal

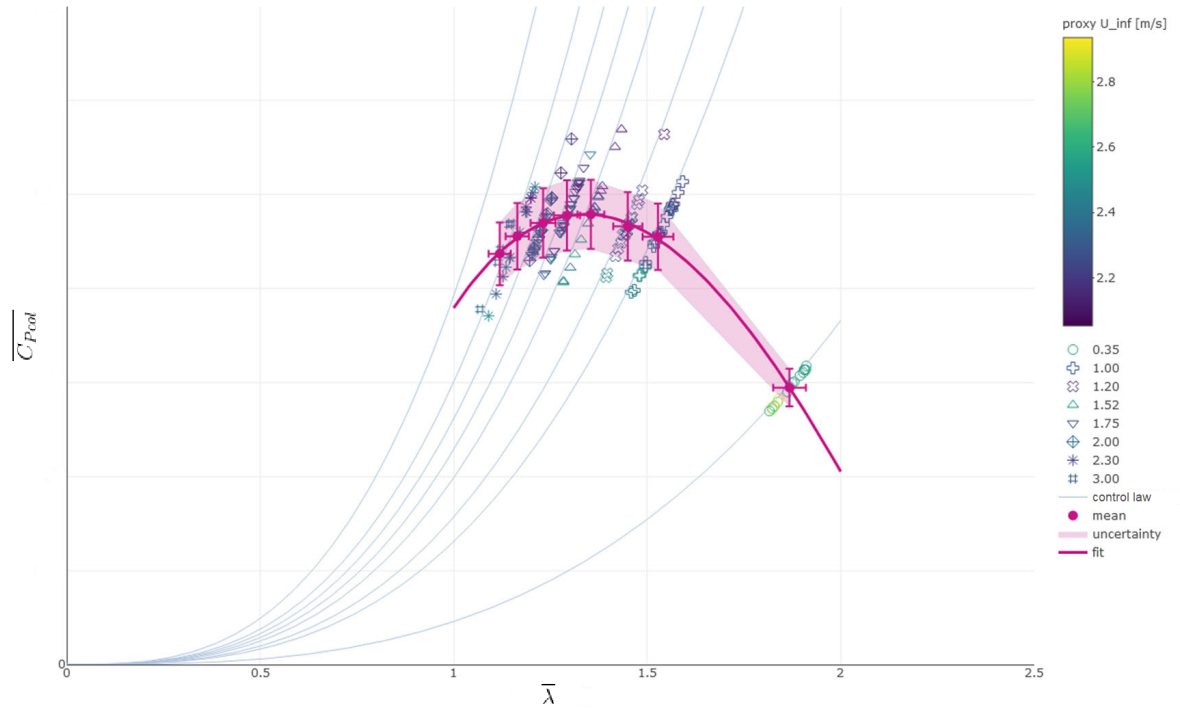


Figure 2.21 – Average power coefficient evolution with the tip speed ratio of the rotor column G1 while G2 was parked during flood tides. From (HydroQuest, 2021).

power coefficient appear to be the same whether the rotor column operates alone or with the second column in operation. In addition, the results seem to indicate that the $C_{Pcol}(\lambda)$ curve widens when the two columns operate together compared to the single column case, which provides a higher power coefficient on a large tip speed ratio range.

The same method is applied to qualify the performance of the second rotor column G2 as well as during ebb tides (HydroQuest, 2021). The results are less consistent as the third order polynomial fit of $C_{Pcol}(\lambda)$ do not follow the typical bell curve shape. This may be the result of a too low number of measurement points with an output power over the defined threshold to get relevant average $C_{Pcol}(\lambda)$ points. Although the polynomial fit is quite inconsistent, the average power coefficient of the second rotor column during flood tides appears to be about 10 % higher than that of G1, which is assumed to be due to the misaligned flow direction with regard to the turbine heading. Finally, maximal averaged power coefficient appears constant for incident velocities from about 1.5 to 2.8 $\text{m}\cdot\text{s}^{-1}$ (HydroQuest, 2021). The present $C_{Pcol}(\lambda)$ results can explain part of the power performance difference between MC1 and MC2 seen in the section 2.1.3.1 since the rotational speed was higher than its optimal value with $k = 1.0$ during MC1 while it was optimal with $k = 1.5$ during MC2.

To sum up, selecting specific instants in the two year-long measurement database, this chapter provides an overview of the full-scale ducted 2-VATT performance as well as of the wake and the mechanical behaviour. The performance results, slightly different between the two independent ADCP measurement campaigns, question the reference velocity position choice for performance assessment and suggest an effect of the flow direction on the 2-VATT behaviour. The wake of the device is observed but the measurements are insufficient to characterise it properly. Focusing on the influence of the

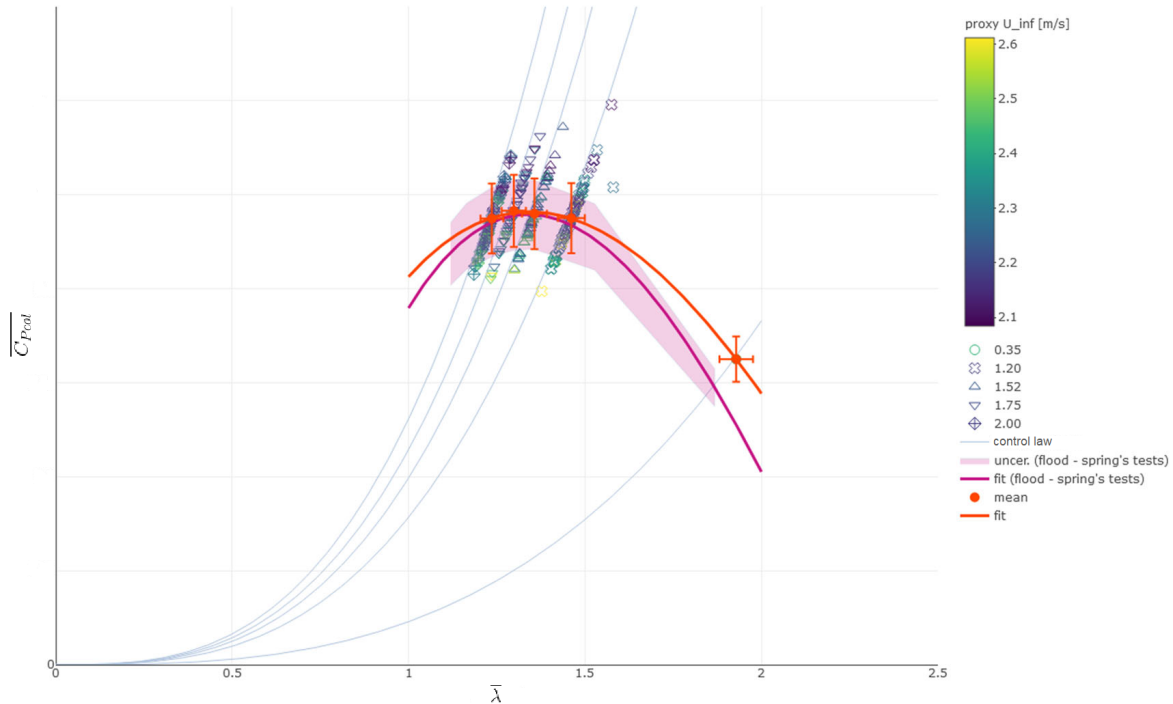


Figure 2.22 – The orange curve is the average power coefficient evolution with the tip speed ratio of the rotor column G1 while G2 was operating too, during flood tides. The pink curve is that obtained with G1 operating with G2 parked (Fig. 2.21). From (HydroQuest, 2021).

sea state, we found that the presence of surface waves (with H_s higher than 2 m and T_p higher than 10 s) multiplies the fluctuation intensities of the rotational speed, the torque and the thrust by almost 3 compared to the cases in calm sea state, while not significantly impacting the average values. We also characterised the average power performance of the prototype and the streamwise force coefficient based on the two dedicated measurement campaigns. Despite a one year extension of the initial testing period at the Paimpol-Bréhat test site, the prototype was retrieved during the first year of the preparation of this thesis, which prevented us from carrying out additional measurements at sea. The database and the results presented in this chapter are the starting point for the work that follows, including the comparison between full- and reduced-scale as well as the definition of the flow conditions in which the turbine response needs to be studied in more details.

Reduced-scale model behaviour and scale effects assessment

In the perspective of the next turbine generation, HydroQuest wants to improve its experimental and numerical design tools to gain confidence in its capacity to predict the full-scale performance and loads from the experiments at reduced-scale. This can only be done by comparing the results obtained at sea to those obtained in the laboratories. Therefore, we developed a 1/20 scale model of the ducted 2-VATT prototype that we tested in the Ifremer wave and current flume tank. In the first part of this chapter (3.1), we study the model behaviour in the typical idealised experimental flow conditions, with a low ambient turbulence level, a still free surface, a uniform velocity profile and a current direction collinear with the turbine heading. That first study at reduced-scale aims at defining the baseline both to characterise the scale effects compared to the results at full-scale, and to analyse the effect of the flow conditions on the ducted 2-VATT behaviour. Indeed, we analyse the validity of the experimental results by comparing them to the full-scale results presented in the previous chapter in the second part (3.2). We discuss the extrapolation of the power performance, the loads and the wake measurements from reduced- to full-scale with the use of numerical models.

3.1 Reduced-scale model behaviour and wake in idealised flow conditions

3.1.1 Introduction

This part was originally published as Moreau et al. (2023c), “Experimental performance and wake study of a ducted twin vertical axis turbine in ebb and flood tide currents at a 1/20th scale”, in *Renewable Energy*. The introduction is made short to avoid redundancy with the general introduction of the thesis. The direction of the flow

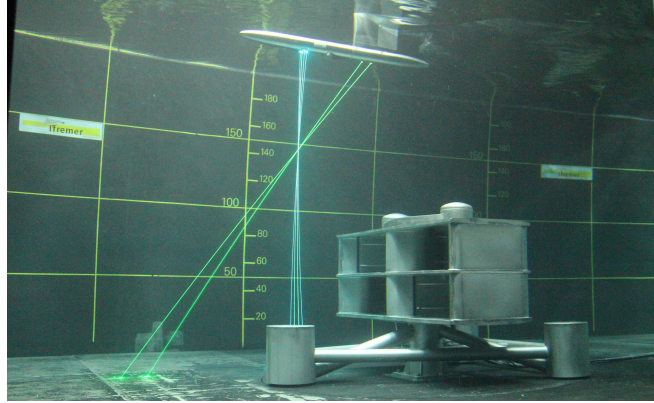


Figure 3.1 – Model of HydroQuest’s ducted 2-VATT during 3C-LDV flow measurements in the Ifremer wave and current flume tank.

reverses between ebb and flood tides, so the flow goes through the TEC from one side or the other. As a result, the relative counter-rotation direction of the two vertical axis rotor columns that compose HydroQuest’s 2-VATT is reversed too (Fig. 1.2). It was shown experimentally on non-ducted twin vertical axis wind turbines that the counter-rotational direction affects the turbine’s wake, without affecting significantly the mean power coefficient (Lam et al., 2017; Müller et al., 2021; Vergaerde et al., 2020a). Müller et al. (2021) shows that, when the blades move against the flow at the turbine centre, the wakes of the two rotors merge immediately downstream of the turbine and the merged wake expands mainly in the vertical direction; whereas, when the blades move with the flow at the centre, the wakes of the two rotors remain separated and the global wake mostly expands horizontally. Lam et al. (2017) finds similar effects of the relative counter-rotation direction and observes pairs of stationary counter-rotating vortices at both sides of the twin rotors that contribute to the flow mixing, similarly to the wake of isolated vertical axis turbines (Bachant et al., 2015; Rolin et al., 2018). Furthermore, Grondeau et al. (2019) presents numerical simulations of HydroQuest’s ducted 2-VATT tidal turbine wake in 3D during ebb tide, without the gravity base, and Jégo et al. (2021) considers it in 2D in both ebb and flood tide flow directions. The numerical results show that the power production is insensitive to the flow direction and that the rotor wakes merge faster with a stronger velocity deficit downstream of the central fairing in the flood tide configuration compared to the ebb. However, the numerical models are only validated by comparison to experimental results on a single non-ducted VATT since no results existed for a ducted 2-VATT.

Thus, in this part, the ducted 2-VATT is tested in the two relative heading directions in the Ifremer flume tank to analyse the effect on the response and the wake of the ducted 2-VATT. The results also provide ad hoc data for numerical models validation. Section 3.1.2 first describes the turbine model and its setup in the tank before presenting the database acquisition and processing. Section 3.1.3 reports on the flow direction effects on the performance of the 2-VATT in terms of power and drag and on the angular distribution of the torque. Then, section 3.1.4 presents the effects of the flow direction on the wake of the turbine with regard to its width, height, dynamics and overall recovery. Finally, we summarise and discuss the results in section 3.1.5.

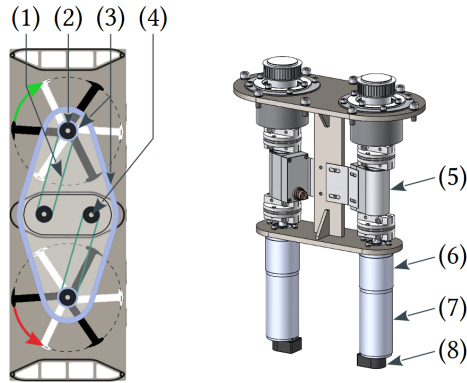


Figure 3.2 – Schematic top view of the twin counter-rotating VATT model on the monopile base, with the transmission system on the top (left). Composition of the secondary shafts, located in the central fairing of the model (right). Caption: (1) Belt; (2) Rotor shaft; (3) Seals; (4) Secondary shaft; (5) Torquemeter with angle encoder *Scaime DR2112-W*; (6) 1/26 reduction gear; (7) DC motor *Maxon RE50*; (8) Rotational speed encoder.

3.1.2 Material and method

3.1.2.1 Experimental setup

The 2-VATT model is geometrically similar to the full-scale demonstrator tested at sea with a scale factor of 1/20 (Fig. 1.2 and 3.1). It is composed of two independent counter-rotating vertical axis rotor columns. Each column is made of two levels of Darrieus type rotors with a 60° phase difference between them, and each rotor is made of $N = 3$ blades with NACA 0018 profiles projected on the swept cylinder. The blade height (H_{blade}) is 190 mm. The rotor radius ($R = D/2$) is 200 mm with a blade chord (c) of 73 mm. Thus, the rotor solidity (Nc/R) is 1.1, similarly to the full-scale demonstrator. The columns are mounted in a $W_{struc} = 1.24$ m wide mechanical structure made of fairings and plates. The overall model height, from the floor to the top of the structure is $H_{struc} = 0.84$ m. The turbine height is defined as the distance between the top and the bottom horizontal plates such that $H = 0.45$ m.

The central fairing of the turbine and the volume inside the top casing are watertight to host the electronics and the transmission system (Fig. 3.2). Indeed, the rotor shafts are linked to secondary shafts (one for each rotor column) through a belt system on the top of the turbine. Each secondary column is composed of a *Maxon RE50* DC motor equipped with a 1/26th gear reducer and a speed encoder. A *Scaime DR2112-W* torquemeter with a relative angular position encoder is also mounted on the column. The motors are piloted using remote *Escon 70/10* servo-controllers in constant speed mode. In addition, the turbine is fixed on a pseudo-tripod base through a 6-component load cell (*SIXAXES* 1.5 kN, Fig. 3.3). The tripod structure only models the hydrodynamics of the demonstrator’s gravity base. At reduced-scale, the model is actually fixed to the floor of the tank at the bottom of the central pile of the base, right below the turbine, on another 6-component load cell (*SIXAXES* 20 kN) to measure the overall loads on the turbine and the base. The tripod piles are 1 cm above the floor to avoid interferences with the load cell measurements. The reduced-scale turbine can also be fixed on a central monopile of the same height as the tripod and equipped with the same load cells

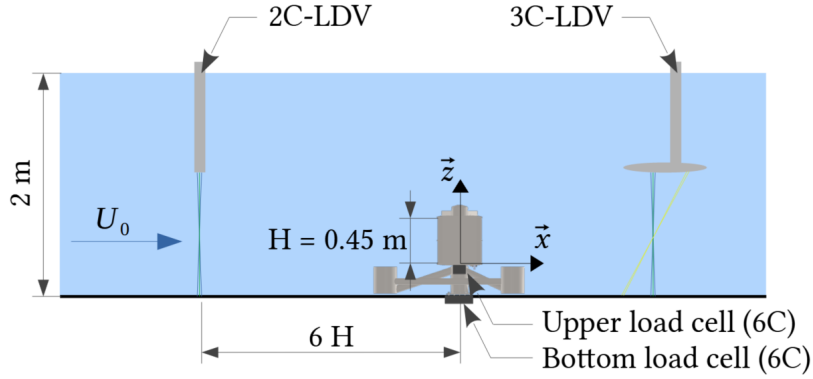


Figure 3.3 – Scheme of the experimental setup in the Ifremer wave and current flume tank (in FC).

to assess the base influence on the TEC performance and wake.

In this part, we study the effect of two flow directions representing ideal flood and ebb tides opposed at 180 degrees (Fig. 1.2). To do so, the turbine and the base are turned around in the tank as the flow direction cannot be reversed. On one hand, in the Flood tide Configuration (FC), the counter-rotating rotor blades move against the flow at the 2-VATT centre, along the central fairing, and the upstream flow encounters a single base pile, aligned with the central fairing of the turbine. On the other hand, in the Ebb tide Configuration (EC), the rotors rotate along with the flow at the centre and the upstream flow encounters two base piles, each aligned with the outer side of the circles swept by the rotors.

The 2-VATT model was tested in the Ifremer wave and current flume tank in Boulogne-sur-mer, France. The water depth is $H_{wat} = 2$ m and the width is $W_{wat} = 4$ m, with a working section of approximately 18 m long (Gaurier et al., 2020d). Consequently, the vertical blockage is equal to the one of the demonstrator at the Paimpol-Bréhat test site (41 %) and the projected surface blockage ($b = \frac{(HW)_{struc}}{(HW)_{wat}}$) is about 12 % in the tank with the tripod base, and 8 % with the turbine only. According to the literature review by Murray (2016), this surface blockage ratio is at the limit between small enough and too high to consider results as they are. Corrections due to some blockage effects might be needed to estimate performance and wake extent accurately (Bahaj et al., 2007; Ross et al., 2020b; Ross et al., 2022), but none are applied in this study.

The orthogonal coordinates system considered is such that x is in the current direction with its origin at the centre of the model and z points towards the surface with its origin at the bottom horizontal plate of the turbine (Fig. 3.3). The inlet condition in the tank is conditioned by a homogeneous grid and a honeycomb structure. The streamwise average velocity and turbulence intensity profiles at the turbine position in the empty tank are presented in Fig. 3.4. The streamwise turbulence intensity is defined as $TI_u = \sigma(u)/\bar{u}$, with u the streamwise velocity, the bar on top indicating the time average and $\sigma(\)$ the time standard deviation of the quantity between brackets. It appears that the boundary layer extends up to the bottom of the turbine, with TI_u decreasing from 7.5 to 1.5 %. The profiles are uniform over the turbine height (between $z/H = 0$ and 1).

The tests were conducted at a current setpoint of $1 \text{ m}\cdot\text{s}^{-1}$. At this speed, the Reynolds number based on the blade chord (Re_c) is of the order of $1.0 \cdot 10^5$ in the tank (Eq. 3.1,

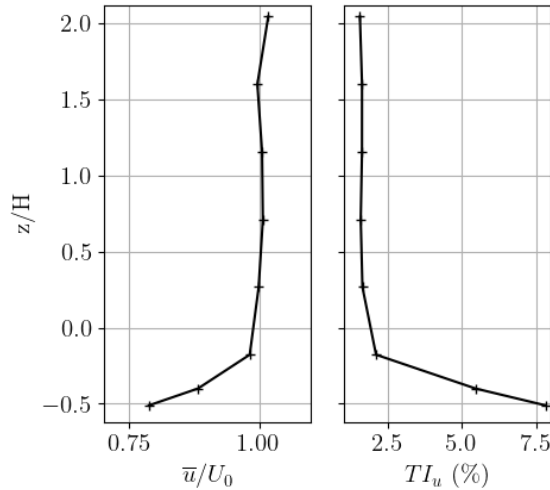


Figure 3.4 – Mean normalised streamwise velocity and turbulence intensity measured with the 3C-LDV probe at $(x, y) = (0, 0)$ without turbine.

Table 3.1 – Recap of the main similitude values between tank tests and in-situ operation at Paimpol-Bréhat.

Scale	H_{wat} (m)	H_{struc} (m)	U (m.s ⁻¹)	Fr_s	Re_c (at $\lambda = 1.5$)
1/20	2	0.84	1.0	0.30	$1.0 \cdot 10^5$
1	40	17	2.5	0.17	$5.2 \cdot 10^6$

with $\nu = 1.05 \cdot 10^{-6} \text{ m}^2 \cdot \text{s}^{-1}$ the water kinematic viscosity and λ the tip speed ratio – Eq. 3.5). At the Paimpol-Bréhat test site, the maximal current speed experienced by the demonstrator was about $2.5 \text{ m} \cdot \text{s}^{-1}$ which gives a Reynolds number at full-scale about 50 times higher than at reduced-scale (Tab. 3.1). The Froude number based on the turbine submergence (Fr_s , Eq. 3.2, with $g = 9.81 \text{ m} \cdot \text{s}^{-2}$ the gravity constant) is 1.8 times higher in the tank than at sea but it remains low enough to avoid interactions with the free surface.

$$Re_c = \frac{\lambda c U}{\nu} \quad (3.1)$$

$$Fr_s = \frac{U}{\sqrt{g(H_{wat} - H_{struc})}} \quad (3.2)$$

3.1.2.2 Data acquisition and processing

Performance measurement For hydrodynamic performance assessment, the current velocity is measured using a *Dantec* 2-Component Laser Doppler Velocimeter (2C-LDV). To do so, the tank is seeded with $10 \mu\text{m}$ diameter silver coated glass micro-particles. That probe measures the velocity along (x, y) in non-coincident mode (*i.e.* each velocity component is measured independently by each pair of lasers) with an acquisition data rate of the order of 200 Hz. The probe is placed at $x/H = -6$ and at the centre of

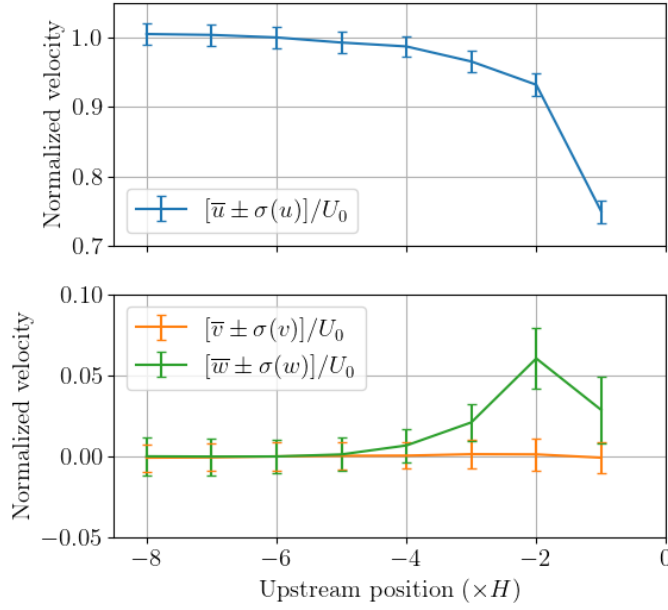


Figure 3.5 – Flow velocity measured upstream of the model in flood tide configuration at the centre of the turbine ($(y, z) = (0, 0.5H)$) and varying x positions using the 3C-LDV. Normalized streamwise velocity u at the top and transverse velocities (v, w) at the bottom.

the turbine projected area (ie. $(y, z) = (0, 0.5H)$). The mean streamwise component of the velocity at this point is considered as the reference velocity (noted U_0) and is $0.95 \pm 0.02 \text{ m}\cdot\text{s}^{-1}$ overall. Fig. 3.5 shows that the upstream flow is undisturbed by the TEC induction from this position. In addition, it also shows that the incident flow tends to avoid the turbine with a vertical velocity component value up to $0.05U_0$ at $x/H = -2$. As expected, the lateral component of the incident velocity is null at this point (centre of the tank and of the projected area of the turbine).

Synchronously with the 2C-LDV, each rotor column torque (Q), rotational speed (ω) and the two load cell signals are acquired using *National Instruments PXI* and *LabView* systems. The acquisitions last 3 minutes with a 128 Hz sampling frequency for each run to guarantee the time convergence of the mean and standard deviation of the signals. The friction torque induced by the seals and the transmission system for each rotor column (Fig. 3.2) was measured before the tests with the rotor shafts rotating without blades. It is added to the torque measurements for the hydrodynamic performance assessment. The performance results are presented in terms of power coefficient (C_P) and drag coefficient (C_x) with regard to the tip speed ratio (λ), defined in Eq. 3.3 to 3.5; with $\rho = 1000 \text{ kg}\cdot\text{m}^{-3}$ the density, P the power extracted by the two rotor columns ($P = \sum \omega Q$) and F_x the load in the streamwise direction measured by the upper load cell (Fig. 3.3). The reference surface considered is the projected area of the four rotors ($4DH_{blade}$).

$$C_P = \frac{P}{2\rho DH_{blade} U_0^3} \quad (3.3)$$

$$C_x = \frac{F_x}{2\rho DH_{blade} U_0^2} \quad (3.4)$$

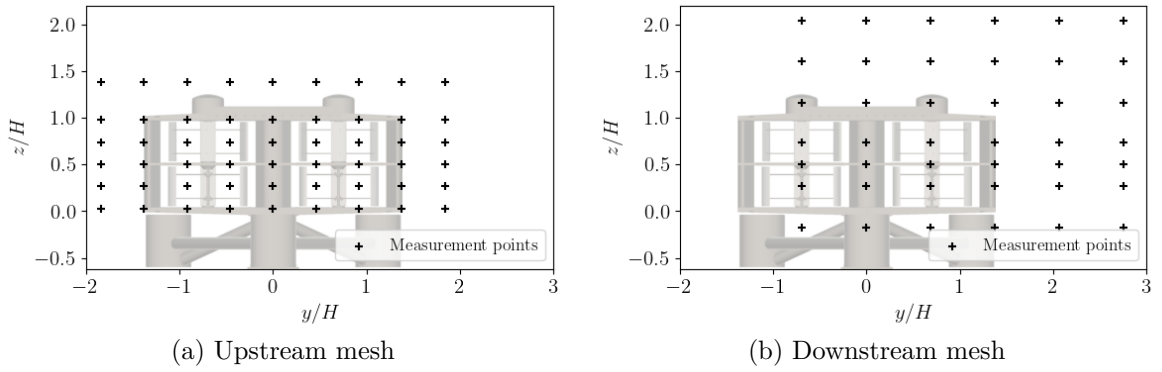


Figure 3.6 – Meshes used for velocity measurements by the 3C-LDV at a given x positions.

$$\lambda = \frac{\omega R}{U_0} \quad (3.5)$$

The distribution of the torque coefficient (C_Q , Eq. 3.6) with regard to the rotor angular position of the green column (Fig. 1.2) is also analysed. The instantaneous relative angular position (positive in the rotational direction) is computed by Hilbert transform of the torque filtered at the rotational frequency ± 0.005 Hz. The angular position being relative, the absolute angle values displayed cannot be compared between graphs. The phase-average torque coefficient, \widetilde{C}_Q , is computed over 75 revolutions with 3° angle bins. The reference surface for the computation of C_Q is the projected area of a single rotor column ($2DH_{blade}$).

$$C_Q = \frac{Q}{\rho DH_{blade} R U_0^2} \quad (3.6)$$

Wake measurement The flow surrounding the ducted 2-VATT is characterised in the two flow directions at the same operating point ($\lambda = 1.6$) using *Dantec* 3-Component LDV, in non-coincident mode. Upstream of the turbine, the flow is mapped following the mesh of measurement points presented in Fig. 3.6 (a) at $x/H = \{-1, -2\}$. At $x/H = -1$, the geometry of the 3C-LDV makes it unable to measure the points from $z/H = 0.0$ to 0.5 . Therefore, only (u, v) are measured by the 2C-LDV at those positions. Downstream, we assumed the wake to be symmetrical so we mapped the flow following the mesh in Fig. 3.6 (b) at $x/H = \{2, 3, 5, 7, 9\}$. At $x/H = 1$, the same mesh is mapped without the bottom line as the 3C-LDV probe would collide with the model. At $x/H = 0$, the top lines at $z/H = \{1.6, 2.0\}$ and the side ones at $y/H = \{2.1, 2.8\}$ are measured.

Given the LDV operating principle (Boutier, 2012), the velocity is measured every time a seeding particle passes through the measurement volume. Therefore, the acquisition rate ranges between about 50 and 300 Hz, where the mean velocity is low and high respectively, depending on the position in the 2-VATT wake. Given the orientation of the three pairs of lasers composing the 3C-LDV (Fig. 3.1), it is necessary to project the lasers measurements into the tank coordinate system to get the velocities (u, v, w) along (x, y, z) . To do so, the measurements in the lasers coordinates system are interpolated

on the same time vector (that matches the lowest data rate of the 3 pairs of lasers) to apply the transformation matrix.

The velocity contours presented hereinafter are drawn based on linear interpolations between the mesh points with a 40 mm step in the y and z directions, and 50 mm in the x direction. Ebdon et al. (2021) suggest that several complementary metrics are needed to characterise a tidal turbine wake as it is difficult to develop quantitative metrics by which to quantify simultaneously the strength of the wake as well as the region it affects. To look at the region affected by the 2-VATT, the wake width and height are computed at each x position measured, using the interpolated velocity flow fields in the (y, z) planes. As is commonly done in the literature (Masters et al., 2013; Ahmadi, 2019; Ebdon et al., 2021), a velocity threshold at $\bar{u}/U_0 = 0.9$ is defined to locate the wake boundary and analyse its shape. The half wake width is computed as the horizontal position where $\bar{u}/U_0 = 0.9$ averaged over the turbine height ($0.00 < z/H < 1.00$) and the wake height is computed as the vertical position of the velocity threshold averaged over the half turbine width ($0.00 < y/H < 1.38$). To look at the wake intensity and its recovery at each x position measured, we compute surface averages of the time averaged streamwise velocities, noted $\langle \bar{u} \rangle$, downstream of the turbine. Two surfaces in the (y, z) planes are considered to provide complementary information. The first one is the projection of the half capture area of the turbine ($\langle \bar{u} \rangle_{cap}$). The projection of the capture area is commonly used in the literature to assess the wake recovery and study turbine's interactions in an array (Mycek et al., 2014; Ebdon et al., 2021). That area is constant at all the x positions so it ignores all the wake expansion outside that restricted area. The second averaging area is the one where $\bar{u}/U_0 < 0.9$ ($\langle \bar{u} \rangle_{0.9}$). That area changes with x but it quantifies the strength of the velocity deficit in the whole region affected by the turbine wake, in contrast to $\langle \bar{u} \rangle_{cap}$. Finally, contours of turbulent kinetic energy, defined in Eq. 3.7, are also analysed at the different x positions measured, with the same interpolation steps as for the velocity contours.

$$k_{UV} = \frac{1}{2}(\sigma(u)^2 + \sigma(v)^2) \quad (3.7)$$

3.1.3 Flow direction effect on the behaviour of the ducted 2-VATT

To characterise the hydrodynamic behaviour of the ducted twin vertical axis tidal turbine in the tank and the effect of the flow direction, whether similar to Flood tide Configuration (FC) or to Ebb tide Configuration (EC), the overall turbine performance is studied before addressing the angular distribution of the torque generation.

3.1.3.1 Overall performance

The mean and standard deviation of the drag coefficient and the normalised power coefficient (Eq. 3.3 and 3.4) are presented in Fig. 3.7 with regard to the tip speed ratio (Eq. 3.5). Each curve is the average over 3 test campaigns and the error bars represent the extreme average or extreme standard deviation values among these campaigns. The amplitude between extreme average values is less than 5 % for $\overline{C_x}$ and about 10 % for $\overline{C_P}$ at the maximal performance point. Fig. 3.7(a) reveals that the drag coefficient of the 2-VATT is similar in flood and ebb tide configurations, both in terms of average

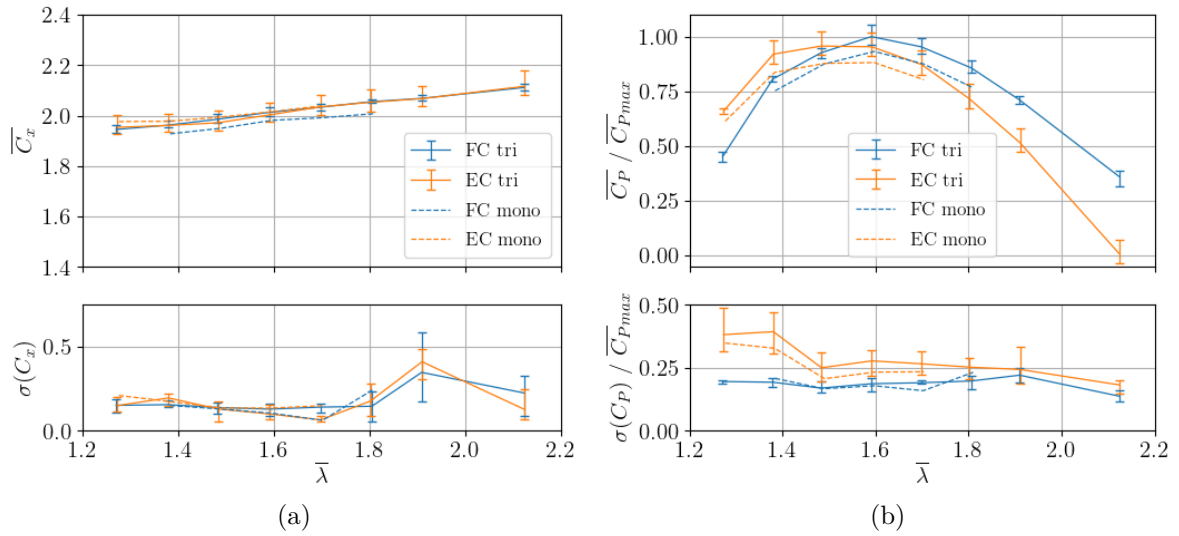


Figure 3.7 – Average (top) and standard deviation (bottom) of the drag (a) and power (b) coefficients in FC and EC on the tripod base and on the monopile base. Each curve is an average over 3 test campaigns with the error bars representing the extreme average and extreme standard deviation values over the 3 campaigns.

and fluctuation, no matter the base geometry. We notice that 60 % of the average drag coefficient is composed of the rotors thrust and the other 40 % is due to the friction drag on the structure as the $\overline{C_x}$ measured without rotors is about 0.8. The maximal $\overline{C_P}$ value is also hardly affected by the flow orientation (4 % difference in average over the 3 campaigns). However, the optimal λ is clearly lower and the power standard deviation is 1.5 times higher in average over the λ range in ebb tide than in flood tide configuration. The results with the turbine fixed on the central monopile show the same shift in the optimal λ between the two flow directions. Therefore, this result is due to the difference of relative counter-rotation direction rather than to the tripod base asymmetry. The average power extracted with the turbine on the monopile appears lower than with the turbine on the tripod; this is probably due to the lower projected area of the whole model which induces a lower blockage ratio and so a lower flow through the turbine. Besides, the gap of power fluctuation between EC and FC narrows when the turbine is fixed on the monopile. The effect of the flow orientation on the power production can be further explained by looking at the torque angular distribution on one column of rotors.

3.1.3.2 Torque angular distribution

Fig. 3.8 displays the normalised torque coefficient with regard to a relative angular position at the optimal λ (at which $\overline{C_P}$ is maximal) in the two configurations, on the tripod base (a & b) and on the monopile (c & d). The overall averaged C_Q is equal between EC and FC. For all the cases, we observe six torque peaks corresponding to the contribution of each blade as one rotor column is made of two levels of 3 bladed rotors with 60 degrees shift between them. However, with the tripod base, the rose shape differs significantly between the two configurations. The torque distribution in EC shows clearer peaks and reveals an asymmetry between the top and the bottom rotors whereas the torque distribution is much smoother in FC. Consequently, the standard deviation of

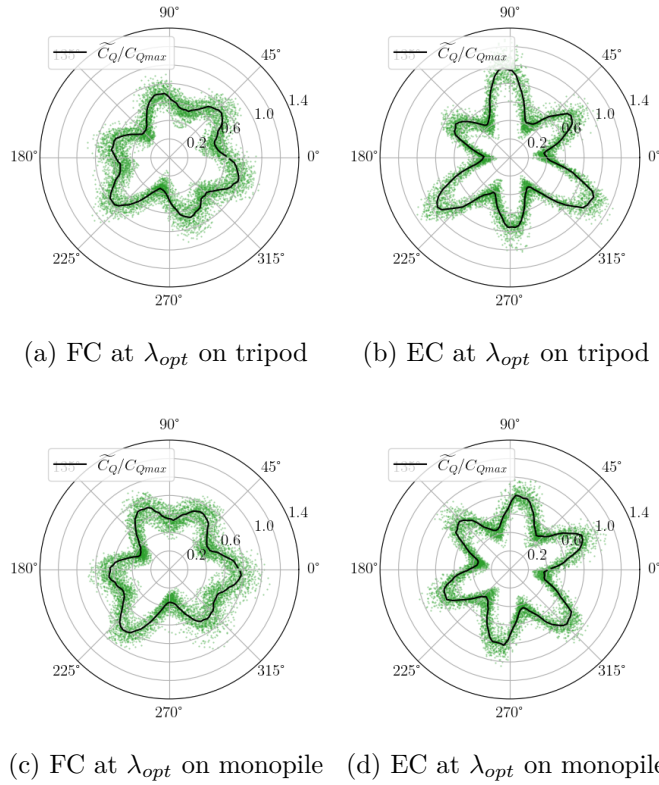


Figure 3.8 – Angular distribution of the torque coefficient for the green rotor column at the optimal λ for the two flow orientations (1.6 in FC, 1.5 in EC). Torques are normalised by the maximal phase-average value, measured in EC on the tripod base. The green dots are the instantaneous measurements and the black line is the phase average. *Reminder*: the angular position is relative, so the absolute angle values cannot be compared between graphs.

\widetilde{C}_Q is 1.8 times higher in EC than in FC, which directly leads to the $\sigma(C_P)$ gap observed in Fig. 3.7(b). Fig. 3.8 (c & d), with the monopile, show that the torque distribution in FC is unchanged compared to the case with the tripod but that the asymmetry between the top and the bottom rotors in EC disappears. Consequently, the standard deviation gap between the two configurations narrows. It still remains a 1.25 ratio between $\sigma(\widetilde{C}_Q)$ in EC compared to FC as the contribution of each blade remains more marked.

In EC, the base feet are aligned with the outer part of the rotors (Fig. 1.2 and 3.6). The streamwise velocity profiles in Fig. 3.9 show that the flow deflection around the tripod structure upstream generates an overspeed in front of the bottom rotors compared to the case on the monopile. That overspeed exceeds the average velocity in front of the upper rotor so we assume the highest \widetilde{C}_Q peaks to be generated by the bottom rotor. Besides, the velocity standard deviations are between 3 and 5 times stronger above the two base feet compared to the case on the monopile at the same positions. Those two observations can explain the difference of torque angular distribution, and therefore of power coefficient fluctuation, in EC between the case on the tripod and on the monopile. Conversely, in FC, the central base foot upstream is aligned with the central fairing of the turbine. The flow deflection around that foot does not impact much the rotors which explains the absence of difference torque angular distribution

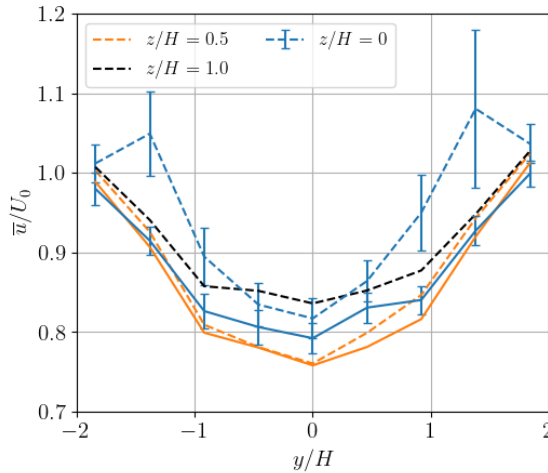


Figure 3.9 – Streamwise velocity profiles measured by LDV upstream of the turbine at $x/H = -1$ in EC, with the turbine on the tripod base (dashed lines) and on the monopile (solid lines). This x position is located above the tripod feet in EC (Fig. 3.10). The error bars represent the normalized standard deviation of the streamwise velocity.

and power coefficient fluctuation between the cases on the tripod and on the monopile base.

3.1.4 Flow direction effect on the wake of the ducted 2-VATT

Beyond the effects on the hydrodynamic behaviour of the turbine, this section aims at analysing how opposed flow directions between ebb and flood tide can affect the wake of the ducted 2-VATT. The latter is studied in terms of width, height, dynamics and recovery.

3.1.4.1 Wake width evolution

Fig. 3.10 displays average streamwise velocity contours of the wake at different altitudes downstream of the turbine in FC and EC on the tripod base. It reveals significant wake differences between the two configurations at the first glance. In the near wake, down to $x/H = 3$, the maximal velocity deficits are located behind each rotor column over the turbine height in the two configurations. However, the velocity deficits behind each column merge at $x/H = 3$ in FC (i.e. a single maximal deficit at $y/H = 0$) while they merge past $x/H = 5$ in EC at $z/H = 0.50$ (Fig. 3.12). This is due to the difference of counter-rotation since the merging distance in FC on the monopile base is similar to that on the tripod (Fig. 3.11).

Besides, Fig. 3.10 (i & j) show that the wake boundary ($\bar{u}/U_0 = 0.9$) of the tripod base expands laterally in FC up to $y/H = 2.0$ while it remains of constant width in EC from $x/H = 3$ to 9 at $y/H = 1.8$. Overall, Fig. 3.13 presents the half wake width averaged over the turbine height ($0.00 < z/H < 1.00$) with regard to the downstream position in EC and in FC on the tripod and the monopile base. It reveals that the base wake strongly interferes with the turbine wake, leading to an increase of the turbine

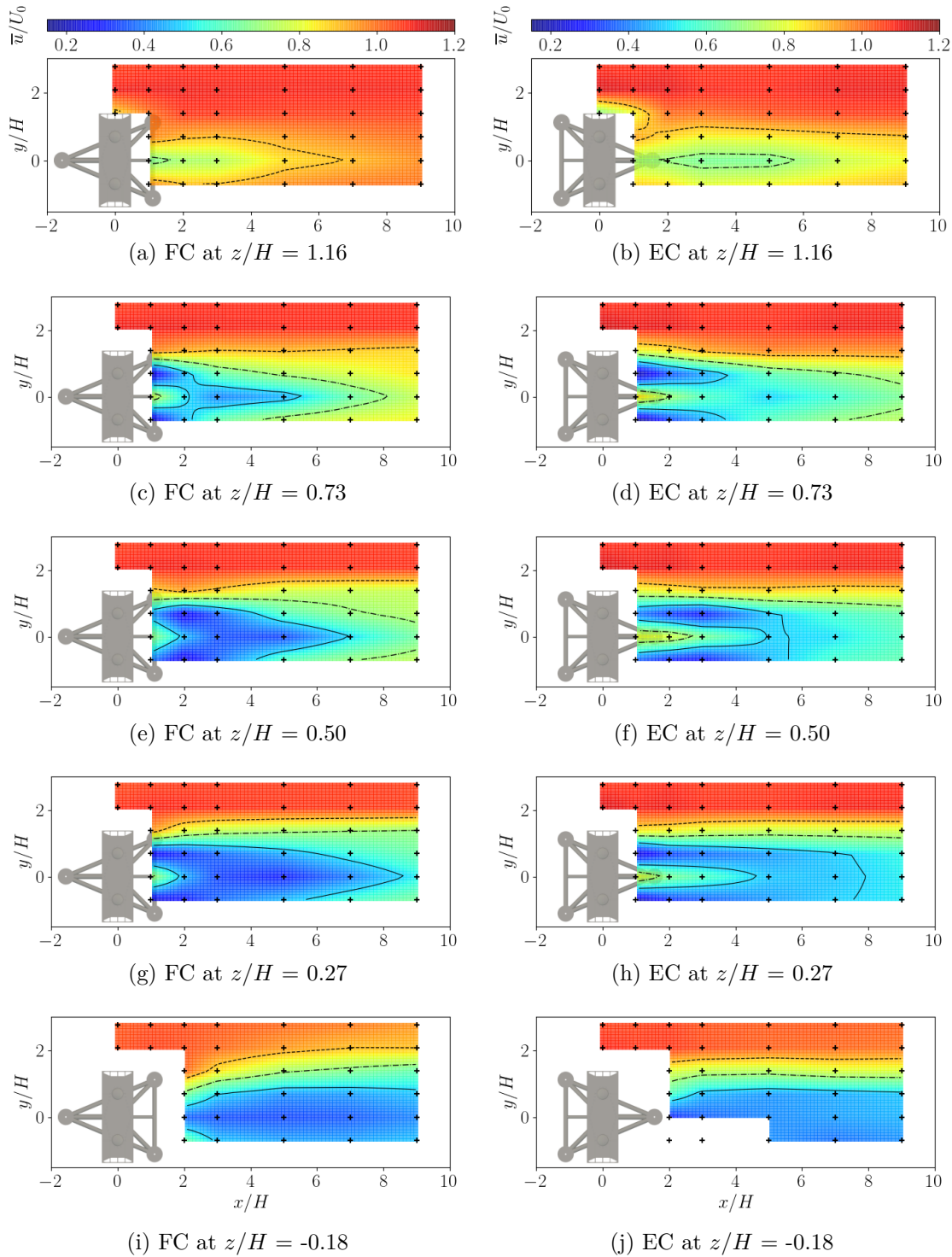


Figure 3.10 – Contours of the normalised average streamwise velocity in (x, y) planes at different vertical positions, in FC on the left and in EC on the right, on the tripod base. The black crosses show the measurement point positions; the dashed, dash-dot and solid lines are iso-contours of $\bar{u}/U_0 = 0.9, 0.7$ and 0.5 respectively. The lacking points in (j) are due to some air bubble releases from model cavities that resulted in poor quality measurements.

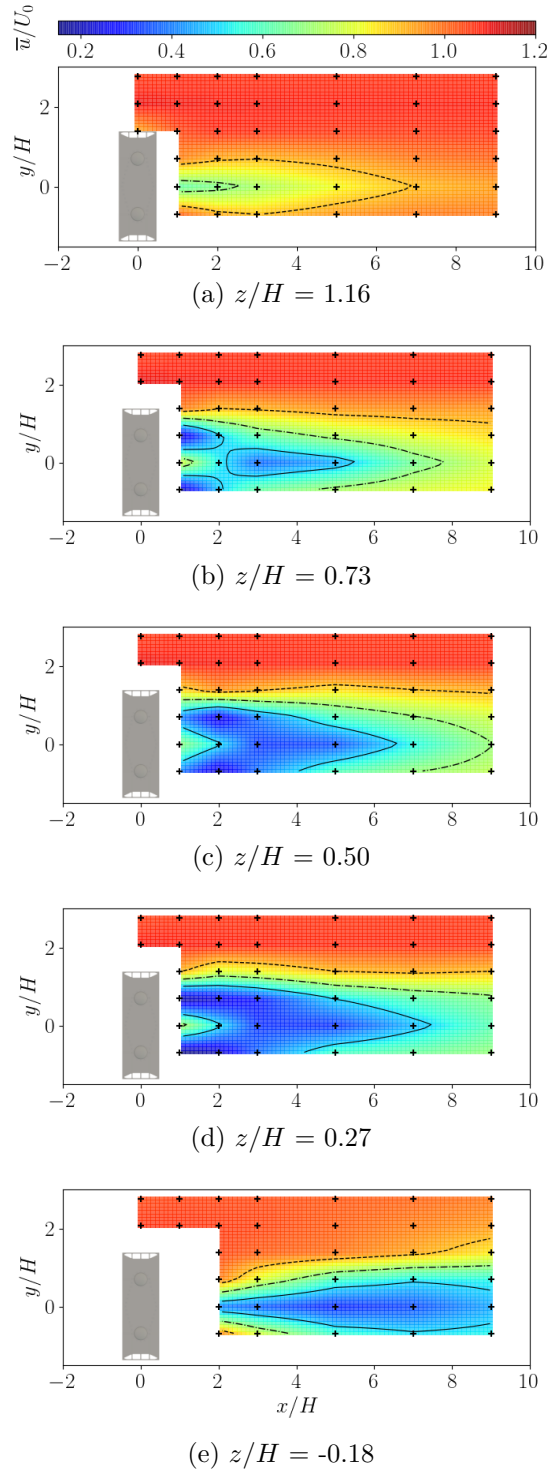


Figure 3.11 – Contours of the streamwise velocity at different altitudes in FC on the monopile base. The black crosses show the measurement points positions; the dashed, dash-dot and solid lines are iso-contours of $\bar{u}/U_0 = 0.9$, 0.7 and 0.5 respectively.

wake width in FC on the tripod from $x/H = 2$ to 7 while it only decreases on the monopile and in EC. In the end, at $x/H = 9$, the wake is 5% wider in FC on the tripod base than in EC on the tripod and is 31% wider in FC on the tripod than in FC on the monopile base. Thus, despite the clear difference of wake merging distance due to the

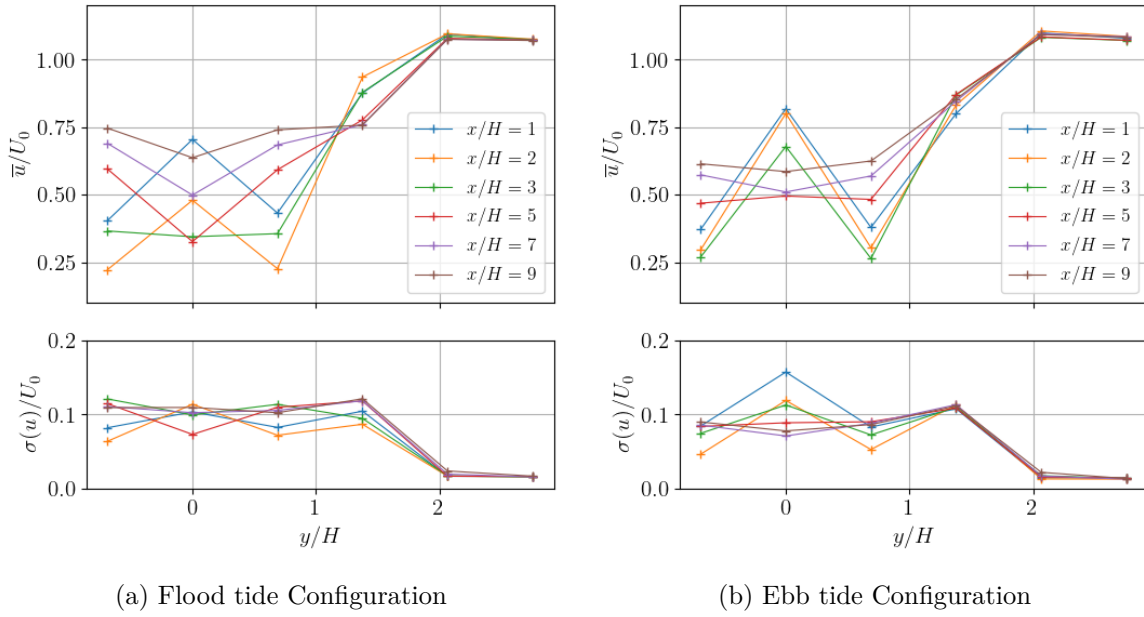


Figure 3.12 – Horizontal streamwise velocity profiles at the turbine mid-height ($z/H = 0.5$) and at different downstream distances, in FC on the left and in EC on the right.

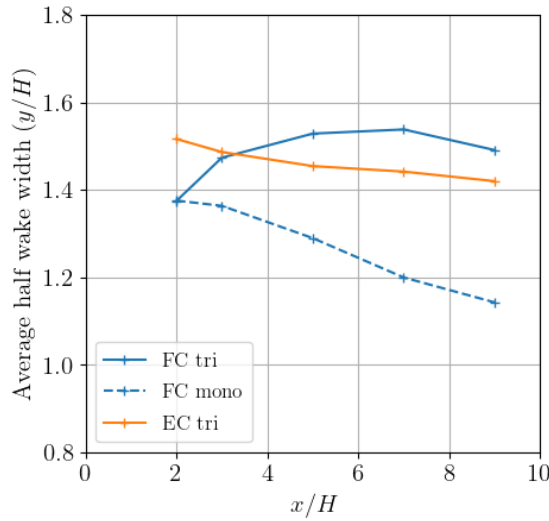


Figure 3.13 – Average half wake width ($\bar{u}/U_0 = 0.9$) over the turbine height ($0.00 < z/H < 1.00$) as a function of the downstream distance in FC and EC on the tripod base, and in FC on the monopile base.

opposed counter-rotation direction, the turbine wake width appears to be more affected by the base geometry than the rotation direction. Furthermore, Fig. 3.10 (a & b) show that the wake expands more vertically in EC than in FC. The next section deals with this topic in depth.

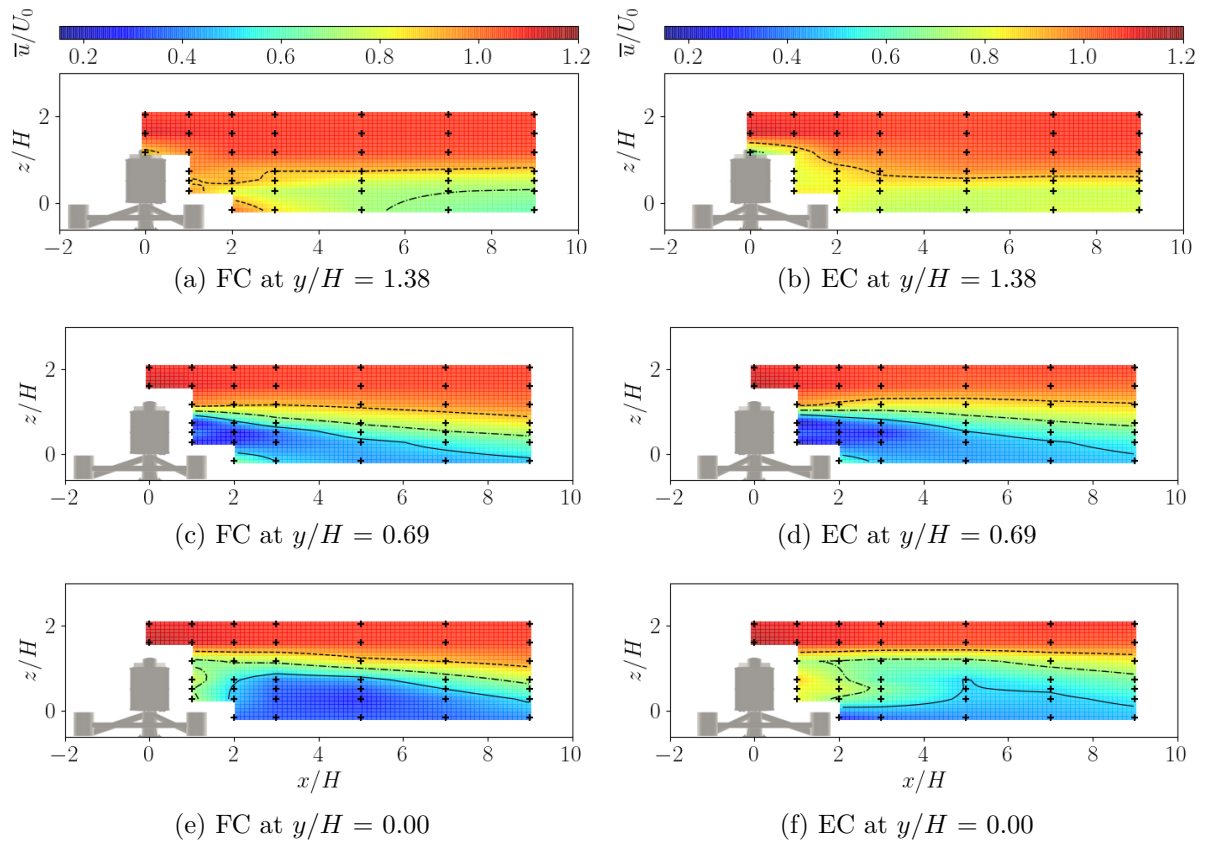


Figure 3.14 – Contours of the normalised average streamwise velocity in the (y, z) plane at different positions along the width, in FC on the left and in EC on the right, on the tripod base. The black crosses show the measurement point positions; the dashed, dash-dot and solid lines are iso-contours of $\bar{u}/U_0 = 0.9, 0.7$ and 0.5 respectively.

3.1.4.2 Wake height development

Fig. 3.14 displays the average streamwise velocity contours of the wake at different lateral positions in FC and EC on the tripod base. Firstly, Fig. 3.14 (a & b) highlight the effect of the base asymmetry in the plane of the turbine edge ($y/H = 1.38$), showing from another point of view the larger spreading of the wake in FC, as discussed in the previous section. These contours also show that the turbine wake is more intense in this plane down to $x/H = 3$ in EC. As a comparison, when the turbine is installed on the monopile base, the velocity deficit in the plane of the turbine edge appears significantly limited (Fig. 3.15). By subtracting the velocity field measured at $y/H = 1.38$ in the wake of the turbine on the monopile to the one measured downstream of the turbine on the tripod in the same operating conditions, we can observe that the wake of the base influences that of the turbine over the whole turbine height (Fig. 3.16). In the far wake, the tripod base is responsible for about 20 % more velocity deficit at the height of the bottom rotors compared to the case on the monopile.

Secondly, the velocity fields in the plane of the central fairing of the turbine ($y/H = 0.00$) strongly differ between EC and FC (Fig. 3.14 (e & f)). The velocity profiles in this plane show with more precision that the average velocity profiles are of similar shape right behind the turbine, at $x/H = 1$ (Fig. 3.17). However, from $x/H = 2$ to 5, the

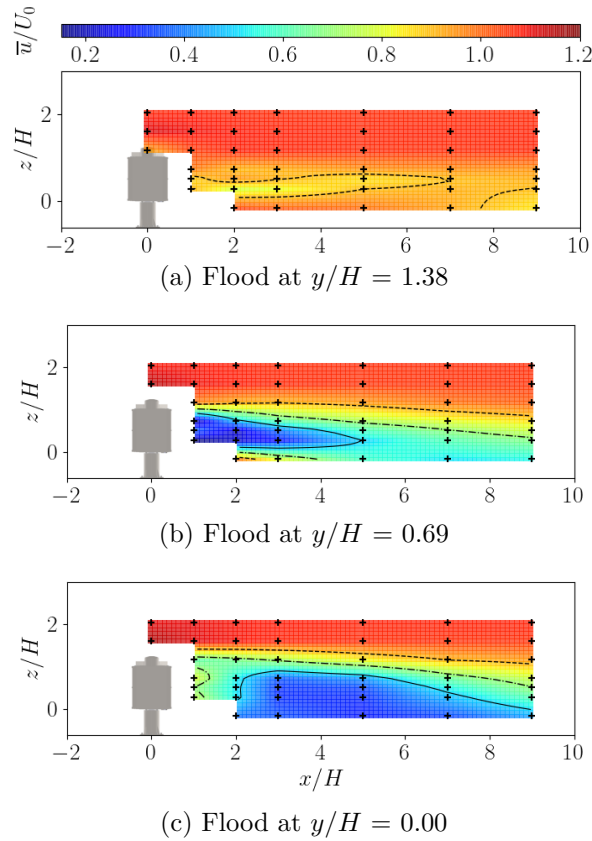


Figure 3.15 – Contours of the normalised average streamwise velocity in the (y, z) plane at different positions along the width, in FC on the monopile base. The black crosses show the measurement points' positions; the dashed, dash-dot and solid lines are iso-contours of $\bar{u}/U_0 = 0.9, 0.7$ and 0.5 respectively.

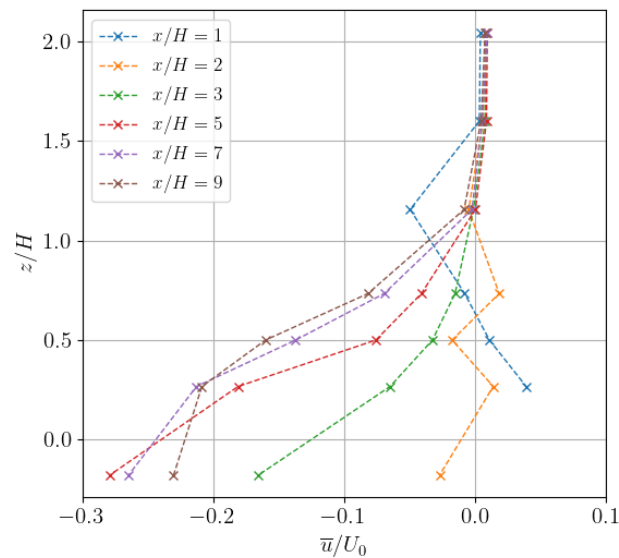


Figure 3.16 – Difference of streamwise velocity at $y/H = 1.38$ between the wake downstream of the turbine in FC on the tripod and on the monopile base, along vertical profiles at different downstream distances.

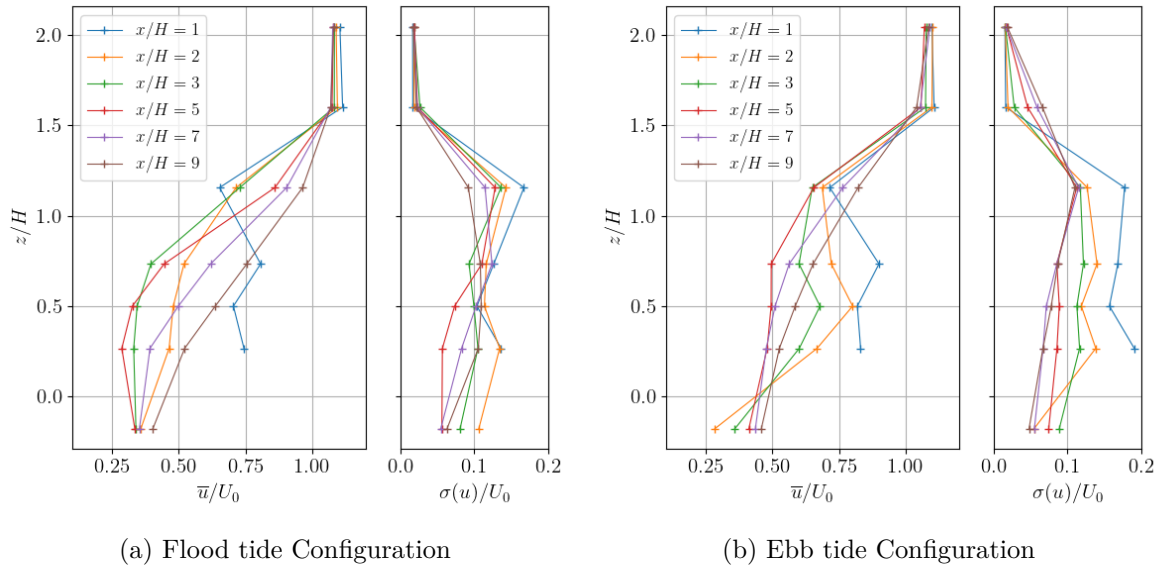


Figure 3.17 – Vertical streamwise velocity profiles at the turbine mid-width ($y/H = 0.00$) and at different downstream distances at the centre of the turbine, in FC on the left and in EC on the right.

velocity profiles in EC present a maximum at half the turbine height that is absent in FC. This downstream distance interval corresponds to the positions where the wakes of the two rotor columns have already merged in FC whereas they are still separated in EC, as shown in the previous section. Once the wakes are merged in the two configurations, past $x/H = 5$, the velocity profiles present similar shapes but the velocity gradient is steeper in FC. The velocity is about 1.2 times higher at $x/H = 9$ in FC than in EC at the top of the turbine ($z/H = 1$) while it is equal at the turbine bottom. Consequently, the vertical shear layer between the wake maximal velocity deficit and the faster free-stream velocity is much thinner in FC than in EC. Besides, the overall maximal velocity deficit over the turbine height in that centre plane is located at $x/H = 5$ and $z/H = 0.27$ in both configurations, but it is 56 % higher in FC ($\bar{u}/U_0 = 0.27$) than in EC ($\bar{u}/U_0 = 0.48$).

Thirdly, the streamwise velocity deficit behind the rotors ($y/H = 0.69$) appears quite similar in EC and FC (Fig. 3.14 (c & d)). Despite this relative similarity, the wake height of the three iso-velocity contours displayed ($\bar{u}/U_0 = 0.9, 0.7$ and 0.5) are lower in FC than in EC, which also reveals a thinner vertical shear layer in FC. This trend of wake height remains true when looking at the average over the half turbine width ($0.00 < y/H < 1.38$, Fig. 3.18). Indeed, the wake is from 8 % higher at $x/H = 1$ to 20 % higher at $x/H = 9$ in EC than in FC overall, which also indicates that the wake height decreases faster in FC. The comparison to the results on the monopile shows no difference in the near wake and only a slight influence of the base on the vertical expansion in the far wake as it keeps decreasing faster on the monopile. Consequently, unlike the width, the wake height appears to be more influenced by the difference of relative counter-rotation direction than by the base geometry.

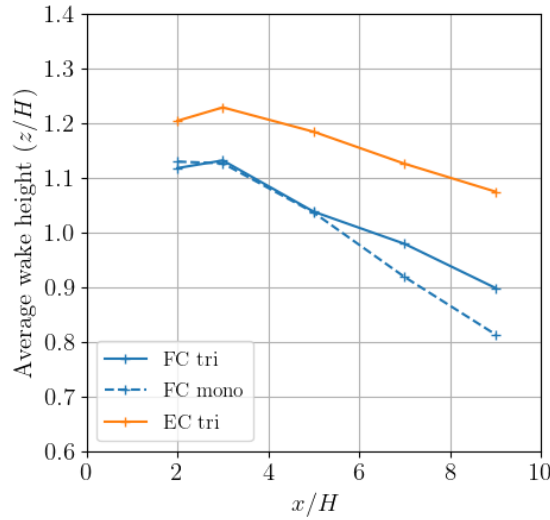


Figure 3.18 – Average wake height of $\bar{u}/U_0 = 0.9$ over the half turbine width ($0.00 < y/H < 1.38$) as a function of the downstream distance in FC and EC on tripod, and in FC on monopile.

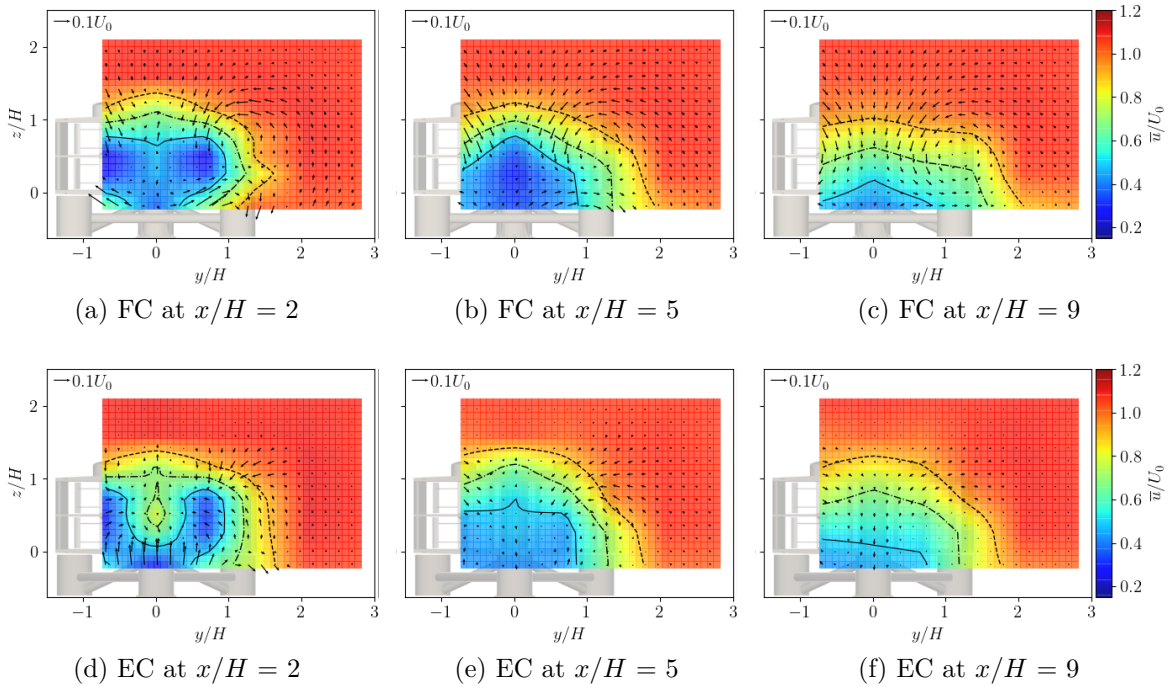


Figure 3.19 – Contours of the mean streamwise velocity (\bar{u}/U_0) in (y, z) planes at 3 downstream positions, viewed from downstream, with superimposition of arrow field of the mean transverse velocities (\bar{v}, \bar{w}); the dashed, dash-dot and solid lines are iso-contours of $\bar{u}/U_0 = 0.9, 0.7$ and 0.5 respectively.

3.1.4.3 Wake dynamics

Fig. 3.19 presents superimpositions of the mean streamwise velocity contours and arrow fields of the mean transverse velocities (\bar{v}, \bar{w})/ U_0 in (y, z) planes at different downstream positions, in FC and EC on the tripod base. Beyond the observations on the

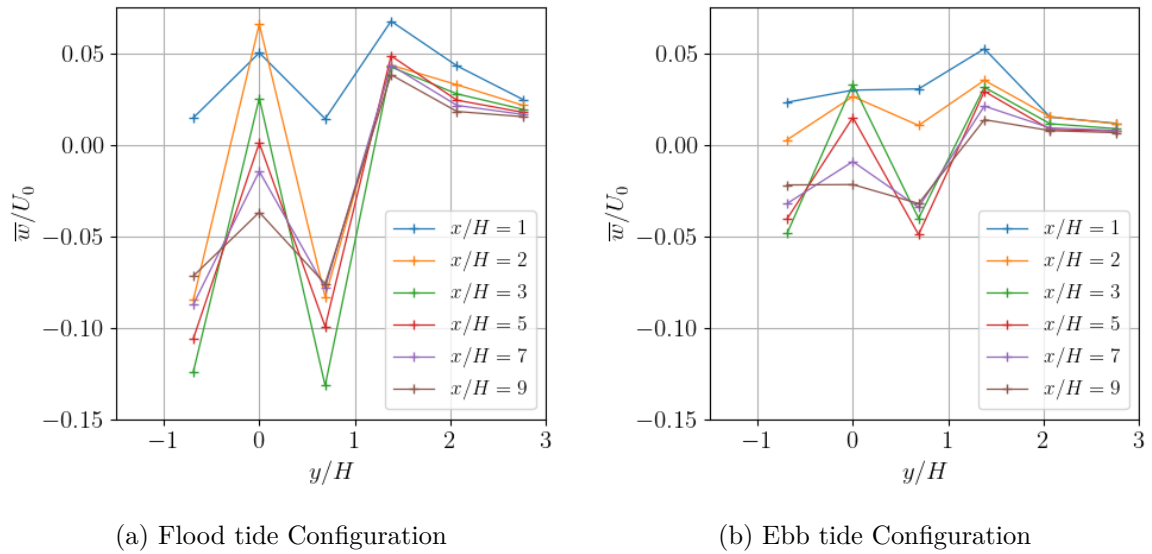


Figure 3.20 – Horizontal profiles of mean vertical velocity at different distances and at $z/H = 0.73$ downstream of the turbine on the tripod base, in FC on the left and in EC on the right.

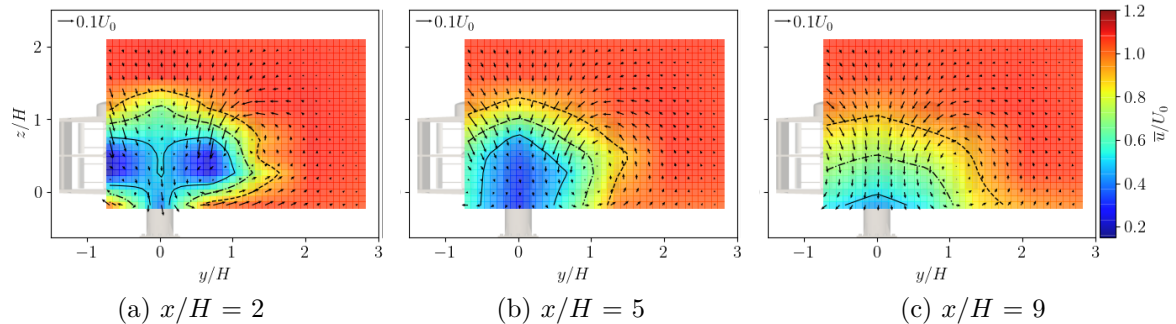


Figure 3.21 – Contours of the mean streamwise velocity in (y, z) planes, viewed from downstream, with superimposition of arrow field of the mean transverse velocities (\bar{v}, \bar{w}) in FC on the monopile base; the dashed, dash-dot and solid lines are iso-contours of $\bar{u}/U_0 = 0.9, 0.7$ and 0.5 respectively.

wake width and height made previously, the arrow fields reveal two large swirls around the x axis behind each rotor column in the two flow configurations. Those swirls are more structured in FC than in EC, and they persist much further downstream in the wake as they are still clearly visible at $x/H = 9$, both when the turbine is on the tripod and the monopile base (Fig. 3.21). Indeed, the maximal transverse velocities in FC are of the order of 2 times those in EC at $z/H = 0.73$ behind the rotors (Fig. 3.20). In addition, those large average swirls are also observed in the wake of the turbine in FC on the monopile base.

Fig. 3.22 and 3.23 display contours of the normalized 2D turbulent kinetic energy (k_{UV} , Eq. 3.7) in (y, z) planes at the 6 downstream positions. Both in FC and EC at $x/H = 1$, similarly to the results of Bachant et al. (2015) in the near wake of a single high solidity VATT, the turbulent kinetic energy is low at the rotors centre. The

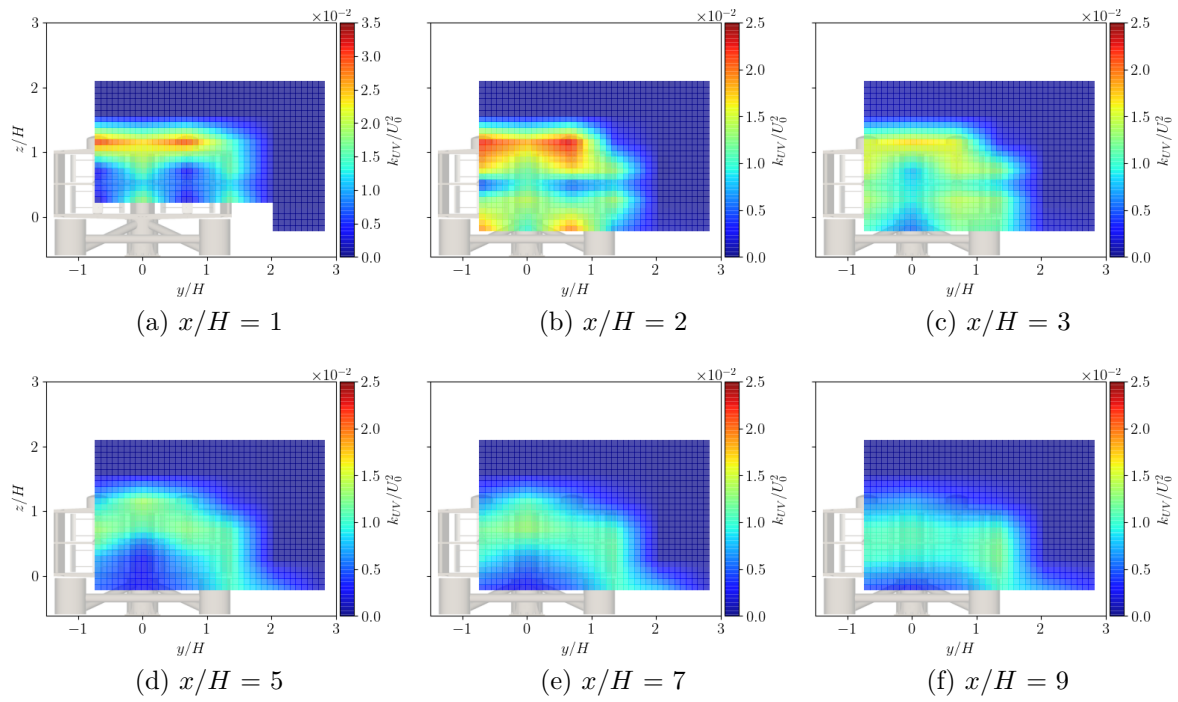


Figure 3.22 – Flood tide Configuration on tripod base – Contours of the turbulent kinetic energy computed on u and v viewed from downstream. *nb*: the color scale is different in (a) compared to others.

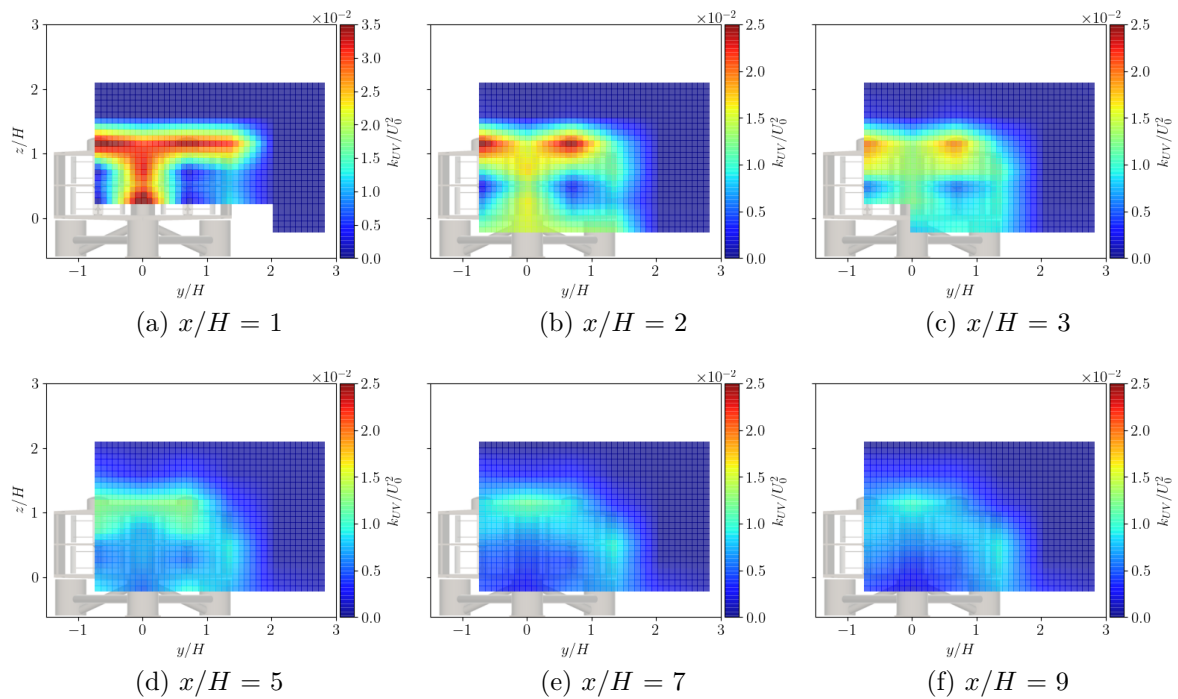


Figure 3.23 – Ebb tide Configuration on tripod base – Contours of the turbulent kinetic energy computed on u and v viewed from downstream. *nb*: the color scale is different in (a) compared to others.

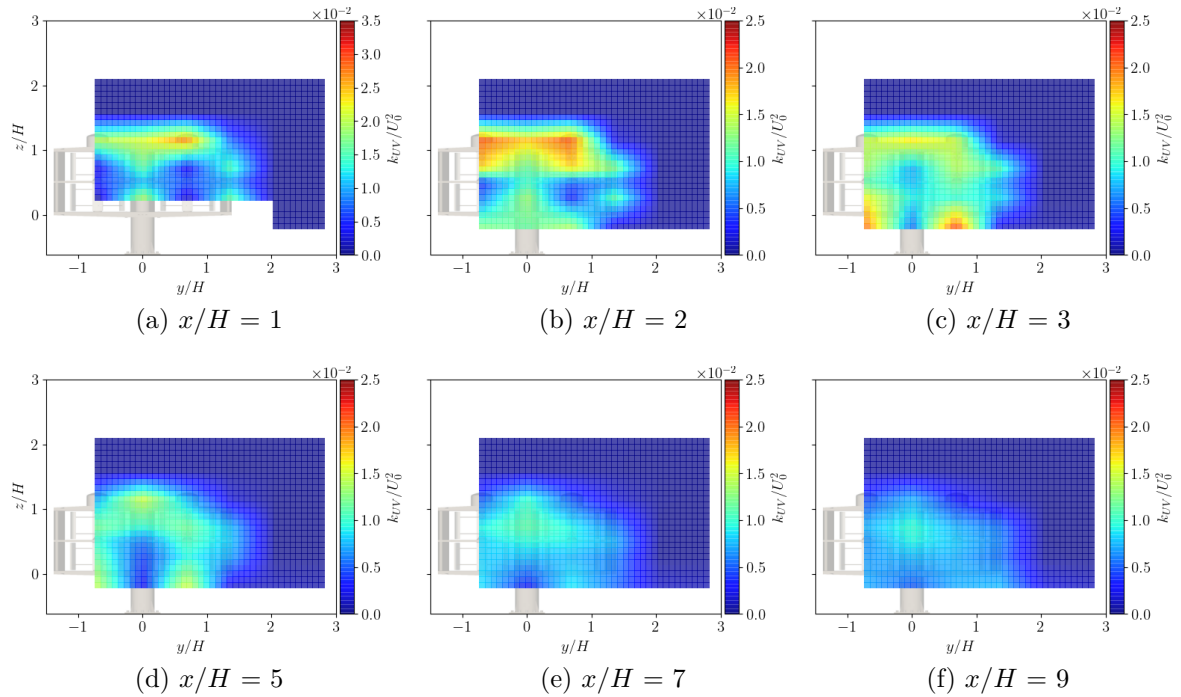


Figure 3.24 – Contours of the turbulent kinetic energy computed on u and v viewed from downstream in FC on the monopile base. *nb*: the color scale is different in (a).

high levels of k_{UV} are focused around the y boundaries of the rotors, where the blades undergo dynamic stall. However, the mesh of LDV measurement points used in this work (Fig. 3.6) is too coarse to locate precisely the k_{UV} maxima and separate the contribution of the blades from that of the support structure, the minimal gap between the blades and the vertical plates being less than 2 cm. Furthermore, we observe that k_{UV} is more intense in the near wake ($0 < x/H < 3$) in EC than in FC, especially at the height of the turbine top lid. The 3C-LDV measurements upstream of the turbine, at $x/H = -1$, reveal a stronger vertical flow bypassing in EC than in FC. The vertical velocity component at $(y, z)/H = (0, 1)$ is almost $0.2U_0$ in EC, which is 15 % higher than in FC. As a result, the top horizontal plate of the turbine faces a current with a greater angle of incidence in EC that may cause larger flow detachment in the wake of the top lid and explain the higher levels of turbulent kinetic energy at this location. At $x/H = 3$, k_{UV} peaks are smoothed and the turbulent kinetic energy is more spread on the whole turbine projected area in the two flow configurations. Then, in the far wake, k_{UV} is gradually dissipated and it remains mostly in the average velocity shear layer. Since that shear layer is thinner in FC than in EC (Fig. 3.19), the turbulent kinetic energy is focused in a thinner area in FC and so the maximum k_{UV} is higher in FC than in EC in the far wake. Finally, to complete the database for numerical models validation, Fig. 3.24 provides the same contours of the normalized 2D turbulent kinetic energy in the wake of the turbine in FC on the monopile base.

3.1.4.4 Wake recovery

To sum up, Fig. 3.25 (a) presents the evolution of the velocity averaged over the area where $\bar{u}/U_0 < 0.9$, noted $\langle \bar{u} \rangle_{>0.9}$, with the downstream distance in EC and FC (on the

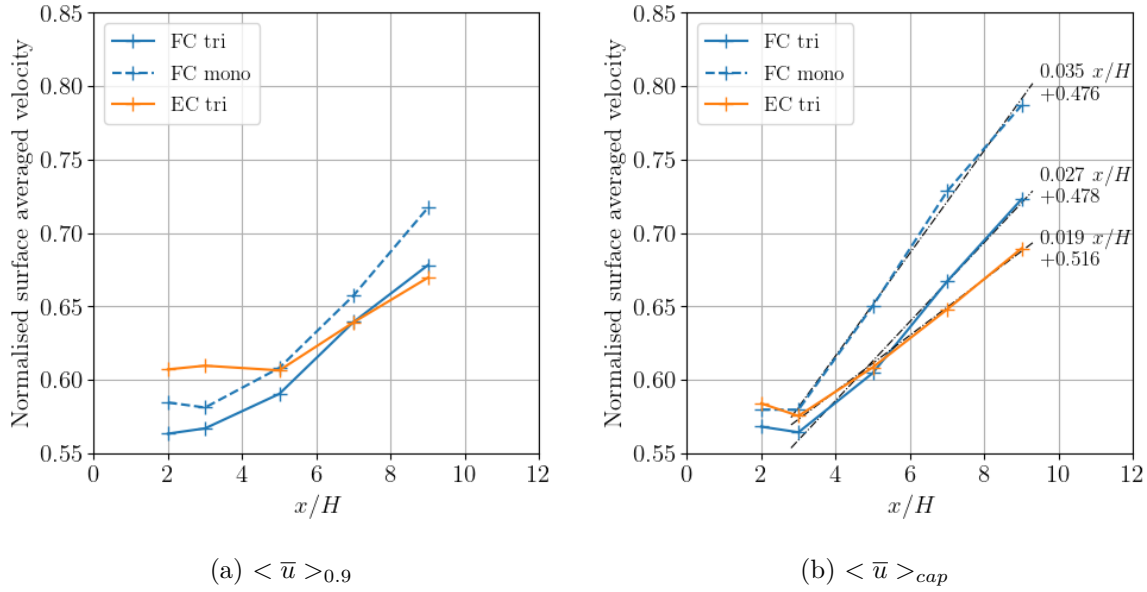


Figure 3.25 – Surface averages of the streamwise velocity at the 6 downstream positions in EC and FC (on tripod -solid line- and on monopile base -dashed line-). (a) Average over the area where $\bar{u}/U_0 < 0.9$. (b) Average over the projected capture area of the turbine. The black lines are linear fits of the points from $x/H = 3$ to 9 .

tripod and the monopile base). This quantity reveals the strength of the velocity deficit over the whole wake region. The comparison of the two curves in FC shows that the base geometry is responsible for the initial velocity deficit, right behind the 2-VATT, which is stronger with the turbine on the tripod base than on the monopile. Then, the base does not influence the recovering dynamics of the wake, so the initial velocity difference remains in the far wake. Besides, the strength of the wake appears significantly lower in EC than in FC in the near wake. As the recovery rate appears smaller in EC than in FC, the relative strength of the deficit reverses in the far wake between the two flow configurations and the average deficit ends up stronger in EC than in FC.

Finally, Fig. 3.25 (b) presents the evolution of the velocity averaged over the projected half turbine capture area ($\langle \bar{u} \rangle_{cap}$) with the downstream distance in EC and FC (on the tripod and the monopile base). First, the velocity decreases between $x/H = 2$ and 3 with the tripod base in the two flow configurations and not with the monopile. This shows the contribution of the tripod base to the turbine wake. Then, past $x/H = 3$, the velocity recovers following a linear trend with the downstream position in the three cases. By extrapolation of these linear trends, $\langle \bar{u} \rangle_{cap}$ would recover $\bar{u}/U_0 = 0.9$ at $x/H \simeq 20$ in the ebb tide configuration with the tripod base, at $x/H \simeq 16$ in the flood tide configuration with tripod base and at $x/H \simeq 12$ with the monopile base in FC. Thus, it appears that the FC recovers about 30 % faster than the EC. That result can be explained by the stronger average transverse velocities (\bar{v}, \bar{w}) in FC revealed previously (Fig. 3.19). Indeed, the measurements of Bachant et al. (2015) and Rolin et al., 2018 in the wake of single vertical axis turbines also reveal pairs of counter-rotating average swirling motions propelling fluid downward towards the turbine centreline. Their analyses of the mean and turbulent kinetic energy budgets show that those swirls are the main contributors to the streamwise momentum and average kinetic energy recovery,

more importantly than the turbulence.

Besides, the velocity recovery behind the ducted 2-VATT is about 20 % faster with the monopile base than with the tripod mainly thanks to the higher flow velocity between the tank floor and the turbine wake that can contribute to filling the velocity deficit faster (Fig. 3.15).

3.1.5 Discussion and conclusions

The results presented in Section 3.1.3 show that the drag of the turbine is not significantly affected by the flow direction nor the maximal average power coefficient. However, the optimal tip speed ratio is 7 % lower in EC ($\lambda_{opt} = 1.5$) compared to FC ($\lambda_{opt} = 1.6$), due to the difference of relative counter-rotation direction of the two rotor columns; and the power fluctuation is about 1.5 higher in EC, explained by stronger torque variations along a revolution. Jégo et al. (2021) simulated numerically the same turbine at full-scale with a model based on a 2D actuator cylinder method. They calculated the power output in the two flow directions with the turbine operating at $\lambda = 2$ and found no difference between the two cases. This is not consistent with the present work as we find a ratio of 1.9 between the average power coefficient in FC and in EC at this λ . Given the method used, the numerical model does not take into account the losses due to blade tips, the rotor arms and the shafts. The absence of these dissipation phenomena leads to an overestimation of the optimal tip speed ratio (Guillaud, 2017). Then, assuming that $\lambda = 2$ is the optimal operating point with the numerical model (not specified by Jégo et al. (2021)), the absence of flow direction effect on the maximal average power coefficient would be coherent with our experimental results.

Secondly, regarding the flow downstream of the turbine presented in Section 3.1.4, the far wake in EC appears to be slightly less wide (5 %) than in FC, mainly due to the tripod base asymmetry, but higher (10 to 20 %), mostly caused by the difference of relative counter-rotation direction. The trends of horizontal and vertical expansion are the opposite to what is presented on the non ducted twin vertical axis wind turbine by Müller et al. (2021), which highlights the effect of the fairings and the base geometry on the turbine wake development. Besides, the flow direction strongly affects the interaction between the wakes of the two rotor columns as they merge further in EC than in FC ($x/H = 5$ and 3 respectively). Given the counter-rotation direction in EC and FC, the difference of merging distance tendency is consistent with the results obtained in the wake of a non-ducted twin vertical axis wind turbines in a tunnel (Lam et al., 2017; Vergaerde et al., 2020a; Müller et al., 2021) and with the 2D numerical simulations of the same ducted 2-VATT (Jégo et al., 2021).

Thirdly, the 3C-LDV mapping of the flow reveals large swirling motions around the x axis behind each rotor column in the two configurations. Grondeau et al. (2019) modelled the wake of the ducted 2-VATT without base nor generator shelters on top, in the counter-rotation direction similar to EC. They also observe large stationary swirls around the x axis behind each rotor column, centred on the top corners of the turbine. However, those swirls rotate in the opposite direction compared to our experimental results. This difference could be a combined effect of the base presence, the blockage in the tank and the difference of turbine scales or to some bias in the numerical model. The results in FC with the turbine fixed on the monopile show that the swirls rotate in the same direction whether on the monopile or on the tripod base, which tends to indicate

that the base is not responsible for this difference between numerical and experimental results. However, this result is insufficient to exclude that the swirls would not rotate in the other direction in EC on the monopile. Our experiments show that those swirls are about 2 times stronger in FC than in EC, injecting more mean kinetic energy from the free-stream into the wake (Bachant et al., 2015; Rolin et al., 2018). Consequently, the overall wake recovers 30 % faster in FC than in EC and would reach $\bar{u}/U_0 = 0.9$ at $x/H = 16$ in FC while it would be at $x/H = 20$ in EC on the tripod base. Since our experiments are performed with a 1.5 % incident turbulence intensity, we can expect lower velocity deficits and faster recovery at full-scale where the turbulence intensity is mostly between 10 and 20 % (Filipot et al., 2015; Mycek et al., 2014; Grondeau et al., 2019).

Finally, from another perspective, this study also shows the influence of the gravity base geometry both on the performance and the wake of the ducted 2-VATT. Indeed, we showed that the presence of the base feet in front of the rotors in EC induces both flow asymmetry between the upper and the lower rotors and more turbulence that increase the torque fluctuation by 25 %. Besides, while the base geometry hardly affects the wake height of the turbine, it strongly impacts the width. The latter being the same right behind the turbine, the turbine far wake in FC is finally more than 30 % wider with the tripod than with the monopile. Furthermore, at the base altitude, the average velocity deficit is up to 30 % stronger behind the tripod than behind the monopile base. Thus, the velocity deficit behind the turbine is partly recovered by energy exchanges with the flow under it when the turbine is on the monopile while it is not possible on the tripod. As a consequence, the average velocity deficit in the turbine wake recovers 20 % faster on the monopile than on the tripod base. These results show the need to consider the base design with care to optimise both the performance and the wake in the perspective of tidal turbine arrays.

In future works, the results presented in this part will allow a better validation of the numerical models applied to twin vertical axis tidal turbines. Experiments in unsteady conditions such as turbulent flows or in presence of waves are also necessary to assess their effects on both the turbine performance and the wake development.

3.2 Scale effects discussion

Putting together the measurements at sea from the previous chapter and those in the flume tank from the previous part, we can assess the accuracy of the typical reduced-scale experiments to predict the full-scale results. As indicated in the general introduction, Ross et al. (2022) showed that the Reynolds number is the most impacting dimensionless number on the performance of an isolated 2-bladed vertical axis tidal turbine, by comparison to the blockage ratio and the Froude number. Furthermore, Miller et al. (2018) found that the evolution of the maximal power coefficient with regard to the Reynolds number can be nicely fitted by an error function (*erf*) from $Re_D = U_0 D / \nu = 0.6$ to 5×10^6 . In their experiment, the turbine performance appears insensitive to the Reynolds number around $Re_D \simeq 3.2 \times 10^6$. In the light of the literature, we expect significant scale effects in the present work, mostly due to the Reynolds number difference since $Re_c \simeq 5 \times 10^6$ ($Re_D \simeq 2 \times 10^7$) at full-scale against 1×10^5 (3×10^5 , respectively) in our reduced-scale experiments (Tab. 3.1). Those scale effects are first analysed by comparing the ducted 2-VATT power performance and loads at reduced-

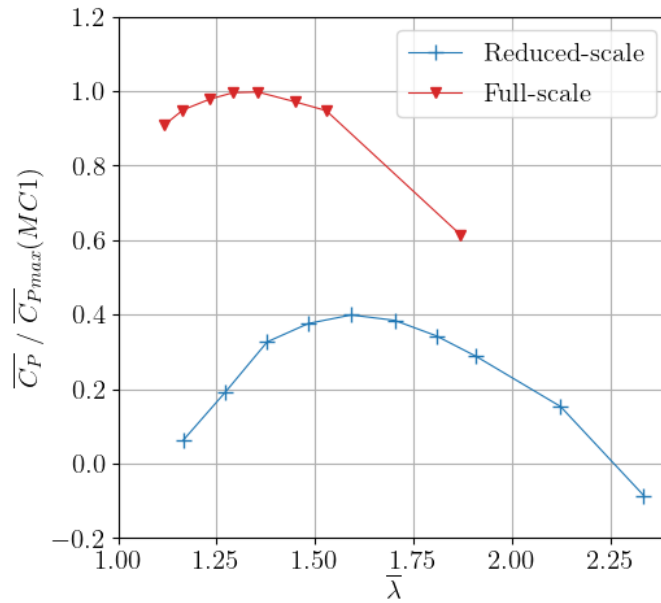


Figure 3.26 – Average power coefficient versus average tip speed ratio at full-scale (from Fig. 2.21) and at reduced-scale (from Fig. 3.7), normalised by the maximal value at full-scale.

and full-scale (3.2.1) before studying the potential scale effects on the characteristics of the flow surrounding the turbine (3.2.2). We also address the complementarity between experimental tests and numerical models to predict the full-scale results.

3.2.1 Scale effects on the turbine performance and loads

The accurate prediction of the average power performance is necessary for the full-scale power performance forecast, which is the starting point for the industrial project developments. Besides, the accurate prediction of the average loads is the starting point for the structural design of the tidal turbines, as explained in the section 2.2.1. Finally, predicting the extreme load values and their fluctuation ranges at full-scale with confidence helps reducing the safety factors in the structural design, which contributes to reducing the turbine construction cost. Thus, this section considers the scale effects between reduced-scale experiments and full-scale operation regarding these three prediction needs.

For a start, Fig. 3.26 displays the evolution of the average power coefficient with the average tip speed ratio obtained in flood tide conditions at full-scale and at reduced-scale. The maximal average power performance appears 60 % lower at the 1/20 scale compared to the prototype performance, at a 0.25 higher optimal tip speed ratio. For a vertical axis turbine, the maximal local angle of attack of the flow on the blade increases when the tip speed ratio decreases (Beaudet, 2014). Therefore, the present result means that the full-scale blades succeed in generating more lift force (and so more torque and power) at higher angles of attack than the reduced-scale blades. That result is assumed to be mostly due to the Reynolds number difference between the two devices as the stall angle of a NACA0018 foil increases with the Reynolds number (Michna et al.,

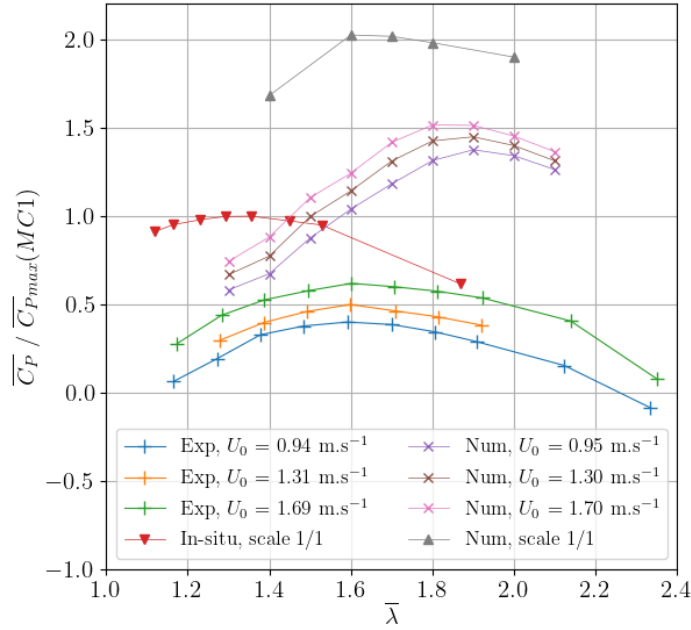


Figure 3.27 – Evolution of the average power coefficient with the tip speed ratio measured in the reduced-scale experiments, measured on the prototype in-situ (from Fig. 2.21) and computed with the URANS2D numerical model. The cross symbols are at a 1/20 scale while the triangles are at full scale. All the $\overline{C_P}$ values are normalised by the maximal value at sea corresponding to MC1.

2022). According to Bachant et al. (2016), a simple model that computes the peak torque coefficient from static foil data at variable Reynolds numbers combined with the vertical axis turbine kinematics could reasonably predict the power performance trend with the Reynolds number. However, such a model fails in providing absolute prediction of the turbine power performance due to the lack of dynamic stall consideration, which is preponderant in vertical axis turbine behaviour.

To better assess the effect of the Reynolds number on the ducted 2-VATT model response and to improve the absolute performance prediction, we tested the turbine facing currents of different magnitudes between $U_0 = 0.8$ and 1.7 m.s^{-1} with the same experimental setup as in the section 3.1.2. Increasing the velocity magnitude also increases the Froude number to the same extent as the Reynolds number, but its effect on the performance is low compared to that of Re (Ross et al., 2022). In addition, HydroQuest carried out numerical simulations of the ducted 2-VATT at a 1/20 scale at $U_0 = \{0.95; 1.30; 1.70\} \text{ m.s}^{-1}$ as well as at full-scale with an inflow velocity of 2.8 m.s^{-1} . The numerical model solves the 2-Dimensional Unsteady Reynolds-Averaged Navier-Stokes equations (URANS2D) in a horizontal cross-section of the ducted 2-VATT using *OpenFoam*. The Spallart-Allmaras linear eddy viscosity model is used to account for the turbulence. The experimental and numerical results are presented in Fig. 3.27 along with those at sea in terms of average power coefficient evolution with the tip speed ratio. We find a 50 % increase of the maximal average power coefficient in the reduced-scale experiments from $U_0 = 0.94$ to 1.69 m.s^{-1} , which reduces the gap to less than 40 % with the full-scale result. However, the optimal tip speed ratio is constant in the three cases, which does not indicate the λ_{opt} decreasing trend compared to the in-situ results. The numerical

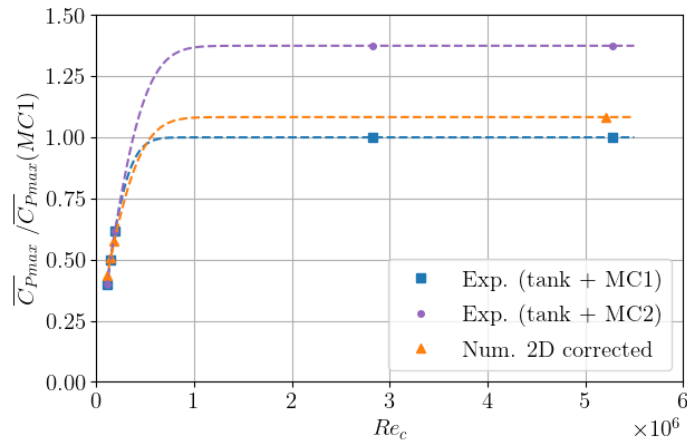


Figure 3.28 – Evolution of the maximal average power coefficient with the chord-based Reynolds number. The dashed lines are *erf* fits of the data within $Re_c = 1.5$ and 5.5×10^6 .

model, whether at reduced- or full-scale, largely overestimates the average power coefficient as well as the optimal tip speed ratio compared to the physical measurements in the flume tank and at sea. This is due to the lack of 3-dimensional dissipative effects in the URANS2D approach (Guillaud, 2017). Indeed, the 2D model does not consider the blade tips, the blade support structures (or struts) nor the strut-blade connection sections. For H-Darrieus type rotors, these rotor parts are known to be responsible for local lift force decrease and drag increase, which results in both lower maximal power coefficient and optimal tip speed ratio (Villeneuve et al., 2021; Guilbot, 2021). That being, the numerical results accurately predict the optimal tip speed ratio decrease by about 0.25 as well as the about 0.5 increase of $\overline{C_P} / \overline{C_{Pmax}}$ between the reduced- and the full-scale results. The reduced-scale numerical results also find a $\overline{C_P}$ increase with U_0 , although that absolute increase is 60% lower than in the experiments. In addition, we observe a light shift of λ_{opt} from 1.9 to 1.8 between $U_0 = 0.95$ to 1.70 m.s^{-1} .

Thus, either the experiments at reduced-scale or the URANS2D numerical model alone are insufficient to predict the absolute power performance at full-scale. However, correcting the numerical results by the experimental ones can give much better prediction. Fig. 3.28 shows the evolution of the maximal average power coefficient with regard to the chord-based Reynolds number (Eq. 3.1). The blue and purple points combine the experimental results at reduced-scale with the measurements at sea corresponding to MC1 and MC2, respectively. Two Re_c values are affected to the full-scale $\overline{C_P}$ with current velocities of 1.5 and 2.8 m.s^{-1} since we found that the power coefficient of the prototype was constant over that velocity range at the Paimpol-Bréhat test site (HydroQuest, 2021). In addition, the orange points correspond to the numerical results corrected by the experimental results at reduced-scale. The correction is a simple offset correction applied to the four numerical points (at reduced- and full-scale) by the average offsets on $\overline{C_P}$ and on λ_{opt} (in $Re_c = c\lambda_{opt}U_0/\nu$) between the experimental and numerical results at reduced-scale. The dashed lines correspond to error function (*erf*) fits, as suggested by Miller et al. (2018), including the results at scales 1/20 and 1/1. It appears that we manage to predict the maximal power coefficient at full-scale within the range of the measurement uncertainties at sea by combining the experimental re-

sults at a 1/20 scale with the simple URANS2D numerical simulations of the ducted 2-VATT. Considering the data fits, the power performance independence regarding the Reynolds number appears when Re_c is between 0.7 and 1.0×10^6 , or Re_D between 2.4 and 3.4×10^6 at reduced-scale, depending on the dataset. That Re -independence occurs later than what is observed by Bachant et al. (2016) on a 3-bladed vertical axis tidal turbine but is rather in line with the results of Miller et al. (2018) on a 5-bladed vertical axis wind turbine. Experiments at an intermediate scale would be needed to refine the Re -independence threshold for that specific ducted 2-VATT geometry.

Beyond the power performance prediction, the full-scale loads prediction is also crucial as it is the starting point for the structural design of the prototype (see section 2.2.1). We found that the drag coefficient of the full-scale prototype averaged over the whole ADCP measurement campaigns, is 1.5 during MC1 and 1.7 during MC2. We also noticed that the drag force measurement uncertainty is at least $\pm 30\%$ due to the quite poor fit of the measured load compared to the applied load during the calibration process and to the weakness of the calibration loads compared to the actual loads measured in operation. Therefore, the overall average drag coefficient of the prototype should be between 1.0 and 2.2. As a comparison, the average drag coefficient in the reduced-scale experiments at $U_0 = 0.94 \text{ m.s}^{-1}$ is about 2.0 at the optimal tip speed ratio (Fig. 3.7). That value falls within the uncertainty range of the full-scale average drag coefficient indicating low scale effects. That result is confirmed by the experimental results as $\overline{C_x}$ increases by less than 5% between $U_0 = 0.94$ and 1.69 m.s^{-1} (Fig. 3.29). It is also in line with the results of Ross (2020) regarding the Reynolds number effects on the drag of a single vertical axis rotor. In addition, Fig. 3.29 also displays the evolution of the average hydrodynamic coefficients of the 6 load components measured by the upper load cell, between the turbine and the gravity base (Fig. 3.3). The force coefficients are defined like C_x in Eq. 3.8 and the moment coefficients like C_{M_x} in Eq. 3.9 in the three directions (x, y, z). Apart from the moment along the vertical axis C_{M_z} that will need further investigations, the five other load components appear only slightly affected by the current velocity. Therefore, we can assume limited scale effects on these load components, like observed on the drag coefficient.

$$C_x(t) = \frac{F_x(t)}{2\rho D H_{blade} U_0^2} \quad (3.8)$$

$$C_{M_x}(t) = \frac{M_x(t)}{2\rho R D H_{blade} U_0^2} \quad (3.9)$$

Finally, in addition to the average loads, the structural design of the turbine requires the prediction of the instantaneous extreme loads and their fluctuation ranges to assess the ultimate limit state and the fatigue stress, respectively. The measurement of the instantaneous loads at sea was limited to a low 1 Hz acquisition frequency for the rotational speed, the rotor column torque and the streamwise load, with an important uncertainty on the later. In addition, the isolated bottom-mounted ADCP measurements may be representative enough of the incident average velocity for the computation of the average load and power coefficients but they appear quite inappropriate for instantaneous loads assessment. The random Doppler noise inherent to that kind of instruments imposes time averaging to get accurate velocity measurements (Thomson et al., 2010). Therefore, the computation of instantaneous load coefficients would be based on a typical 10-minute averaged velocity, under the hypothesis of steady flow conditions. However,

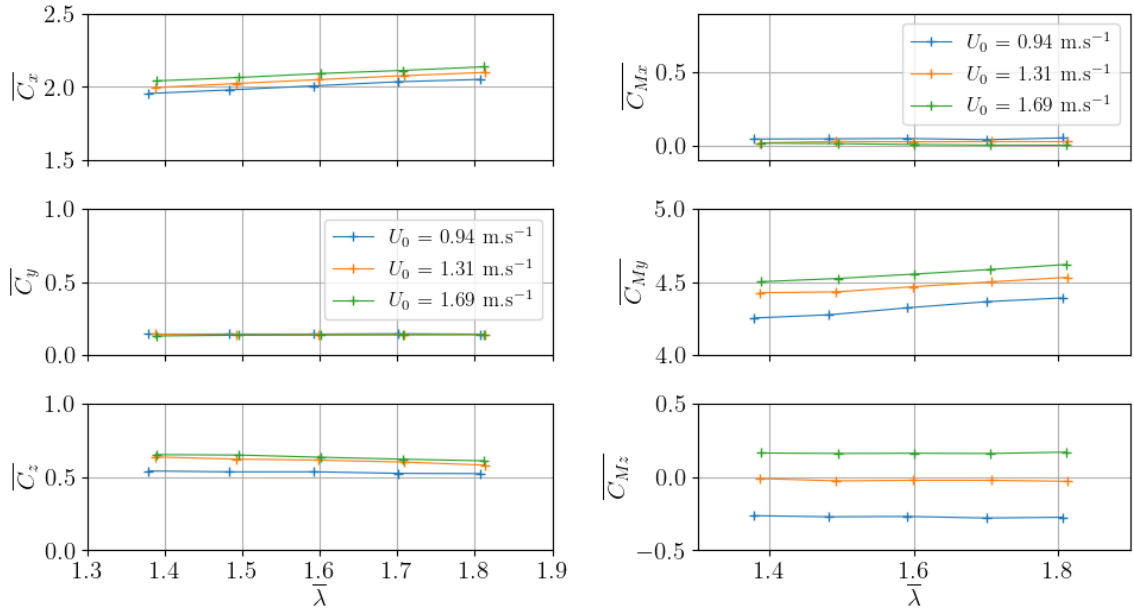


Figure 3.29 – Evolution of the average hydrodynamic force and moment coefficients of the ducted 2-VATT reduced-scale model with the tip speed ratio, facing different incident velocity magnitudes in the flume tank.

Mercier et al. (2022) found a high temporal and spatial variability of the flow characteristics at the Paimpol-Bréhat test site. That result is in contradiction with the steady flow hypothesis and questions the representativeness of spatially isolated incident flow measurement with regard to the flow actually perceived by the turbine. Thus, instead of instantaneous load coefficients, we chose in the previous chapter to analyse the prototype load fluctuation in terms of Fluctuation Intensity (FI). That quantity is analogous to the turbulence intensity as it is the ratio of the standard deviation to the average of the load signals.

Fig. 2.15 showed that the average FI over the selected calm sea state instants is 0.09 for the rotational speed of one rotor column, 0.18 for the torque generated by that rotor column, and 0.16 for the streamwise load on the whole ducted 2-VATT prototype. Fig. 3.30 (a) displays the evolution of the same three fluctuation intensities measured on the reduced-scale model in the typical idealised flow conditions in the flume tank at different upstream velocities. First, we observe that $FI(F_x)$ is about two times lower in the reduced-scale experiments compared to the results at sea. We assume this result to be mostly due to the idealised experimental flow condition with a low 1.5 % turbulence intensity level compared to the 10 to 20 % measured at the Paimpol-Bréhat test site by Filipot et al. (2015). Then, despite that turbulence intensity difference, we find that the rotor column torque FI is in the same range or even higher in the tank compared to at sea while $FI(\omega)$ is almost null. That result can be explained by the difference of rotor control law between the prototype and the reduced-scale model. Indeed, the control law of the prototype imposes a quadratic relation between the torque and the rotational speed (Eq. 2.2) but it lets the two quantities fluctuate freely. Thus, the rotational speed range between the minimal and maximal ω values is of the order of half

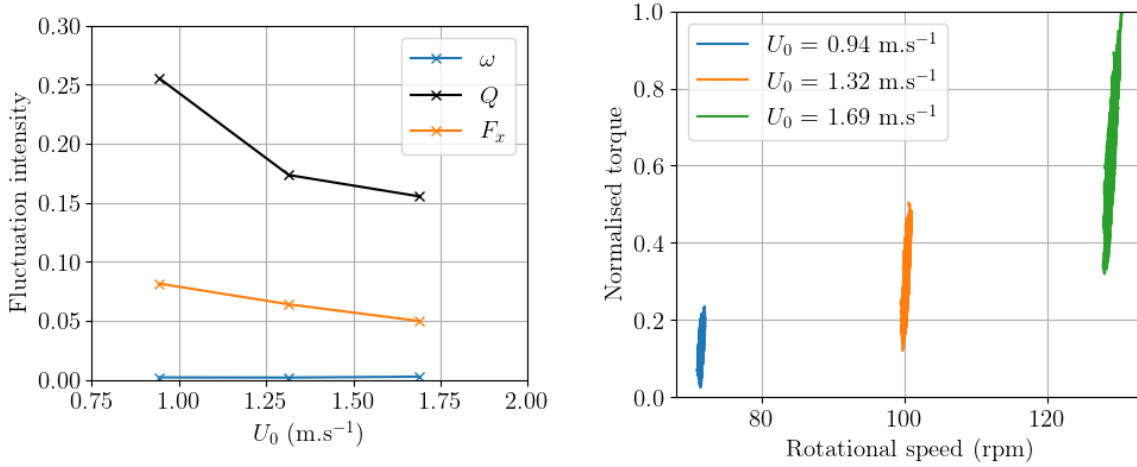


Figure 3.30 – (Left) Fluctuation intensity of the rotational speed and the torque of the green rotor column as well as of the streamwise load on the turbine. (Right) Normalised torque with regard to the rotational speed of the green rotor column. From the measurements on the reduced-scale model at λ_{opt} and at different upstream velocities U_0 .

the average in calm sea states (Fig. 2.12). Conversely, the reduced-scale control law imposes a strictly constant rotational speed to the rotor columns (Fig. 3.30 (b)). As a result, only the rotor torque can vary facing current velocity fluctuation at reduced-scale, which causes a larger torque fluctuation intensity and a lower rotational speed one on the model than on the prototype in similar flow conditions. So, improvements on the setup and the processing of the measurements at sea are needed to improve the instantaneous load characterisation and to be able to provide more fine results both for the design process of such prototypes and for the comparison with the reduced-scale measurements. On the other hand, improvements on the rotor control law at reduced-scale is also needed to better model the response of the rotors facing current velocity fluctuation. That being, despite the inaccurate prediction of the absolute rotor torque fluctuation intensities by the reduced-scale experiments, we can reasonably assume that the evolution of the torque fluctuation measured on the model with regard to the flow characteristics remains relevant.

3.2.2 Scale effects on the flow surrounding the turbine

In the perspective of twin vertical axis tidal turbine farm developments, assessing the potential scale effects on the velocity field upstream of the turbine (the induction zone) and downstream (the wake) is necessary to know whether reduced-scale measurements can be used as inputs for turbine layout optimisation tools. In the previous chapter, Fig. 2.10 revealed the first ever vertical velocity profiles measured simultaneously upstream and downstream of the ducted 2-VATT at sea, which provided preliminary results on the wake of the prototype. However, due to the flow direction asymmetry between ebb and flood tides as well as its important temporal and spatial variability at the Paimpol-Bréhat test site (Mercier et al., 2022), the fixed bottom-mounted ADCP setup developed for power performance assessment is inappropriate for a proper wake characterisation of the ducted 2-VATT prototype. Sweeping the width of the turbine wake region at

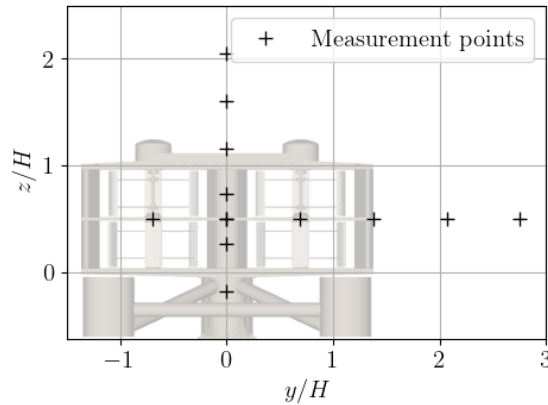


Figure 3.31 – Location of the velocity measurement points using the 3C-LDV in the wake of the ducted 2-VATT at $x/H = \{1; 2; 3; 5; 7; 9\}$ with $U_0 = 1.69 \text{ m.s}^{-1}$.

different downstream positions with vessel-mounted ADCPs would be more adapted (Huchet et al., 2023). Such measurements have not been carried out with the ducted 2-VATT prototype but should be considered with the future 2-VATT deployments at sea.

To still assess the effect of the Reynolds number on the flow surrounding the ducted 2-VATT, we measure the velocity upstream and downstream the reduced-scale model at $U_0 = 0.94$ and 1.69 m.s^{-1} . In the previous part of this chapter, we described the experimental setup for the measurements at $U_0 = 0.94 \text{ m.s}^{-1}$ (3.1.2) and we analysed the results (3.1.4). The measurements at $U_0 = 1.69 \text{ m.s}^{-1}$ are carried out with the turbine in flood tide configuration operating at $\lambda = 1.6$ too. The velocity is measured using the same 3C-LDV probe at the same positions upstream of the turbine at the centre of the projected capture area. We consider fewer points in the turbine wake compared to the tests at $U_0 = 0.94 \text{ m.s}^{-1}$ however as we measure the velocity over a single horizontal profile at mid-turbine height and a single vertical profile at mid-turbine width (Fig. 3.31). The 3 minute-long measurements provide time-converged average and standard deviation of the velocity at each point. Fig. 3.32 presents those two quantities for the three velocity components along the streamwise profile measured upstream of the ducted 2-VATT at the centre of its projected capture area. The results show almost no induction zone difference between the two current velocity setpoints. Furthermore, Fig. 3.33 compares the average streamwise velocity profiles and Fig. 3.34 the 2-dimensional turbulent kinetic energy (Eq. 3.7) profiles in the wake of the ducted 2-VATT at the two velocity setpoints. Similarly to the velocity profiles upstream of the turbine, the wake results present no significant difference between the two current velocity setpoints. These results are in agreement with those of Bachant et al. (2016) regarding the effect of the Reynolds number on the near-wake of an isolated vertical axis rotor. Therefore, we can expect very little scale effects on the ducted 2-VATT wake evolution with confidence.

As already mentioned, Grondeau et al. (2019) and Jégo et al. (2021) already studied the wake of the ducted 2-VATT full-scale prototype using numerical models. The first one studied the effect of the ambient turbulence on the 3-dimensional wake of a single ducted 2-VATT by implementing an Actuator Line Method (ALM) into a Lattice Boltzmann Method (LBM) large eddy simulation solver. The second studied a single

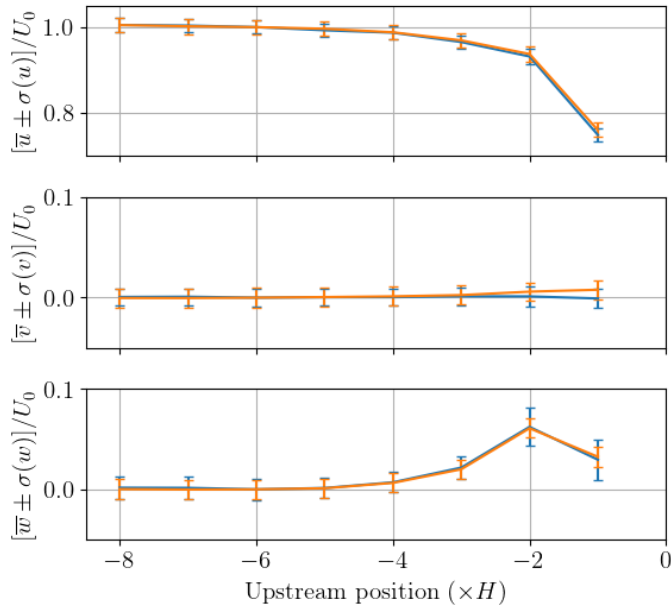


Figure 3.32 – Flow velocity measured upstream of the model in flood tide configuration at the centre of the projected capture area of the ducted 2-VATT and at varying x positions using the 3C-LDV, at $U_0 = 0.94 \text{ m.s}^{-1}$ (blue) and 1.69 m.s^{-1} (orange).

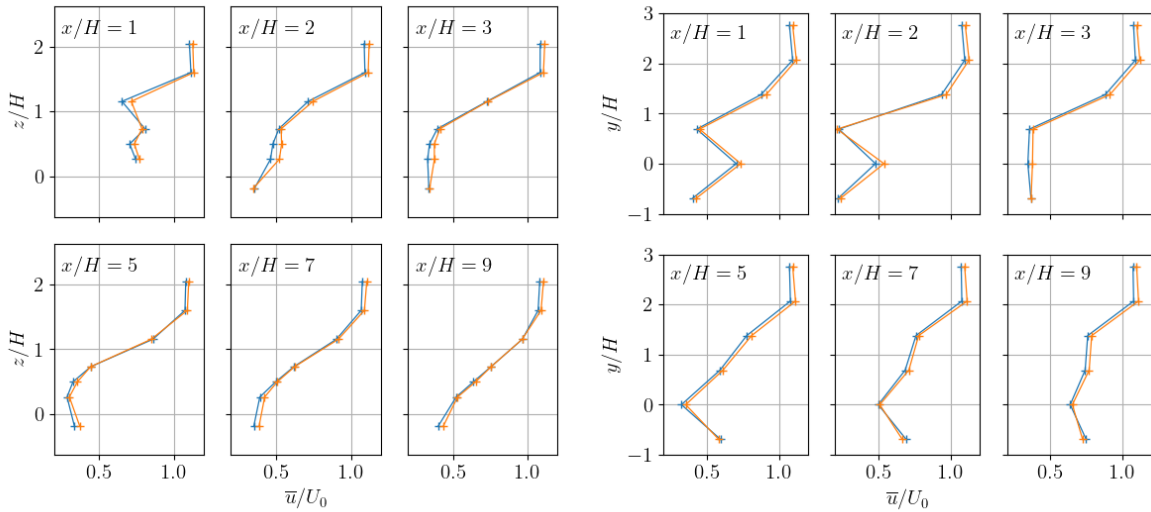


Figure 3.33 – Vertical (left) and horizontal (right) profiles of the average streamwise velocity measured with the 3C-LDV in the wake of the ducted 2-VATT at $U_0 = 0.94 \text{ m.s}^{-1}$ (blue) and 1.69 m.s^{-1} (orange).

ducted 2-VATT as well as several farm configurations under different current conditions by a 2-dimensional approach based on the actuator cylinder model implemented in the steady Reynolds-averaged Navier-Stokes equations in ANSYS Fluent. However, both models were validated compared to experimental results on a single vertical axis turbine only while several studies showed the effect of pairing two VATs on the wake evolution compared to an isolated VAT (Vergaerde et al., 2020a). Therefore, in the direct

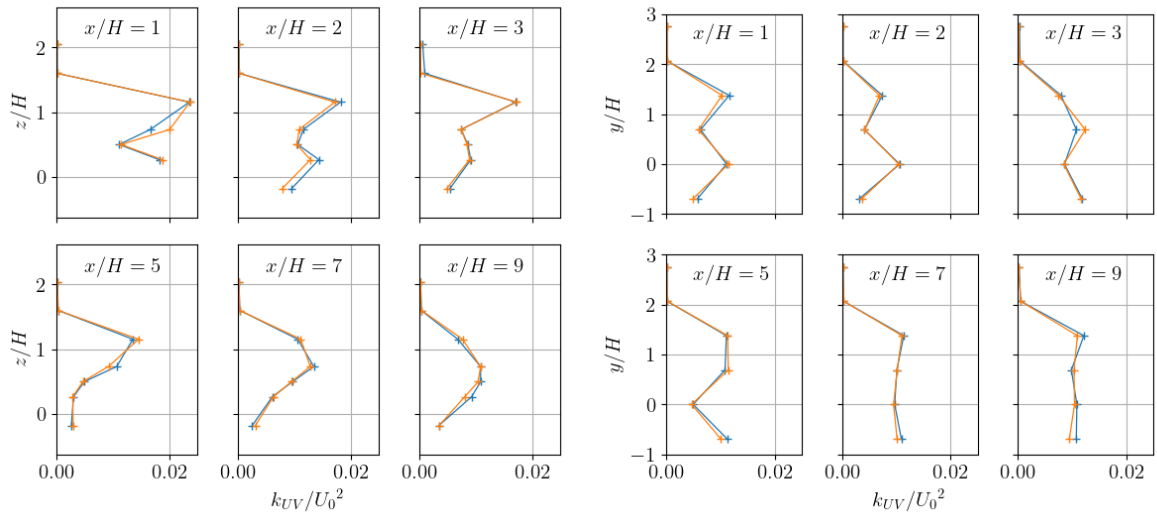


Figure 3.34 – Vertical (left) and horizontal (right) profiles of the 2-dimensional turbulent kinetic energy measured with the 3C-LDV in the wake of the ducted 2-VATT at $U_0 = 0.94 \text{ m.s}^{-1}$ (blue) and 1.69 m.s^{-1} (orange).

extension of the experimental wake characterisation presented in this thesis, Grondeau et al. (2023) compare the ALM-LBM numerical results to the experimental ones in the wake of the reduced-scale ducted 2-VATT. As displayed in Fig. 3.35, they manage to get pretty accurate numerical results compared to the experimental ones in terms of average and fluctuating streamwise velocity, both in the near-wake and in the far-wake, using an appropriate mesh refinement. Once validated, the numerical model can be used to study the wake of the turbine with a more fine spatial resolution, in a larger variety of flow conditions, and potentially to optimise the turbine layout of tidal turbines farms. For instance, Grondeau et al. (2023) study the influence of the turbulence length scale on the wake of the ducted 2-VATT. Fig. 3.36 displays the results with average streamwise velocity contours in the (x, y) plane at the top rotors mid-height and in the (x, z) plane at $y/H = 0$ for one ambient turbulence case. The greater spatial resolution of the numerical results compared to our 3C-LDV measurement mesh provides a better insight into the interaction between the wake of the ducted 2-VATT with that of the gravity base. It also reveals that the 0.5 and 0.8 m.s^{-1} iso-contours are made of three branches in the horizontal planes, which we did not capture with the low spatial resolution of our measurements. Thus, the analysis of the numerical model results will provide a great extension of the ducted 2-VATT wake evolution understanding.

To sum up, after having characterised the behaviour of the full-scale ducted 2-VATT prototype in the previous chapter, we analysed that of a $1/20$ scale model in the typical idealised experimental flow conditions and we assessed the scale effects by comparing the two databases. In the reduced-scale experiments, we focused on analysing the performance and the wake of the ducted 2-VATT when the flow comes from one or the other side of the turbine, like during ebb and flood tides at sea. We found that the optimal tip speed ratio and the maximal average power coefficient are slightly lower in the ebb tide configuration (EC) compared to the flood tide configuration (FC). That result could

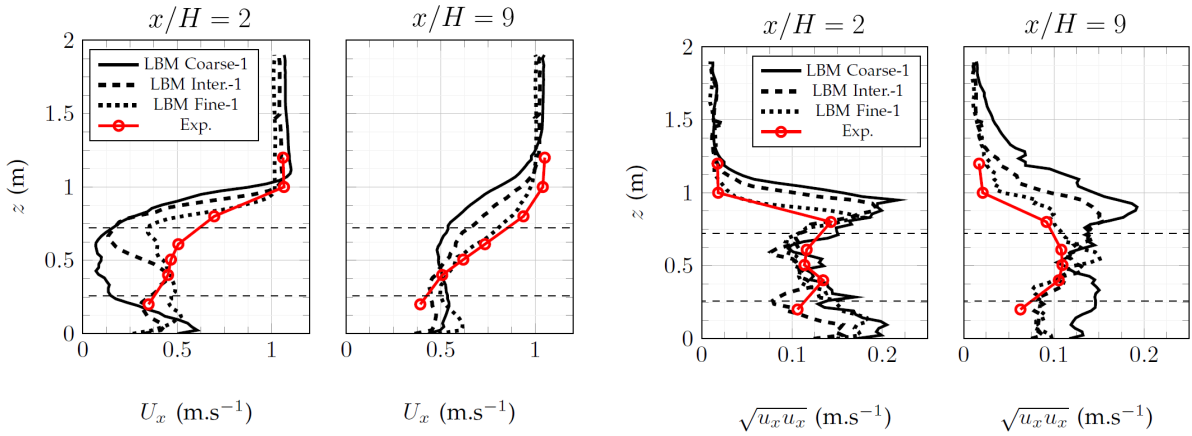


Figure 3.35 – Average streamwise velocity (left) and velocity fluctuation (right) at two downstream distances in the wake of the reduced-scale model ducted 2-VATT at $y/H = 0$, from Grondeau et al. (2023). The black lines are computed with the ALM-LBM numerical model with different mesh refinements while the red line is the experimental data from the section 3.1.4.

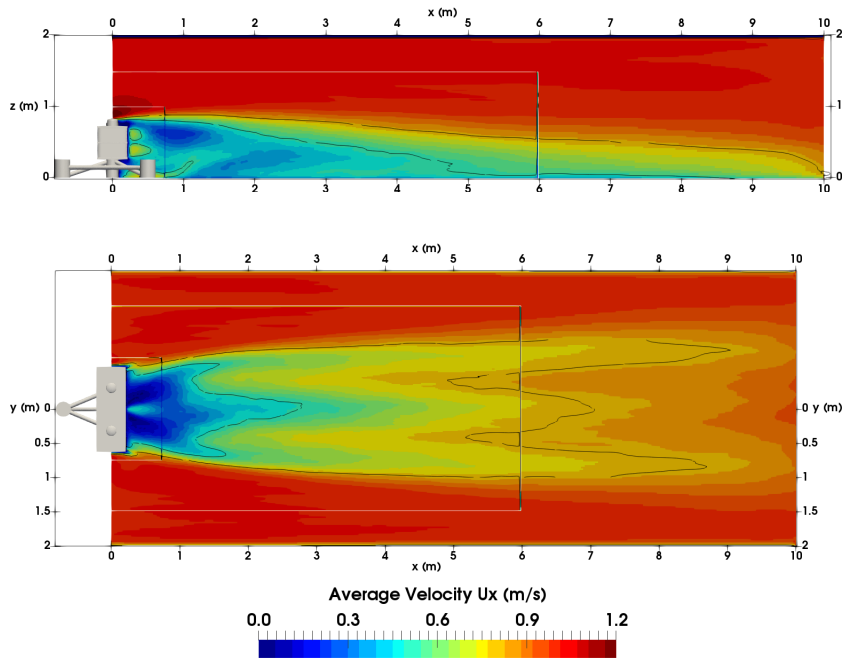


Figure 3.36 – Average streamwise velocity contours computed with the ALM-LBM numerical model in the (x, y) plane at top rotors mid-height (top) and in the (x, z) plane at $y/H = 0$ (bottom), from Grondeau et al. (2023) with 10 % turbulence intensity and synthetic eddy method vortices radius of 0.33 m. Iso-contours of $U_x = 0.5$ and 0.8 m.s^{-1} are displayed.

explain part of the difference observed between the flood and ebb tide power curves of the prototype at sea. In addition, the ducted 2-VATT wake is clearly affected by the difference of relative counter rotation direction of the two rotor columns between EC and FC as well as by the asymmetrical base geometry. The velocity deficit recovers 30 % faster in FC than in EC with a tripod base similar to that of the prototype, and even

20 % faster with a simple monopile base compared to the tripod in FC. Then, we found that the reduced-scale experiments provide similar average drag coefficient to what was measured at full-scale, given the measurements uncertainty, which indicates low or no scale effects on the dimensionless streamwise load. The tests at different velocity set-points (and so Reynolds numbers) at reduced-scale allow to assume this conclusion valid for all the other load components, apart from C_{Mz} that will need further investigations to be well understood. In addition, we showed that the reduced-scale experiments alone fail in predicting the absolute average power performance at full-scale. However, the combination of the reduced-scale results with a simple 2-dimensional numerical model of the ducted 2-VATT succeed in that prediction within the power performance measurement uncertainty at sea. Conversely, the quantification of the scale effects regarding the instantaneous loads remains a challenge that requires improvements on the setup and the processing of the measurements at sea. Still, based on a simple statistical metric, we found that the difference of rotor control law between the prototype and the model causes an overestimation of the absolute rotor torque fluctuation intensity. Finally, although we managed to observe some velocity deficit in the wake of the prototype at sea, the fixed bottom-mounted ADCP setup developed for power performance assessment is inappropriate for a proper wake characterisation of the ducted 2-VATT prototype. Better in-situ wake measurement setups like in Huchet et al. (2023) will have to be studied in the future to allow a comparison between reduced- and full-scale results. That being, the flow measurements around the model at two velocity setpoints along with the existing literature regarding the Reynolds number effect on the wake of vertical axis turbines indicate only low or no scale effects on the average flow characteristics. The experimental wake results in idealised flow conditions presented in this thesis paves the way for the validation of dedicated numerical models that could provide complementary scale effect assessments as well as more detailed wake characterisation. The numerical results still need to be validated considering more realistic operating conditions, such as bathymetry-induced turbulent flows or in presence of surface waves. The validated numerical models will finally be of use for turbines layout optimisation in the prospect of 2-VATT farm deployments.

CHAPTER 4

Reduced-scale model response facing more realistic flow conditions

In the previous chapter, we characterised the behaviour and the wake of a 1/20 scale model of the 1 MW-rated ducted 2-VATT prototype in idealised flow conditions. However, the tidal current flow conditions at sea are much more complex due to the vertical shear of the velocity profile and to the flow misalignment with regard to the turbine heading. In addition, the rough seabed causes high levels of turbulence in the flow and the presence of surface waves generates velocity fluctuation in the whole water column. Indeed, we showed in chapter 2.1 that, at the Paimpol-Bréhat test site, the vertical velocity profile is sheared with about 20 % velocity difference between the top and the bottom of the turbine capture area, and the average direction asymmetry between ebb and flood tides at this location is about 22° (Fig. 2.5 and 2.3). In addition, the turbulence intensity is evaluated about 15 % (Filipot et al., 2015) and extreme wave conditions up to 6 m significant wave height with 12 s peak period were observed between 2019 and 2021. In the present chapter, we study experimentally the behaviour of the reduced-scale ducted 2-VATT in all of these flow conditions individually to better understand their effect on the turbine power performance and loads. The first part (4.1) focuses on the effect of the velocity vertical shear and on the relative flow misalignment with the turbine heading, still in a steady flow. In the second part (4.2), we address one of the flow unsteadiness sources by studying the effect of the turbulent wake generated by large bathymetry obstacles located upstream of the turbine. Finally, we analyse the effect of surface waves on the ducted 2-VATT response in the third part (4.3) by generating waves of several amplitudes and frequencies, following or opposing the current.

4.1 Turbine behaviour in a vertically sheared and misaligned current

4.1.1 Introduction

This work was originally published as Moreau et al. (2023d), “Misaligned sheared flow effects on a ducted twin vertical axis tidal turbine”, in *Applied Ocean Research*. The introduction is made short to avoid repetitions with the general introduction of the thesis. A few studies considered Horizontal Axis Tidal Turbines (HATT) in collinear sheared flows (Magnier et al., 2022; Vinod et al., 2021) and others analysed the effect of flow misalignment with uniform velocity profiles (Frost et al., 2017; Modali et al., 2021), but none combined both, to the author knowledge. Besides, only a few studies considered single vertical axis wind turbines facing vertically sheared velocity profiles (Shamsoddin et al., 2016; Mendoza et al., 2019) and found minor influence on the power coefficient. However, the effect of a vertical velocity gradient has never been considered neither on twin vertical axis turbines (VAT) nor on turbines combining several levels of out-of-phase VATs on a same shaft. Similarly, while pairing two counter-rotating VATs improves the power performance and shortens the wake (Vergaerde et al., 2020a; Müller et al., 2021), it also leads to the loss of the complete symmetry that characterises isolated VATs. But the flow orientation influence on the behaviour of twin VATs has never been studied. Thus, in this part, the effect on HydroQuest’s reduced-scale ducted 2-VATT of both the flow shear and its misalignment is analysed based on experiments in Ifremer’s wave and current flume tank (Fig. 4.1). Section 4.1.2 presents the turbine model and its setup in the tank before describing the data acquisition and processing methods. Next, section 4.1.3 presents the effect of the shear in aligned flow conditions and the effect of the flow misalignment with a sheared flow on the behaviour of the ducted 2-VATT. Finally, the results are discussed with the help of upstream flow measurements in section 4.1.4.

4.1.2 Material and method

4.1.2.1 Experimental setup

The ducted 2-VATT 1/20 scale model is geometrically similar to the full-scale 1 MW-rated demonstrator tested by HydroQuest at Paimpol-Bréhat test site (Moreau et al., 2021). It is composed of two independent counter-rotating vertical axis rotor columns. Each column is made of two levels of rotors with a 60° phase difference between them, and each rotor of radius $R = D/2 = 200$ mm is made of $N = 3$ blades with a height (H_{blade}) of 190 mm and a chord (c) of 73 mm. Thus, the rotors solidity (Nc/R) is 1.1, similarly to the full-scale demonstrator. The rotors are mounted in a structure made of fairings and plates. The turbine height is defined as the distance between the top and the bottom horizontal plates such that $H = 450$ mm. The turbine is fixed on a bottom-mounted base, either a tripod similar to the demonstrator’s base or a central monopile of the same height. The results presented in this study are with the tripod base. The 2-VATT model is tested in Ifremer’s 2 m deep and 4 m wide wave and current flume tank in Boulogne-sur-mer, France, at a velocity set point of $1 \text{ m}\cdot\text{s}^{-1}$ (Gaurier et al., 2018). The orthogonal coordinates system considered is such that x is in the current direction with its origin at the centre of the model and z points towards the surface with its

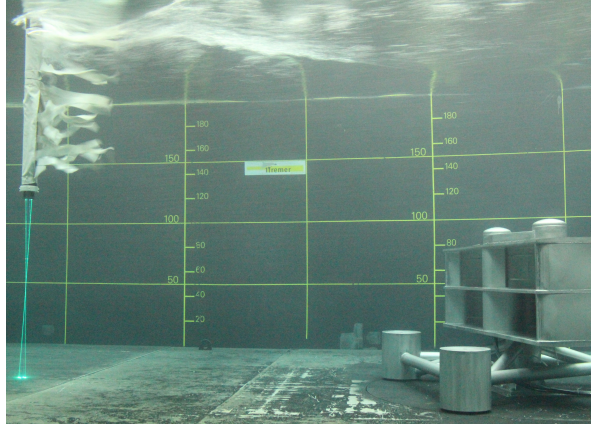


Figure 4.1 – 2C-LDV measurement in the Ifremer’s tank upstream of the ducted 2-VATT model in ebb tide configuration with -15° misalignment between the flow direction and the turbine heading.

Table 4.1 – Recap of the main similitude values between tank tests and in-situ operation at Paimpol-Bréhat, with $g = 9.81 \text{ m.s}^{-2}$ the gravity constant, $\nu = 1.05 \cdot 10^{-6} \text{ m}^2.\text{s}^{-1}$ the water kinematic viscosity and $\lambda = 1.5$ the tip speed ratio (Eq. 4.4).

Scale	Water depth H_{wat} (m)	Structure height H_{struc} (m)	Flow velocity U (m.s^{-1})	Froude number $\frac{U}{\sqrt{g(H_{wat}-H_{struc})}}$	Reynolds number $\frac{\lambda c U}{\nu}$
1/20	2	0.84	1.0	0.30	$1.0 \cdot 10^5$
1/1	40	17	2.5	0.17	$5.2 \cdot 10^6$

origin at the bottom plate of the turbine, such that the turbine capture height ranges between $z/H = 0$ and 1. The model, its instrumentation and the setup in the tank are fully described in Moreau et al. (2023c). The main similitude quantities between reduced- and full-scale are presented in Tab. 4.1. The Reynolds number at full-scale is about 50 times higher than in the present experiment, which is expected to reduce the blades performance (Michna et al., 2022). The Froude number based on the turbine submergence (Tab. 4.1) is 1.8 times higher in the tank than at sea but it remains low enough to avoid interactions with the free surface.

To generate low turbulence flows in the tank, the inlet is conditioned by a grid and a honeycomb structure (Fig. 4.2 (a)). Usually, the grid is homogeneous over the tank section and provides a uniform velocity profile with a $0.6H$ high boundary layer (Fig. 4.3). To generate a sheared current similar to what was measured at Paimpol-Bréhat test site, we developed a special apparatus presented in (Magnier et al., 2022; Moreau et al., 2021). The latter consists of a panel made of multiple layers of wire meshes fixed on the grid upstream of the honeycomb (Fig. 4.2 (b)). The multiple layers are non-uniformly distributed along the vertical direction and are uniform along the tank width. Thus, the panel generates variable friction losses along the height leading to a vertically sheared current profile downstream on the whole tank width. The streamwise average velocity and turbulence intensity profiles at the turbine position in the empty tank are presented in Fig. 4.3. The streamwise turbulence intensity is defined as $TI_u = \sigma(u)/\bar{u}$, with u the streamwise velocity, the bar on top indicating the time average and $\sigma(\)$ the time standard deviation of the quantity between brackets. The sheared average velocity

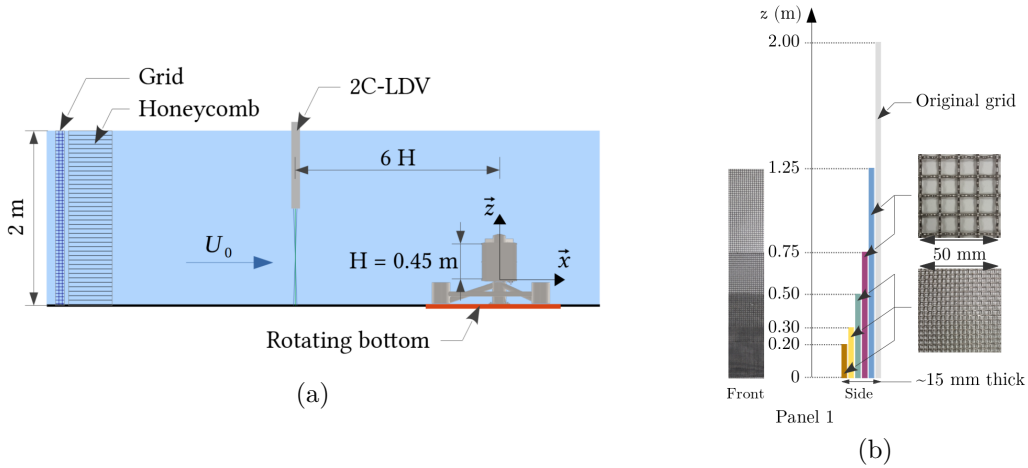


Figure 4.2 – (a) Scheme of the experimental setup in the Ifremer’s wave and current flume tank. (b) Scheme of the grid arrangement developed for the generation of a sheared velocity profile, with $z = 0$ m at the tank bottom.

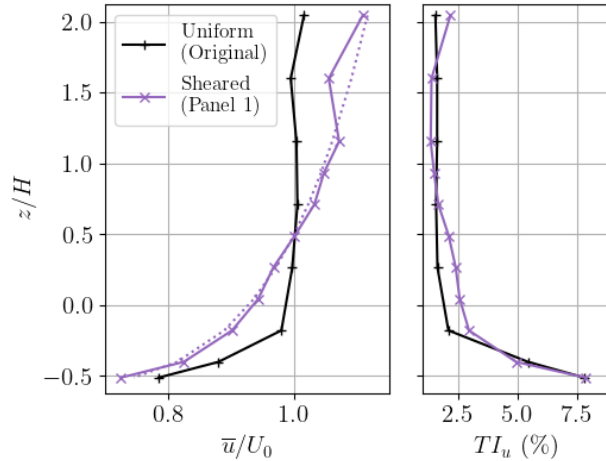


Figure 4.3 – Mean normalised streamwise velocity and turbulence intensity profiles measured with the 3C-LDV probe at the centre of the tank without turbine, with $z/H = 0$ at the turbine bottom. The sheared average velocity profile fit (purple point line) is

$$\bar{u}/U_0 = \left(\frac{z}{0.42H_w}\right)^{1/7.91}.$$

profile power law fit is consistent with such fits at sea (Cossu et al., 2021; Lewis et al., 2017; Moreau et al., 2021) and provides a 13 % velocity difference between the top and the bottom of the turbine capture area.

Furthermore, the flow angle of incidence (α) with regard to the 2-VATT heading was of -7° at flood tides and $+15^\circ$ at ebb tides during full-scale demonstration (Moreau et al., 2022b). In the present paper, we also study the effect of those flow misalignments on the turbine behaviour in presence of the sheared velocity profile in the tank. The model 2-VATT is set in the two flow directions representing Flood and Ebb tide Configurations (FC and EC respectively) at Paimpol-Bréhat test site. For each configuration, we test five relative angles of incidence: 0° , $\pm 7^\circ$ and $\pm 15^\circ$ (Fig. 4.4). To do so, the model is

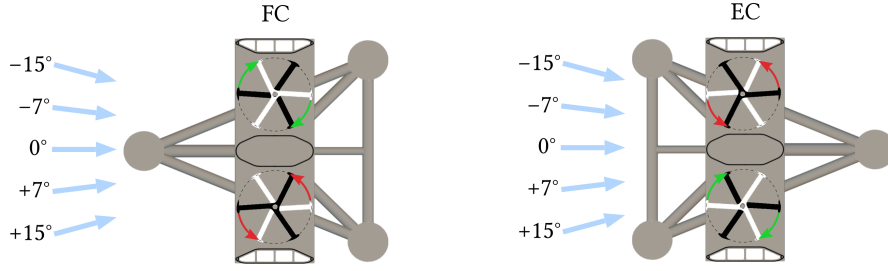


Figure 4.4 – Schematic top view of the ducted 2-VATT with the flow angles of incidence tested in the tank both in the Flood and Ebb tide Configurations (FC and EC respectively).

fixed either in FC or EC on the rotating bottom of the tank. Then, it is rotated using the automated rotating system from -15° to $+15^\circ$ (Fig. 4.2 (a)).

4.1.2.2 Data acquisition and processing

For hydrodynamic performance assessment, the current velocity is measured using a *Dantec* 2-Component Laser Doppler Velocimeter (2C-LDV). The latter measures the velocity along (x, y) in non-coincident mode with an acquisition data rate of the order of 200 Hz. The probe is placed at $x/H = -6$, at the centre of the turbine projected area (ie. $(y, z) = (0, 0.5)H$). At this point, the average u and v are undisturbed by the TEC induction and remain the same whatever the turbine configuration and misalignment. The average streamwise component of the velocity at this point, which is equal to the average over the turbine height for the two velocity profiles, is considered as the reference velocity (noted U_0) and is $0.945 \pm 0.005 \text{ m.s}^{-1}$ overall. Synchronously with the 2C-LDV, each rotor column torque (Q), rotational speed (ω) and the 6 load components applied between the turbine and the base are acquired using *National Instruments PXI* and *LabView* systems. The acquisitions last 3 minutes with a 128 Hz sampling frequency to guarantee the time convergence of the mean and standard deviation of the signals.

The power extracted by the 2-VATT is analysed at two scales. At the rotor column scale, we compute the instantaneous power $P_{col}(t) = Q(t)\omega(t)$ with t the time. The torque signal considered is corrected by the friction torque induced by the seals and the transmission system for each rotor column (Moreau et al., 2023c). The column power coefficient ($C_{P_{col}}$, Eq. 4.1 with $\rho = 1000 \text{ kg.m}^{-3}$) is computed with the two rotors projected area as a reference surface ($S = 2DH_{blade}$). At the turbine scale, we also compute the instantaneous total power (P) as the sum of the power extracted by the two rotor columns. The turbine power coefficient (C_P , Eq. 4.2) is computed with the four rotors projected area as the reference surface ($S = 4DH_{blade}$). The fluctuation of this quantity depends on the random relative phase between the two columns. By nature, VATT loads fluctuate periodically at the blade passing frequency. If the two columns are in phase, the sum of their instantaneous power doubles the periodical fluctuation, similarly to constructive interferences, assuming a perfect symmetry between the two columns. Conversely, if they are in perfect phase opposition, that fluctuation vanishes, similarly to destructive interferences. Thus, given the randomness of those interferences, the standard deviation of the instantaneous total power is irrelevant to study the physical effect of flow condition changes on the behaviour of the 2-VATT. Instead, we define

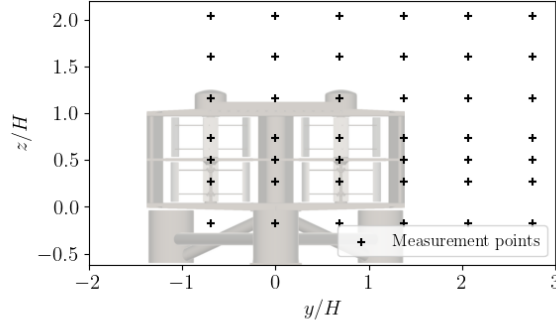


Figure 4.5 – Points mesh used for velocity measurements with the 3C-LDV at $x/H = 3$.

$\bar{\sigma}(C_{Pcol})$ as the average of the standard deviation of the two columns power coefficients to better represent the mechanical fluctuation perceived by the whole turbine.

$$C_{Pcol}(t) = \frac{P_{col}(t)}{\rho D H_{blade} U_0^3} \quad (4.1)$$

$$C_P(t) = \frac{P(t)}{2\rho D H_{blade} U_0^3} \quad (4.2)$$

In addition, the drag coefficient is computed using F_x , the load in the streamwise direction measured between the turbine and the base, considering the projected area of the four rotors as the reference surface (Eq. 4.3). The power and drag results are presented with regard to the tip speed ratio (λ) defined in Eq. 4.4. The distribution of the torque coefficient (C_Q , Eq. 4.5) along the rotor angular position of the green column (Fig. 4.4) is also analysed. The instantaneous relative angular position (positive in the rotation direction) is computed by Hilbert transform of the torque signal filtered around the rotational frequency. The angular position being relative, the absolute angle values displayed cannot be compared between graphs. The phase average, indicated by a tilde on top of the symbol, is computed over 75 revolutions with 3° angle bins. The phase shift between torque maxima are computed by identifying the locations of the smoothed torque phase average maxima. The smoothing is obtained by a low-pass third order Butterworth filter.

$$C_x(t) = \frac{F_x(t)}{2\rho D H_{blade} U_0^2} \quad (4.3)$$

$$\lambda(t) = \frac{\omega(t)R}{U_0} \quad (4.4)$$

$$C_Q(t) = \frac{Q(t)}{\rho D H_{blade} R U_0^2} \quad (4.5)$$

Furthermore, the flow surrounding the ducted 2-VATT is characterised at $\lambda = 1.6$ in FC and EC for the uniform and the sheared velocity profiles without flow misalignments. The measurements are conducted with a *Dantec* 3-Component LDV, in non-coincident mode, as described in Moreau et al. (2023c). The velocity maps presented hereinafter are drawn based on linear interpolations between the mesh points (Fig. 4.5) with a 40 mm step in the y and z directions.

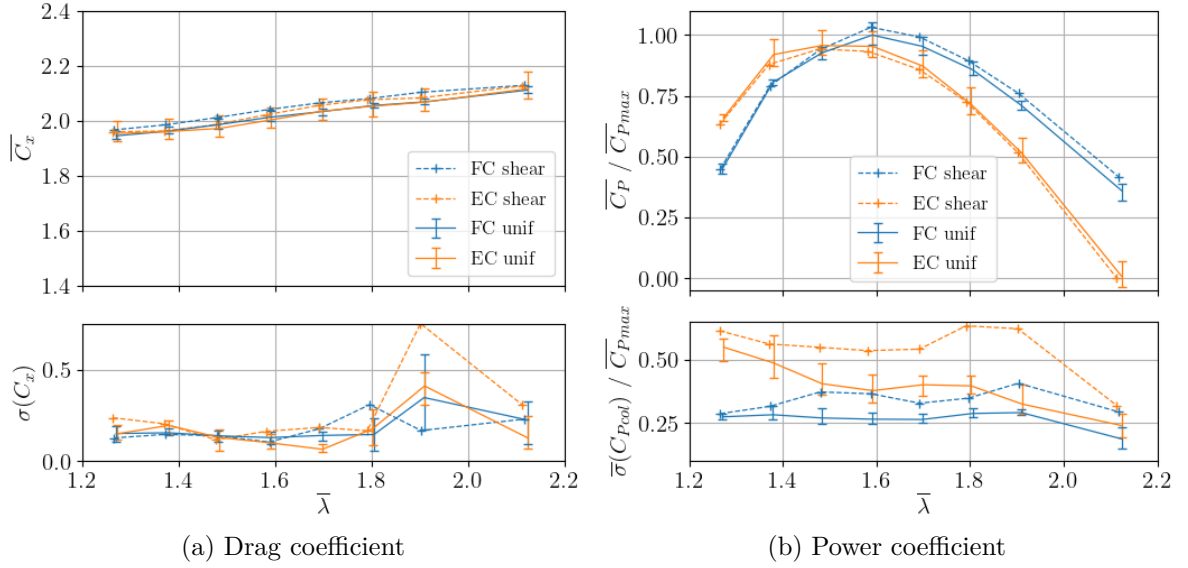


Figure 4.6 – Average (top) and standard deviation (bottom) of the drag and power coefficients in FC and EC with sheared and uniform incident velocity profiles. The curves with the uniform velocity profile are averages over 3 test campaigns with the error bars representing the extreme average and extreme standard deviation values over the 3 campaigns. The C_P are normalised by the maximal average value in "FC unif".

4.1.3 Flow shear and misalignment effects

First, we analyse the effect of a sheared incident flow compared to a uniform one, collinear with the turbine heading. Then, the impact of flow misalignments added to the shear is presented. In the two sections, we study the overall performance of the 2-VATT in terms of power and drag before addressing the effect at a single rotor column scale.

4.1.3.1 Aligned sheared flow effect

Fig. 4.6 displays the drag and power coefficients of the turbine facing the uniform and the sheared flows both in EC and FC. The results show that the ducted 2-VATT drag is insensitive to the incident velocity profile, both in terms of average and standard deviation. We only observe differences of $\sigma(C_x)$ at $\lambda = 1.9$ that are related to vibrations of the model. The average power coefficient is also hardly affected by the flow shear given the measurements repeatability (Fig. 4.6 (b)). However, the power fluctuation strongly increases with the sheared flow as the standard deviation rises by 35 % at the optimal operating point (λ_{opt} , where $\overline{C_P}$ is maximal), both in EC and FC.

To look at the shear effect at the rotors scale, Fig. 4.7 displays the torque coefficient with regard to a relative angular position at λ_{opt} facing the uniform flow (a & c) and the sheared flow (b & d) in EC and FC. On one hand, in uniform flow, the distribution in FC is smoother than in EC where the torque peaks and troughs are more pronounced. We also observe about 20 % difference between the torque generated by the two levels of rotors in EC while the contribution of the two levels is rather balanced in FC. The phase averaged torque maxima are separated by 60° in EC, similarly to the geometrical phase difference between the upper and the lower rotors. However, we observe an additional

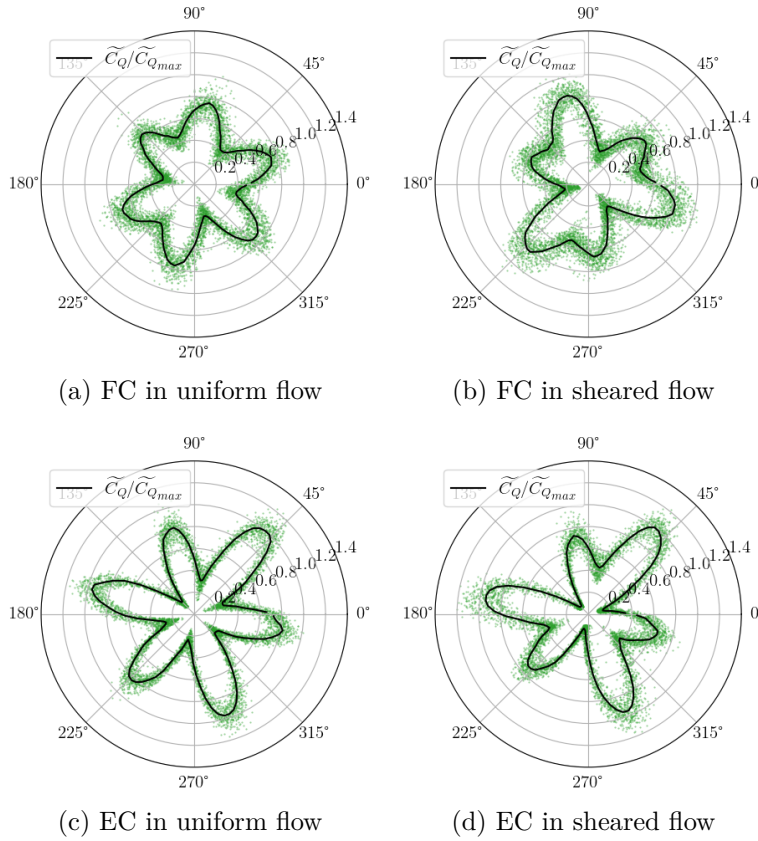


Figure 4.7 – Angular distribution of the green rotor column torque coefficient for the two aligned flow directions and the two velocity profiles at the optimal λ (1.6 in FC and 1.5 in EC). The green dots are the instantaneous measurements and the black line is the phase average. The values are normalised by the maximal phase average value in EC in uniform flow. *Reminder*: the angular position is relative, so the absolute angle values cannot be compared between graphs.

phase shift $\Phi_Q = 5^\circ$ compared to the geometrical phase between the torque peaks of the upper and the lower rotors in FC. The differences between EC and FC in uniform flow are discussed in depth in Moreau et al. (2023c) and are due both to the tripod base asymmetry and to the difference of counter-rotation direction. On the other hand, when the turbine is placed in a sheared flow, a strong torque asymmetry appears between the two rotor levels as three of the peaks are about 30 % lower than the three others, both in FC and EC. In addition, a significant additional phase shift $\Phi_Q = 9^\circ$ appears between the torque peaks of the top and the bottom rotors for the two configurations.

The Fourier Transform of the torque (\mathcal{Q}) presented in Fig. 4.8 reveals the effect of the flow shear on the frequency content of the green column torque in FC. The results show that the component at 6 times the rotational frequency (f_ω), representing the 6 blades that compose the column, is dominant both in the uniform and the sheared flows. However, the amplitude ratio between the peaks at $3f_\omega$ and $6f_\omega$ is more than doubled in the sheared flow compared to the uniform flow, which is congruent with the phase shift and amplitude asymmetry observed in the torque angular distributions. This result is observed in EC as well as in FC although not plotted here.

Beyond the turbine performance, Fig. 4.9 displays the average streamwise velocity

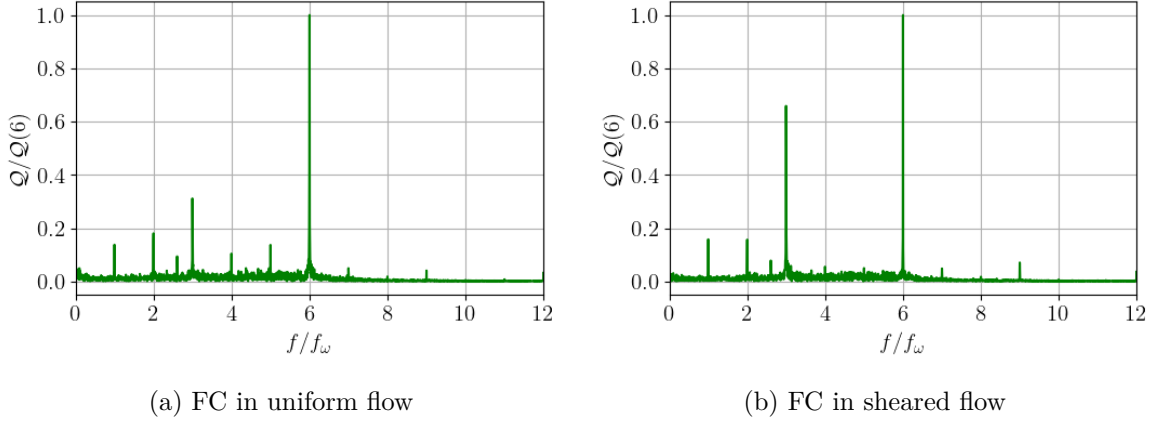


Figure 4.8 – Fourier transform of the green column torque in FC at the optimal operating point. The frequencies are normalised by the rotational frequency (f_ω) and the amplitudes by the $6f_\omega$ peak amplitude.

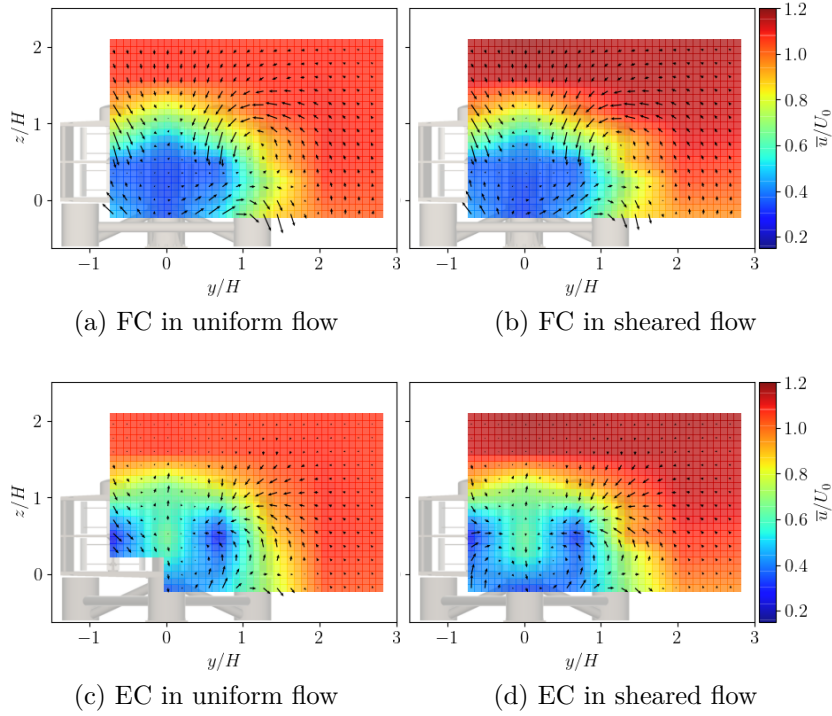


Figure 4.9 – Maps of the mean streamwise velocity (\bar{u}/U_0) in (y, z) planes at $x/H = 3$, viewed from downstream, with superimposition of an arrow field representing the mean transverse velocities $(\bar{v}, \bar{w})/U_0$.

in the wake of the ducted 2-VATT facing the uniform flow in FC and EC (a & c) and facing the sheared flow (b & d). In the four cases, the turbine operates at $\lambda = 1.6$ and the measurements are at $x/H = 3$. Apart from the incident shear that is also identified downstream of the turbine, the wake geometry seems unchanged. Indeed, as it is described in Moreau et al. (2023c), at this downstream position, the wake of the two columns are merged in FC but not in EC, regardless of the incident velocity profile.

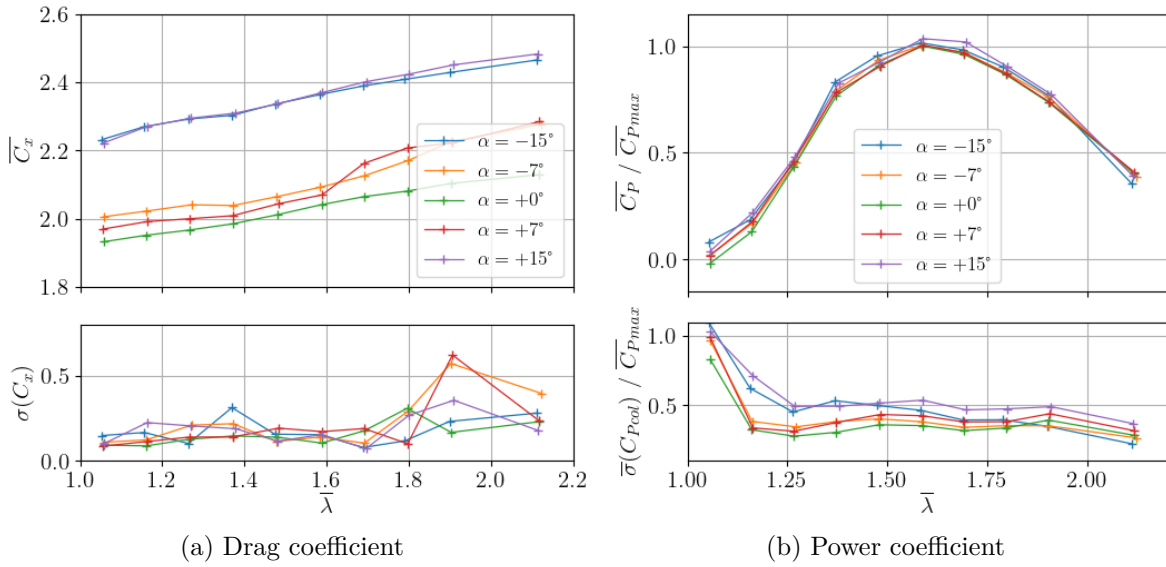


Figure 4.10 – Average and standard deviation of the drag and power coefficients in FC with the sheared velocity profile and various misalignment angles. The power coefficients are normalised by the maximal $\overline{C_P}$ at $\alpha = 0^\circ$.

The dynamics in (v, w) is also barely affected by the shear with large swirls around the x axis in FC that are less present in EC.

4.1.3.2 Misaligned sheared flow effect

To go further in the reproduction of realistic tidal current conditions in the tank experiments, we add flow misalignment to the sheared velocity profile. Fig. 4.10 displays average and standard deviation of the drag and power coefficients of the ducted 2-VATT in the flood tide configuration with five flow angles of incidence (α) between -15° and $+15^\circ$. On one hand, it appears that $\overline{C_D}$ increases with α up to 15 % when $\alpha = \pm 15^\circ$ compared to the case at $\alpha = 0^\circ$. That evolution is symmetrical in the positive and negative angles of incidence but it is not linear with the angle. We observe no effect on the drag fluctuation though. On the other hand, the flow misalignment with the turbine heading hardly affects the power coefficient both in terms of average and fluctuation. The same observations can be made on the performance at the whole turbine scale when studying the turbine in EC as well as on the monopile base (not plotted).

However, when we look at the rotor column scale, the misalignment affects significantly the power extraction. Fig. 4.11 displays the power coefficient of the green rotor column with regard to the tip speed ratio in FC and EC. At first glance, we observe that the maximal average power coefficient increases when α increases in the negative side and that it slightly decreases with a widening of the curve when α increases in the positive side. When $\alpha < 0$, that green rotor column is downstream of the red column in EC while it is upstream in FC, and vice versa (Fig. 4.4). Thus, the tendency with regard to the angle is reversed between FC and EC: $\overline{C_{Pcol}}$ increases when the rotor column goes upstream in FC whereas that increase occurs when the column is downstream in EC. Note that those tendencies are the same with the 2-VATT fixed on the monopile base so they are not due to the base asymmetry. Furthermore, we notice that the flow mis-

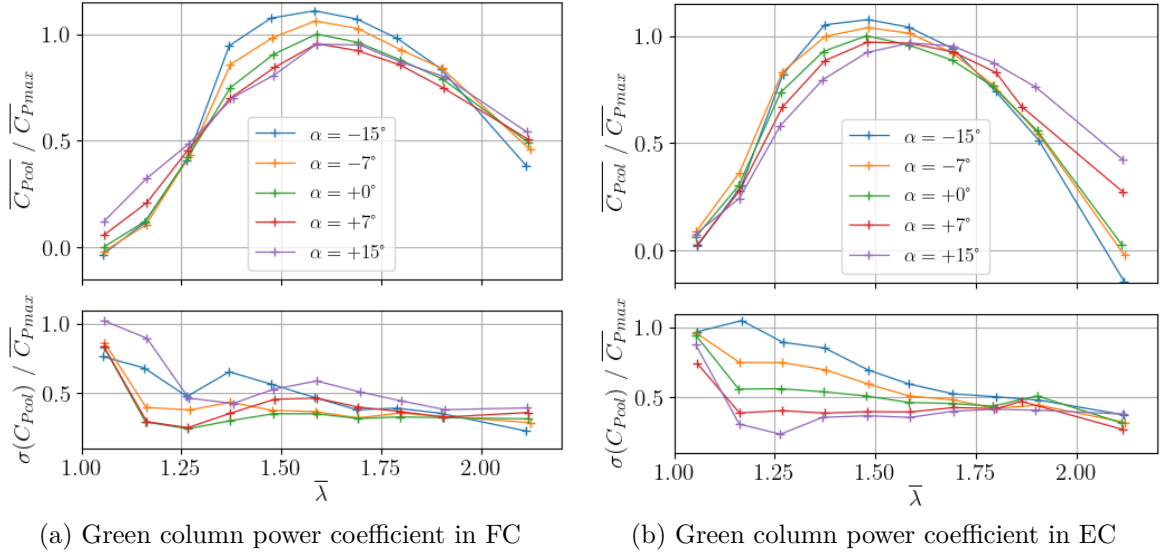


Figure 4.11 – Average and standard deviation of the green rotor column power coefficients in FC and EC with the sheared velocity profile and various misalignment angles, normalised by the maximal $\overline{C_{Pcol}}$ at $\alpha = 0^\circ$ in each plot.

alignment induces an increase of the standard deviation of the column power coefficient in EC from $\alpha = -15$ to $+15^\circ$, mainly at low λ , whereas no trend appears in FC.

The torque angular distribution evolution with the angle of incidence shows that the evolution of C_{Pcol} relies on different physical phenomena between FC and EC (Fig. 4.12). In EC, the torque distribution is rather unchanged by α . Only the overall torque magnitude increases when α decreases leading to the increase of $\overline{C_{Pcol}}$ when the column goes downstream. In FC, the torque angular distribution is modified by the angle of incidence as it affects the asymmetry between the upper and the lower rotors. When α goes negative, the phase difference between the upper and the lower rotors remains but the contribution of the two levels of rotors balances and increases the C_{Pcol} . Whereas, when α goes positive, the difference of torque amplitude due to the shear is unaffected but the phase difference between the two levels of rotors goes back closer to the geometrical phase. Those tendencies in FC intensify when α increases up to $\pm 15^\circ$ and they are similar on the monopile base. Finally, despite those differences between FC and EC, the maximal $\overline{C_Q}$ appears when the column is downstream of the other rotor column in the two configurations (at $+15^\circ$ in FC and -15° in EC).

Similarly, the relative contribution of the $3f_\omega$ and $6f_\omega$ harmonics in the torque Fourier transform evolves differently with α in EC and FC (Fig. 4.13). In FC, the peaks amplitude ratio decrease compared to the aligned configuration whether with positive or negative misalignments. Whereas in EC, the contribution of $3f_\omega$ tends to decrease with positive misalignment angles and increase with negative α .

4.1.4 Discussion

The section 4.1.3.1 revealed that the whole turbine drag and average power performance are unaffected by the incident current shear. However, we saw that the power standard deviation increases by 35 % at the optimal operating point which goes along

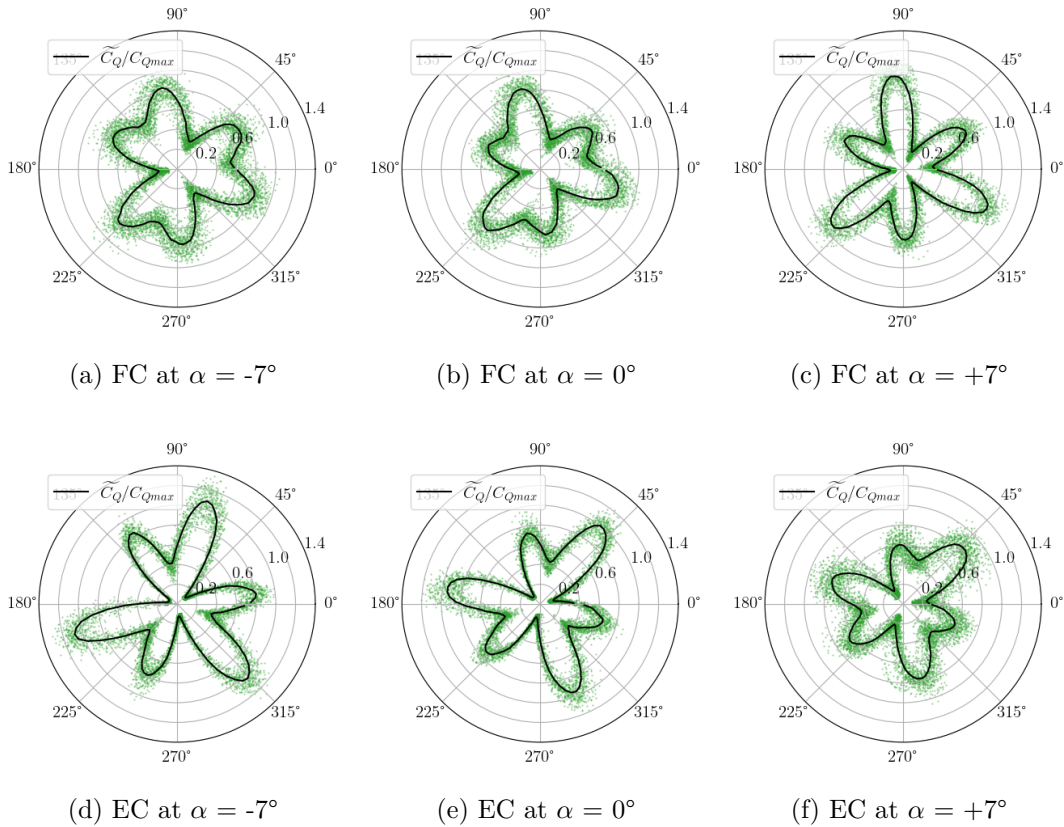


Figure 4.12 – Angular distribution of the torque coefficient for the green rotor column for the two flow orientations at the optimal λ (1.6 in FC and 1.5 in EC) with the sheared velocity profile and various misalignment angles. Torques are normalised by the maximal phase average in EC at $\alpha = 0^\circ$. The green dots are the instantaneous measurements and the black line is the phase average. *Reminder*: the angular position is relative, so the absolute angle values cannot be compared between graphs.

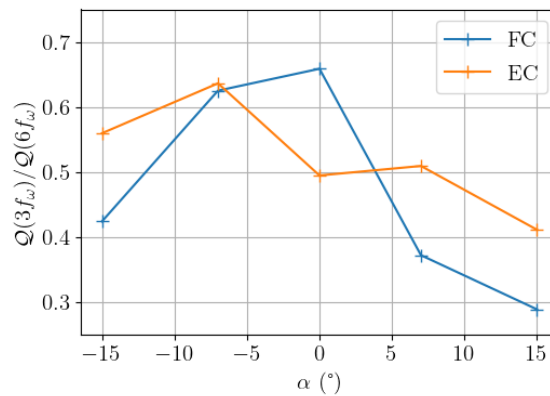


Figure 4.13 – Amplitude ratio between the torque Fourier transform peaks of the the green column at 3 and 6 times the rotational frequency with regard to the flow misalignment angle in EC and FC at the optimal operating point.

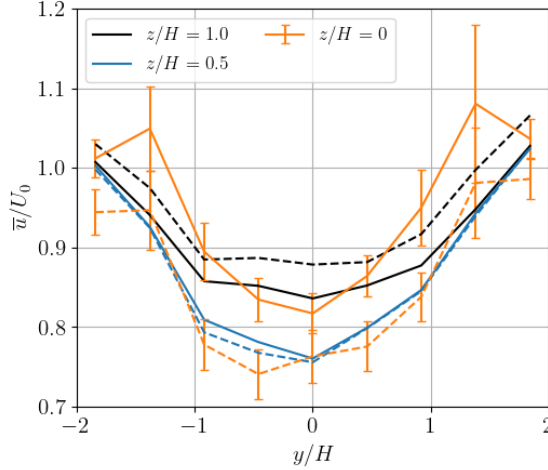


Figure 4.14 – Streamwise velocity horizontal profiles measured by LDV upstream of the turbine at $x/H = -1$ in EC, with the turbine on the tripod base facing a uniform velocity profile (solid lines) and facing a sheared profile (dashed lines). The error bars represent the normalized standard deviation of the streamwise velocity.

with the modification of the torque angular distribution. Indeed, when the incident current is sheared, the torque peaks of one of the rotors (either the upper or the lower one of the column) are about 30 % higher than those of the other rotor and an additional phase shift of 9° compared to the geometrical phase between the blades appears between the two rotor levels. In the spectral analysis of the torque, the shear effect manifests through a 2 times higher contribution of the peak at $3f_\omega$ relatively to that of the peak at $6f_\omega$ with the sheared flow compared to the uniform flow. Fig. 4.14 and 4.15 present profiles of the streamwise velocity at $x/H = -1$ in front of the turbine in EC with both the uniform and the sheared flow. In EC, the base feet are in front of the outer part of the bottom rotors and their bypassing affects the velocity perceived by the turbine (Moreau et al., 2023c). With the uniform flow, the base bypassing generates an important velocity increase in front of the bottom rotors, so we assume that the bottom rotors recover more torque from the flow than the upper ones. Conversely, with the sheared flow, the base bypassing also generates a velocity increase in front of the bottom rotors but this only reduces the initial shear. As a consequence, the bottom rotors still perceive a lower velocity than the top rotors. In FC, the single central base foot by-passing does not interact significantly with the flow in front of the rotors (not presented here). So we assume that, with a sheared incident current profile, the greatest torque peaks observed in Fig. 4.7 are generated by the upper rotor due to the higher flow velocity squared, both in FC and EC. In addition, since the upper and lower rotors are fixed together and kept at a constant rotational speed, the velocity asymmetry in the sheared current induces a difference of λ between the two rotor levels. For vertical axis turbines, the absolute angular position of maximal C_Q varies with λ (Jaquier, 2011). Consequently, the phase between the upper and lower rotors torque peaks differs from the geometrical phase between the blades, as observed in the experiments.

Section 4.1.3.2 revealed that the global power coefficient evolution with regard to the tip speed ratio of the ducted 2-VATT is unchanged when the flow is misaligned with the turbine heading up to $\pm 15^\circ$ in the sheared current. We also showed that the average

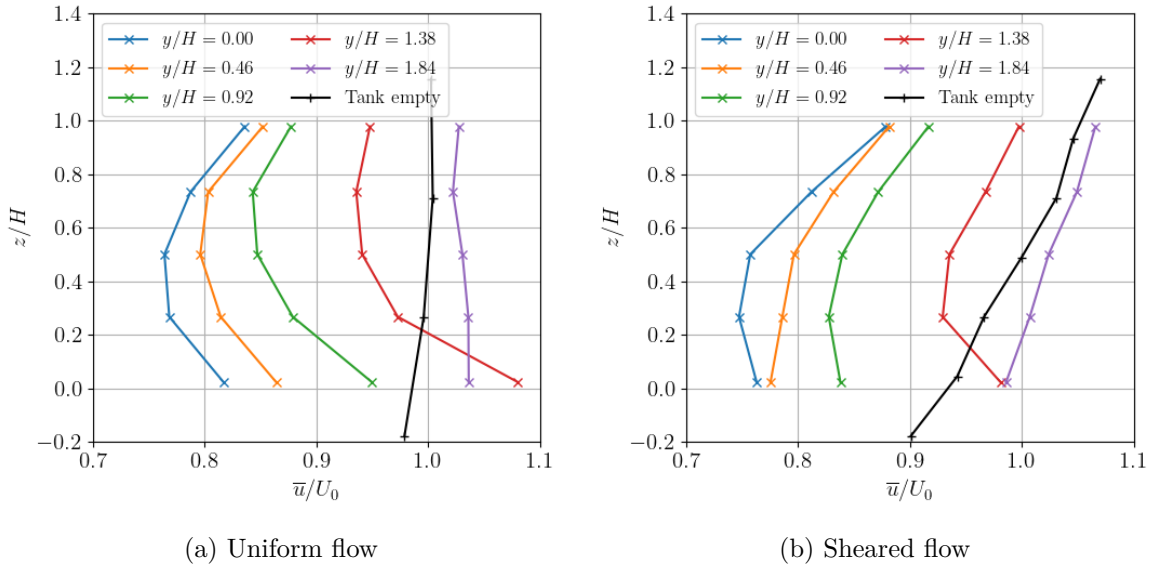


Figure 4.15 – Streamwise velocity vertical profiles measured by LDV upstream of the turbine at $x/H = -1$ in EC.

drag coefficient of the turbine increases with the angle of incidence up to +15 % at $\pm 15^\circ$. The increase is only of a few percent when $\alpha = \pm 7^\circ$ which indicates that the effect of the misalignment on the drag coefficient is not linear. Some flow detachments from the vertical fairings might occur between 7° and 15° , even though the drag standard deviation is unchanged, that could explain the significant difference between α equals 7° and 15° compared to that between 0° and 7° . In addition, when looking solely at the green rotor column (Fig. 4.4), in FC, the maximal average power coefficient increases when the column moves upstream and the C_P curves with regard to λ widens when the column moves downstream with a slight decrease of the maximal $\overline{C_P}$. It appeared that the effect of the misalignment on that single column is similar but reversed in the ebb tide configuration, with the increase of maximal average power coefficient when the column moves downstream instead of upstream in FC. That reversed tendency is the same with the 2-VATT fixed on the monopile base so it is rather due to the difference of counter-rotation direction between FC and EC than to the base geometry. Indeed, the blades go against the current along the central fairing in FC whereas that occurs along the lateral fairings in EC. When the flow is misaligned with the turbine heading, we suppose that the local velocity increases on the downstream side of the vertical fairings, similarly to aerofoil extrados. If we still focus on the green rotor column, at -15° for instance, the flow would be accelerated where the blades move in the current direction in the two cases given the rotation direction. Thus, the apparent velocity on the blade would be lowered, which would lower the torque trough and so increase the power coefficient when the column is upstream in FC and downstream in EC.

Furthermore, we observed an increase of $\sigma(C_{P_{col}})$ in EC from $\alpha = +15$ to -15° , mainly at λ lower than the optimal for the green rotor column but on the whole λ range on the red side, which is also present but less clear on the monopile base, and absent in FC anyway. This result is hardly explained to this date. Similarly, the torque frequency content and its angular distribution evolution with the angle of incidence show that the physical phenomena affecting the ducted 2-VATT behaviour are different between FC

and EC. The torque distribution is hardly modified in EC when α increases from -7 to $+7^\circ$ and only the torque magnitude decreases whereas the torque distribution is significantly affected by the flow misalignment in FC. However, the rotor angular position being only relative, we lack the geometrical location of the torque peaks occurrence to explain these phenomena.

4.1.5 Conclusion

Most of the time, tidal turbines tank tests are carried out in idealised current conditions characterised by a uniform velocity over the turbine capture area and a velocity direction collinear with the turbine heading. However, the real tidal currents at sea present vertically sheared velocity profiles and variable directions in space and time. The present study aims at assessing the effect of both the flow shear and its misalignment on the behaviour of a bottom mounted and ducted twin vertical axis tidal turbine (2-VATT). To this end, a 1/20 scale model is tested in Ifremer’s wave and current flume tank facing a uniform velocity profile and a sheared one, in ebb and flood tide configurations, with a flow misalignment ranging from -15 to $+15$ degrees.

The results show that the drag and the average power coefficients of the ducted 2-VATT are unaffected by the upstream flow shear. Only the torque angular distributions are modified and so the power coefficient standard deviation is 35 % higher at the optimal operating point in a sheared current compared to a uniform one. The flow misalignment with regard to the turbine heading increases the average drag coefficient by 15 % for a flow incidence of $\pm 15^\circ$. The power performance of the whole 2-VATT is barely affected by the misalignment as the power lost by one rotor column is roughly compensated by a gain on the other column. However, the misalignment affects the torque angular distribution of a rotor column and does so differently whether the turbine is in the flood or the ebb tide configuration. To explain the physics of these torque distribution changes, we would need better instrumentation such as absolute angular position encoder or separate torque measurements between the upper and the lower rotors. Local flow measurements by particle image velocimetry or numerical simulations would also be of great help to understand the underlying physics. Be that as it may, the increase of torque fluctuation induced by the flow shear and the misalignment must be considered at the design stage of tidal turbines.

4.2 Turbine behaviour in the turbulent wake of a bathymetry obstacle

4.2.1 Introduction

The previous part focused on the effect of the vertical velocity shear and the relative flow misalignment on the turbine behaviour, as it is encountered at sea, but the inflow conditions were still steady while they are fully unsteady offshore. To analyse the effect of the flow unsteadiness on the ducted 2-VATT response, we start by testing the reduced-scale model in the turbulent wake of large bathymetry obstacles. This part is extracted from Moreau et al. (2023a), “Experimental study of the upstream bathymetry effects

on a ducted twin vertical axis tidal turbine”, under review in *Renewable Energy*.

Flow measurements in tidal straits showed that the rough bathymetry is responsible for a high spatial and temporal variability of the flow characteristics (Mercier et al., 2022). Besides, large bathymetric singularities generate highly energetic coherent flow structures with a rising trajectory from the seabed to the free surface (Mercier et al., 2021a; Lucas et al., 2022). Specific studies have been carried out in Ifremer’s wave and current flume tank to reproduce such flow configurations at a 1/20 scale and to better understand the flow physics induced by bathymetry obstacles (Ikhennicheu et al., 2019a; Magnier et al., 2021). The response of horizontal axis turbines in those specific configurations have been analysed (Gaurier et al., 2020c; Druault et al., 2022) but no vertical axis turbine have ever been studied downstream of large bathymetric singularities. Therefore, we initially tested the ducted 2-VATT reduced-scale model in the wake of two bathymetry obstacle configurations amongst those of Ikhennicheu et al. (2019a), with two turbine-to-obstacle distances for each obstacle. This work was presented in Bloch et al. (2022) and is provided in appendix A. We found that the ducted 2-VATT power and load fluctuations are strongly increased compared to a flat bathymetry configuration, with a variable intensity depending on the obstacle shape and on the relative distance to the turbine. However, that study focuses on the 2-VATT response alone and lacks the analysis of the flow measurements to further explain and discuss the observed results. So, the aim of the present part is to compare experimentally the behaviour of the ducted 2-VATT between a flat bed configuration and the most impacting bathymetry obstacle configuration found in Bloch et al. (2022) to deeper investigate the effects of that particular flow on the turbine power generation and on the loads. To do so, section 4.2.2 first describes the turbine model as well as the flat bed and the uneven bathymetry setups before describing the flow characteristics in these two configurations and the data processing carried out. Then, section 4.2.3 presents the effects of the bathymetry obstacle wake on the 2-VATT power performance and on its loads. Finally, the study shines a light on the interaction between the flow fluctuation induced by the coherent structures shed in the bathymetry obstacle wake and the 2-VATT response.

4.2.2 Material and method

First, this section aims at describing the ducted twin vertical axis tidal turbine model, the instrumentation used and their setup in the tank. Then, we describe the upstream flow characteristics either with the flat floor or with the bottom mounted bathymetry obstacle before describing the data processing carried out for this study.

4.2.2.1 Turbine model

The ducted 2-VATT 1/20 scale model is geometrically similar to the 1 MW-rated demonstrator tested by HydroQuest at Paimpol-Bréhat test site from 2019 to 2021 (Moreau et al., 2022b). It is composed of two independent counter-rotating vertical axis rotor columns. Each column is made of two levels of H-Darrieus type rotors with a 60° phase difference between the levels. Besides, each rotor of radius $R = D/2 = 200$ mm is made of $N = 3$ blades that are $H_{blade} = 190$ mm high with a chord c of 73 mm. Thus, the rotor solidity (Nc/R) is 1.1. The rotors are mounted in a $W = 1.24$ m wide structure made of fairings and plates. The turbine height is defined as the



Figure 4.16 – 2C- and 3C-LDV measurement between the bathymetry obstacle and the ducted 2-VATT model in the Ifremer's tank.

distance between the top and the bottom horizontal plates such that $H = 450$ mm; and the 2-VATT capture area is $H \times W$. For this study, the turbine is fixed on a tripod bottom-mounted base similar to the demonstrator's one. The two rotor columns are controlled at a constant rotational speed by two independent *Maxon RE50* DC motors and *Escon 70/10* servo-controllers. The torque Q of each rotor column is measured using *Scaimé DR2112-W* torque-meters and the rotational speeds ω are measured by the motor encoders. The 6 load components applied between the turbine and the base and those between the base and the tank floor are measured using *SIXAXES* 1.5 kN and 20 kN load cells, respectively (Fig. 4.17). All of these analog signals are acquired at a sampling frequency of 128 Hz using *National Instruments PXI* and *LabView* systems. The model and its instrumentation are fully described in Moreau et al. (2023c).

Whether the flow comes from one side or the other of the device, the base geometry upstream and the relative counter-rotation direction of the two column reverses. The two flow directions are referred to either as FC, corresponding to the Flood tide Configuration at Paimpol-Bréhat test site, or as EC for the Ebb tide Configuration (Fig. 1.2).

4.2.2.2 Experimental setup

The 2-VATT model is tested in the Ifremer's 2 m deep and 4 m wide wave and current flume tank in Boulogne-sur-mer, France (Fig. 4.16). It is operated in its low turbulence configuration with the inlet conditioned by a honeycomb structure and a uniform grid. The flood and ebb tide relative flow directions are modelled by turning the 2-VATT around as the flume tank allows a single flow direction. We used two experimental setups to assess the effect of the bathymetry obstacle wake on the behaviour of the 2-VATT compared to the case without obstacle. The 2-VATT is placed at the centre of the tank $(x, y, z) = (0, 0, 0)$ with x in the main flow direction, y towards the wall and z towards the free surface with $z = 0$ at the tank bottom. The first configuration models a flat bathymetry and is referred to as G0 (Fig. 4.17 (a)). In that case, a *Dantec* 2-Component Laser Doppler Velocimeter (2C-LDV) measures the velocities (u, v) along (x, y) at $x = -6H$ at the centre of the turbine capture area, ie. $(y, z) = (0, 0.505)$ m. At this far upstream distance, the flow is not disturbed by the 2-VATT (Moreau et al., 2023c). The time average of u at this location is considered as the reference

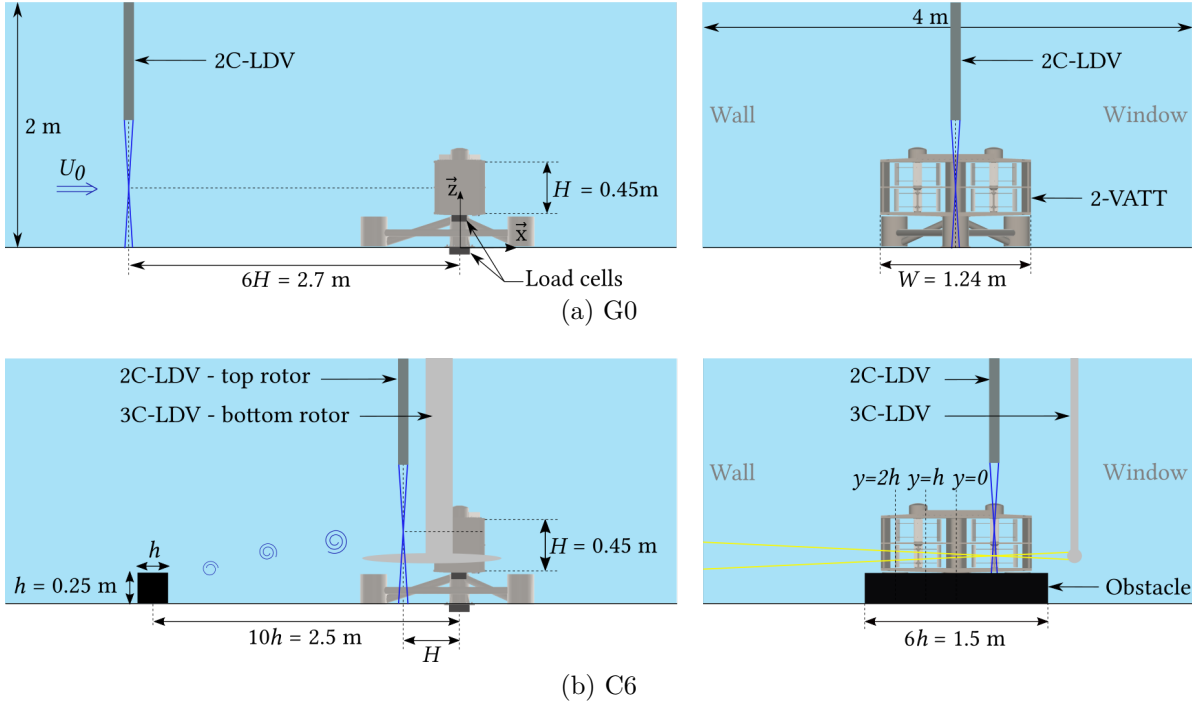


Figure 4.17 – Schematic side view (left) and front view (right) of the experimental setups in the G0 (top) and C6 (bottom) configurations.

far upstream velocity and is noted U_0 . The 2C-LDV and the turbine related signals are acquired simultaneously during 3 minutes to guarantee the time convergence of the average and the standard deviation of the signals.

The second setup models a strong bathymetry variation upstream of the turbine and is referred to as C6 (Fig. 4.17 (b)). The wide square base cylinder of size $6h \times h \times h$ studied by Ikhennicheu et al. (2019b) is placed 10 obstacle heights upstream of the 2-VATT ($x = -10h$). We placed two LDV devices at $x = -H$ to measure the flow velocity right in front of the 2-VATT. The 2C-LDV measures (u_{2C}, v_{2C}) at the centre of the top rotor at $(y, z) = (0.31, 0.61)$ m and a *Dantec* 3C-LDV measures (u_{3C}, v_{3C}, w_{3C}) in front of the bottom rotor at $(y, z) = (0.31, 0.41)$ m. The LDV measurements are in front of the red column in FC and in front on the green column in EC (Fig. 1.2). The two LDV probes and the turbine related signals are acquired simultaneously during 5 minutes to guarantee the time convergence of the average and the standard deviation of the signals.

In the two setups, the tank operates at the same velocity setpoint of $1 \text{ m}\cdot\text{s}^{-1}$ which, gives a blade chord based Reynolds number ($Re_c = \frac{e\lambda U_0}{\nu}$, with ν the water kinematic viscosity and λ the tip speed ratio - Eq. 4.8) of the order of 10^5 ; the two rotor columns are controlled separately with the same constant rotational speed setpoint; and the LDV devices operate in non-coincident mode, meaning that the different velocity components are measured independently by each pair of lasers. The data rate for each velocity component is of the order of 200 Hz.

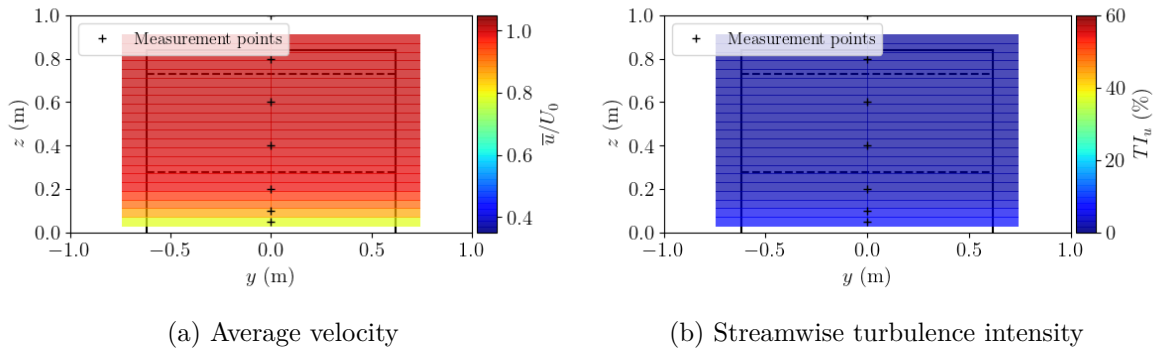


Figure 4.18 – Streamwise average velocity (a) and turbulence intensity (b) profiles measured with the 3C-LDV at the centre of the empty tank and extruded along the y axis. The black lines represent the overall boundaries of the 2-VATT (absent during those measurements) and the dashed lines its capture area. The colour scales are the same as in Fig. 4.20 for the comparison.

4.2.2.3 Flow characteristics

To compare the 2-VATT behaviour in one or the other flow configurations, it is necessary to characterise the flow beforehand, similarly to a resource assessment within the framework of a full-scale turbine installation at sea. The flow characteristics in the empty tank, corresponding to the G0 configuration have already been characterised extensively. Gaurier (2020) shows that the flow characteristics are uniform over the tank width, so the velocity profiles measured with the 3C-LDV at the tank centre by Moreau et al. (2023c) can be extruded along y (Fig. 4.18). Above the 0.3 m high boundary layer, the streamwise average velocity profile is uniform over the 2-VATT height and the streamwise turbulence intensity is about 1.5 %. The later is defined as $TI_u = \sigma(u)/\bar{u}$ with σ indicating the standard deviation and the bar indicating the time average. The transverse velocity components (v, w) are negligible.

Regarding the C6 configuration, Ikhennicheu et al. (2019b) characterised the turbulent wake of the wide bathymetry obstacle extensively using PIV measurements in the Ifremer wave and current flume tank. Fig. 4.19 displays the average streamwise and vertical velocity contours in the wake of the obstacle alone in (x, z) planes at the three lateral positions $y = 0, h$ and $2h$ illustrated on the scheme in Fig. 4.17 (b). The wake evolution appears to be fully three-dimensional with a recirculation zone extending down to $x = 6h$ at $y = 0$ and to $x = 4.5h$ at $y = 2h$, followed by a strong velocity gradient downstream. Besides, the turbulence characteristics of that specific flow were analysed both experimentally and numerically (Ikhennicheu et al., 2019b; Mercier et al., 2020). Thus, the turbine placed $10h$ downstream of the obstacle is out of the recirculation zone, in the sheared layer and on the coherent turbulent structures path. For the present study, we also mapped the flow similarly to a resource assessment at sea (without turbine) using the 3C-LDV in a (y, z) plane $8.2h$ downstream of the obstacle, i.e. at $x = -H$ which is the same position as the LDV measurements in front of the turbine in operation (Fig. 4.17). Fig. 4.20 (a) presents the average velocity field in the (y, z) plane with \bar{u}/U_0 in colour and (\bar{v}, \bar{w}) as an arrow field; and Fig. 4.20 (b) presents the streamwise turbulence intensity with the location of the 3C-LDV measurement points. The measurements along the profile at $y = +0.31$ m are the same as at $y = -0.31$ m so

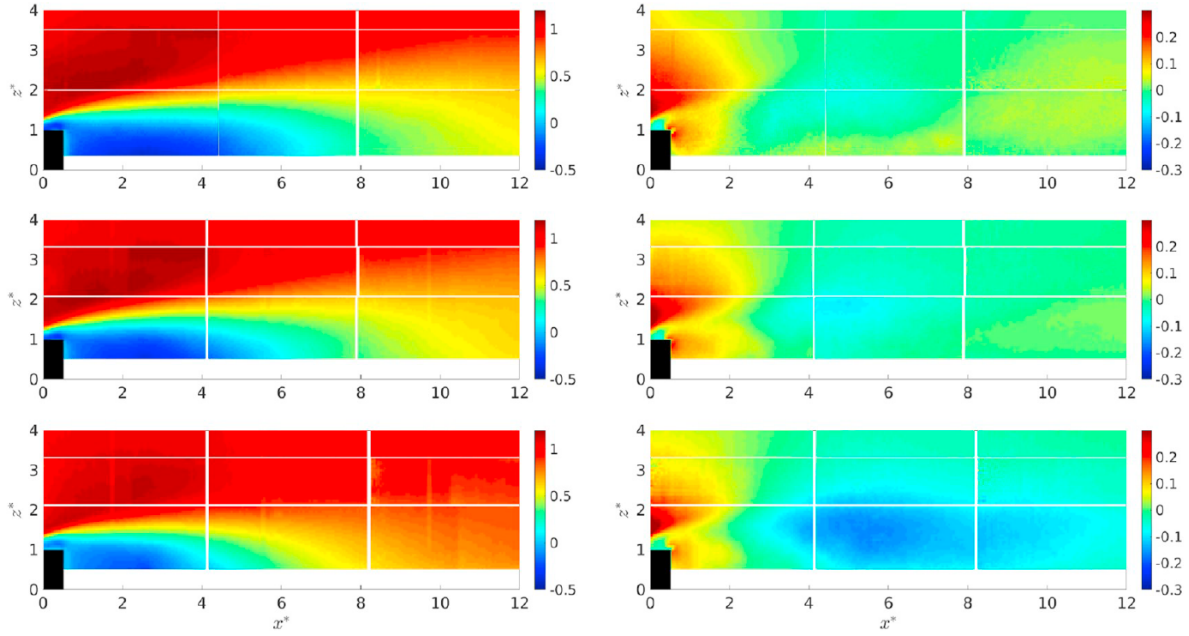


Figure 4.19 – Average streamwise velocity (left) and vertical velocity fields (right) from PIV measurements in the wake of the square cylinder (black), both normalised by the far upstream average streamwise velocity, from Ikhennicheu et al. (2019b). $x^* = x/h$ is the streamwise direction, $z^* = z/h$ is the vertical one and y is the transverse one. The top figures are at $y = 0$, the tank and the obstacle centre, the middle figures are at $y = h$ and the bottom ones at $y = 2h$.

we display the y -positive side as a symmetry of the negative side. The maps are obtained by linear interpolation between the measurement points with a 40 mm step in the y and z directions. The wide bathymetry obstacle is represented by the grey filled rectangle and the 2-VATT overall boundaries are represented by the black lines to illustrate the relative flow scale, even though the turbine was absent during this flow characterisation. The average velocity map reveals a strong flow shear with a maximum of 45 % difference between the top of the turbine capture height ($z = 0.73$ m) and its bottom ($z = 0.28$ m) at the centre of the tank and an average difference over the turbine width of 34 %. In addition, the transverse velocities appear to be significant as \bar{v} ranges in $\pm 0.13 U_0$ and \bar{w} , mostly towards the tank bottom, ranges in $[-0.10; 0.07]U_0$. The average kinetic energy loss due to the velocity deficit in the cylinder wake is compensated by an increase of the turbulent kinetic energy. Thus, the turbulence intensity is also at its maximum at the centre of the obstacle wake with 54 % at the bottom of the turbine capture height and 20 % at the top. The average TI_u over the 2-VATT capture area is about 27 %.

The difference of turbulence levels between the configurations G0 and C6 is clearly depicted by the probability density functions of the streamwise velocity measured at $(x, y, z) = (0, 0, 0.6)$ m without turbine in the two configurations (Fig. 4.21). Indeed, at that location, the first and the last percentile of the normalised velocity are 0.98 and 1.06 in the flat bed configuration whereas they are 0.09 to 1.19 in the cylinder wake. Furthermore, the flow measurements in the flat bed configuration and in the wake of the bathymetric obstacle are presented in the spectral domain in Fig. 4.22. Power spectral densities of the fluctuating part of u , $\mathcal{S}(u'/U_0)$, are computed using Welch's method with 64 s long windows and 50 % overlap. Several observations can be made.

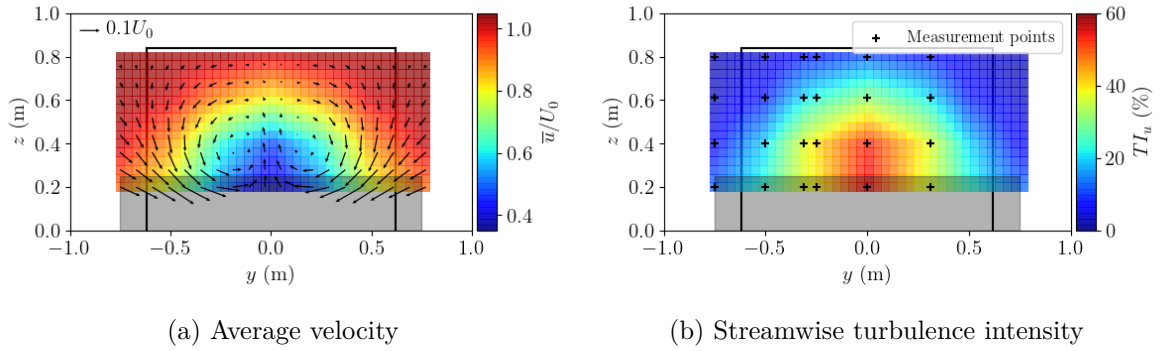


Figure 4.20 – Downstream view of the 3C-LDV measurements in the wake of the obstacle without turbine at $x = -H$. (Left) Average streamwise velocity map with transverse velocities (v, w) arrow field. (Right) Streamwise turbulence intensity and position of the measurement points. The y -positive side is obtained by symmetry. The grey filled rectangle represents the obstacle and the black lines represent the overall boundaries of the 2-VATT (absent during the measurements).

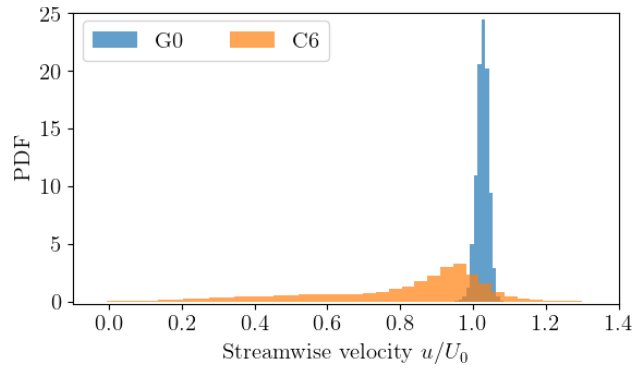


Figure 4.21 – Probability density function (PDF) of the streamwise velocity measured by the 3C-LDV at $(x, y, z) = (0, 0, 0.6)$ m without turbine in the empty tank (G0) and in the wake of the bottom-mounted cylinder (C6).

Firstly, the level of energy at the centre of the tank in the cylinder wake is about 100 times higher than without obstacle on the whole frequency range. That level of energy is constant between $y/h = \pm 1$ and decreases away from the tank centre. Secondly, the spectra behind the obstacle present a peak around $f_u = 0.25$ Hz, indicated by the vertical dashed line, which was found to be the shedding frequency of large coherent flow structures (Ikhennicheu et al., 2019b). That peak is the strongest at the tank centre ($y = 0$) at the two altitudes. However, it is almost absent at $y/h = 1$ and 2 at $z = 610$ mm whereas the peak remains marked at all the lateral positions at $z = 410$ mm. This result suggests that the bottom rotors of the 2-VATT will face wider coherent structures than the top ones. The energy peak at f_u appears again at $y/h = 3$, downstream of the lateral edge of the obstacle, only with 30 to 50 times less energy than at $y/H = 0$.

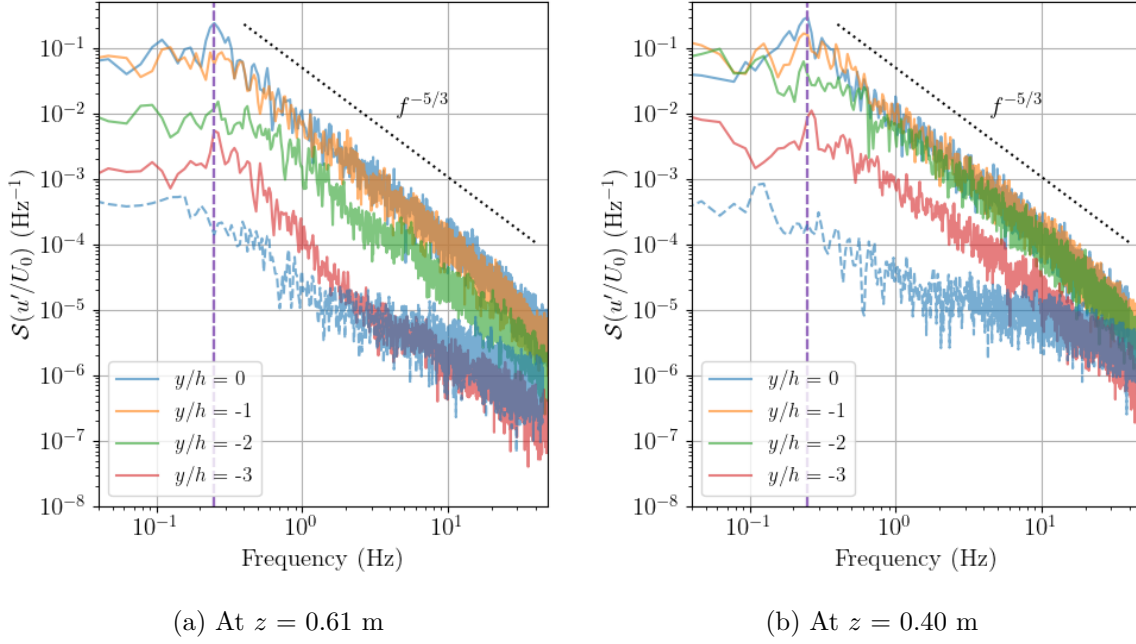


Figure 4.22 – Power spectral density of the fluctuating streamwise velocity measured by 3C-LDV. Solid lines are measurements behind the obstacle, without turbine, at $x = -H$ at the centre height of the top rotor (a) and of the bottom rotor (b). The blue dashed lines correspond to measurements in G0 without turbine at $y = 0$ and $z = 0.60$ m (a) and 0.40 m (b). The vertical dashed line indicates the vortices shedding frequency $f_u = 0.25$ Hz in the wake of the obstacle (Ikhennicheu et al., 2019b).

4.2.2.4 Data processing

To compute the hydrodynamic coefficients, we consider two reference velocities: U_0 , the time averaged far upstream velocity at the mid-height of the turbine, as defined in the section 4.2.2.2, and U_S , the time and space averaged velocity at the turbine position without turbine, averaged over the capture area. Defined that way, U_0 is equivalent to the velocity measured upstream while operating a turbine at sea whereas U_S represents the velocity measured during a resource assessment prior turbine installation. The far upstream velocity U_0 is considered the same for the configurations G0 and C6 as the tank operates at the same velocity setpoint. In G0, the flow being homogeneous on the tank width (Gaurier, 2020), U_S is obtained by extruding the velocity profile on the turbine width (Fig. 4.18). This method is similar to the one used with acoustic Doppler current profilers at sea for the certification of full scale tidal turbine performance according to the Technical Standard 62600-200 (IEC, 2013). As required in that standard, the velocity signals are powered before temporal and spatial averaging for the computation of hydrodynamic coefficients. That averaging method, called power weighted average, is expressed in Eq. 4.6 with U_{ref} being either U_0 or U_S and n representing the number of samples in the temporal or the spatial spaces.

$$U_{ref}^p = \frac{1}{n} \sum_n u^p \quad (4.6)$$

Table 4.2 – Power weighted average reference velocities considered for the computation of the hydrodynamic coefficients in the two flow configurations.

	G0	C6
U_0 (m.s ⁻¹)	0.944	
U_S (m.s ⁻¹)	0.963	0.821
U_0^2 (m ² .s ⁻²)	0.891	
U_S^2 (m ² .s ⁻²)	0.928	0.709
U_0^3 (m ³ .s ⁻³)	0.841	
U_S^3 (m ³ .s ⁻³)	0.895	0.631

The values of U_0 and U_S at the powers 1 to 3 are displayed in Tab. 4.2. We notice that, for the measurements in the undisturbed flow (U_S in G0 and U_0), the power weighted averages are equal to the arithmetic averages powered. However, in turbulent flows like in the wake of the bathymetry obstacle, the power weighted average gives higher values than the arithmetic average powered due to the flow fluctuation around the mean value. In addition, we observe that the velocity averaged over the 2-VATT capture area U_S is 15 % lower in C6, in the wake of the bathymetry obstacle, than in G0, with a flat bathymetry.

Considering either one or the other above mentioned reference velocities, the power coefficient of each rotor column C_{Pcol} is computed as in Eq. 4.7 with $P_{col}(t) = Q(t)\omega(t)$ and t the time. The reference surface is that of the rotors projected area and the torque signal considered is corrected by the friction torque induced by the seals and the transmission system for each rotor column (Moreau et al., 2023c). Then, the overall average power coefficient $\overline{C_P}$ is the average of the two $C_{Pcol}(t)$ and the power fluctuation are analysed considering the average standard deviation between the two rotor columns, noted $\overline{\sigma}(C_{Pcol})$.

$$C_{Pcol}(t) = \frac{P_{col}(t)}{\rho D H_{blade} U_{ref}^3} \quad (4.7)$$

In the same way, either with one reference velocity or the other, the tip speed ratio (λ) is defined in Eq. 4.8 and λ_{opt} refers to the operating point providing the maximal power coefficient. The force and moment coefficients are defined in Eq. 4.9 and 4.10 for the components along x with the four rotors projected area as a reference surface. They are defined the same way for the loads along y and z . The loads measured without current are subtracted to consider only the hydrodynamic loads on the device, without the gravity. Besides, in this study, we consider the forces applied by the turbine on the gravity base, measured by the upper load cell, and the moments measured at the bottom (Fig. 4.17). In addition to the load coefficients evolution with the tip speed ratio, we also analyse their probability density functions (PDF) with 50 equal-width bins to consider the loads repartition and look at their extrema.

$$\lambda(t) = \frac{\omega(t)R}{U_{ref}} \quad (4.8)$$

$$C_x(t) = \frac{F_x(t)}{2\rho D H_{blade} U_{ref}^2} \quad (4.9)$$

$$C_{Mx}(t) = \frac{M_x(t)}{2\rho R D H_{blade} U_{ref}^2} \quad (4.10)$$

To deeper analyse the hydrodynamics, we compute the normalised cross-correlation \mathcal{R} of some velocity components measured at $x = -H$ with some 2-VATT loads and with the torque of the rotor column facing the LDV probes (Eq. 4.11 where τ is the time lag). All the signals s are decomposed into $s = \bar{s} + s'$ with the bar indicating the average and the prime the fluctuating part of the signal. In this study, the cross-correlations are presented with three of the velocity components measured: u'_{2C} , u'_{3C} and w'_{3C} . Finally, the power spectral densities \mathcal{S} of Q' , F'_x and F'_z are computed using Welch's method with 64 s long windows and 50 % overlap to analyse the periodical characteristics of the 2-VATT related signals compared to the ones of the flow.

$$\mathcal{R}(U', F')[\tau] = \frac{\overline{(U(t) - \bar{U}) (F(t + \tau) - \bar{F})}}{\sqrt{\overline{(U(t) - \bar{U})^2} \overline{(F(t) - \bar{F})^2}}} \quad (4.11)$$

4.2.3 Bathymetry effects on the ducted 2-VATT behaviour

The effects of the bathymetry obstacle wake on the behaviour of the ducted 2-VATT are first analysed regarding the power performance of the turbine. We compare the effect between FC and EC as well as the effect of the reference velocity choice on the power coefficient. Then, we consider the effect of the bathymetry generated turbulence on the hydrodynamic load coefficients to discuss the risks of structural damage. Finally, the relations between the flow and the load fluctuations are assessed both in the temporal and the spectral domain.

4.2.3.1 Effects on the 2-VATT power performance

Fig. 4.23 (a) displays the average and the standard deviation of the power coefficient with regard to the tip speed ratio computed with U_0 in G0 and C6 with the 2-VATT either in the Flood Configuration or the Ebb Configuration. The results reveal that the average C_P curves drop, both in EC and FC, in C6 compared to G0 and that the differences between FC and EC in G0 remain in C6. Indeed, in C6 as in G0, the maximal $\overline{C_P}$ are rather equal given the measurement repeatability (Moreau et al., 2023c) and the optimal tip speed ratio is 0.1 lower in EC compared to FC. Besides, $\sigma(C_{Pcol})$ at λ_{opt} is more than doubled in C6 compared to G0 and the difference between FC and EC narrows in C6, showing that the obstacle wake affects more the fluctuating part of the turbine response than the relative counter-rotation direction of the two columns. In the following, we focus on the Flood tide Configuration to study the effect of the bathymetry obstacle wake on the behaviour of the 2-VATT.

Fig. 4.23 (b) presents the evolution of the power coefficient with regard to the tip speed ratio in FC in G0 and C6, depending on the reference velocity considered. On one hand, with U_S , the λ_{opt} are equal between G0 and C6 which means that the velocity field measured during a resource assessment at the turbine position (without it) is a

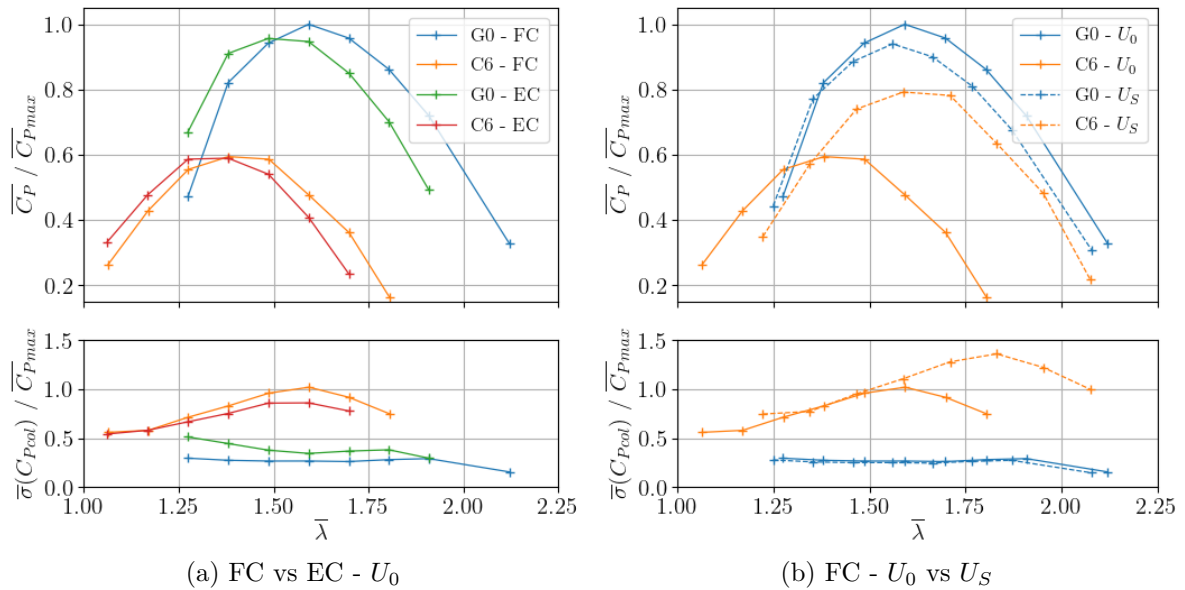


Figure 4.23 – Average and standard deviation of the power coefficient with regard to the tip speed ratio in G0 and C6. (a) $C_P(U_0)$ in the Flood and Ebb tide Configurations. (b) $C_P(U_0)$ and $C_P(U_S)$ in FC only. The values are normalized by the maximal $\overline{C_P}(U_0)$ in G0 - FC.

good estimation of the velocity really perceived by the 2-VATT in operation. However, the maximal $\overline{C_P}$ is 16 % lower in C6 than in G0 with U_S as a reference velocity. With the velocity arithmetic average powered instead of the cubic power weighted average U_S as a reference in C6, $\max(\overline{C_P} / \overline{C_{Pmax}})$ would be 0.91 instead of the 0.79 in Fig. 4.23 (b). Thus, the decrease of $\overline{C_P}$ computed with U_S between G0 and C6 is mainly due to the higher level of turbulence in the wake of the bathymetry obstacle that increases the reference velocity due to the cubic weighted average of the velocity in the power coefficient computation. Part of the performance difference between G0 and C6 could also be due to a Reynolds number effect as U_S , and so the Reynolds number, is 15 % lower in C6 than in G0, which affects the blades lift and drag performance (Michna et al., 2022).

On the other hand, with U_0 as the reference velocity, the maximal $\overline{C_P}$ drops by 40 % between G0 and C6 and the optimal tip speed ratio is shifted from 1.6 to 1.4. That result shows that for a constant far upstream velocity, the hydrodynamic power really perceived by the turbine can significantly differ depending on the bathymetry shape between the velocity measurement point and the turbine (Mercier et al., 2022). Thus, in the perspective of tidal turbines monitoring at sea, the choice of the reference velocity measurement location is crucial to properly control the devices and analyse their performance. The latter conclusion is true for all bottom mounted tidal turbines, whatever their geometry. It is also instructive to notice that the little 2 % difference between U_0 and U_S values in G0 is responsible for the 6 % difference of the maximal $\overline{C_P}$. That result is due to the power 3 on U_{ref} in the computation of the power coefficient and shows once again the sensitivity of $\overline{C_P}$ to the reference velocity assessment.

Furthermore, the bathymetry obstacle wake also affects strongly the power fluctuation. First, the evolution with regard to λ is modified as $\overline{\sigma}(C_{Pcol})$ presents a maximum

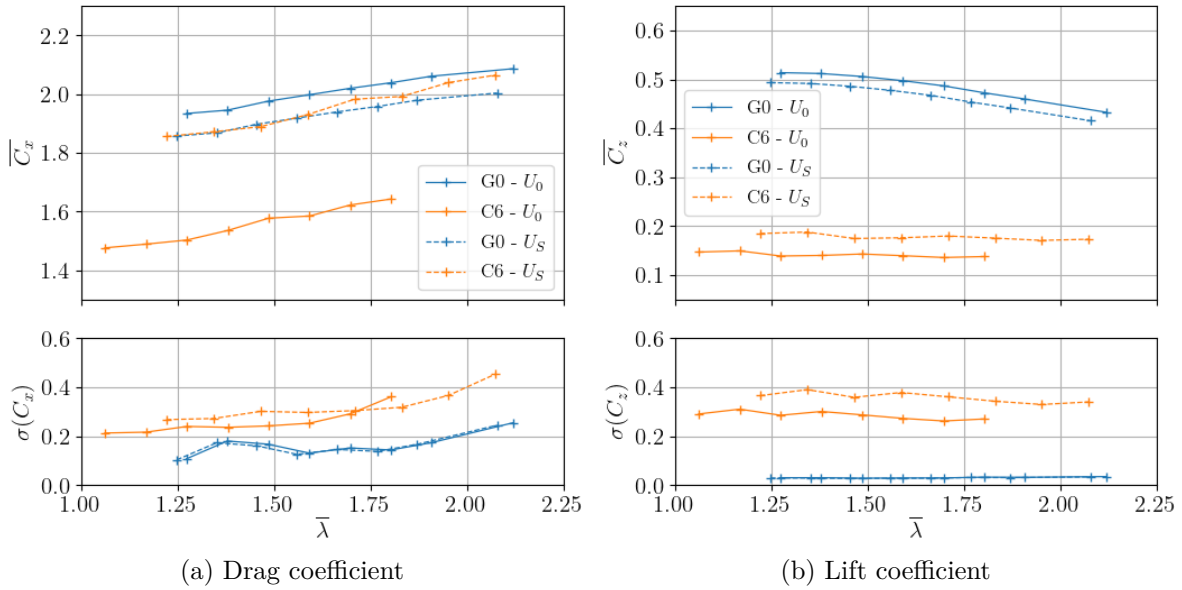


Figure 4.24 – Average (top) and standard deviation (bottom) of the drag and lift coefficients with regard to the tip speed ratio in G0 and C6 computed with either U_0 or U_S .

at $\lambda > \lambda_{opt}$ in C6 whereas the maximum is at low λ in G0. Then, and more challenging, $\bar{\sigma}(C_{P_{col}})$ is multiplied by 3.1 at λ_{opt} when considering the constant far upstream velocity U_0 and by 5.4 when considering the velocity really perceived by the turbine U_S . That power fluctuation is due to a 3.8 times greater torque standard deviation at the optimal operating point in C6 compared to G0. The fluctuation intensity (standard deviation divided by average, FI) of the torque at λ_{opt} is 1.43 in C6 against 0.24 in G0, as a consequence of both the increased standard deviation and the decreased average. We also observe a 3.0 times higher standard deviation of the rotational speed at λ_{opt} , although $FI(\omega)$ is only 0.002 and 0.006 in G0 and C6 resp. given the motors control at constant speed. That small temporal scale fluctuation of the power generation when the tidal turbine is in the wake of a large bathymetry obstacle must be taken into account in the design of the electricity conversion system to provide a smooth signal to the grid.

4.2.3.2 Effects on the loads applied to the 2-VATT

Fig. 4.24 presents the average and the standard deviation of the drag (a) and the lift (b) coefficients computed either with U_S or U_0 both in G0 and C6. Similarly to the power coefficient, the presence of the bottom mounted obstacle leads to a 23 % drop of \bar{C}_x computed with U_0 between G0 and C6 due to the decreased velocity in the wake of the bathymetry obstacle. Computed with U_S , the \bar{C}_x values are of the same order of magnitude in G0 and C6, indicating no effect of the turbulence and the flow shear on the average drag coefficient. However, the drag standard deviation is multiplied by 2 at λ_{opt} in C6 compared to G0. The results on C_{M_y} are the same as on C_x but the effect of the bathymetry obstacle wake on the vertical load applied to the 2-VATT is different (Fig. 4.24 (b)). Indeed, \bar{C}_z is more than 2.5 times lower in C6 compared to G0, independently from the reference velocity. This result means that the turbine apparent weight on the base is higher when the 2-VATT is in the wake of that bathymetry obstacle compared to the flat floor configuration. We explain this result by the negative vertical velocity

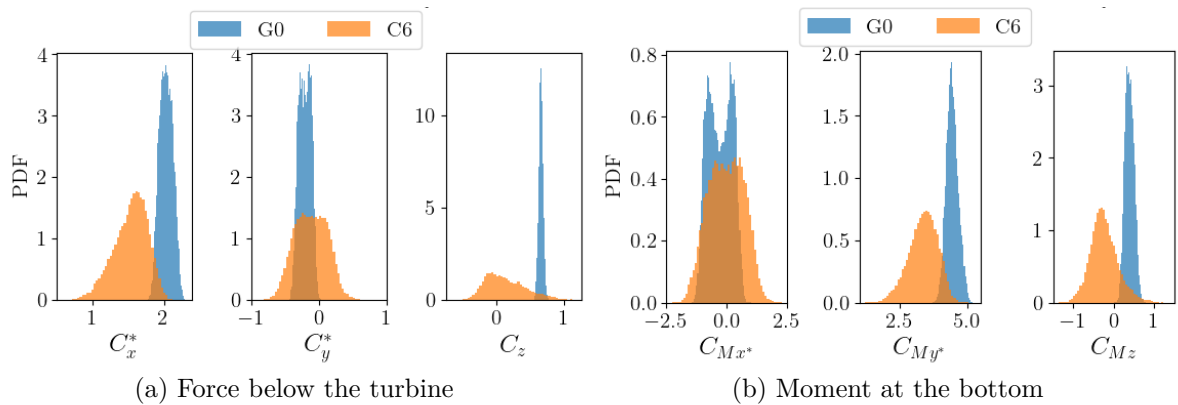


Figure 4.25 – Probability Density Functions of the load coefficients computed with U_0 in G0 and C6.

field, up to $w = -0.1U_0$, measured in the wake of the bottom mounted cylinder near the turbine position (Fig. 4.20). Conversely, the vertical load fluctuation is strongly increased by the presence of the bathymetry obstacle upstream as $\sigma(C_z)$ is multiplied by 10 between G0 and C6 at λ_{opt} with U_S as the reference velocity. Similarly to the torque fluctuation intensity, the difference in $FI(C_z)$ is even bigger than in $\sigma(C_z)$ as the average vertical load decreases while its standard deviation increases. Thus, $FI(C_z)$ is less than 10 % in G0 whereas it is more than 200 % in C6, both with U_0 and U_S at λ_{opt} .

To further investigate the effect of the bathymetry obstacle wake on the 2-VATT load fluctuation, we compute the probability density functions (PDF) of the 6 load components. Fig. 4.25 presents the PDF of the 3 force coefficients (a) and of the 3 moment coefficients at the bottom of the base (b) in G0 and C6 at λ_{opt} . Here, the coefficients are computed with U_0 to analyse the effect of the bathymetry-modified flow on the loads for a given far upstream hydrodynamic power potential. The results show that, for all of the 6 load components, the range between the minimum and maximum values are significantly wider in C6 than in G0, which is due to the wider velocity range induced by the turbulence in the wake of the bathymetry obstacle (Fig. 4.21). As a consequence, the fatigue stress of the 2-VATT structure is increased (Milne et al., 2010). In addition, C_x and C_{My} reach the highest absolute values among the 6 load components, placing them as the most critical quantities for the drifting and overturning risk considerations at the gravity base design stage. It appears that their maximal values in C6 are lower than those in G0. Thus, for a given far upstream velocity, the drifting and overturning risks are lowered by the presence of a wide bathymetry obstacle upstream of the 2-VATT. To moderate that conclusion, Fig. 4.25 (a) also shows that, despite the decrease of C_z average, its maximal values are exceeded in the configuration C6 compared to G0. That result means that, in some extreme cases, the apparent weight of the turbine on the base is lightened by the incident flow, which lowers the device resistance to the drifting. Thus, the occurrence of maximal C_z simultaneously with maximal C_x could increase the drifting risk. Finally, the transverse forces and moments maximal values are all overtopped, probably due to the instantaneous flow asymmetries induced by the coherent flow structures.

Independently from the flow characteristics, the PDF shapes are affected by the (random) relative phase of the two rotor columns since the loads are measured on the

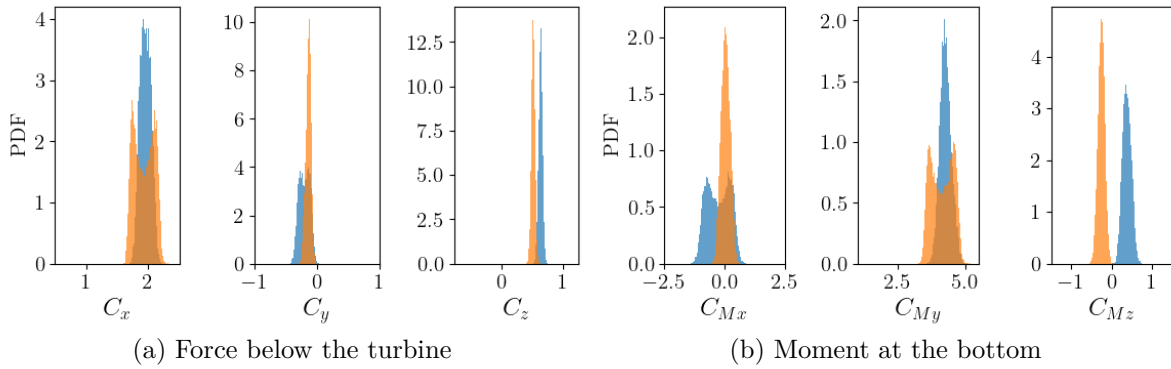


Figure 4.26 – Probability Density Functions of the load coefficients computed with U_0 at λ_{opt} in G0 when the two rotor columns are rather in phase (orange) or out of phase (blue).

whole turbine. Among several repetitions of the same operating point in G0, we observe that when the two columns are rather in phase (i.e. when the blades absolute positions are symmetrical), the C_x and C_{My} PDF present two maxima, whereas they have a single maximum when the rotor columns are rather out of phase (Fig. 4.26). In addition when the rotors are parked, the 6 loads PDF are narrower and they present a single maximum. We suggest that the presence of two C_x (and C_{My}) PDF maxima at λ_{opt} may correspond to the cases when the two phased columns are either at a maximum or at a minimum of torque generation, inducing two mostly probable C_x values on each side of the average value. Whereas the presence of a single C_x PDF maximum could mean that the torque fluctuation of one rotor column are compensated by the other out of phase column, which smooths the overall C_x signal and provides a single maximum of probability at the average coefficient value. The number of maxima in C_y and C_{Mx} PDF is opposed to that of C_x and C_{My} . This can be explained by an analogous line of thinking on the balancing of the fluctuating lateral loads generated by the two vertical axis rotor columns, whether in phase or out of phase. When comparing the loads between the C6 and the G0 configurations (Fig. 4.25), we chose to present the loads PDF for the repetition cases when the two columns are rather out of phase in the two flow conditions. That being, the conclusions regarding the effect of the bathymetry-generated turbulent flow on the 2-VATT compared to the flat bed configuration remain, as the load ranges in C6 largely exceed those in G0, regardless of the rotor column phasing.

The two last sections showed a significant increase of both the power and the load fluctuation when the bottom mounted 2-VATT is placed in the wake of a wide bathymetry obstacle compared to the configuration with a flat bathymetry. In the following section, we focus on that fluctuation origin through analyses in the temporal and in the spectral domain.

4.2.3.3 Fluid induced torque and load fluctuation

Fig. 4.27 displays the cross-correlation of the fluctuating torque of the red column Q'_R , the drag force F'_x and the lift force F'_z with the fluctuating velocity components measured at $x = -H$ by the 2C- and 3C-LDV in front of the top and bottom rotors respectively. The results at λ_{opt} show a maximum of correlation close to 0.4 between

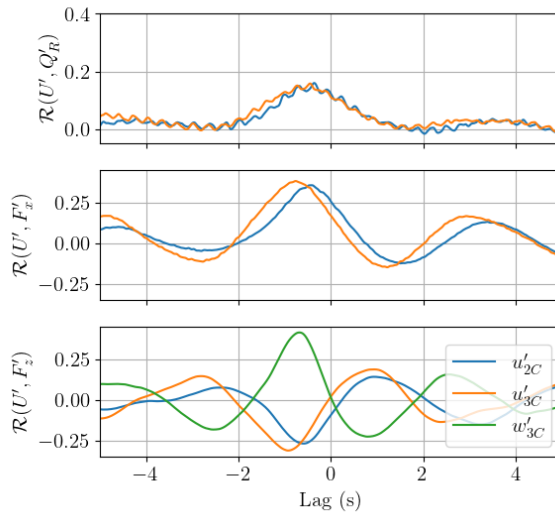


Figure 4.27 – Cross-correlation of the fluctuating torque Q'_R of the red column, the drag force F'_x and the lift force F'_z with the fluctuating velocity components measured at $x = -H$ by the 2C- and 3C-LDV in front of the top and bottom rotors respectively. The blue and orange curves are correlations with the streamwise velocity whereas the green one is with the vertical velocity component.

the drag and the two streamwise velocity measurements. However, the lag at which the maxima occur are -0.45 s with u'_{2C} against -0.75 s with u'_{3C} while the maximum of the cross-correlation between u'_{2C} and u'_{3C} occurs at $\tau = 0$ s. This difference of lag is simply explained by the shear in the bathymetry obstacle wake that provides a faster transport of the flow fluctuation towards the turbine at the height of the 2C-LDV probe (top rotor) than at the height of the 3C-LDV probe (bottom rotor). Besides, the results on the lift reveal a negative correlation with the streamwise velocities and a stronger positive correlation with the vertical velocity fluctuation w' . Overall, those lift and drag results feed the discussion on the drifting risk as they mean that peaks of w generate peaks of F_z whereas peaks of u produce peaks of F_x but troughs of F_z . Therefore, maxima of F_z cannot occur simultaneously with maxima of F_x and so the device drifting risk is actually decreased by the presence of the bathymetry obstacle for a given far upstream velocity. Fig. 4.27 also reveals that the lag at the maximum torque correlation with the streamwise velocity is equal for the two velocities considered despite the flow shear, in opposition to the results on the lift and drag forces. That maximum torque correlation lag is the same as the one of the drag with the 2C-LDV measurement (top rotor), which indicates that the whole rotor column response is dominated by the response of the top rotor. In an undisturbed flow, the authors already found that the top rotor dominates the torque generation when the 2-VATT faces a sheared velocity profile (Moreau et al., 2023d) as it is the case in the cylinder wake. We also observe that the maximum of torque correlation at λ_{opt} is less than 0.5 times that of the drag, indicating that the flow fluctuation impact is lesser on the 2-VATT rotating parts than on the overall structure.

Furthermore, $\mathcal{R}(U', Q'_R)$ presents high frequency oscillations and the loads correlations show secondary maxima with about 4 s lag compared to the absolute maxima, which indicates related periodical fluctuation of the flow and the loads. To better characterise that periodical fluctuation, Fig. 4.28 displays the torque, drag and lift power

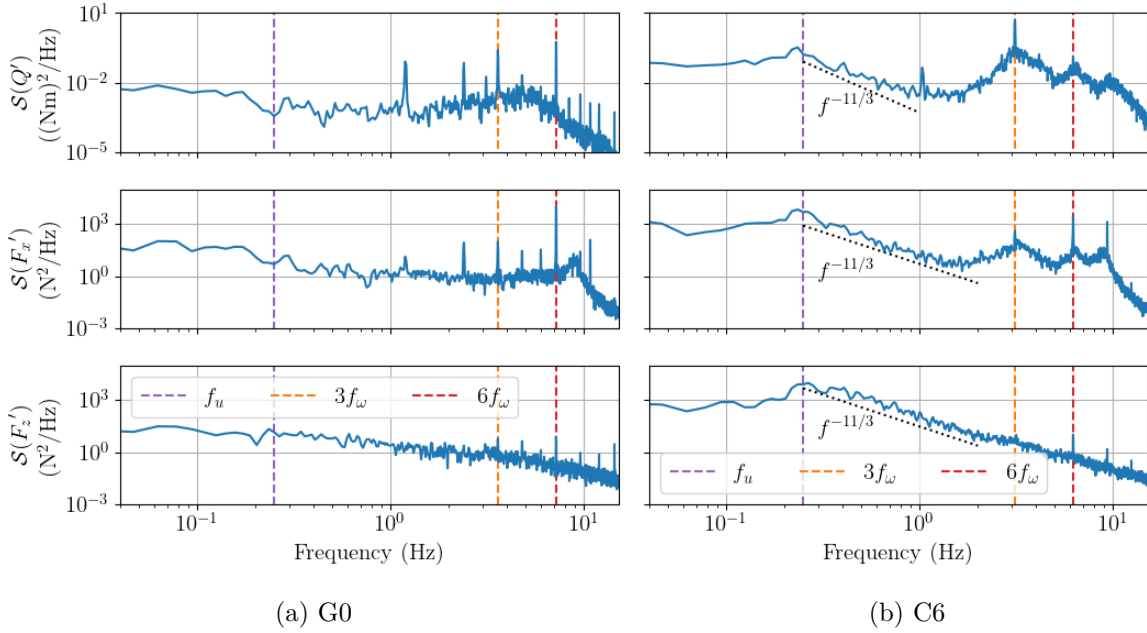


Figure 4.28 – Power spectral density of the fluctuating torque Q' , the drag force F'_x and the lift force F'_z at λ_{opt} in G0 and C6. f_ω is 1.20 Hz in G0 against 1.04 Hz in C6 at λ_{opt} due to the difference of U_S .

spectral densities \mathcal{S} . First, we can observe that the overall amplitude of the three spectra is about 10 times higher in C6 than in G0, up to about $f_c = 4\text{--}5$ Hz on the loads and on the whole frequency range for the torque. This result is in line with the higher levels of the velocity spectra observed in the wake of the bathymetry obstacle compared to the flat bathymetry configuration (Fig. 4.22). The frequency at which the loads spectra level in C6 reach the level of G0 indicates that the 2-VATT is less sensitive to higher frequency turbulence fluctuation. Considering the surface averaged velocity U_S in C6, we deduce that the 2-VATT drag and lift are sensitive to turbulence structures whose characteristic length l is greater than $l = U_S/f_c \simeq 0.2$ m, which is between $H/2$ and $H/3$. That critical size of turbulent structure is consistent with the observations on HATTs (Chamorro et al., 2015; Gaurier et al., 2020c). The rotors projected area being smaller than the overall structure, the torque response is indeed impacted by smaller turbulence structures revealed by the higher \mathcal{S} level in C6 on the whole frequency range.

Then, on one hand, between 1 and 10 Hz, $\mathcal{S}(Q')$ in C6 is dominated by a peak at 3 times the rotational frequency (f_ω) despite the 6 blades that compose the rotor column. Indeed, the peak amplitude at $3f_\omega$ is about 40 times higher than the one at $6f_\omega$. Fig. 4.20 shows that the flow is strongly sheared behind the bathymetry obstacle and the authors previously found that the torque spectral peak at $3f_\omega$ becomes stronger relatively to the one at $6f_\omega$ in presence of a sheared flow as the bottom rotor contribution to the whole column torque diminishes (Moreau et al., 2023d). By comparing Fig. 4.28 (a) and (b), we also observe that the higher levels of torque and loads spectra in C6 exceeds the level of most of the rotational frequency harmonics observed in G0. As a consequence, only the 1st, 3rd, 6th and 9th harmonics can be observed in C6 spectra. On the other hand, between 0.1 and 1 Hz, the loads spectra in C6 are dominated by a frequency peak around $f_u = 0.25$ Hz which carries more power than the lower frequencies and

than the rotational frequency harmonics. Those low frequency peaks are absent in G0. The velocity spectra behind the bathymetry obstacle presented in Fig. 4.22 also display large peaks around that frequency and was found to be due to the coherent turbulent structures shedding in the obstacle wake (Ikhennicheu et al., 2019b). Thus, the present results show that the load fluctuation is more affected by the periodical impacts of the vortices on the structure than by the blades rotation. However, that flow induced spectral response around f_u is a lot weaker in the torque spectra as its power is about 15 times lower than that at $3f_\omega$. From the flow spectra in Fig. 4.22, it appears that the high energy vortices are mainly located at the centre of the tank ($y/h = 0$), which is also the centre of the obstacle and of the 2-VATT; but the vortices signature around f_u is barely visible at $y/h = 1$ and 2 and appears again at $y/h = 3$ with about 50 times less power than at $y/h = 0$. Consequently, the high energy vortices impact the central fairing of the ducted 2-VATT, which explains the high spectral content on the lift and drag at the vortex shedding frequency. However, the rotors, located between $y/h = 0.5$ and 2, are away from the most energetic vortices path, which explains the relatively low spectral content on the rotor torque at the vortex shedding frequency. Thus, the torque and so the power fluctuation rise in the wake of the bathymetry obstacle is mostly due to the flow shear that unbalances the contribution of the upper and lower rotors, and by the coherent flow structures to a lesser extent. Finally, although the VATT blades sweep a 3-dimensional surface by opposition to those of a HATT which sweep a 2-dimensional disc, the torque and load spectra also decay following a $-11/3$ power law in the turbulent bottom-mounted obstacle wake (Druault et al., 2022).

4.2.4 Conclusion

This part aims at studying the response of a ducted bottom-mounted twin vertical axis tidal turbine (2-VATT) placed in the wake of a wide bathymetry obstacle. To do so, we tested a 1/20 scale model of such a 2-VATT in Ifremer's tank either on a flat bed (configuration G0) or downstream of a wide bottom-mounted square cylinder (configuration C6) and we measured the turbine response simultaneously with the flow velocity. The wake of that obstacle is characterised by a strong velocity shear, both vertically and laterally, a high level of turbulence with an average turbulence intensity above 25 % on the 2-VATT capture area, and the shedding of large coherent flow structures every 4 s. Those scaled flow characteristics are similar to what can be measured in offshore tidal energy sites with uneven sea beds. The main results of our study are what follows.

First, it appears that the reference velocity chosen to compute the average power and loads coefficients strongly influences the results. On one hand, considering a constant far upstream velocity as a reference, regardless of the bathymetry between the measurement point and the turbine, the presence of a wide bathymetry obstacle upstream of the 2-VATT leads to a 40 % average power loss compared to the flat bed case. That result highlights mainly the effect of the velocity deficit in the obstacle wake. On the other hand, considering the velocity really perceived by the 2-VATT in the two bathymetry configurations, *i.e.* the power weighted average velocity at the device location prior to its installation, the power coefficient appears just 16 % lower in C6 than in G0. That result is partly due to the higher levels of turbulence in the wake of the bathymetry obstacle that increases the reference velocity value due to the cubic weighted average and probably to some Reynolds number effects.

In addition, we observe that the power standard deviation is more than 3 times higher in C6 than in G0 which is due to a similar increase of the torque fluctuation. The spectral analysis of the torque signal reveals that its fluctuation in C6 is mostly due to the strong vertical flow shear, and to the passing of coherent flow structures to a lesser extent.

Then, regarding the 2-VATT loads for a given far upstream velocity, the average hydrodynamic coefficients are lower in C6 than in G0 but their probability density functions are substantially wider, indicating larger fluctuation. That fluctuation is directly due to coherent structures passing as the loads spectral content is dominated by a peak at the coherent structures shedding frequency in the bathymetry obstacle wake. Quantitatively, the drag and lift standard deviations are multiplied by 2 and 10 respectively. The high fluctuation rates of the loads must be considered in the design of the structure for fatigue considerations. However, the maximal drag and pitch values in C6 remain below those in G0, so the 2-VATT drifting and overturning risks are not exceeded when the device is downstream of a wide bathymetry obstacle.

In a previous study, we tested two types of bathymetry obstacles with two obstacle-to-turbine distances for each (Bloch et al., 2022). That study revealed that the C6 configuration was the most impacting on the turbine behaviour among the 4 bathymetry obstacle configurations tested. Indeed, the 2-VATT power and load fluctuations are less intense, although significantly stronger than in the flat bed configuration, when it is located further downstream of the square cylinder or when the bathymetry obstacle is a combination of a cube with the square cylinder. In future works, we could conduct an analysis similar to that of the present paper regarding the effect of the combined cube and cylinder wake on the 2-VATT behaviour as the wake structure of that combination differs from the single cylinder case (Magnier et al., 2021).

In the light of these results, the authors recommend to carefully consider the bathymetry of each high potential tidal energy site not only for laying considerations but also to avoid lower velocity (and so power) areas due to upstream bathymetric singularities. In addition, the flow characterisation at the precise projected location of each turbine should be carried out as early as possible in the project timeline to qualify the site specific velocity probability density functions and design appropriate fatigue-proof structures. Finally, the choice of the upstream velocity measurement location(s) for the tidal turbines monitoring and performance assessment should also carefully consider the bathymetry to provide a relevant reference of the incident hydrodynamic power. The quite large area indicated as suitable by the IEC TS 62600-200 for current profiler placement to measure the incident resource at sea may need to be refined regarding the upstream bathymetry (IEC, 2013).

4.3 Turbine behaviour in presence of surface waves

4.3.1 Introduction

In the previous part, we found that the bathymetry variations can be responsible for large turbulent structures that cause important power and loads fluctuation for the ducted 2-VATT. In the chapter 2, we also found that the presence of surface waves with a significant wave height close to 3 m on top of the current at sea leads to strong load fluctuation on the full-scale prototype, with torque and drag standard deviations

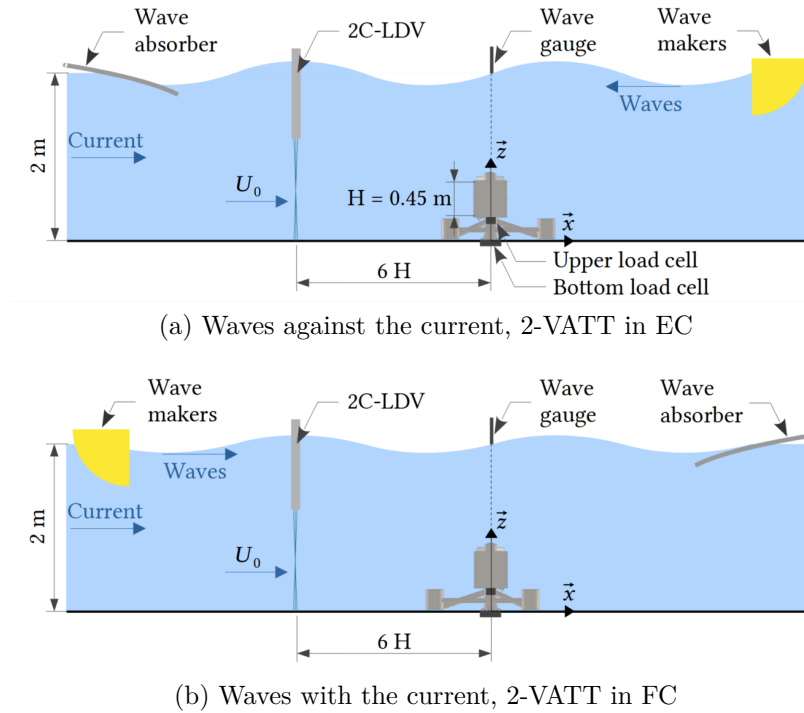


Figure 4.29 – Schematic side view of the experimental setups with surface waves opposing the current (a) or following it (b).

of the order of 0.7 times the average values. Many papers consider the effect of waves on reduced-scale HATT in towing tanks or flumes to better understand the wave-current-turbine interaction (Martinez et al., 2020; Gaurier et al., 2020d; Draycott et al., 2020) and provide reliable assessment of the unsteady loads endured by the turbine. However, to our knowledge, no study considered the effect of waves on 2-VATTs and only a few on isolated VATTs (Bachant et al., 2011; Zhang et al., 2014; Lust et al., 2021). To better understand how those waves affect the HydroQuest’s turbine response, we test the reduced-scale model in many controlled wave conditions in the tank. To reproduce the Paimpol-Bréhat test site wave-current conditions (Fig. 2.3 and 2.6), we place the reduced-scale ducted 2-VATT in the Ebb tide Configuration (EC, Fig. 1.2) while generating waves propagating against the current direction, and in the Flood tide Configuration (FC) while generating waves propagating with the current. To that end, the wave makers (and the wave absorber) are placed downstream (upstream respectively) of the turbine in the wave opposing the current case, and the other way round for the waves following the current, as illustrated in Fig. 4.29. With those apparatus immersed in the tank, the current velocity setpoint has to be reduced to $0.8 \text{ m}\cdot\text{s}^{-1}$ (Gaurier et al., 2018).

Fig. 4.30 displays the wave amplitude and period measured by a *Kenek SHT3-30* dynamic wave gauge above the ducted 2-VATT model in all the test cases, both with following and opposing waves. For the regular wave cases, we plot the average amplitude of the Hilbert transform of the surface elevation and its standard deviation with the error bars. The flow characteristics are extensively described in the same wave conditions for the opposing waves and in close conditions for the following waves in Magnier (2023). For a given wave makers displacement, the generated surface waves are different whether they propagate with or against the current. Indeed, the linear wave theory shows that

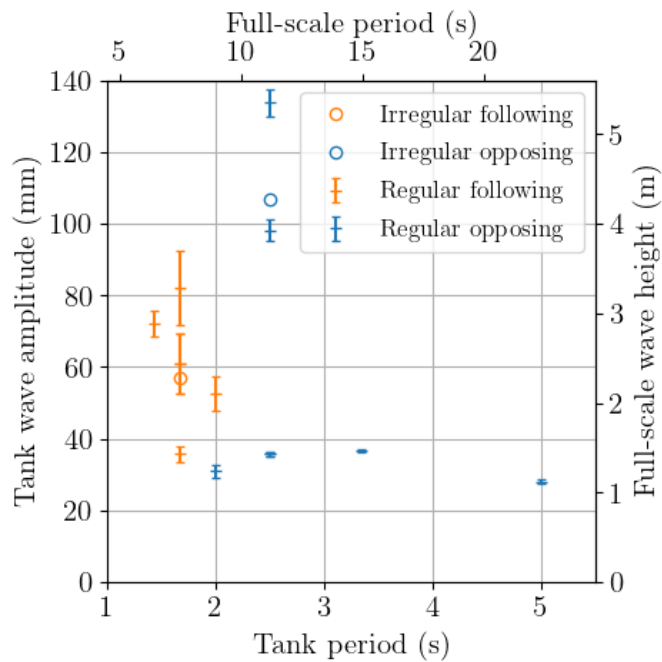


Figure 4.30 – Amplitude and peak period of the waves generated in the tank (left and bottom axes), measured above the turbine. For the regular wave cases, we represent the average of the amplitude of the surface elevation Hilbert transform and its standard deviation with the error bars. For the irregular waves with a JONSWAP spectrum, the amplitude value is the average of the highest third waves. The right and top axes provide the wave height and period at a 20/1 scale according to the Froude similitude law.

the wave-current interaction increases the wave-length and reduces the wave height for following waves whereas it does the reverse for opposing waves (Brevik et al., 1979). Therefore, the realisable wave amplitude and period ranges in the tank are different between the two relative wave directions due to the wave makers limits, which explains why the period ranges barely overlap between following and opposing waves in Fig. 4.30. According to the Froude similitude law with the 1/20 geometrical scale factor, the realisable wave period range matches the full-scale wave characteristics for the opposing waves whereas the wave periods are about two times lower for the following waves. In addition, the amplitude error bars representing the wave regularity in Fig. 4.30 reveal that the surface waves are more regular from one period to the other with opposing waves than with following ones. That result is supposed to be due to the turbulence generated by the unsteady flow perturbations induced by the moving wave makers at the inlet of the test section when generating following waves (Magnier, 2023).

As a consequence, we chose to focus on the effect of the opposing waves, which better respect the Froude similitude law and are better controlled and characterised, on the response of the ducted 2-VATT model. The analyse that follows was published as Moreau et al. (2023b), “Experimental investigation of surface waves effect on a ducted twin vertical axis tidal turbine”, in *Journal of Marine Science and Engineering*. Section 4.3.2 describes the turbine model, the experimental setup, the flow conditions in the different wave cases and the data processing carried out for the analysis. Then, we anal-

analyse the effects of the wave amplitude and frequency on the turbine power performance and the structural loads in section 4.3.3.1, as well as the difference between regular and irregular waves. The wave-current-turbine interaction is studied further in section 4.3.3.2 focusing on one a specific regular and irregular wave case, either with the rotors parked or operating at the optimal tip speed ratio. In the last section, as a complement to the article, we compare the effect of irregular waves either following or opposing the current on the model loads.

4.3.2 Material and method

4.3.2.1 Turbine model

The 1/20 scale model is a ducted 2-VATT geometrically similar to the 1 MW-rated demonstrator tested by HydroQuest at the Paimpol-Bréhat test site from 2019 to 2021 (Moreau et al., 2022b). It is composed of two independent counter-rotating vertical axis rotor columns. Each column is made of two levels of H-Darrieus type rotors with a 60° phase difference between them, and each rotor of radius $R = D/2 = 200$ mm is made of $N = 3$ blades that are $H_{blade} = 190$ mm high with a chord c of 73 mm. Thus, the rotor solidity (Nc/R) is 1.1. The rotors are mounted in a $W = 1.24$ m wide structure made of fairings and plates. The turbine height is defined as the distance between the top and the bottom horizontal plates such that $H = 0.45$ m; and the 2-VATT capture area is $H \times W$. For this study, the turbine is fixed on a tripod bottom-mounted base similar to the demonstrator's one so the whole structure height is $H_{struc} = 0.84$ m. The two rotor columns are controlled at a constant rotational speed by two independent *Maxon RE50* DC motors and *Escon 70/10* servo-controllers. The torque Q of each rotor column is measured using *Scaime DR2112-W* torque-meters and the rotational speeds ω are measured by the motor encoders. The 6 load components applied between the turbine and the base and those between the base and the tank floor are measured using *SIXAXES* 1.5 kN and 20 kN load cells, respectively (Fig. 4.29). All of these analog signals are acquired at a sampling frequency of 128 Hz using *National Instruments PXI* and *LabView* systems. The model and its instrumentation are fully described in Moreau et al. (2023c).

The base geometry upstream and the relative counter-rotation direction of the two column is different when the flow comes from one side or the other of the device. The two flow directions are referred either to FC, corresponding to the Flood tide Configuration at the Paimpol-Bréhat test site, or to EC for the Ebb tide Configuration (Fig. 1.2). The performance and wake differences between these two flow directions is presented in Moreau et al. (2023c).

4.3.2.2 Experimental setup

The 2-VATT model is tested in the Ifremer wave and current flume tank in Boulogne-sur-mer, France, whose depth is $H_{wat} = 2$ m and width is 4 m. It is operated at a velocity setpoint of $0.8 \text{ m}\cdot\text{s}^{-1}$ in its low turbulence configuration with the inlet conditioned by a honeycomb structure and a uniform grid (Gaurier et al., 2018). The 2-VATT is placed in the ebb tide configuration at the centre of the tank $(x, y, z) = (0, 0, 0)$ with x in the main flow direction, y towards the wall and z towards the free surface with $z = 0$ at the tank bottom. The 2-Component Laser Doppler Velocimeter (2C-LDV) measures

Table 4.3 – Wave against current cases’ characteristics measured in the tank above the turbine.

Case	Wave type	f_η (Hz)	T_p (s)	A_η (mm)
<i>f00A0</i>	No wave	–	–	–
<i>f02A1</i>	Regular	0.2	5.0	30
<i>f03A1</i>	Regular	0.3	3.3	38
<i>f04A1</i>	Regular	0.4	2.5	37
<i>f04A2</i>	Regular	0.4	2.5	102
<i>f04A3</i>	Regular	0.4	2.5	141
<i>f05A1</i>	Regular	0.5	2.0	42
<i>JS</i>	JONSWAP	0.4	2.5	107

the velocities (u, v) along (x, y) at $x = -6H$ at the centre of the turbine capture area, ie. $(y, z) = (0, 0.505)$ m. At this far upstream distance, the flow is not disturbed by the 2-VATT (Moreau et al., 2023c). The time average of u at this location is considered as the reference far upstream velocity and is $U_0 = 0.825 \text{ m}\cdot\text{s}^{-1}$.

In addition to the current, waves are generated to propagate against it, like during ebb tides at the Paimpol-Bréhat offshore test site (Moreau et al., 2022b). To do so, wave makers are immersed downstream of the test section and a wave absorber is installed upstream (Gaurier et al., 2018). In that configuration, the wave-current interaction tends to increase the wave height and shorten the wave length compared to waves on still water (Brevik et al., 1979). A servo type wave height meter (*Kenek SHT3-30*) measures the free surface elevation (η) right above the 2-VATT at $(x, y) = (0, 0)$. Seven wave cases are presented in this study including one irregular wave case noted *JS* and six regular wave cases noted *f0 – A–*, which indicates first the wave frequency (f_η) and then the amplitude level (Table 4.3). The feasible wave frequency range narrows when the wave amplitude increases, and vice versa, due to the limits of the wave makers capabilities (Magnier, 2023). Therefore, to study the influence of the wave amplitude, we chose the frequency $f_\eta = 0.4$ Hz that allows the largest amplitude range among the feasible wave conditions in the tank, and three arbitrary amplitude levels noted *A1* (low), *A2* (medium) and *A3* (high). Similarly, to study the impact of the wave frequency, we chose the low amplitude level *A1* to be able to cover a frequency range from 0.2 to 0.5 Hz. Finally, to compare the effect of regular and irregular waves on the turbine, we chose an irregular wave case with a similar peak period ($T_p = 1/f_\eta$) and significant wave amplitude (A_η , the average amplitude of the highest third of the waves) to the intermediate regular wave case *f04A2*. The irregular wave case is generated according to the standard JONSWAP spectrum with a peak enhancement factor of 3.3 (Hasselmann et al., 1973).

For all the test cases, the 2C-LDV, the wave gauge and the turbine related signals are acquired simultaneously during 3 minutes to guarantee the time convergence of the average and the standard deviation of the signals. Over this time, the 2-VATT sees

between 36 and 89 wave crests when $f_\eta = 0.2$ Hz and 0.5 Hz respectively. In this setup, the blade chord based Reynolds number ($Re_c = c\lambda U_0/\nu$, with ν the water kinematic viscosity and λ the tip speed ratio - Eq. 4.16) is of the order of $8.5 \cdot 10^4$ which is about 60 times smaller than at full-scale; and the Froude number based on the submergence depth ($Fr_s = U_0/\sqrt{g(H_{wat} - H_{struc})}$, with $g = 9.81$ m.s⁻² the gravity constant) is 0.24 against 0.17 at full-scale. Due to the relatively low Reynolds number in the tank, we expect depreciated rotor performance compared to the full-scale 2-VATT (Bachant et al., 2016) but we expect the effect of the surface waves to be similar given the close Froude numbers.

4.3.2.3 Flow conditions

The velocity $U = u+v+w$, with (u, v, w) along (x, y, z) , can be decomposed such that $U(t) = \bar{U} + U'(t)$ with $U'(t) = U''(t) + U_\eta(t)$, the bar above indicating the time average, the prime the overall signal fluctuating part, $U''(t)$ the turbulence contribution to the velocity fluctuation and $U_\eta(t)$ the waves contribution, called orbital velocity. According to the linear wave theory (Molin, 2002), the free surface elevation η in presence of regular waves propagating along x can be defined as a cosine function of the time t and the space (Eq. 4.12 with k_η the wave number and $\omega_\eta = 2\pi f_\eta$ the wave pulsation). This surface elevation generates streamwise and vertical orbital velocities (u_η and w_η) in the water column. The orbital velocities are defined in Eq. 4.13 and 4.14 as a cosine and a sine function of time and space respectively, with A_u and A_w the orbital velocity amplitudes that depend on the depth and the surface wave characteristics. When waves propagate on top of a current, the definitions of A_u and A_w as well as the dispersion relation between k_η and ω_η are modified but the orbital velocities remain defined by the same cosine and sine functions of time and space (Brevik et al., 1979).

$$\eta = A_\eta \cos(k_\eta x - \omega_\eta t) \quad (4.12)$$

$$u_\eta = A_u(z) \cos(k_\eta x - \omega_\eta t) \quad (4.13)$$

$$w_\eta = A_w(z) \sin(k_\eta x - \omega_\eta t) \quad (4.14)$$

The flow characteristics in presence of waves opposing the current in Ifremer's tank were first presented in Saouli et al. (2022) and thoroughly described in Magnier (2023). Fig. 4.31 displays the wave amplitude with regard to their period measured in the tank without turbine for the seven wave cases and gives the similar wave height and period at full-scale according to the Froude similitude law. At full-scale, the A2 (medium) amplitude level was roughly the limit below which the 1 MW-rated demonstrator of the ducted 2-VATT was operating and above which the rotors were parked to avoid extreme loading on the structure. At the first order for regular waves, Saouli et al. (2022) obtain the orbital velocity $U_\eta(t)$ by filtering the velocity signal around the wave frequency. Then, the remaining velocity fluctuation is fully attributed to the turbulence $U''(t)$. Defined that way, Fig. 4.32 presents the streamwise average velocity and turbulence intensity profiles for all the wave cases, with σ indicating the standard deviation. The transverse average velocities (\bar{v}, \bar{w}) are insignificant. The profiles labelled *CO* refer to the tank configuration in current only with the wave makers and absorber out of the

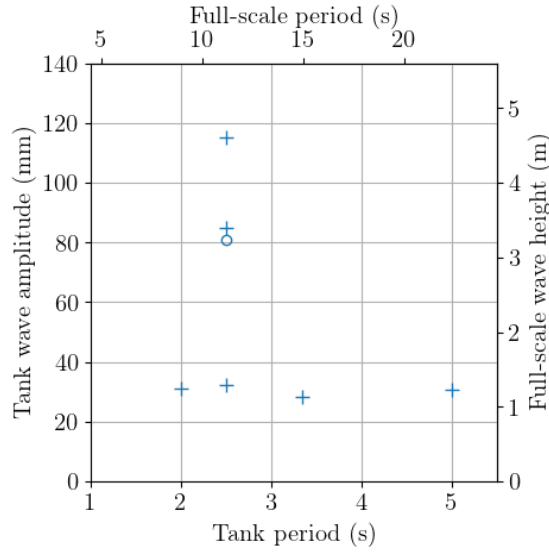


Figure 4.31 – Amplitude A_η and period Tp of the waves generated in the tank (left and bottom axes), measured without turbine (Magnier, 2023). The crosses represent the regular wave cases and the circle is the JONSWAP case. The right and top axes provide the waves period and height at a 20/1 scale according to Froude similitude law.

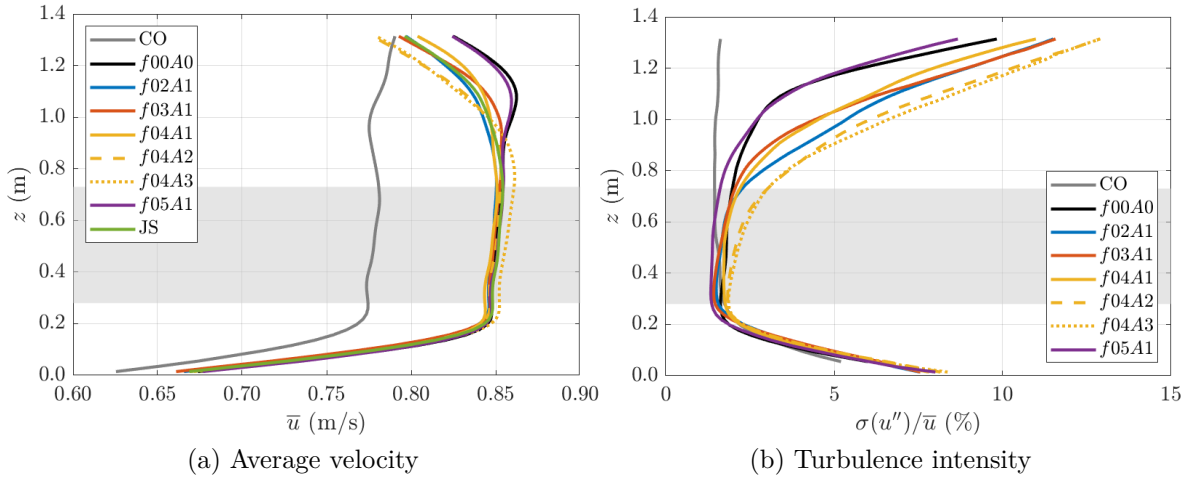


Figure 4.32 – Average (a) and turbulence intensity (b) streamwise velocity profiles in the classical current only case (CO), with the damping beach and wave makers immersed ($f00A0$) and in all the wave cases considered. The data is from Saouli et al. (2022). The grey area represents the 2-VATT capture height.

water whereas the $f00A0$ profiles refer to the condition in current only with the wave makers and absorber immersed but inactive. It appears that the immersion of the wave makers and absorber in the top 0.5 m of the water column significantly modifies the average velocity and turbulence intensity profiles with a velocity increase in the bottom part of the tank and a turbulence increase in the top part. That being, \bar{u} and $\sigma(u'')/\bar{u}$ profiles remain rather homogeneous over the 2-VATT capture height, from $z = 0.28$ to 0.73 m. This observation justifies the use of a single velocity measurement point

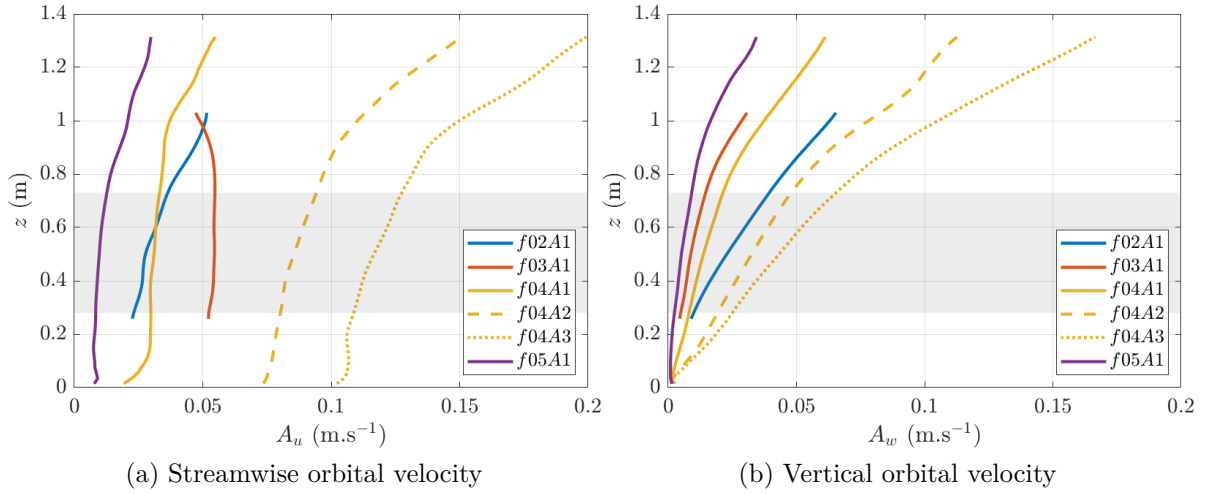


Figure 4.33 – Amplitude of the streamwise (a) and vertical (b) orbital velocities along the water depth in the regular wave cases. The data is from Magnier (2023). The grey area represents the 2-VATT capture height.

at the centre of the capture area as the reference velocity U_0 . In the following, the $f00A0$ current only case will be the reference when assessing the effect of surface waves. Furthermore, Fig. 4.33 displays the oscillation amplitude of the streamwise and vertical orbital velocities for all the regular wave cases, presented in Magnier (2023). For the low amplitude case (A1), both the streamwise and vertical orbital velocities are less than 0.05 m.s^{-1} ($0.06U_0$) over the whole 2-VATT height. As predicted by the linear wave theory, the orbital velocity amplitude increases with the wave amplitude such that $A_u \simeq 0.09U_0$ in $f04A2$ and $A_u \simeq 0.13U_0$ in $f04A3$ at mid-turbine height.

Among the seven wave cases, we will specially focus on the regular wave case $f04A2$ and the irregular wave case compared to the current only case. Using the linear wave theory, Fig. 4.34 displays one theoretical period of the surface elevation in $f04A2$ along with the streamwise and vertical velocities at the turbine mid-height ($z = 0.505 \text{ m}$), where the velocity characteristics are approximately $\bar{u} = U_0 = 0.825 \text{ m.s}^{-1}$, $A_u = 0.09U_0$ and $A_w = 0.04U_0$ (Fig. 4.33). The figure also displays the angle α_w between the total velocity direction and the horizontal direction. Fig. 4.34 shows that the streamwise velocity fluctuation is in phase opposition with regard to the surface elevation while the vertical orbital velocity is $\pi/2$ out of phase. In that wave-current condition, the total velocity direction is in phase with w and reaches almost $\pm 2^\circ$ with regard to the horizontal direction. In addition, Fig. 4.35 (a) presents the Probability Density Function (PDF) of the streamwise velocity measured with the 2C-LDV upstream of the 2-VATT at $x = -6H$ and at the centre of the projected capture area in these three flow conditions. The arithmetic average of the velocity at this position is equal to U_0 in the three cases but the velocity distribution around that average value varies. In presence of waves, the velocity range is extended compared to the current only case, due to the orbital velocities induced by the waves. However, with regular waves the distribution presents two maxima, related to the periodical increase and decrease of the velocity occurring when a wave trough and crest passes, respectively; whereas a single PDF maxima is present at the average value in JS as the orbital velocities do not have favourite amplitudes with irregular waves. Besides, Fig. 4.35 (b) presents the power

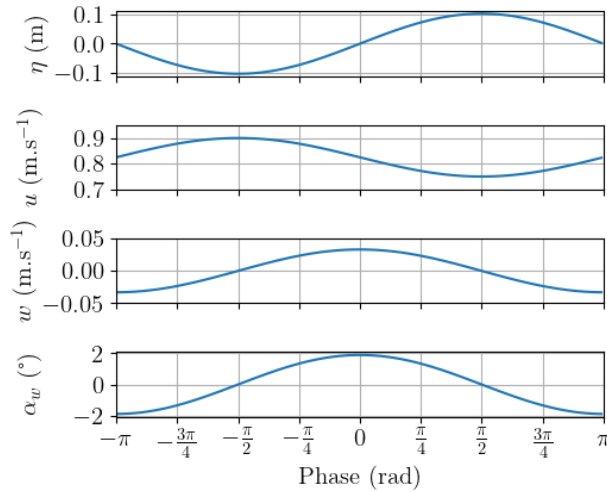


Figure 4.34 – Theoretical period of the surface elevation η , the streamwise and the vertical velocities u and w and the angle α_w between the velocity direction and the horizontal direction, with $\bar{u} = 0.825 \text{ m.s}^{-1}$, $A_u = 0.09\bar{u}$ and $A_w = 0.04\bar{u}$. This corresponds approximately to the flow conditions in *f04A2* at $z = 0.5 \text{ m}$ according to the linear wave theory.

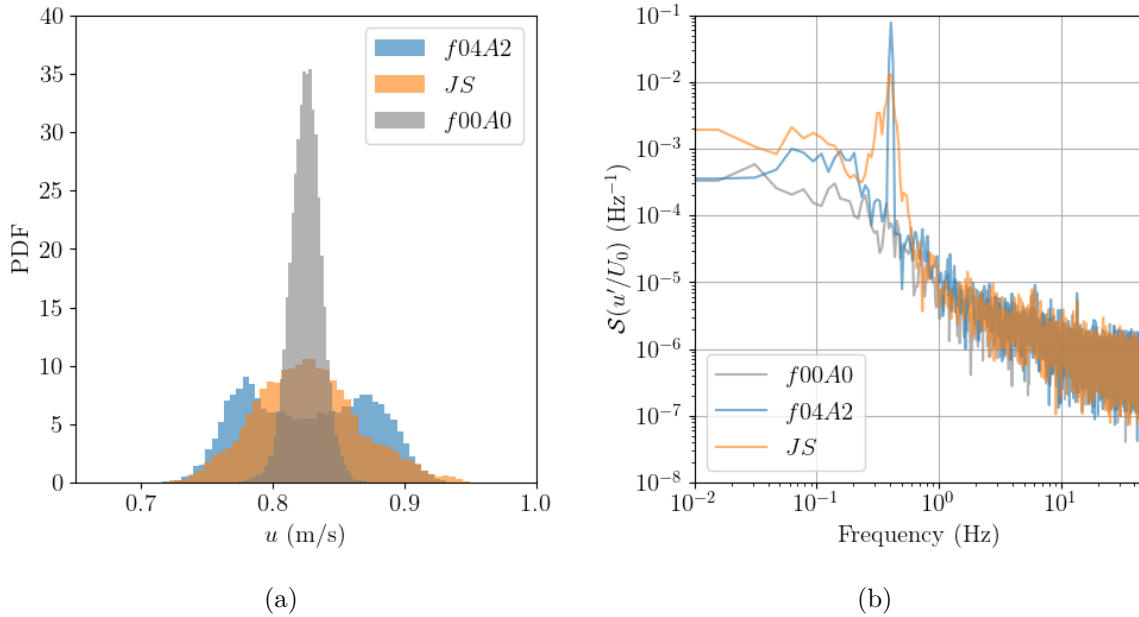


Figure 4.35 – (a) Probability Density Function and (b) Power spectral density of the streamwise velocity measured with the 2C-LDV at $x = -6H$ upstream of the 2-VATT at the centre of the projected capture area.

spectral density of the same 2C-LDV streamwise velocity measurements. The power spectral densities of the fluctuating part of u ($\mathcal{S}(u'/U_0)$) are computed using Welch's method with 64 s long windows and 50 % overlap. The spectral analysis reveals a strong energy peak at the wave frequency, as expected, with a sharp peak for the regular wave case and an increased level of energy between about 0.25 and 0.55 Hz in the JONSWAP

case.

4.3.2.4 Data processing

The power coefficient of each rotor column C_{Pcol} is computed as in Eq. 4.15 with $P_{col}(t) = Q(t)\omega(t)$ and t the time. The reference surface is that of the rotors projected area ($4DH_{blade}$) and the torque signal considered is corrected by the friction torque induced by the seals and the transmission system for each rotor column (Moreau et al., 2023c). Then, the overall average power coefficient $\overline{C_P}$ is the average of the two $C_{Pcol}(t)$ and the power fluctuation is analysed considering the average standard deviation between the two rotor columns, noted $\overline{\sigma}(C_{Pcol})$.

$$C_{Pcol}(t) = \frac{P_{col}(t)}{\rho DH_{blade} U_0^3} \quad (4.15)$$

The tip speed ratio (λ) is defined in Eq. 4.16. Thus, λ_0 refers to the tests with parked rotors and λ_{opt} refers to the those at the operating point providing the maximal power coefficient. The force and moment coefficients are defined in Eq. 4.17 and 4.18 for the components along x with the four rotors projected area as a reference surface. They are defined the same way for the loads along y and z . The loads measured without current at λ_0 are subtracted to consider only the hydrodynamic loads on the device without the gravity. In this study, we consider the forces applied by the turbine on the gravity base, measured by the upper load cell, and the moments applied to the ground, measured by the bottom load cell (Fig. 4.29). These are the loads to consider for the design of a stable gravity base. For all the hydrodynamic coefficients the reference upstream velocity measurement U_0 is averaged with the appropriate power weighting (power 1 for λ , 2 for the load coefficients and 3 for the power) (Moreau et al., 2023a).

$$\lambda(t) = \frac{\omega(t)R}{U_0} \quad (4.16)$$

$$C_x(t) = \frac{F_x(t)}{2\rho DH_{blade} U_0^2} \quad (4.17)$$

$$C_{Mx}(t) = \frac{M_x(t)}{2\rho RDH_{blade} U_0^2} \quad (4.18)$$

In addition to the load coefficients evolution with the tip speed ratio, we also analyse their probability density functions with 50 equal-width bins to consider the load distributions and extrema. The extreme load value is considered as the maximum between the absolute value of the first and the last percentile ($\max[\text{abs}(p01), \text{abs}(p99)]$) and the load range is considered as the difference between p01 and p99. The correlation between the wave-induced velocity fluctuation and the loads fluctuation is analysed by computing the normalised cross-correlation coefficient \mathcal{R} with regard to the time lag (τ) between the free surface elevation (η) above the 2-VATT and the loads or the rotor torque (Eq. 4.19, with s indicating the load or torque signals).

$$\mathcal{R}(\eta', s')[\tau] = \frac{\overline{(\eta(t) - \overline{\eta})(s(t + \tau) - \overline{s})}}{\sqrt{\overline{(\eta(t) - \overline{\eta})^2} \overline{(s(t) - \overline{s})^2}}} \quad (4.19)$$

We also study the fluctuation of the rotor torque, the drag and lift coefficients averaged according to the wave phase with 3 degrees phase bins, indicated by a tilde above the symbols. The wave phase is obtained by Hilbert transform of the surface elevation signal filtered at the wave frequency ± 0.1 Hz. Finally, the Fourier transform (\mathcal{F}) of Q' , F'_x and F'_z are computed as well as their coherence with the upstream velocity measurement using Welch's method with 32 s long windows and 50 % overlap to analyse the periodical characteristics of the 2-VATT related signals compared to those of the wave-induced flow fluctuation.

4.3.3 Effect of waves against current on the ducted 2-VATT behaviour

4.3.3.1 Wave amplitude and frequency effect

Figure 4.36 gives an overview of the wave effect on the average and standard deviation of the power performance and on the loads of the ducted 2-VATT with regard to the tip speed ratio. The general trend is that the presence of surface waves barely affects the average values at the optimal operating point but it increases the standard deviations, whether the 2-VATT rotors are parked or in operation. In addition, the waves modify the evolution of the power coefficient with the tip speed ratio, both in average and fluctuation, but they do not affect the one of the load coefficients. More specifically, we observe an average power coefficient decrease with the wave amplitude at the tip speed ratios below λ_{opt} , without changing the maximal $\overline{C_P}$ at $\bar{\lambda} = 1.6$. The data may indicate an increase of λ_{opt} with A_η but complementary measurements at $\bar{\lambda} > 1.6$ would be needed to confirm this supposition. Besides, the waves induce a slight increase of the average loads on the 2-VATT with less than 5 % difference compared to the case without waves, and without modifying the loads evolution with regard to λ . The limited effect of the surface waves on the average power and loads is consistent with the homogeneity of the average velocity profiles over the wave cases (Figure 4.32 (a)). The power performance decrease at the low tip speed ratios may reveal an increase of the dynamic stall due to the wave-induced velocity fluctuation (Figure 4.33).

Besides, those wave-induced orbital velocities strongly affect the standard deviation of the power and loads coefficients. Indeed, the latter increase linearly with the wave amplitude such that an A_η increase of 0.1 m generates roughly a 2, 3 and 4 times higher $\sigma(\overline{C_{Pcol}})$, $\sigma(C_z)$ and $\sigma(C_x)$ respectively at λ_{opt} (Fig. 4.37). As a consequence, $\sigma(C_z) \simeq \overline{C_z}$ for the wave case with the highest amplitude. Those linear trends between the load standard deviations and the wave amplitude are rather independent of λ , which indicates a low interaction between the rotors rotation and the waves on the loadings. We only observe an offset in $\sigma(C_x)$ and $\sigma(C_{My})$ when comparing between λ_0 and λ_{opt} due to the blades passing, but the linear trends with A_η are unchanged (Fig. 4.37). Regarding the power coefficient, the impact of waves on $\overline{\sigma(C_{Pcol})}$ grows with λ . Indeed, the slope of the linear fit with A_η increases with λ , which indicates an interaction between the rotors rotation and the waves on the power performance, unlike the loads. To the authors knowledge, such a linear relationship between the surface wave height and the load's standard deviation of a turbine had never been shown. However, using a theoretical model, Xin et al. (2023) also found a linear relationship between the wave height and the standard deviation of the horizontal force applied to a bottom-fixed vertical slender cylinder subjected to surface waves and a tidal current.

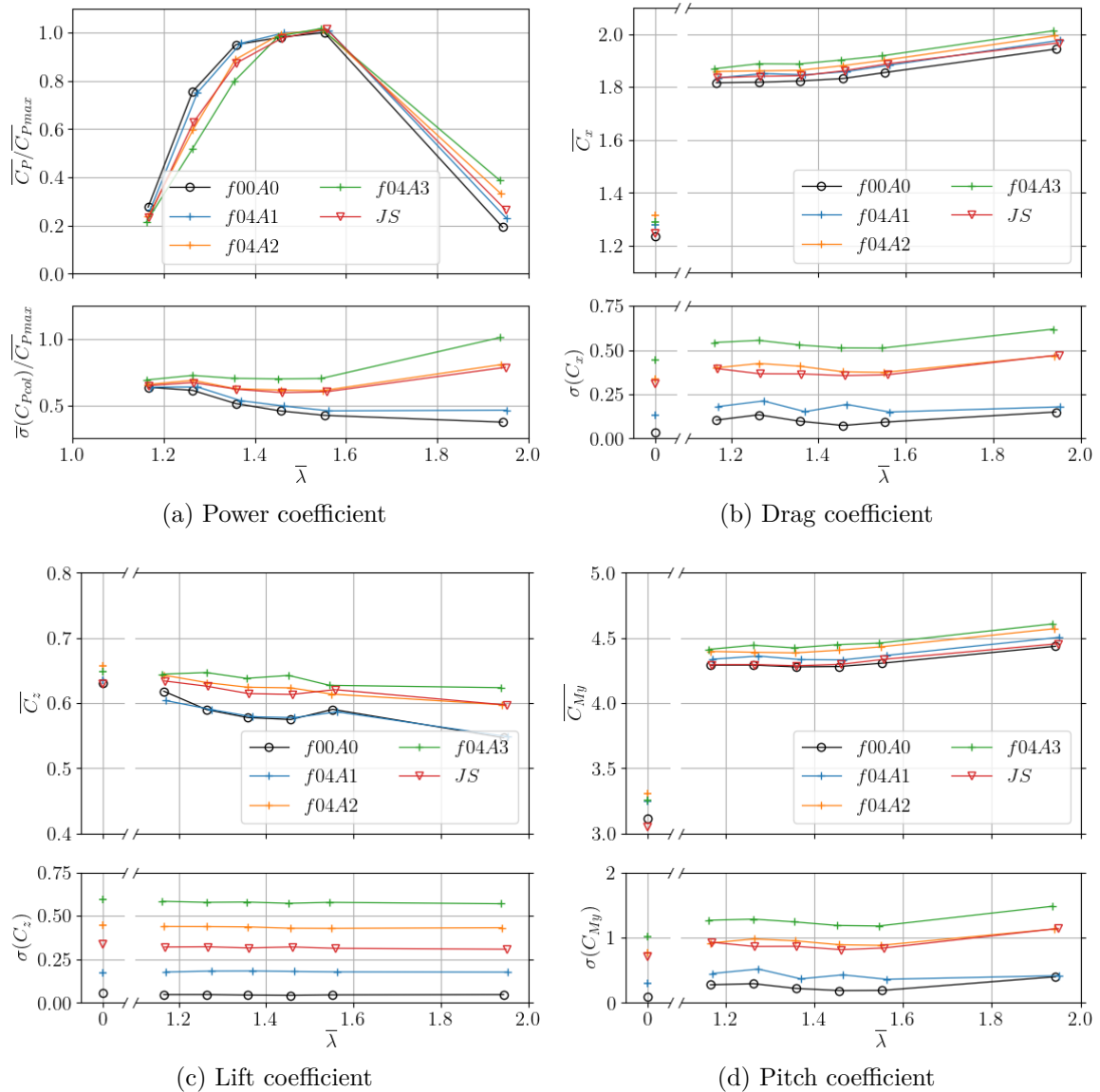


Figure 4.36 – Evolution with the tip speed ratio of the power (a), drag (b), lift (c) and pitch (d) coefficients with the average at the top and standard deviation at the bottom of each sub-figure. The C_P values are normalised by the maximal average value in the $f00A0$ case (without waves).

In the design process, under the assumption of a normal law of distribution, the extreme loads to which the turbine can be submitted are estimated combining the average and the standard deviation values. For instance, the extreme drag coefficient value is estimated as $C_{x,max} = \overline{C_x} + 3\sigma(C_x)$. Here, $C_{x,max} = 3.01$ at the optimal operating point in the medium wave case $f04A2$ against 1.32 with the rotors parked in the extreme wave case $f04A3$. This result justifies the choice to park the rotors in presence of extreme wave conditions to limit structural damages and to carry out experiments with the 2-VATT operating in wave conditions to assess the maximal loads for the design process. Following the linear trends in Fig. 4.37 for regular waves at 0.4 Hz, we find that the extreme loads on the turbine would be greater with the rotors

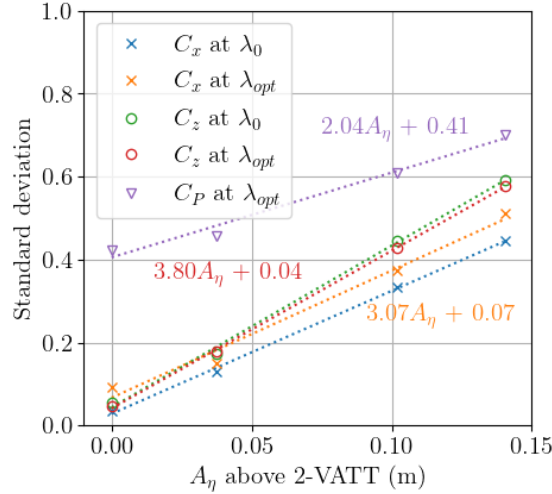


Figure 4.37 – Coefficients’ standard deviation with regard to the waves amplitude for $f_\eta = 0.4$ Hz, when the turbine is parked or operating at λ_{opt} . Dashed lines are linear fits of the data points. The points labelled C_P are the values of $\bar{\sigma}(C_{Pcol})/\bar{C}_{Pmax}$.

parked compared to the limit case at λ_{opt} with intermediate wave conditions ($f04A2$) if $A_\eta > 0.18$ m, which gives 7.2 m wave height at full-scale according to Froude similitude law. That wave height at sea is likely to be encountered during winter storms, with about a 5 years return period at the Paimpol-Bréhat tidal turbine test site (EDF et al., 2022).

Still looking at Fig. 4.36, it appears that regular and irregular waves with similar peak period and significant wave amplitude, namely $f04A2$ and JS (Table 4.3), affect the C_P evolution with λ the same way, both in terms of average and fluctuation. However, we observe little load differences between the regular and the irregular wave cases. The average loads in JS at λ_0 are equal to the case without waves while they are slightly higher with regular waves. In addition, with the rotors in operation, \bar{C}_z is similar with regular and irregular waves but \bar{C}_x and \bar{C}_{My} are a few percent lower in JS ; while $\sigma(C_x)$ and $\sigma(C_{My})$ are unchanged but $\sigma(C_z)$ is 37 % lower in JS compared to $f04A2$.

Beyond the wave amplitude, its frequency is also expected to affect the 2-VATT response. However, the power and drag coefficients evolution with the tip speed ratio are almost the same in the four wave cases at variable frequency (Fig. 4.38). Due to the wave-current interaction and the wave makers amplitude limits at low frequency, multiple wave frequency cases could only be generated at the amplitude level $A1$. Since the previous results on the effect of the wave amplitude have shown that the 2-VATT response is barely affected by waves of that amplitude level, we assume that the absence of frequency effect observed here is actually due to the smallness of the waves amplitude. Indeed, the wave-induced velocity fluctuation in those wave cases is less than 6 % of the average velocity at the turbine mid-height (Figure 4.33).

4.3.3.2 Wave-current-turbine interaction

To better understand how the surface waves increase the ducted 2-VATT power and loads fluctuation, we focus on the $f04A2$ regular wave case and the JS irregular wave case. The turbine’s response is studied with parked rotors first to look at the wave effects

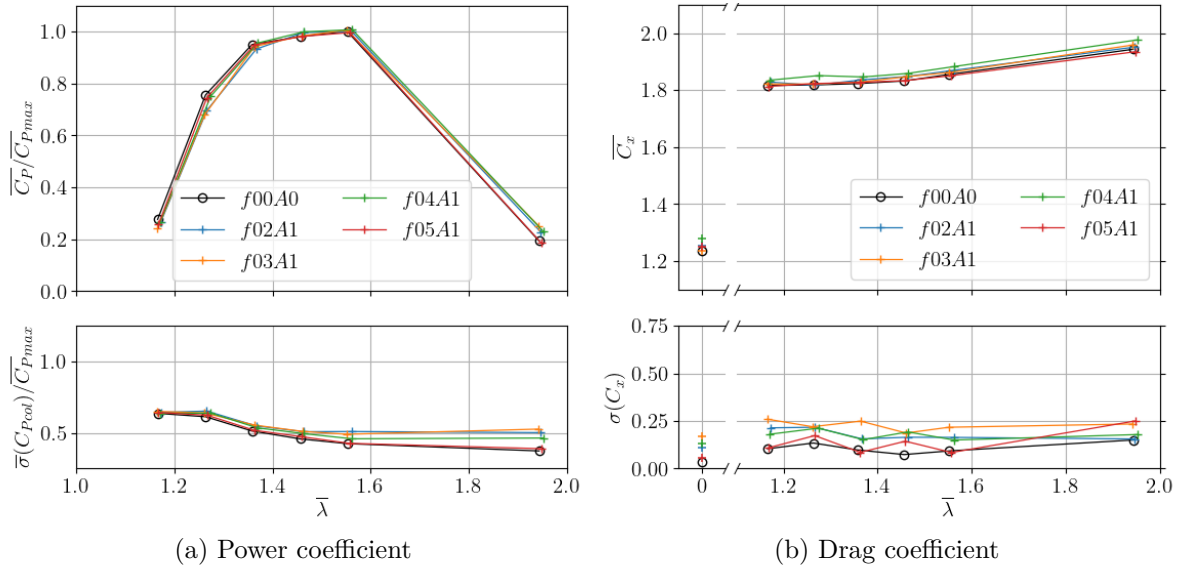


Figure 4.38 – Power (a) and drag (b) coefficients with the average at the top and standard deviation at the bottom of each sub-figure. The C_P are normalised by the maximal average value in the $f00.A0$ case (without waves).

on the static structure before addressing the interaction with the turbine in operation.

Parked turbine

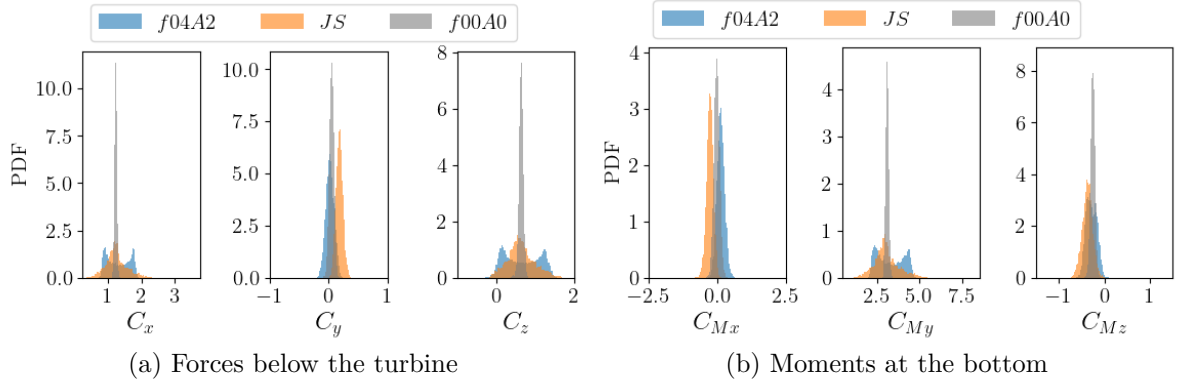


Figure 4.39 – Probability Density Functions of the load coefficients at λ_0 computed without waves, with regular waves and with irregular waves of the same characteristic amplitude and frequency.

The waves direction is collinear with the current direction, which causes additional velocity fluctuation in the streamwise and the vertical direction (Figure 4.33). Therefore, the ranges of C_x , C_z and C_{M_y} between the first and the last percentile (p99-p01) are strongly extended in presence of surface waves (Figure 4.39). Indeed, the three load ranges are 5.7 to 6.7 times higher in $f04.A2$ at λ_0 than without waves (Table 4.4). That range increase goes along with extreme values breaking by +40 % for C_x and C_{M_y} and by +87 % for C_z in $f04.A2$ compared to $f00.A0$. Those results are critical for the

Table 4.4 – Load range (p99 – p01) and extreme value ($\max[\text{abs}(p01), \text{abs}(p99)]$) ratios between the cases with waves and the case $f00A0$ without waves at λ_0 .

(a) Ratio of load ranges				(b) Ratio of extreme loads			
Case	C_x	C_z	C_{My}	Case	C_x	C_z	C_{My}
$f04A2/f00A0$	6.68	5.72	6.22	$f04A2/f00A0$	1.41	1.87	1.38
$JS/f00A0$	9.58	5.87	8.81	$JS/f00A0$	1.76	1.96	1.49

structural design both in terms of fatigue and ultimate limit. On the other hand, the waves collinear with the current barely modify the transverse velocity v , so the 3 other load components are less affected by the presence of those surface waves. Furthermore, we notice that the C_x and C_{My} ranges are more than 40 % higher in irregular waves than in regular ones, although Figure 4.36 revealed higher standard deviations with the regular wave case. That result is due to the load distribution difference between the regular wave case, with 2 PDF modes, and the irregular wave case, with a single PDF mode. The difference of load distribution mimics the difference of velocity distribution between the two cases (Figure 4.35), which indicates a strong correlation between the wave-induced velocity fluctuation and the load fluctuation.

Fig. 4.40 (a) presents the cross-correlation coefficients (\mathcal{R}) of the surface elevation measurement above the 2-VATT with a rotor column torque and with the whole 2-VATT drag and lift forces in the $f04A2$ case. The extreme cross-correlation coefficients are almost ± 1 for F_x and F_z , and \mathcal{R} is close from ± 0.8 for the torque, which already quantifies the strong impact of the surface waves on the loads and rotor torque fluctuation. The interpretation of the time lags at which \mathcal{R} is maximum or minimum is not straightforward however and requires to get back to the linear wave theory. As presented in the section 4.3.2.3, in this wave against current case, the streamwise orbital velocity (u_η) is in phase opposition with the surface elevation while the vertical one (w_η) (and so the pitch angle between the velocity and the turbine) is $\pi/2$ out of phase (Fig. 4.34), ie. a quarter of the wave period ($Tp/4 = 0.625$ s in $f04A2$). Assuming that the fluctuation of the rotor torque Q and F_x is mainly caused by the fluctuation of u and that the one of F_z can be mainly attributed to the fluctuation of w , we expect F_x and Q to be in phase with u_η (and so in phase opposition with η) while F_z would be in phase with w_η (and so $\pi/2$ out of phase with η). That assumption is valid for Q as a minimum of $\mathcal{R}(\eta, Q)$ occurs with zero time lag, meaning that a crest of η generates a trough of Q without lag, similarly to u_η . The two maxima at $Tp/2 = \pm 1.25$ s reveal the maxima of Q generated by the surface elevation trough. That perfect phase opposition between η and Q is also observed in the wave phase-averaged graphs (Fig. 4.40 (b)). In contrast, the minimum of $\mathcal{R}(\eta, F_x)$ expected with a 0 s lag, and the maximum of $\mathcal{R}(\eta, F_z)$ expected with a $Tp/4 = 0.625$ s lag, appear with a ~ 0.35 s lag compared to the expected values. That lag is also observed in Fig. 4.40 (b) as the wave phase averages of the fluctuating C_x and C_z are about $-\pi/4 = -45^\circ$ shifted compared to the relative phase of u and w with regard to η (Fig. 4.34). Phase shifts from -5 to -80° between the surface elevation and the drag force were also observed by Martinez et al. (2020) on a HATT. Those results mean that the force extrema (crest or trough) occur before the surface elevation extrema and so before the orbital velocity extrema, as it was demonstrated regarding the force exerted

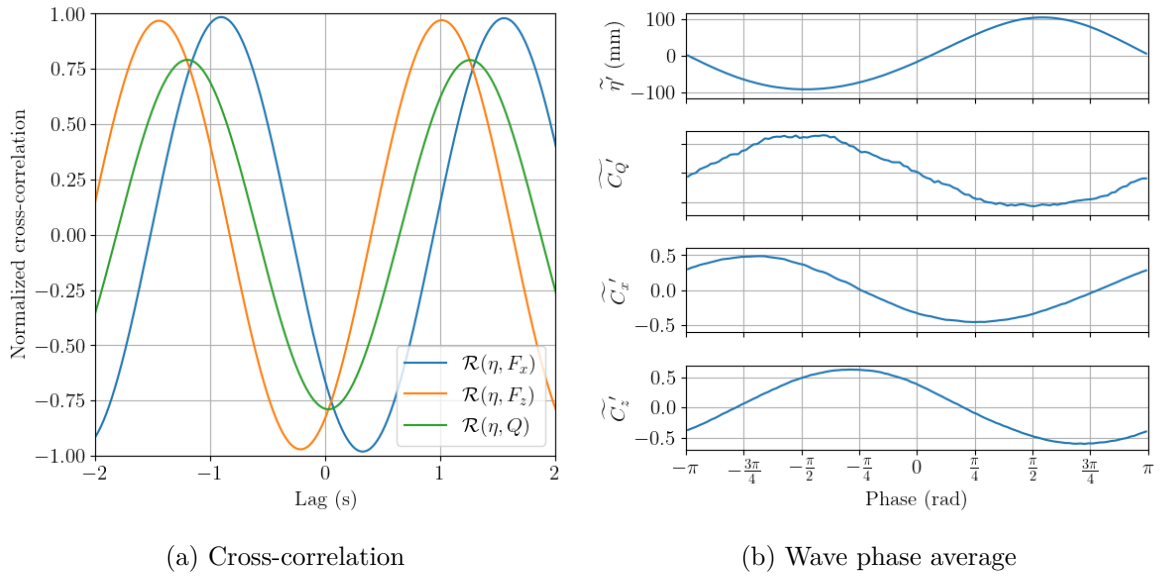


Figure 4.40 – In the case *f04A2* with the rotors parked, (a) the cross-correlations of the surface elevation with the torque of a rotor column, the drag and the lift forces on the turbine, and (b) the surface elevation, the torque coefficient of a rotor column, the drag and the lift coefficients averaged according to the surface elevation phase.

by surface waves on piles by Morison et al. (1950). According to the later, the phase shift increases with the pile diameter relatively to the water depth. Therefore, the small blade size relatively to water depth, by opposition to the large size of the whole 2-VATT, may explain the absence of such a phase shift on the rotor torque Q while it is observed on the whole turbine loads.

Operating turbine

To look at the combination of the wave-induced loads with the rotors rotation-induced loads, Fig. 4.41 presents the loads PDF with the turbine operating at λ_{opt} and λ_0 when subjected to the regular waves *f04A2*. The results show that C_z is unaffected by the rotors rotation as its distribution is the same whether with parked or operating rotors. C_x and C_{My} appear to be shifted in average due to rotors thrust and their distribution are slightly widened but they remain with 2 modes at λ_{opt} like at λ_0 . However, the distribution of C_y and C_{Mx} shows 2 modes at λ_{opt} whereas these were made of a single mode at λ_0 . That C_y and C_{Mx} bimodal distribution was already observed without waves and was supposed to be due to the asymmetrical thrust of the two rotor columns when their angular position is asymmetrical (Moreau et al., 2023a). Therefore, the loads PDF at λ_{opt} present a combination of the wave-induced characteristic distribution (on C_x and C_{My}) and of the rotor-induced one (on C_y and C_{Mx}) without showing clear interaction between the two. Similarly, the cross-correlations of the surface elevation with a rotor column torque and with the turbine drag and lift forces, and their phase average results are barely affected by the rotors operation. We only observe a reduction of $\mathcal{R}(\eta, Q)$ extrema to less than ± 0.7 with a slight time lag that could indicate the appearance of some added mass effects on the rotating rotors compared to the case with parked rotors.

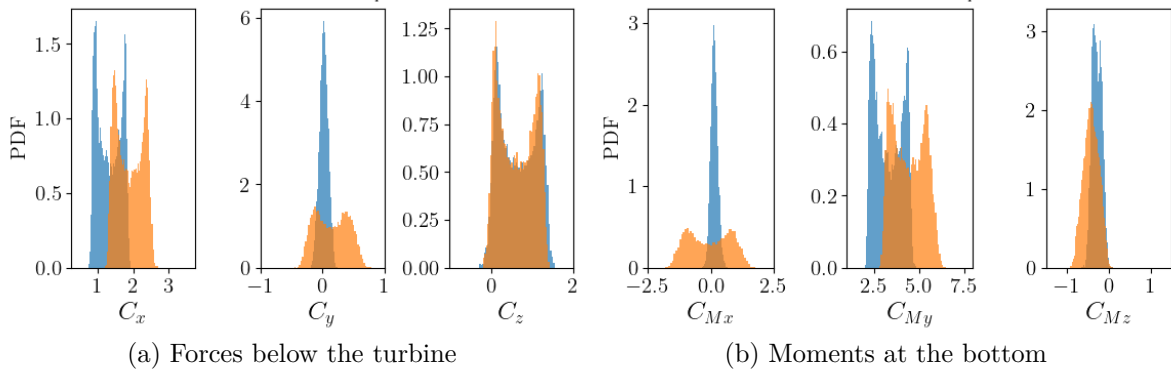


Figure 4.41 – Probability Density Functions of the load coefficients in $f04A2$ when the 2-VATT rotors are parked (blue) against when they operate at λ_{opt} (orange).

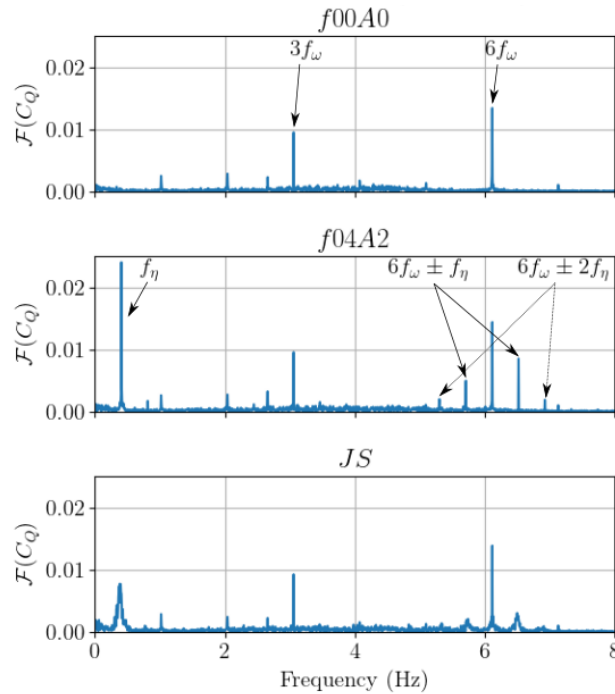


Figure 4.42 – Fourier transform of the torque coefficient of one rotor column without waves (top), with regular waves $f04A2$ (middle) and with irregular waves JS (bottom).

The Fourier transform (\mathcal{F}) of one rotor column torque in the case without waves $f00A0$, with regular waves $f04A2$ and with irregular waves JS gives a better insight into the origin of the increased load fluctuation in presence of surface waves and the wave-rotation interaction (Fig. 4.42). First, without waves, the torque spectral content is mainly located at 3 and 6 times the rotational frequency (f_ω), that corresponds to the blade passing frequency since the rotor columns are made of two levels of out-of-phase 3 bladed rotors. When adding surface waves to the current, those rotor-induced spectral peaks are unchanged but other peaks raise. A strong peak appears at the wave frequency (f_η) both with regular and irregular waves on the Fourier transform of the torque, as well as on the loads Fourier transform, similarly to the results on HATT (Gaurier et al., 2013; Martinez et al., 2018; Draycott et al., 2020). With regular waves,

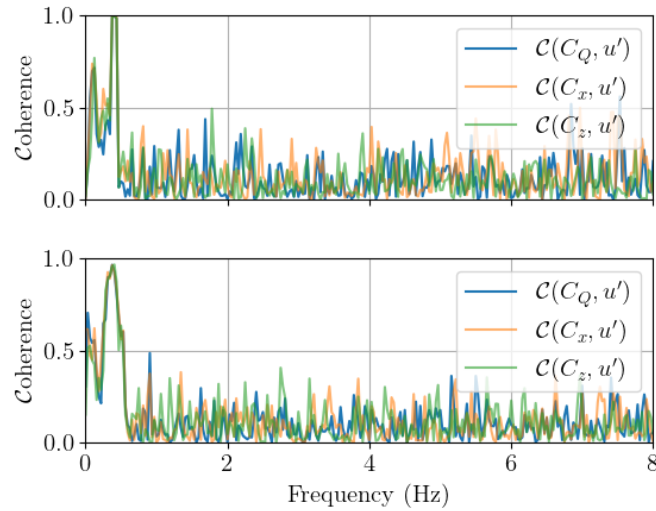


Figure 4.43 – Coherence function of the torque coefficient of one rotor column, the drag and lift coefficients of the 2-VATT at λ_{opt} with the upstream streamwise velocity measurement at $x = -6H$ in regular waves *f04A2* (top) and irregular waves *JS* (bottom).

the peak at f_η dominates the rotor-induced peaks in $\mathcal{F}(C_Q)$ whereas the peaks at 3 and $6f_\omega$ remain the highest with irregular waves. Both in the regular and irregular wave cases, the coherence function between the upstream velocity measurement and the torque, the drag and the lift force reaches almost 1 around f_η , meaning that the torque and loads spectral content at that frequency is fully due to the wave-induced orbital velocity (Fig. 4.43). Those coherence functions also reveal that the 2-VATT responds to the whole wave spectrum width in the irregular wave case as the three coherences exceed 0.5 from 0.25 to 0.55 Hz. Finally, in addition to the strong peak at f_η in the torque Fourier transform, additional peaks appears at $6f_\omega \pm kf_\eta$, with $k = 1$ and 2, both with regular and irregular waves. Those peaks evidence the interaction between the periodical loadings induced by the surface waves and those induced by the rotor columns rotation. Similar peaks combining the turbine rotational frequency harmonics and the wave frequency have also been observed on horizontal axis tidal turbines by Draycott et al. (2020). These are explained by a rotational sampling of the waves by the turbine blades that do several rotations during one wave period.

4.3.4 Conclusion

While numerous studies analysed the effect of surface waves on horizontal axis tidal turbines, only a few considered vertical axis ones, in limited wave and operating conditions, and none considered twin vertical axis tidal turbines (2-VATT). In this paper, we tested a 1/20 scale bottom mounted and ducted 2-VATT, similar to HydroQuest’s 1 MW-rated demonstrator, in a larger range of wave and operating conditions compared to the previous studies on vertical axis turbines. Seven wave conditions are presented to assess independently the effect of the waves amplitude and their frequency as well as to compare the effect of regular and irregular waves on the turbine behaviour.

The results show that the maximal average power coefficient is unaffected by the presence of waves, although the power curve may be slightly shifted towards higher

tip speed ratios. The average hydrodynamic loads on the turbine increase with the regular wave amplitude but they remain less than 5 % higher than without waves. The effect of the waves on the power and loads fluctuation is much more important. The standard deviation of the power, the drag and the lift follow a linear trend with a slope of 2, 3 and 4 respectively with regard to the wave amplitude. However, the too low wave amplitude of the variable-frequency cases prevented us from highlighting the wave frequency influence on the turbine behaviour. Looking in more detail at the effect of the intermediate frequency and amplitude wave case, we find that the drag, lift and pitching moment distribution ranges are extended up to 6.7 times greater, and that the extreme values are exceeded by 40 to 90 % with the regular waves compared to the conditions with current only. The rotor torque and load fluctuation increase is highly correlated to the surface elevation and to the orbital velocity with a cross-correlation coefficient exceeding 0.75 and a coherence function exceeding 0.5 on all the wave spectrum bandwidth.

In addition, the 2-VATT response is similar in terms of average and standard deviation of the power and the loads between the regular and irregular wave cases of similar period and height. However, the streamwise load range is 1.4 times larger in irregular waves and the extreme values are exceeded compared to the regular wave case due to the load distribution shape difference, with a single mode in irregular waves and two in regular ones. Thus, testing vertical axis tidal turbine models in regular waves only is insufficient to accurately predict the wave-induced loads for the mechanical design of full-scale turbines operating at sea.

In the future, tests with several wave directions relatively to the current direction could extend the present study and improve the understanding of the ducted 2-VATT response to surface waves at sea. Furthermore, studying the effect of the surface waves on the turbine wake would also be of interest in the perspective of tidal turbine farm deployments.

4.3.5 Supplement: surface waves effect analysis extension

To start extending the wave effect analysis to other relative directions with regard to the current, we study some cases with waves following the current. The experimental setup and the instrumentation are the same as with opposing waves, apart from the position of the wave makers and absorber that is reversed between the tank inlet and outlet (Fig. 4.29). Although the period of the waves generated following the current is shorter than that with the opposing waves, the following regular wave case "f06A2 fo." ($A_\eta \simeq 60$ mm, $Tp = 1.67$ s) has a wave length of the same order of magnitude as the opposing wave case "f04A2 op." due to the wave-current interaction (Magnier, 2023). The streamwise orbital velocity amplitude at the mid-turbine height is still about 40 % lower in f06A2 fo. than in f04A2 op.. Since the regular waves are not that regular when generating following waves (see 4.3.1), we chose to compare the effect of either following or opposing waves on the 2-VATT with irregular waves. Both irregular wave cases have a JONSWAP spectrum (with a peak enhancement factor $\gamma = 3.3$, according to Hasselmann et al. (1973)). The following wave case, noted JS fo., has similar significant wave height and peak period (Hs , Tp) as the regular wave case f06A2 fo.; and the opposing wave case, noted JS op., has a similar (Hs , Tp) as the f04A2 op. case (Fig. 4.30). Fig. 4.44 displays the probability density function (PDF) of the streamwise velocity measured by the 2C-LDV upstream the 2-VATT at $x = -6H$ and at the centre

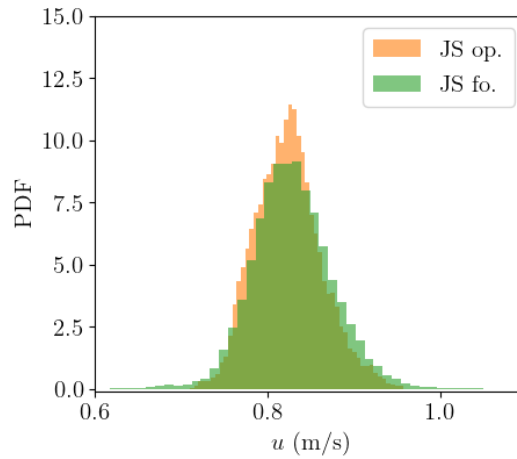


Figure 4.44 – Probability density function of the streamwise velocity measured by the 2C-LDV upstream the 2-VATT at $x = -6H$ and at the centre of the projected capture area, with following and opposing irregular waves.

of the projected capture area, in the following and opposing irregular wave cases. The distributions are pretty similar in the two cases with the same average velocity $\pm 0.003 \text{ m.s}^{-1}$. We still observe little differences as the PDF edges in JS fo. show wider extreme values with a low probability compared to the opposing wave case. That result may be due to the more than two times higher turbulence intensity in the following wave case ($\sim 5\%$) compared to the opposing wave case ($\sim 2\%$) at the mid-turbine height (Magnier, 2023).

Since we aimed at reproducing the Paimpol-Bréhat test site flow conditions, we tested the ducted 2-VATT model in the Flood tide Configuration (FC) with following waves and in the Ebb tide Configuration (EC) with opposing waves (Fig. 1.2). In the chapter 3, we showed that the evolution of the average and standard deviation of the power coefficient with regard to the tip speed ratio as well as the wake of the 2-VATT are different between those two relative flow directions. Therefore, the analysis of the relative wave direction effect on the response of the turbine is not straightforward. No significant difference appeared on the loads between FC and EC however, so we will focus on these to study the wave direction effect on the ducted 2-VATT. Fig. 4.45 displays the probability density function of the 3 load components affected by the surface waves with irregular waves opposing the current in EC or following it in FC. The data corresponds to measurements with the rotors operating close from λ_{opt} and with the two rotor columns angular position rather symmetrical. The results show that the extreme values, considered as the highest percentile value, are 13 to 19 % lower in JS fo. than in JS op. for the three load components. Similarly, the load ranges between the first and the last percentile are 30 to 35 % lower with following waves than with opposing ones. Since the velocity distributions are similar between JS op. and JS fo., it seems that the waves opposing the current impact more the load fluctuation than the following ones. However, the velocity measurement at $x = -6H$ might be a poor indicator of the velocity fluctuation perceived by the 2-VATT in the case of opposing waves. Indeed, that measurement position is downstream of the turbine from the surface waves point of view. Consequently, it could be that the measured orbital velocity amplitude is reduced compared to that between the wave makers and the turbine (Fig. 4.29).

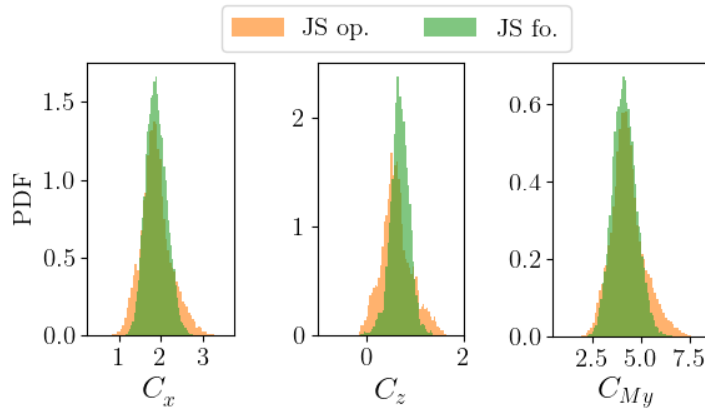


Figure 4.45 – Probability density functions of the 3 load components affected by the surface waves with the 2-VATT subjected to irregular waves either opposing the current in EC or following the current in FC. The rotors operate close from λ_{opt} with the two columns angular position rather in phase.

Finally, works are ongoing in the framework of Robin Linant’s master thesis under the supervision of Grégory Germain, in collaboration with the author, to characterise the surface wave effects on the wake of the ducted 2-VATT. The results will be presented in a near future.

To sum up, after having characterised the scale effects between reduced-scale tests in typical idealised flow conditions and full-scale tests at sea, the present chapter focused on studying the response of the reduced-scale ducted 2-VATT facing a more realistic flow complexity. Indeed, sea sites identified for potential tidal turbine installations are characterised by complex current conditions including vertically sheared velocity profiles, flow direction variability, turbulent flows and surface waves. The effect of these flow characteristics on the ducted 2-VATT behaviour were all analysed individually. In the next and last chapter, we draw up a synthesis of the reduced-scale model response in the whole flow condition diversity tested before concluding on the ability of reduced-scale experiments to predict the full-scale behaviour of such a device.

General discussion and prospects

Given the large diversity of the tested experimental configurations, from idealised conditions in the chapter 3 to more complex and realistic ones in the chapter 4, we start this concluding chapter by synthesising both the flow conditions in which we tested the reduced-scale ducted 2-VATT and the turbine response in terms of power performance and mechanical loads. That synthesis of the flow conditions influence provides additional material to extend the discussion started in 3.2 regarding the scale effects on the load fluctuation. Finally, a more general conclusion sums up all the results to answer the initial objectives of this three year-long work before opening up on the prospects.

5.1 Synthesis of the flow conditions influence

5.1.1 Tested flow conditions at reduced-scale

The ducted twin vertical axis tidal turbine (2-VATT) model was tested in many configurations to assess independently the effect of the flow direction, the vertical shear, the bathymetry-generated turbulence and the surface waves on its behaviour. The scheme in Fig. 5.1 displays the elements used to model all these conditions in the Ifremer's wave and current flume tank and to measure the turbine response, although they were never used simultaneously altogether. The orthogonal coordinates system (x, y, z) is fixed with x pointing downstream and z towards the free surface and with $x = 0$ at the 2-VATT centre and $z = 0$ at the tank bottom. The table 5.1 recaps the abbreviations used to refer to either one or the other of the flow configurations. In the following, when not specified, the grid at the test section inlet is the homogeneous one (G0) and the relative angle between the flow direction and the 2-VATT heading (α) is 0° .

To assess the effect of the flow direction and of the shear in steady flows, the wave-related apparatus and the bathymetry obstacles were absent from the experimental setup. With a homogeneous grid at the inlet, we can generate a uniform velocity field over the turbine capture area whereas with a variable grid porosity over the tank height

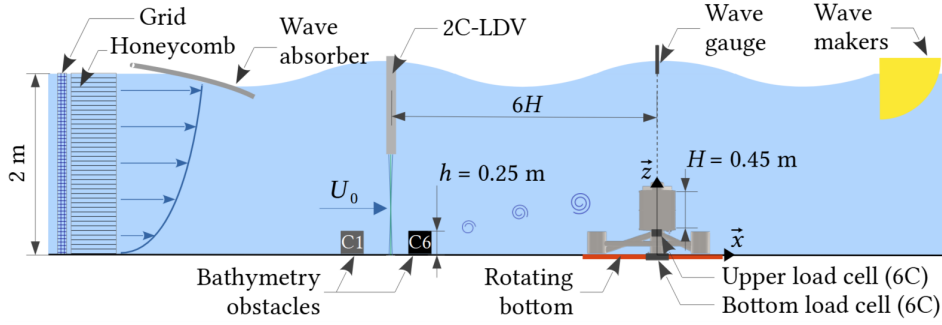


Figure 5.1 – Scheme of all the experimental setups gathered. Depending on the test cases, the wave makers and absorber, the bathymetry obstacles and the 2C-LDV could be removed.

Table 5.1 – Flow configuration abbreviations and symbols.

Label	Description
EC	Ebb tide Configuration (Fig. 1.2)
FC	Flood tide Configuration (Fig. 1.2)
G0	Homogeneous grid providing a uniform velocity field
G1	Grid arrangement providing a vertically sheared velocity field
α	Relative angle between the flow direction and the 2-VATT heading
$f00A0$	G0 with the wave absorber and wave makers immersed for waves against current but inactive, in EC
$f04A2$	Regular waves propagating against the current ($f_\eta = 0.4$ Hz, $A_\eta \simeq 100$ mm), in EC
JS op.	Waves with a Jonswap Spectrum opposing the current direction ($f_\eta = 0.4$ Hz, $A_\eta \simeq 110$ mm), in EC
C6	Wide bathymetry obstacle ($h \times 6h \times h$) placed either at (@) 10 or 16 h upstream the 2-VATT
C1C6	Combined bathymetry obstacles ($h \times h \times h$ in front of $h \times 6h \times h$) either at (@) 10 or 16 h upstream the 2-VATT

(G1), we manage to generate a vertically sheared incident flow. We tested the 2-VATT in the flood and the ebb tide configurations (FC and EC, respectively) with both G0 (in part 3.1) and G1 (in part 4.1). The turbine was also tested with $\pm 7^\circ$ and $\pm 15^\circ$ relative misalignment angles between its heading and the flow direction, both around the reference FC and EC at $\alpha = 0^\circ$ (in part 4.1). In all these configurations, the tank operated at a current velocity setpoint of $1 \text{ m}\cdot\text{s}^{-1}$. The 2-Component Laser Doppler Velocimeter (2C-LDV) measured the far upstream velocity at $x = -6H$, at the centre of the projected capture area, ie. $(y, z) = (0, 0.505) \text{ m}$. We found that this upstream distance is outside the 2-VATT induction zone in the section 3.1.2.2. The power weighted average of the streamwise velocity at this position is noted U_0 and is considered as the reference velocity for the hydrodynamic coefficients computation. Using the same experimental setup, we also tested the 2-VATT at multiple velocity setpoints between 0.8 and $1.8 \text{ m}\cdot\text{s}^{-1}$ to assess the effect of the Reynolds number with G0 and $\alpha = 0^\circ$.

In addition, we studied the influence of surface waves on the behaviour of the ducted

2-VATT model in wave-current conditions similar to those met at the Paimpol-Bréhat test site (in part 4.3). Waves propagating against the current were generated with the turbine in EC and waves following the current with the turbine in FC. In the first configuration, the wave makers are placed downstream of the test section and the wave absorber upstream, like in Fig. 5.1, and vice versa for the following waves. A wave gauge was placed above the 2-VATT to measure the free surface elevation (η) and the 2C-LDV was placed at the same position as in steady flows to measure the far upstream velocity synchronously with the turbine-related signals. The inlet was conditioned with the homogeneous grid G0 and the current velocity setpoint was 0.8 m.s⁻¹, which is the maximum capacity with the wave apparatus immersed. The 2-VATT was tested facing many wave conditions (Fig. 4.31) to assess the effect of the waves' amplitude and frequency in regular waves. The effect of irregular waves with a JONSWAP spectrum compared to that of regular waves with similar significant wave amplitude (A_η) and peak frequency (f_η , or period Tp) was also considered. Due to the wave-current interaction, the waves following the current are limited to quite low periods while the waves against current match the full-scale conditions according to the Froude similitude with a geometric scale factor of 1/20. In the present synthesis, we compare the turbine behaviour in the conditions where the wave absorber and wave makers are immersed but inactive (*f00A0*) to the regular wave case *f04A2* opposing the current with $f_\eta = 0.4$ Hz and $A_\eta \simeq 100$ mm and to the irregular waves with a JONSWAP Spectrum (JS op.) with a similar peak frequency and significant amplitude.

Finally, we tested the ducted 2-VATT model both in FC and EC with bathymetry obstacles placed on the tank bottom upstream while the inlet was conditioned with G0 (in part 4.2 and appendix A). Two obstacle combinations were considered: either a single square cylinder of base $h \times h$ and width $6h$, with $h = 250$ mm, referred to as C6, or a combination of that square cylinder with a cube of side h placed $2h$ upstream C6 at the centre of the tank, referred to as C1C6 (Fig. A.2). A relative distance of $10h$ and $16h$ between the C6 centre and the 2-VATT centre was tested for both the C6 and C1C6 configurations. In that experimental setup, unlike the previous ones, the 2C-LDV (and the 3C-LDV) was placed at $x = -1H$, right in front of the 2-VATT to measure simultaneously the current velocity fluctuation and the turbine response. The tank operated at a current velocity setpoint of 1 m.s⁻¹, similarly to the reference cases in steady flow.

To provide an overview of the flow conditions in all the test cases mentioned before, Fig. 5.2 shows the streamwise average velocity and turbulence intensity in G0, G1, *f00A0* and C6@10*h*. The average velocity profile is uniform over the 2-VATT height in G0 and in *f00A0* with a low level of turbulence intensity (below 2 %). Note that the streamwise velocity profiles are similar to *f00A0* over the 2-VATT capture height with surface waves opposing the current (Fig. 4.32). G1 provides a sheared average velocity profile that follows a power law similar to those at sea ($\bar{u}(z) = 1.2(z/H_w)^{1/7.9}$) (Furgerot et al., 2018), with a low level of turbulence intensity like the two previous conditions. With G0, G1 and waves, the flow conditions are homogeneous over the tank width with negligible transverse velocities. However, the flow characteristics are fully 3-dimensional with significant transverse velocities in the wake of the bathymetry obstacles placed upstream of the turbine (Fig. 4.19). A single profile is displayed in Fig. 5.2 at $y = W/4$, the lateral position of the rotor axis, to highlight the strong average velocity shear and turbulence intensity over the turbine height in C6@10*h*.

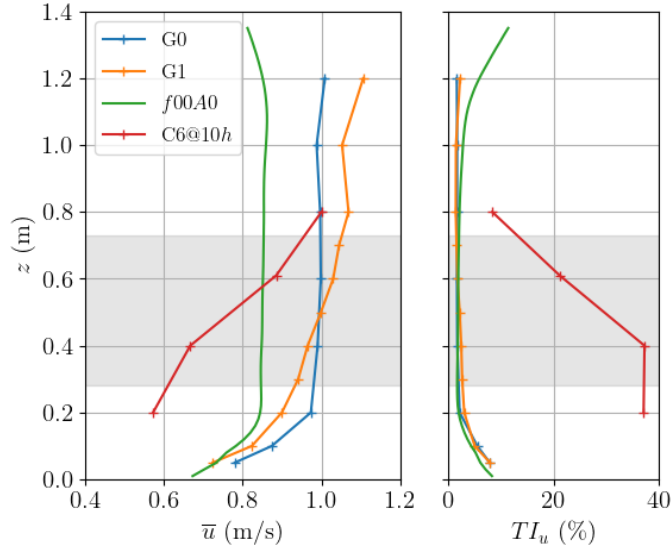


Figure 5.2 – Vertical profiles of the average streamwise velocity (left) and of the turbulence intensity (right) at the 2-VATT location. The data in G0, G1 and C6 are from 3C-LDV measurements whereas the data in $f00A0$ is particle image velocimetry from (Magnier, 2023). The profile C6 is at $y = W/4$ (rotor axis lateral position), the others are at $y = 0$. The grey shade represents the 2-VATT capture height.

Another important feature of the flow past the bathymetry obstacles is the presence of coherent flow structures at a shedding frequency about 0.25 Hz with a characteristic size about half the ducted 2-VATT width in the wake of C6 (Ikhennicheu et al., 2019b). Furthermore, in G0 and G1 like in $f00A0$, the streamwise velocity Probability Density Function (PDF) is centred on the average velocity U_0 with a single mode and a narrow velocity range (Fig. 5.3). With regular waves, the periodical orbital velocities increase the velocity range and generate two PDF modes. The amplitude of the streamwise orbital velocity is about $0.09U_0$ in $f04A2$. With irregular waves JS op., the PDF shows a single mode centred on U_0 again and a range between the first and the last velocity percentile that exceeds that of $f04A2$ by about 10 %. Finally, the velocity distribution in the wake of the bathymetry obstacle C6 shows a single mode at U_0 and a wide velocity range with a low probability due to the turbulence in the obstacle wake.

5.1.2 Flow condition influence on the turbine behaviour

On the power performance

Without bathymetry-generated turbulence nor surface waves, the maximal average power coefficient and the optimal tip speed ratio (λ_{opt}) are about 5 % lower in EC than in FC (Fig. 5.4). This result is completely due to the difference of rotor column relative counter-rotation direction between FC and EC, and not to the base geometrical asymmetry. In the reference condition with aligned uniform flow, the power coefficient standard deviation is 35 % higher at λ_{opt} in EC than in FC mostly due to the base geometry as the flow accelerates around the base feet, which are in front of the bottom rotors in EC against in front of the central fairing in FC. As a consequence, a torque

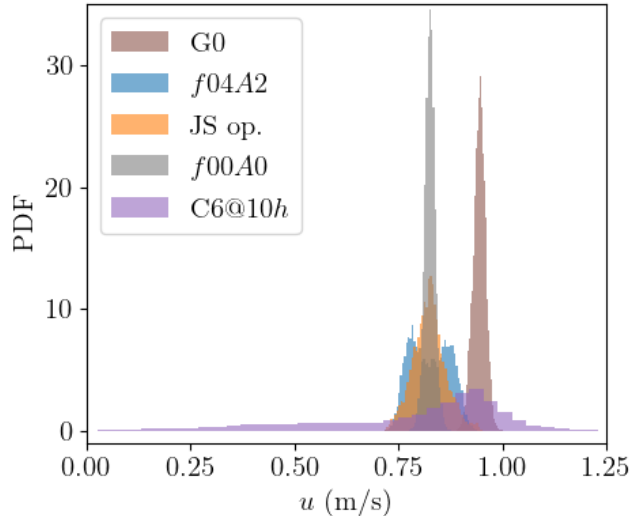


Figure 5.3 – Probability Density Function (PDF) of the streamwise velocity measured with the 2C-LDV at $(x, y, z) = (-6H, 0, 0.505\text{m})$ in front of the 2-VATT except for C6@10h whose measurement is with the 3C-LDV prior the turbine installation at $(x, y, z) = (-1H, 0, 0.610\text{m})$.

generation asymmetry occurs between the lower and the upper rotors in EC that leads to higher power coefficient fluctuation than in FC. Besides, in the limits of the measurement repeatability, neither the vertically sheared velocity nor the flow misalignment affect significantly the overall average power performance of the ducted 2-VATT (Fig. 5.4). That being, we observed a growing asymmetry with α between the average power coefficient of each rotor column (Fig. 4.11), meaning that one rotor column is more loaded than the other one when operating with a misalignment angle. Furthermore, the rotor column torque distribution over the rotor angular position (Fig. 4.7) and the spectral analysis of the torque signal (Fig. 4.8) revealed torque amplitude asymmetry and phase shift between the upper and the lower rotors due to both local tip speed ratio and available kinetic energy differences in the vertically sheared flow. That results in an increase of the torque fluctuation in G1 compared to G0 and so to about 35 % higher power coefficient standard deviation in G1 than in G0, both in FC and EC at λ_{opt} . The flow misalignment also affects the torque angular distribution (Fig. 4.12), in a different way whether the relative angle is positive or negative, but we lack absolute angular position measurement and local flow visualisation in the vicinity of the blades to explain that observation.

Fig. 5.2 showed that the average streamwise velocity is lower in the unsteady flow configurations, either in the wake of bathymetry obstacles or in presence of surface waves, compared to the steady flow conditions. With $U_0 \simeq 1 \text{ m.s}^{-1}$, the Reynolds number based on the blade chord (Eq. 3.1) is about $Re_c = 1 \cdot 10^5$. Around this value, the foil lift and drag coefficients are dependent on the Reynolds number (Michna et al., 2022), and so does the rotor power performance (Fig. 3.28). Fig. 5.5 displays the evolution of the maximal average power coefficient with U_0 when the ducted 2-VATT operates in the idealised flow conditions. It shows about 20 % power performance loss between $U_0 = 1.0$ and 0.8 m.s^{-1} , which must be taken into account for the experimental cases comparison that follows.

In a first approach regarding the influence of the bathymetry obstacles, we compared

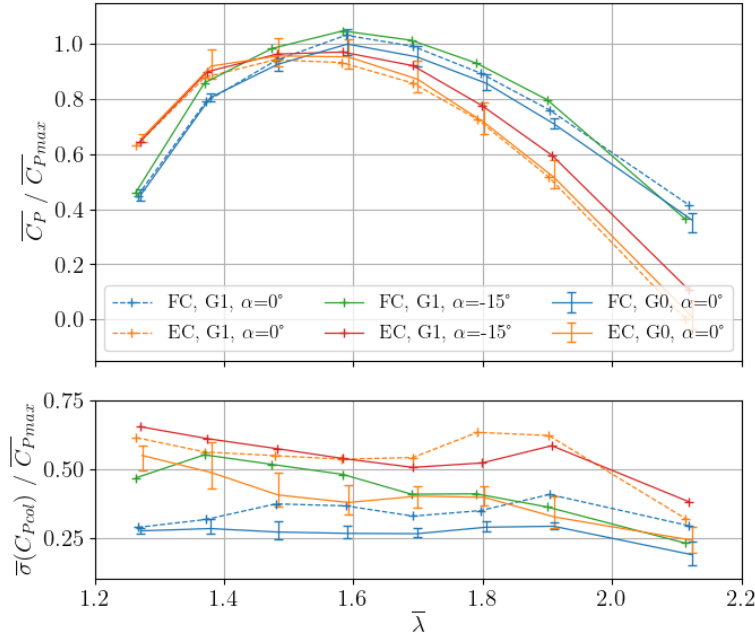


Figure 5.4 – Average (top) and standard deviation (bottom) of the power coefficient with regard to the tip speed ratio. The curves in the configuration G0 are averages over 3 test campaigns with the error bars representing the extreme average and extreme standard deviation values over the 3 campaigns. The C_P are normalised by the maximal average value in FC, G0, $\alpha = 0^\circ$.

the performance of the 2-VATT whether the bathymetry is flat or made of obstacles for a given far upstream velocity. We considered the same reference velocity value U_0 as in the reference case with G0 for all the cases since the tank operated at the same current velocity setpoint of $1 \text{ m}\cdot\text{s}^{-1}$. The average velocity and kinetic energy really seen by the 2-VATT are lower in the wake of the bathymetry obstacles though. Therefore, the optimal tip speed ratio is lower and the maximal average power coefficient is lower too compared to G0, up to 40 % in the worst configuration tested with C6@10h (Fig. A.6), with an evolution of $\overline{C_{P,max}}$ in relation to the turbine-obstacle distance that depends on the obstacle combinations. In addition, the sheared and turbulent flow in the wake of the bathymetry obstacles is responsible for up to 3 times higher power coefficient standard deviation at λ_{opt} in the worst configuration compared to G0 (Fig. 4.23). The Fourier transform of the torque signal reveals a higher peak at $3f_\omega$ than at $6f_\omega$, with f_ω the rotational frequency, which reveals a strong asymmetry between the two rotor levels due to the sheared flow, as well as a peak at the coherent flow structures shedding frequency in the wake of C6. When computing the power coefficients with the velocity averaged over the turbine capture area at the turbine location before its installation (U_S), similarly to a resource assessment, λ_{opt} is the same in C6@10h as in G0, and it is also the same as with U_0 in G0 (Fig. 4.23). Thus, U_S seems to be a good estimation of the velocity really perceived by the 2-VATT in operation. The average power coefficient remains 16 % lower in C6@10h compared to G0 when computed with U_S , which is a combined effect of the turbulent flow, whose velocity fluctuation increases the cubic power weighted average, and of the difference of Reynolds number (Fig. 5.5) as U_S is $0.96 \text{ m}\cdot\text{s}^{-1}$ in G0 against $0.82 \text{ m}\cdot\text{s}^{-1}$ in C6@10h. We further discuss the influence of the

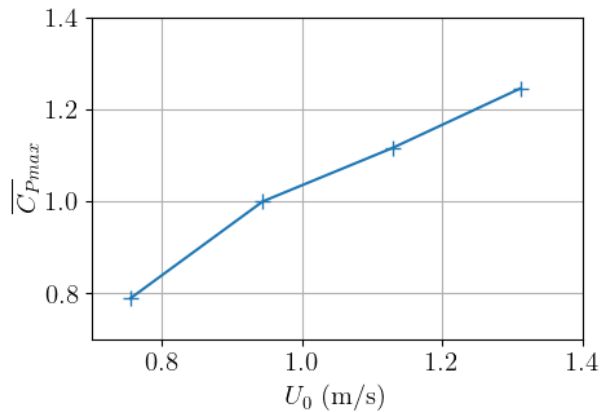


Figure 5.5 – Evolution of the normalised maximal average power coefficient with the far upstream average velocity measured by the 2C-LDV with the ducted 2-VATT model in FC, G0, $\alpha = 0^\circ$.

reference velocity measurement location on the performance assessment in the appendix B.

Finally, the average power coefficient is about 20 % lower with the inactive wave apparatus immersed to generate opposing waves (*f00A0*) than in G0 (Fig. 5.6), mostly due to the Reynolds number effect as U_0 is 0.95 m.s^{-1} in G0 against 0.83 m.s^{-1} in *f00A0*. When generating surface waves, the optimal tip speed ratio and the maximal average power coefficient are unchanged compared to *f00A0* but the power coefficient standard deviation increases by about 50 %, in the same way whether with the regular *f04A2* or the irregular JS op. wave cases (that have similar significant wave height and peak period). Besides, the power coefficient standard deviation increases quite linearly with the regular wave amplitude in the tested range at a 0.4 Hz peak frequency (Fig. 4.37). Those power fluctuation are directly due to the wave orbital velocity as the Fourier transform of a rotor column torque shows peaks at the wave frequency and at frequencies combining the rotor rotational one and the wave one (Fig. 4.42), and as the coherence function between the upstream velocity and the torque exceeds 0.5 on the whole wave frequency spectrum range (Fig. 4.43).

To sum up, first regarding the average power performance, neither the incident vertical velocity shear, the relative flow misalignment up to 15° nor the presence of surface waves affect the overall maximal power coefficient and the optimal tip speed ratio of the ducted 2-VATT model compared to the tests in the typical idealised flow condition. Thus, the experimental tests in idealised flow conditions are sufficient to asses the average power performance of such a 2-VATT. However, the flow misalignment causes a power generation asymmetry between the two rotor columns, meaning that the loads applied on a rotor column can be higher than what is measured in aligned flow conditions. Moreover, a rough bathymetry may generate severe velocity deficits locally compared to the theoretical potential of a given tidal energy site. This bathymetry effect must be considered carefully by tidal turbine developers both for turbine positioning to optimise the power output, and for velocity measurement positioning to correctly assess and monitor the power performance of the turbines. Then, all the tested flow conditions lead to an increase of the power fluctuation compared to the idealised flow condition with an aligned uniform flow in FC. A velocity shear over the rotor column height, either

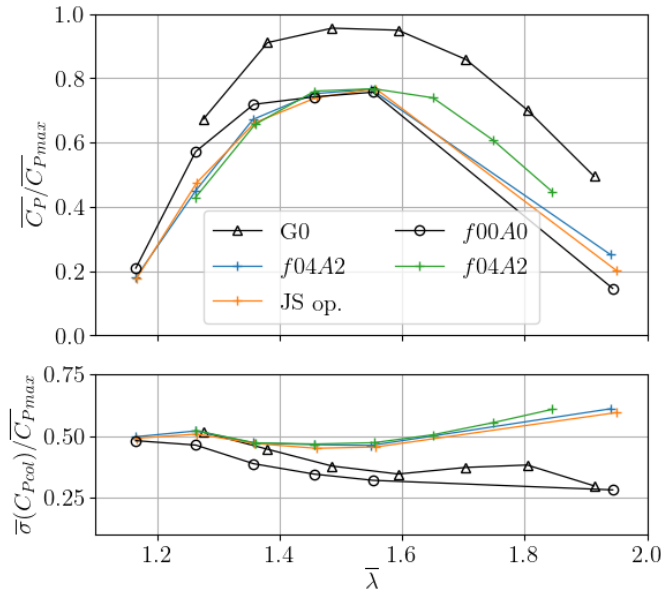


Figure 5.6 – Average and standard deviation of the power coefficient of the 2-VATT in EC at $\alpha = 0^\circ$ in G0 with $U_0 = 0.95 \text{ m.s}^{-1}$ and in wave conditions with $U_0 = 0.83 \text{ m.s}^{-1}$ (two *f04A2* data sets). The values are normalised by the reference maximal average value in FC, G0, $\alpha = 0^\circ$.

present in the incident flow or due to the base geometry, generates a tip speed ratio and a torque generation asymmetry between the upper and the lower rotors that affect the torque angular distribution and increase the power fluctuation by about 35 %. The flow misalignment also affects the torque angular distribution but further analyses are needed to understand the underlying physics. The power standard deviation increases with the surface wave amplitude due to the orbital velocity, by about 50 % in the intermediate opposing wave condition tested and up to + 70 % for the highest wave case. Finally, the presence of large bathymetry obstacles upstream of the ducted 2-VATT is responsible for the strongest power fluctuation with a power coefficient standard deviation of the order of its average. The spectral analysis of the torque signals revealed that this is due to the strong velocity shear and to the coherent flow structures shed in the wake of such obstacles. These torque and power fluctuations must be considered carefully at the turbine design stage for power output conditioning and for an appropriate structural design of the rotor columns. Indeed, beyond the power performance, tidal turbine developers also need to know the influence of the flow characteristics on the mechanical loads applied to the turbine to improve its design and reduce the damage risks.

On the mechanical loads

Key parameters for the structural design are the load distributions for fatigue stress assessment to ensure the turbine integrity over its whole life time and the extreme loads to ensure that the turbine will withstand extreme events without mechanical failure nor stability issue. As explained in 2.2.1, the device stability means avoiding the overturning around the gravity base axes, caused by extreme moments, and the sliding, caused by extreme horizontal forces and extreme vertical force that lighten the turbine apparent weight on the base.

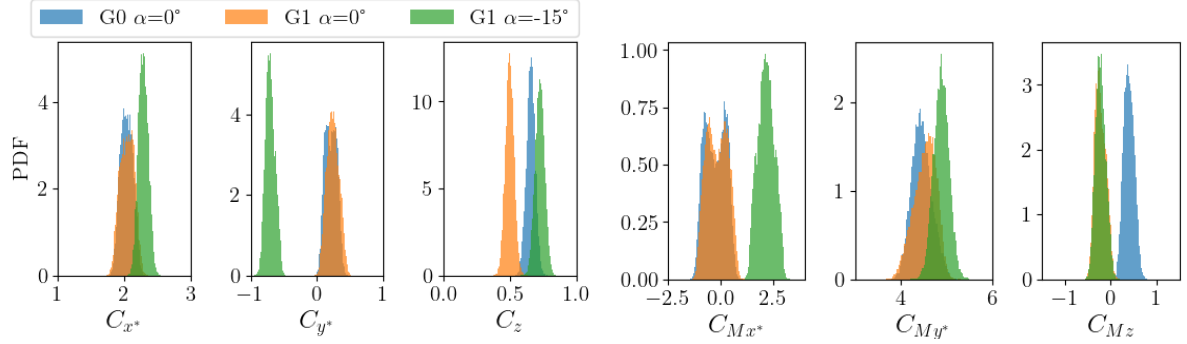


Figure 5.7 – Probability density functions of the 6 load components in the turbine coordinates system with the 2-VATT in FC in a uniform flow, a sheared flow and with a misalignment angle, close from λ_{opt} .

Typically, the streamwise force increases with the tip speed ratio whichever the flow condition, and we noticed that the Reynolds number barely affects the 2-VATT loads, unlike the power performance, as $\overline{C_x}$ rises by less than 5 % between $U_0 = 0.76$ and 1.69 m.s^{-1} (Fig. 3.29). Independently from the flow conditions, the load fluctuation is affected by the relative rotor columns phasing, generating either one or two probability density function modes and affecting the load ranges. The phased columns lead to the maximal range and value for C_x and C_{My} with two PDF modes and the minimal one for C_y and C_{Mx} with one PDF mode in aligned flow conditions (Fig. 4.26). The rotor columns phase opposition leads to the contrary. Given the model control at constant rotational speed, the columns phasing is random at the rotation start but is kept the same during the test run. Conversely, the control of the full-scale demonstrator was more flexible so the columns phasing varied along time and the situation with rotors out of phase was the most likely. Thus, in the following, we compare the loads PDF with the 2-VATT operating at λ between 1.4 and 1.6 (around λ_{opt}) and with the rotor columns rather out of phase. Besides, we analyse the loads in the orthogonal coordinates system (x^*, y^*, z) rotating with the 2-VATT around z when $\alpha \neq 0^\circ$, with x^* the turbine heading pointing downstream. That system is more relevant for the gravity base stability design than the fixed one. The force and moment coefficients are defined like before with the four rotors projected area as a reference surface. On one hand, the velocity vertical shear barely affects the load extremes along x^* and y^* (Fig. 5.7) but it reduces the C_z , which has a stabilising effect on the device regarding the sliding and the overturning. On the other hand, the turbine misalignment increases all the hydrodynamic coefficient extreme values compared to the aligned flow conditions (apart from C_{Mz}). The most impacted components are C_{y^*} and C_{Mx^*} whose absolute extreme values are both about 2.5 times higher with $\alpha = -15^\circ$ compared to 0° . The load ranges, for their part, are barely modified by the velocity shear nor the misalignment compared to the uniform and aligned flow condition.

In the turbulent wake of the wide bathymetry obstacle C6, the ducted 2-VATT streamwise and vertical load spectra are dominated by a peak at the coherent flow structures shedding frequency (Fig. 4.28). As expected, the turbulent flow is responsible for an extension of the six load component ranges compared to the steady flow conditions. The range between the first and the last percentile (p01 and p99 respectively) of the hydrodynamic coefficients computed with U_0 is 1.7 times higher is C6@10h

for C_{Mx^*} , 2.5 to 3.5 times higher for C_{x^*} , C_{y^*} , C_{My^*} and C_{Mz} , and up to 8.6 times higher for C_z . The extremes of the cross-flow loads are also exceeded by 30 to 60 % in C6@10h compared to the idealised flow conditions in G0 but the streamwise extreme loads C_{x^*} and C_{My^*} are 10 % lower as the average velocity deficit in the obstacle wake reduces their average value by ~ 25 %. In addition, the cross-correlation of the streamwise and the vertical force with the velocity measurements in front of the turbine showed that the C_{x^*} maxima, correlated with the u maxima, occur simultaneously with the C_z minima, correlated with the w minima, and vice versa (Fig. 4.27). Finally, the C_{x^*} and C_z spectral comparison between C6@10h and G0 also revealed that the load fluctuation is insensitive to turbulent structures with a characteristic length smaller than a third of the ducted 2-VATT height.

By opposition to the influence of the turbulence on all the 6 load components, the presence of surface waves only affects C_{x^*} , C_z and C_{My^*} while the three others are unchanged compared to the current only condition (Fig. 4.39). We noticed that the affected load PDF shapes is the same as that of the far upstream velocity both with regular and irregular waves (Fig. 4.35), showing the strong correlation between the orbital velocity induced by the surface waves and the loads applied to the turbine. Indeed, the cross-correlation coefficient between these loads and the free surface elevation is close from 1, and the coherence function between them and the upstream velocity measurement is higher than 0.5 on the whole wave frequency spectrum range. Similarly to the power coefficient, we find that the standard deviations of the affected load components increase linearly with the wave amplitude in regular waves. Besides, the load extreme values and ranges are larger in irregular waves than in regular ones of similar amplitude and period, although the C_{x^*} standard deviation is larger in *f04A2* than in JS op. due to the bimodal distribution. That bimodal PDF is specific to the regular periodic waves and is not representative of the random wave conditions at sea. Therefore, we recommend conducting tests in irregular waves to get more realistic load distribution inputs for the turbine fatigue stress design.

To sum up, the two rotor column phasing affects the load distributions, extending the load ranges and their extreme values when the columns are perfectly either in phase or in phase opposition. Apart from these specific situations, Tab. 5.2 and 5.3 recap the load ranges and extreme values with the rotor columns out of phase in some representative flow conditions, with maximal values in red and minimal ones in green. As expected, the turbulent wake of a bathymetry obstacle and the surface waves essentially condition the fatigue stress design as they are responsible for the six load components largest range, from 1.7 to 10 times larger than in the steady flow conditions. Those unsteady flow conditions also cause most of the load extreme values but the maximal transverse loads C_{y^*} and C_{Mx^*} occur when the 2-VATT operates with a misalignment angle of $\pm 15^\circ$. Therefore, the combination of a flow misalignment in the turbulent wake of a bathymetric protuberance with large surface waves and the two rotor columns in phase would provide the worst situation in terms of extreme loadings on the turbine. That situation causes 1.25 to 2.25 times higher extreme loads than in the reference idealised flow condition and was rightly considered as the ultimate limit state for the structural design of the full-scale prototype. Moreover, the streamwise loads C_{x^*} and C_{My^*} increase with the tip speed ratio, meaning that the extreme mechanical loads are likely to appear after a control failure causing the rotors to coast. Finally, the cross-correlation between the loads and the velocity measurements in front of the 2-VATT revealed that the

Table 5.2 – Loads range between the first and the last percentiles, depending on the flow condition, with the 2-VATT operating close from the optimal tip speed ratio and the rotor columns out of phase.

Flow condition	C_x^*	C_y^*	C_z	C_{Mx}^*	C_{My}^*	C_{Mz}
Idealised, $\alpha=0^\circ$, in FC	0.38	0.35	0.15	1.79	0.99	0.50
Sheared with $\alpha=0^\circ$, in FC	0.43	0.39	0.15	1.89	1.06	0.51
Sheared with $\alpha=-15^\circ$, in FC	0.59	0.25	0.16	0.82	1.71	0.42
Obstacle C6 at $10h$, $\alpha=0^\circ$, FC	1.06	1.03	1.31	2.98	2.43	1.69
Irregular opposing waves, $\alpha=0^\circ$, EC	1.71	0.64	1.52	1.91	3.92	0.76
Ratio of maximal value to idealised	4.47	2.94	9.96	1.67	3.95	3.40

Table 5.3 – Loads extreme (absolute value of the first or the last percentile whether the extreme value is negative or positive) depending on the flow condition, the 2-VATT operating close from the optimal tip speed ratio with the rotor columns out of phase.

Flow condition	C_x^*	C_y^*	C_z	C_{Mx}^*	C_{My}^*	C_{Mz}
Idealised, $\alpha=0^\circ$, in FC	2.23	0.39	0.73	1.16	4.98	0.66
Sheared with $\alpha=0^\circ$, in FC	2.25	0.44	0.58	1.12	5.00	0.46
Sheared with $\alpha=-15^\circ$, in FC	2.54	0.87	0.81	2.63	5.67	0.42
Obstacle C6 at $10h$, $\alpha=0^\circ$, FC	1.98	0.63	0.94	1.53	4.42	0.96
Irregular opposing waves, $\alpha=0^\circ$, EC	2.79	0.47	1.48	1.08	6.47	0.91
Ratio of maximal value to idealised	1.25	2.24	2.02	2.26	1.30	1.47

streamwise load maxima occur when the vertical load is minimal, and vice versa, in the bathymetry obstacle wake. Future works considering the whole flow complexity will have to define whether the 6 load extreme values may occur synchronously altogether or if some of the components cannot be maximal simultaneously, to eventually reduce the mechanical design criteria.

5.1.3 Scale effects discussion extension

In part 3.2, we found that the streamwise load fluctuation intensity (FI , ratio of the standard deviation to the mean of a signal) is about two times lower in the typical idealised reduced-scale experiments than in the full-scale results at sea, and that the difference of rotor control law would lead to larger torque fluctuation intensity and a lower rotational speed FI at reduced-scale. To extend that discussion, Tab. 5.4 gives the fluctuation intensity of the streamwise load on the ducted 2-VATT as well as of a rotor column torque and its rotational speed for the prototype and the reduced-scale model in some representative flow conditions among the tested ones. As recalled in the previous synthesis, the experimental tests in a vertically sheared current, as it is the case at sea, leads to a power coefficient standard deviation increase by 35 % compared to the tests in the idealised uniform current. That power fluctuation increase appears to the same extent on the rotor column torque fluctuation intensity as it reaches 0.35 in the aligned sheared condition and 0.42 with a 15° misalignment against 0.26 in the idealised uniform condition. Thus, when the reduced-scale experimental flow conditions get closer

Table 5.4 – Fluctuation intensity of the streamwise load on the ducted 2-VATT, of a rotor column torque and rotational speed depending on the flow condition, with the 2-VATT model operating close from the optimal tip speed ratio. The first line is the result at sea and the others are from the reduced-scale experiments.

Flow condition	F_x^*	Q	ω
Prototype in calm sea states	0.16	0.18	0.09
Exp. idealised, $U_0 = 1 \text{ m.s}^{-1}$, $\alpha = 0^\circ$, FC	0.08	0.26	0.00
Exp. sheared with $\alpha = 0^\circ$, FC	0.05	0.35	0.01
Exp. sheared with $\alpha = -15^\circ$, FC	0.07	0.42	0.01
Exp. obstacle C6 at $10h$, $\alpha = 0^\circ$, FC	0.15	1.43	0.01
Exp. irregular waves against, $\alpha = 0^\circ$, EC	0.19	0.54	0.00

to the full-scale in-situ ones, although still weakly turbulent, the torque fluctuation intensity appears more than two times higher on the model than on the prototype, while the rotational speed fluctuation intensity is barely affected by the flow conditions at reduced-scale. That result agrees with the discussion in part 3.2 regarding the control law difference between the reduced-scale model and the full-scale prototype. It highlights again the need to use more realistic rotor control laws at reduced-scale to accurately predict the instantaneous rotor loads.

Furthermore, $FI(F_x)$ is doubled in the turbulent wake of the bathymetry obstacle compared to the steady conditions. It reaches similar values to what was measured on the full-scale prototype operating in calm sea conditions (ie. without waves). Thereby, testing the reduced-scale model in turbulent flow conditions rather than in steady ones seems to provide a better prediction of the full-scale prototype streamwise load fluctuation intensity without surface waves. However, the average of the turbulence intensity over the turbine capture area is about 27 % in the wake of the bathymetry obstacle C6 while it is between 10 and 20 % at the Paimpol-Bréhat test site. Supposing the turbulence to be the main streamwise load fluctuation source in absence of surface waves, we would expect larger $FI(F_x)$ in the experiment downstream of the bathymetry obstacle than in the operation at sea. Thus, $FI(F_x)$ may still remain underestimated to a certain extent that will have to be quantified to keep improving the load assessment for the structural design of the full-scale turbines. On the other hand, the large surface waves in the reduced-scale experiment result in a 2 to 3 times higher streamwise load fluctuation intensity, which is in agreement with the influence of the surface waves on the full-scale prototype in-situ.

5.2 General conclusion

Several tidal stream energy prototypes have been tested around the world over the past decade to help diversifying the energy production system with low greenhouse gas emitting systems. Among them, the first 1 MW-rated ducted twin vertical axis tidal turbine (2-VATT) developed by HydroQuest was tested from 2019 to 2021 at the Paimpol-Bréhat test site, off the northern coast of Brittany, France. The power performance and the mechanical loading predictions are the starting point for the development of such industrial projects. To refine those predictions, we need to better characterise

the scale effects, from reduced-scale experiments to full-scale operation, and to better understand the flow conditions influence on the turbine behaviour. Indeed, the tidal currents are characterised by complex flow conditions, mainly due to their directional variability, to the vertical shear of the velocity, to the bathymetry-generated turbulence and to the presence of surface waves. Thus, the ducted 2-VATT power and loading prediction improvement can only be achieved by comparing the prototype behaviour at sea to the one of a scaled model in a large diversity of controlled flow conditions.

For that purpose, the first chapter of the thesis started with the description of the full-scale ducted 2-VATT prototype and of the flow characteristics at the Paimpol-Bréhat offshore test site. We analysed the prototype power performance and streamwise loading after that, with a focus on the influence of the sea states on its response. Using two dedicated acoustic Doppler current profiler measurement campaigns, we assessed the evolution of each rotor column average power coefficient with the tip speed ratio and the average drag coefficient of the whole ducted 2-VATT in operation. We observed power and drag coefficient differences between the two campaigns that are partly, but not fully, due to a difference of operational tip speed ratio. We assume the flow spatial variability to cause the additional difference as it would lead to a difference of reference upstream velocity depending on the measuring instrument location. We also suppose a flow direction effect on the relative power performance difference between the ebb and the flood tides, on one hand, and between the two rotor columns, on the other hand. In addition, we found that the presence of surface waves (with a significant wave height higher than 2 m and a peak period higher than 10 s) increases the fluctuation intensities (ratio of the standard deviation to the average of a signal) of the rotational speed, the torque and the drag force by a factor close to 3 compared to the cases in calm sea state, while not significantly impacting the average values. Finally, we presented some velocity deficit in the prototype wake, but the measurement setup was inappropriate to characterise the wake decently as it was not dedicated to that purpose.

Next, we described the 1/20 scale model of the prototype that we tested in many controlled flow conditions in the Ifremer's wave and current flume tank. In the chapter 3, we focused on the typical idealised experimental flow conditions with a flow direction aligned with the turbine heading, a uniform velocity profile upstream, a low turbulence intensity and no surface waves. We studied the model power performance and the loads when it operates in the ebb or flood tide configurations (EC or FC, respectively) with two turbine base geometries at several upstream velocity magnitudes from 0.8 to 1.7 m.s⁻¹. We observed a ~ 5 % lower optimal tip speed ratio and maximal power coefficient in EC than in FC, due to the inversion of the two rotor columns relative counter rotation direction, which can explain part of the power curve difference observed at sea between the ebb and the flood tides. The drag coefficient, on the other hand, appeared unaffected by the relative flow direction. We also took the advantage of the reduced-scale experiments to measure the flow field surrounding the ducted 2-VATT, which is essential for tidal turbine farm developments. The induction zone upstream extends up to six turbine height in FC with a tripod base similar to the one of the prototype. Besides, the wake geometry is clearly affected by the difference of relative counter rotation direction of the two rotor columns between EC and FC as well as by the asymmetrical base geometry. Indeed, the velocity deficit recovers 30 % faster in FC than in EC with a tripod base, and even 20 % faster with a simple monopile base compared to the tripod, in FC.

In the chapter 4, we studied the influence of the flow characteristics on the reduced-scale model response, including the flow vertical shear, its misalignment with the turbine heading, the bathymetry-generated turbulence and the presence of surface waves, as it is the case at sea. Overall, as synthesised in the previous section, neither the incident vertical shear, the relative flow misalignment nor the presence of surface waves affect the maximal average power coefficient and the optimal tip speed ratio of the ducted 2-VATT compared to the idealised flow condition. The wake of bathymetry obstacles, on the other hand, causes significant power loss compared to the idealised conditions as the average kinetic energy available in front of the turbine is reduced. Thus, the typical idealised experimental flow condition is sufficient to characterise the average power performance of such a device, but the local bathymetry must be considered carefully in the future deployments at sea for both turbines and velocity measurements positioning, respectively to optimise the power output and to reliably assess the power performance. Furthermore, the average velocity vertical shear, which causes torque asymmetry between the upper and the lower rotors, and the flow unsteadiness, either caused by the bathymetry-generated turbulence or the surface waves, lead to increased power fluctuation that must be considered for the power output conditioning and the rotor column structural design. On the other hand, the flow vertical shear barely affects the mechanical loads on the whole ducted 2-VATT while a 15° flow direction misalignment with the turbine heading causes the highest transverse loads among all the tested conditions, with an increase of all the average load components apart from the vertical torsion. The flow unsteadiness, for its part, is responsible for all the other extreme loadings and all the maximal fluctuation ranges. Therefore, the combination of a flow misalignment in the turbulent wake of a bathymetric protuberance with large surface waves and the two rotor columns in phase is the worst situation in terms of extreme loadings on the turbine. The combined analysis of the flow-related and the turbine-related signals in the temporal and the spectral domains provides valuable insights into the ducted 2-VATT model response to the current velocity fluctuation.

Within the limits of the measurement uncertainties at sea, we found that the reduced-scale experiments in the idealised flow conditions predict similar average drag coefficient to what was measured on the full-scale prototype. The tests at different velocity set-points (and so Reynolds numbers) at reduced-scale suggest similarly low scale effects on all the load components except for the vertical torsion. We also found that the reduced-scale experiments alone fail in predicting the absolute average power performance at full-scale. However, the combination of the reduced-scale results with a simple two-dimensional numerical model of the ducted 2-VATT succeed in that prediction. Conversely, the quantification of the scale effects regarding the instantaneous loads remains a challenge that requires improvements on the setup and the processing of the measurements at sea. Still, we found that the difference of rotor control law between the prototype and the model causes an overestimation of the absolute rotor torque fluctuation intensity. On the other hand, the drag force fluctuation intensity is two times lower in the typical idealised reduced-scale experiments than in the results at sea. It still appears underestimated, although higher, by the scaled experiments in turbulent flows, whereas the relative influence of surface waves seems preserved.



Figure 5.8 – OceanQuest 1 MW prototype (left) and FloWatt 2.5 MW turbine (right).

5.3 Prospects

During the last months of preparation of this thesis, the French government committed to financially support the FloWatt project for the installation of the first tidal stream energy pilot farm, including seven 2.5 MW-rated turbines in the Alderney race, off the coast of La Hague. The pilot farm will be composed of a new generation of HydroQuest twin vertical axis tidal turbines with two rotor levels, similarly to the prototype described in the chapter 2. However, the new turbines are free of lateral fairings and they are made of a new rotor design which improves the power performance (Fig. 5.8). Therefore, one of the main prospects of the present work will be to assess how much our results regarding the behaviour of the ducted 2-VATT remain valid for the new design. The PhD work started by Yanis Saouli in May 2023 aims at answering this question, among others, based on 1/20 scale tests of the new 2-VATT design in the Ifremer wave and current flume tank. Specific attention will have to be paid to the model control law in order to improve the validity of the instantaneous rotor column response compared to the full-scale behaviour. Studies regarding the potential synchronicity of the six load components extreme values in realistic flow conditions could be carried out to keep refining the design process of the future 2-VATTs. The wake of the new turbine will also have to be characterised experimentally to provide valuable inputs for numerical models validation, including realistic unsteady upstream flow conditions and wake interactions. The validated numerical models will allow a finer turbine wake analysis in many flow conditions and will contribute to optimise the turbines layout in the perspective of large farm developments. Furthermore, the new installation of full-scale 2-VATTs at sea offers the opportunity to implement measurement setup improvements to better characterise the spatial flow variability influence on the average power and loading assessment, as well as better quantify the dimensionless instantaneous loadings. A dedicated in-situ measurement campaign would also be necessary to properly characterise the full-scale wake of such a 2-VATT. All those additional full-scale measurements would contribute to improving the design process by better validating the experimental and numerical results.

Effect of different bathymetry obstacles on the ducted 2-VATT

This appendix is the result of Noam Bloch’s internship for his master’s degree in engineering, under the supervision of the author. It was originally presented as Bloch et al. (2022), “Experimental study of bathymetry variation effects on a cross-flow water turbine”, in the *18èmes Journées de l’Hydrodynamique* symposium.

A.1 Introduction

Considering the climate change that we are now facing and the ever growing energy demand, renewable energy technologies show an important growth. Solar and wind are headlining the market but tidal energy converters (TEC) are making their way too. In Europe, the most energetic spots are mainly located in France and the United Kingdom (Guillou et al., 2020). *HydroQuest* is one of the companies in line to implement full-scale TECs after more than ten years of design and development. Its concept is composed of two counter-rotating vertical axis energy converters installed on a gravity base. Between 2019 and 2021, a 1 MW rated demonstrator was tested at EDF’s test site in Paimpol-Bréhat, France (Moreau et al., 2022b). This step provided the company an important insight on the turbine’s behaviour at full-scale. For further developments of its twin vertical axis tidal turbine (2-VATT), to isolate design parameters and save both money and time, the company wishes to better rely on lab-scale experiments. This can only be achieved by comparing the experimental results to those obtained at sea. To that aim, a lab-scale model, similar to the demonstrator, was designed with a scale factor $\epsilon = 1/20$. This model has been tested in several conditions in the Ifremer’s wave and current flume tank, located in Boulogne-sur-Mer, France (Moreau et al., 2022a).

Experiments conducted in Ramsey Sound (Wales, United Kingdom) show on another kind of tidal turbine the necessity to know the bathymetry for accurate performance assessment, as a reduced inflow and an increased turbulence may lower the turbine’s performance compared to numerical predictions (Harrold et al., 2019). Indeed, it has

been shown that a high level of turbulence can have a significant effect on a TEC's behaviour, decreasing slightly the mean values of its performance while increasing substantially their fluctuations (Blackmore et al., 2016; Mycek et al., 2014). Experimental studies conducted on an horizontal axis tidal turbine (HATT) indicates that bathymetry variations generate important turbulent structures which can impact the TEC, inducing intense and periodic load fluctuations (Gaurier et al., 2020c). The aforementioned HATT experiences a local flow velocity varying with the type of bathymetry encountered and the distance between the turbine and the bathymetry variations (Magnier et al., 2020). This phenomenon needs to be taken into account as the evaluation of the incident flow velocity plays an important role in the turbine's performance assessment. However, the HATT studied in Gaurier et al. (2020c) and Magnier et al. (2020) and the present 2-VATT have different geometries and flow direction sensitivity. Their location in the water column is also different. They are hence likely to be impacted differently by bathymetry variations.

The present work focuses on assessing experimentally the impact of bathymetry variations on the bottom-mounted 2-VATT from the comparison of two bathymetric configurations with an ideal flat floor. The turbine model and the experimental set-up is first described in the section A.2. The section A.3 presents the effects of bathymetry variations on the global turbine behaviour with an analysis in both the temporal and spectral domain. Finally, we discuss and conclude the results in the section A.4.

A.2 Materials and Methods

A.2.1 Turbine model

The 2-VATT model is geometrically similar to *HydroQuest's* demonstrator at a 1/20 scale (Moreau et al., 2022a). It is composed of two independent counter-rotating vertical axis rotor columns. Each column is made of two levels of rotors with a 60° phase difference between them, and each rotor is made of three blades with NACA 0018 profiles projected on the swept cylinder. The rotors radius ($R = D/2$) is 200 mm with blades chord of 73 mm and a blade height (H_{blade}) equal to 190 mm. The columns are mounted in a $W_{model} = 1.24$ m wide mechanical structure made of fairings and plates. The overall model height, from the floor to the top of the structure is $H_{model} = 840$ mm. The turbine height is defined as the distance between the top and the bottom horizontal plates such that $H = 450$ mm.

The central fairing of the turbine and the volume inside the top casing are watertight to host the electronic and the transmission system (Fig. A.1). Indeed, the rotor shafts are linked to secondary shafts (one by rotor column) through a belt system on the top of the turbine. Each secondary column is composed of a *Maxon RE50* DC motor equipped with a 1/26th gear reducer and a speed encoder. A *Scaimé DR2112-W* torque-meter with a relative angular position encoder also composes the column. The motors are piloted using remote *Escon 70/10* servo-controllers in constant speed mode. In addition, the turbine is fixed on a tripod base through a 6-component load cells (*SIXAXES* 1.5 kN) in order to model the demonstrator's gravity base. At lab-scale, the model is fixed to the tank floor at the bottom of the central pile of the base, right below the turbine, on another 6-component load cell (*SIXAXES* 20 kN) to measure the overall loads on the turbine and the base. The tripod piles are 1 cm above the floor to avoid interference

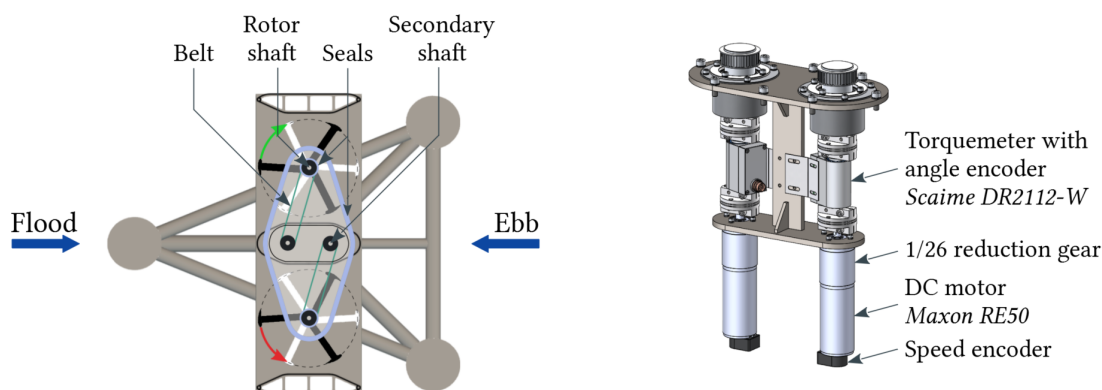


Figure A.1 – Schematic top view of the twin counter-rotating VATT model (on the left) and the instrumentation, located in the central part of the model (on the right).

with the load cell measurements.

A.2.2 Ifremer flume tank

The 2-VATT model is tested in the Ifremer wave and current flume tank in Boulogne-sur-mer, France (Fig. A.2). The test section is $H_{tank} = 2$ m deep and $W_{tank} = 4$ m wide with a working section of approximately 18 m long (Gaurier et al., 2020d). Thus, the vertical blockage in the tank (H_{model}/H_{tank}) is equal to the one in-situ (41 %). Consequently, the projected surface blockage ($b = \frac{(HW)_{model}}{(HW)_{tank}}$), is about 12 % in the tank with the base, and 8 % with the turbine only. According to the literature review in Murray (2016), this surface blockage ratio is on the edge between small enough and too high values to consider results as they are. Corrections due to some blockage effects might be needed to estimate power performance accurately, like done in Bahaj et al. (2007).

The orthogonal coordinates system considered is such that the streamwise coordinate x is in the current direction and the spanwise coordinate y is oriented from the observation window towards the wall. Both origins are set at the centre of the model. Finally, z points towards the surface with its origin on the tank floor. The three instantaneous velocity components are noted (U, V, W) along the (x, y, z) directions respectively. Using the Reynolds decomposition, each instantaneous velocity component is separated into a mean value and a fluctuating part: $U = \bar{U} + u'$, where the overbar indicates the time average. In the following, the average Reynolds shear stress corresponds to $\tau_{uw} = \overline{u'w'}$.

The inlet condition in the tank is conditioned by a homogeneous grid and a honeycomb structure. The streamwise turbulent intensity is defined as $TI_u = \sigma(U)/\bar{U}$, where σ is the standard deviation. Considering the empty tank, it appears that the boundary layer extends up to the bottom of the turbine, with TI_u decreasing from 7.5 to 1.5 % (Moreau et al., 2022a). The turbulent intensity and streamwise velocity profiles are then uniform over the turbine height. The tests are conducted at a current set point of 1 m.s⁻¹. This is similar to a full-scale velocity of 4.5 m.s⁻¹ according to Froude similitude law, which is in the range of tidal current velocities present at sea in areas suitable for tidal applications (Furgerot et al., 2020). At this speed, the Reynolds number based on the blade chord and the rotational speed is of the order of 10^5 in the tank, which is

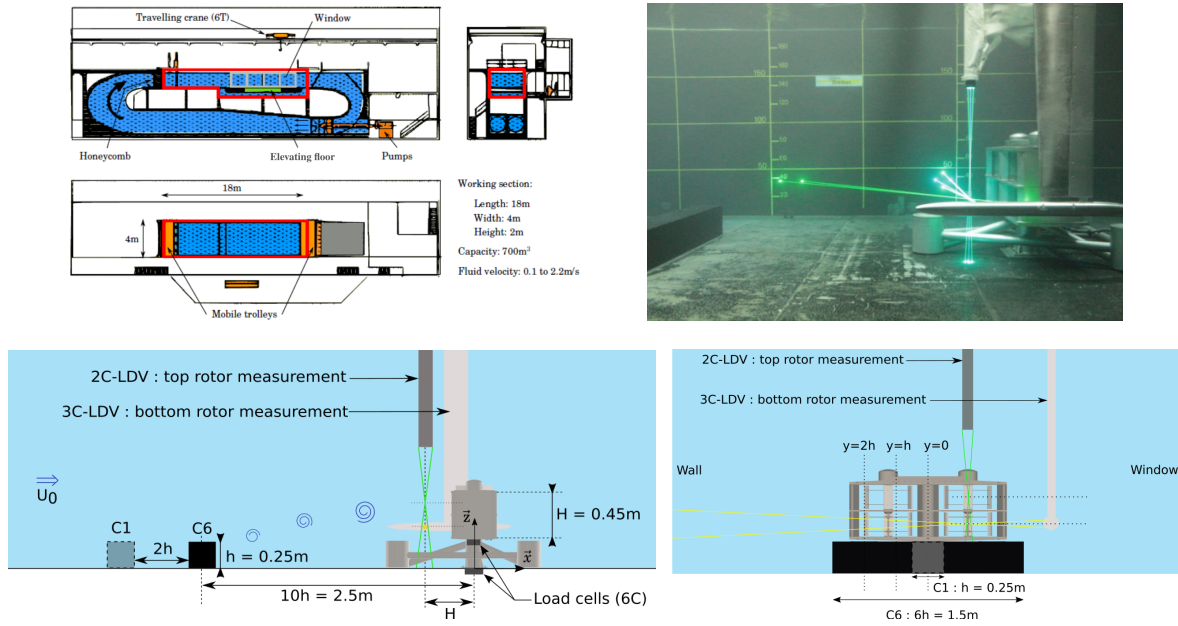


Figure A.2 – Top: schematic view of the Ifremer’s flume tank and illustration of LDV measurement. Bottom: Schematic view of the experimental set-up

about 100 times lower than the Reynolds number at full scale.

A.2.3 Bottom-mounted obstacles

Previous studies lead in the Ifremer flume tank showed that the main flow characteristics induced by bathymetry variations in-situ could be modelled using simple bottom-mounted obstacles (Ikhennicheu et al., 2019a; Ikhennicheu et al., 2019b; Magnier et al., 2020; Magnier et al., 2021). The obstacles chosen in the present work are a square cylinder and a cube, both square sections side being of dimension $h = 0.25$ m. The length of the cylinder is $6h$, corresponding to an aspect ratio of 6. Two configurations are then studied: the cylinder isolated (C6) and a tandem configuration where the cube is placed $2h$ upstream of the cylinder (C1C6). Ikhennicheu et al. (2019a) showed that isolated obstacles with a large aspect ratio, like C6, produce the most energetic wakes with vortices rising up to the free surface. However, when a cube is placed ahead of the cylinder, like for C1C6, the wake development is deeply modified. The present work analyses the differences for the turbine operation when it is placed behind those obstacles.

Fig. A.3 and A.4 recall the wake generated by the obstacles without turbine, both in terms of streamwise velocity and shear stress, as presented in Magnier et al. (2020). Those wake maps are made along three planes following the y -direction: at $y = 0$, $y = h$ and $y = 2h$. The symmetry is assumed for the y -negative part of the tank. The general pattern for the mean velocity in the C6 wake is a flow detachment at the leading edge of the cylinder, resulting in a recirculation zone and an outer steady region, separated by a shear layer with a strong velocity gradient. The flow reattaches further downstream. While the wake of C1C6 looks similar to C6 at $y = 2h$, the presence of the cube deeply modifies the flow behaviour when we look closer to the symmetry plane. There, the cube wake hits the cylinder and therefore modifies the global wake development: the

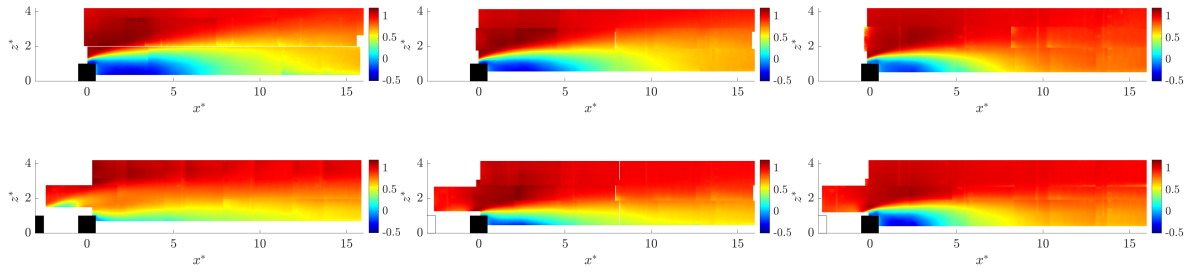


Figure A.3 – Mean streamwise velocity \bar{U} behind C6 (top) and C1C6 (bottom) with $x^* = x/h$, $y^* = y/h$ and $z^* = z/h$. Left: $y^* = 0$; middle: $y^* = 1$; right: $y^* = 2$, (Magnier et al., 2020).

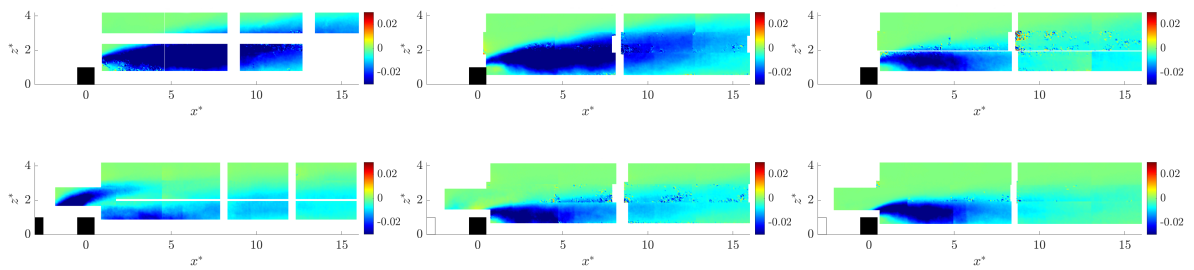


Figure A.4 – Average Reynolds shear stress τ_{uw} behind C6 (top) and C1C6 (bottom) with $x^* = x/h$, $y^* = y/h$ and $z^* = z/h$. Left: $y^* = 0$; middle: $y^* = 1$; right: $y^* = 2$, (Magnier et al., 2020).

recirculation area is smaller for C1C6 than for C6 and the shear layer reaches an upper limit of approximately $z = 3.5h$ behind C1C6 whereas its height keeps increasing behind C6.

The average Reynolds shear stress (Fig. A.4) is a good marker of the shear layer and of the generated turbulence. Apart from the $y = 2h$ planes, where the shear stresses are very much alike, shear layers appear smaller and less intense for C1C6 than for C6. Moreover, spectral analyses conducted on the wake of those two configurations revealed the shedding of large energetic vortices at a frequency around 0.25 Hz (Gaurier et al., 2020c; Ikhennicheu et al., 2019b; Magnier et al., 2020; Magnier et al., 2021). However, they behave differently depending on the configuration. Behind C6, the vortices form quickly downstream the obstacle and are ejected towards the free surface. On the other hand, behind C1C6, they are visible only further in the wake as they need more time to aggregate. The vortices are also smaller than behind C6 and their movement is horizontal as they do not rise in the water column. The cube wake inhibits the development of the energetic and upward-directed wake of the cylinder.

Given the wake developments in the two configurations, both set of obstacles are placed upstream of the turbine, either at $x = -10h$ or $x = -16h$, and are compared with the denoted "Flat floor" case for which no obstacle is set in the tank.

A.2.4 Data acquisition and processing

The torques (Q), the rotational speeds (ω), the angular positions of the two columns as well as the signals from the two load cells are acquired synchronously using *National Instruments PXI* and *LabView* systems. The acquisition frequency is set at 128 Hz during 3 minutes per run in the Flat floor case and 5 minutes per run with the obstacles to guarantee the time convergence of the mean and standard deviation of the signals. The performance results are presented in terms of power coefficient (C_P) and drag coefficient (C_x) with regard to the tip speed ratio (λ), defined in Eq. A.1; with ρ the water density, P the power extracted by the two columns ($P = \sum \omega Q$) and F_x the load in the streamwise direction measured by the upper load cell. The reference surface considered is the projected area of the four rotors ($4DH_{blade}$). The reference velocity, $U_0 = 0.944 \text{ m.s}^{-1}$, is the mean streamwise component of the velocity far ahead of the turbine measured during prior tests, on a flat floor, at the center of the turbine (Moreau et al., 2022a). It is considered as the constant reference velocity to compute the hydrodynamic coefficients for all cases, either with or without bathymetry obstacle.

$$C_P = \frac{P}{2\rho DH_{blade} U_0^3} \quad C_x = \frac{F_x}{2\rho DH_{blade} U_0^2} \quad \lambda = \frac{\omega R}{U_0} \quad (\text{A.1})$$

For fluid-structure interaction assessment, the current velocity is measured using two *Dantec* Laser Doppler Velocimeters (LDV). They are placed in the induction zone, at $x = -H$, facing the rotors axis, that is to say at $y = -0.31 \text{ m}$ (Fig. A.2). The 2-Component LDV (2C-LDV) is put in front of the upper rotor ($z = 0.61 \text{ m}$) and the 3-Component one (3C-LDV) is in front of the lower rotor ($z = 0.41 \text{ m}$). They both measure the velocity components in non-coincident mode. The 3C-LDV works similarly to the 2C-LDV (which measures U, V along x, y) but given the orientation of the three pairs of lasers, it is necessary to project the probe measurements into the tank coordinate system to get (U, V, W) along (x, y, z) . To do so, the measurements in the lasers coordinate system are interpolated on the same time vector to apply the transformation matrix. The acquisition data rate is of the order of 150 Hz for both probes.

A.3 Bathymetry variation effects on turbine behaviour

A.3.1 Effects on the global performance

Fig. A.5 presents scatter plots of the torque and the rotational speed of the rotors for every acquisition point during a run. Those data are at the operating point giving the best average power coefficient, which is not the same point for each configuration as shown in Fig. A.6 (between $\lambda = 1.38$ and $\lambda = 1.59$). It appears that the presence of an obstacle in the flow generates huge fluctuations in the turbine's operation. The dispersion is also slightly lower behind C1C6 than behind C6. It shows that the turbulence generated by the bathymetry has a substantial impact on the turbine which depends on the bathymetry configuration. Another noteworthy point is the fact that the torque is below 0 Nm part of the time in the cases with obstacles. At lab scale, the regulation keeps the rotational speed constant with a high gain. Therefore, the 2-VATT sometimes needs energy to stay at the set point and thus works in motor mode in the obstacles'

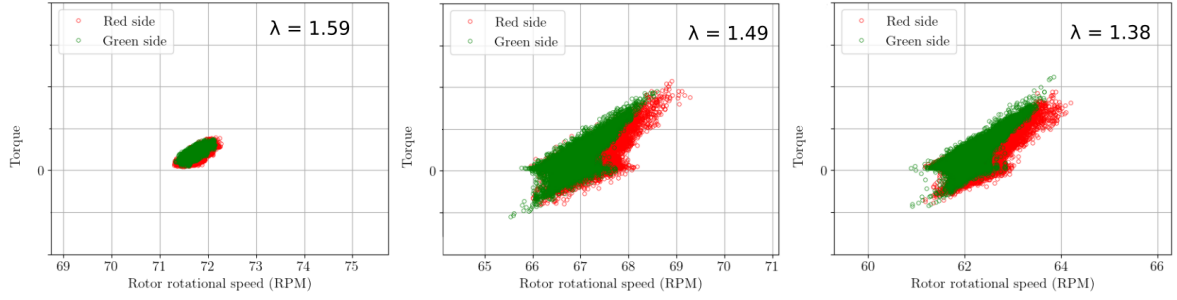


Figure A.5 – Torque as a function of the rotor rotational speed at the best performance point. Left: Flat floor; middle: C6 at $x = -16h$; right: C1C6 at $x = -16h$.

wake. It also leads to the noticeable cluster around 0 Nm which is explained by the recovery of mechanical plays when switching between generator and motor modes.

Fig. A.6 displays the power and drag coefficients (Eq. A.1), in terms of mean value and standard deviation, with respect to the tip speed ratio. Between C6 and Flat floor cases, \overline{Cp} decreases strongly behind the obstacle: at the optimum point, it plummets by 41 % with the cylinder at $x = -10h$ and by 33 % at $x = -16h$. Two factors are involved in this drop of \overline{Cp} . First, we use the same U_0 value for coefficients calculation in Flat floor and C6 while physically the flow velocity is reduced in the cylinder wake. Then, the turbulence is much higher behind the obstacle and Blackmore et al. (2016) showed that an increase of turbulence reduces the power coefficient by up to 10 % in extreme cases. The standard deviation of Cp at the optimum point is multiplied by 2.4 at $x = -10h$ and by 2.0 at $x = -16h$ from Flat floor to C6. This must be due to the turbulence increase in the obstacle wake and to the periodic vortex shedding as shown on a HATT (Gaurier et al., 2020c). The same pattern applies for the drag, but with smaller differences. From Flat floor to C6, \overline{Cx} decreases by 23 % at $x = -10h$ and by 19 % at $x = -16h$ while its standard deviation is greater by a factor 1.8 at $x = -10h$ and 1.6 at $x = -16h$. The shift of the curves along the tip speed ratio axis is also due to the use of a reference velocity greater than the one perceived by the turbine. In C6, the cylinder’s impact is greater when the turbine is closer. This is consistent with the wake maps in Fig. A.3. Indeed, the average velocity over the capture area of the turbine ($0.28 \text{ m} < z < 0.73 \text{ m}$) at $x = -10h$ is lower than at $x = -16h$ so there is no surprise we find $\overline{Cp}(x = -10h) < \overline{Cp}(x = -16h)$ and $\overline{Cx}(x = -10h) < \overline{Cx}(x = -16h)$. Furthermore, Fig. A.4 shows a greater level of turbulence at $x = -10h$ than at $x = -16h$, thereby leading to $\sigma(Cp(x = -10h)) > \sigma(Cp(x = -16h))$ and $\sigma(Cx(x = -10h)) > \sigma(Cx(x = -16h))$.

Looking at the C1C6 case curves, \overline{Cp} and \overline{Cx} also decrease behind the obstacle compared to the Flat floor case: at the optimum operating point, they drop respectively by 23 and 16 % at $x = -10h$ and by 34 and 22 % at $x = -16h$. However, the effect of the downstream distance is reversed from what it is behind C6 since \overline{Cp} and \overline{Cx} are lower far from the obstacles ($x = -16h$) than closer ($x = -10h$). We explain that phenomenon thanks to the average velocity over the capture area, noted \overline{U} , computed from the wake maps (Fig. A.3). Since the wake height is lower at $x = -10h$, $\overline{U}(x = -10h) > \overline{U}(x = -16h)$. Hence having $\overline{Cp}(x = -10h) > \overline{Cp}(x = -16h)$ and $\overline{Cx}(x = -10h) > \overline{Cx}(x = -16h)$ is consistent.

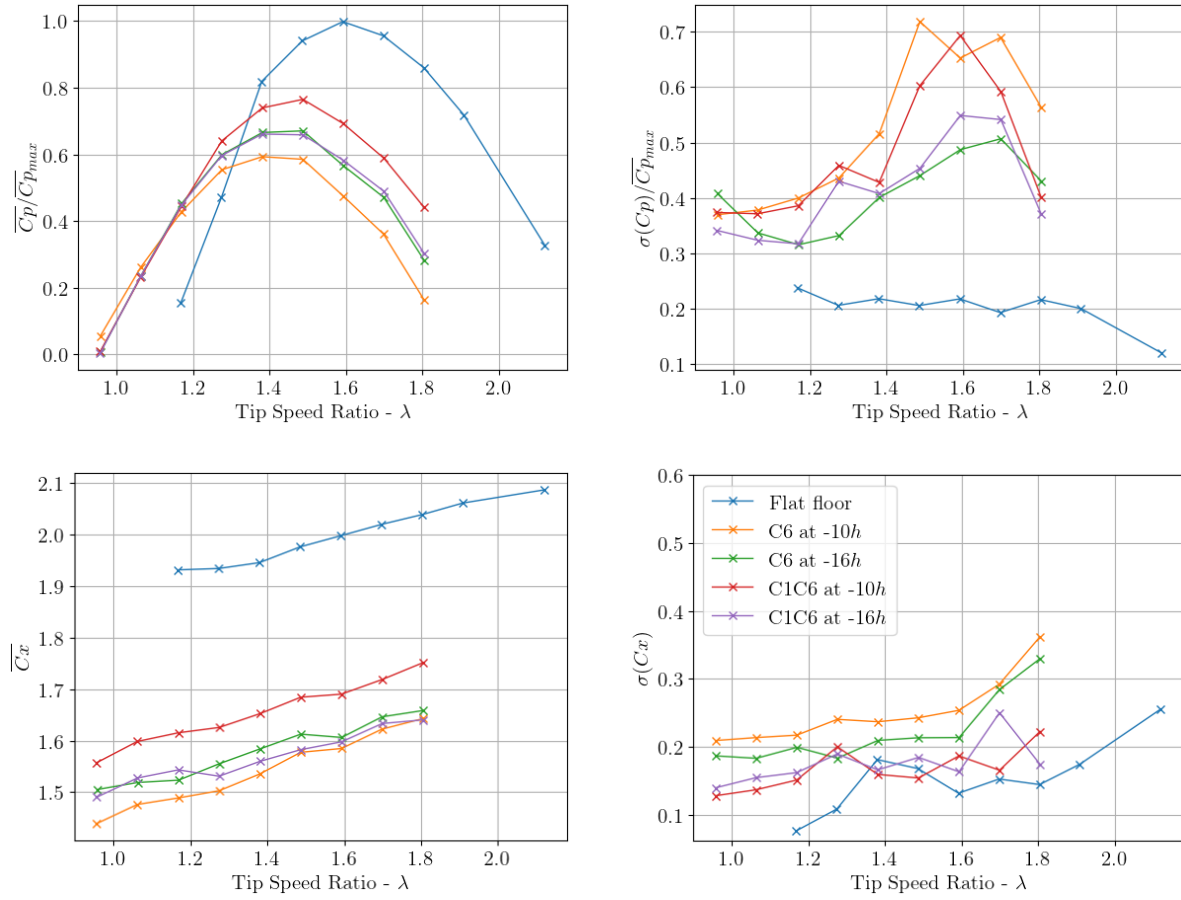


Figure A.6 – Power (top) and drag (bottom) coefficients. Left: Mean value over a run; right: standard deviation

Next, $\sigma(C_p)$ is greater behind C1C6 than in Flat floor. At the optimum point it is multiplied by 2.8 at $x = -10h$ and by 1.9 at $x = -16h$. Unlike for the mean values, the effect of the downstream distance on the standard deviation is the same as behind C6: the fluctuations are greater at $x = -10h$ than at $x = -16h$. Indeed, the close wake is more turbulent than further downstream as previously shown with Fig. A.4 where $\tau_{uw}(x = -10h) > \tau_{uw}(x = -16h)$, leading thus to $\sigma(C_p(x = -10h)) > \sigma(C_p(x = -16h))$. The drag's standard deviation is also greater behind C1C6 than in the Flat floor case (multiplied by 1.2 at $x = -10h$ and by 1.3 at $x = -16h$) but to a lesser extent compared to what it is behind C6. On a global point of view, C1C6 seems less impactful than C6 on the turbine behaviour. The key finding here is that the bathymetry must be taken into account when choosing the position of the reference upstream velocity measurement to deduce reliable performance results. To give a closer look at what happens structurally to the turbine, the next sections focus on the best performance operating point for each configuration.

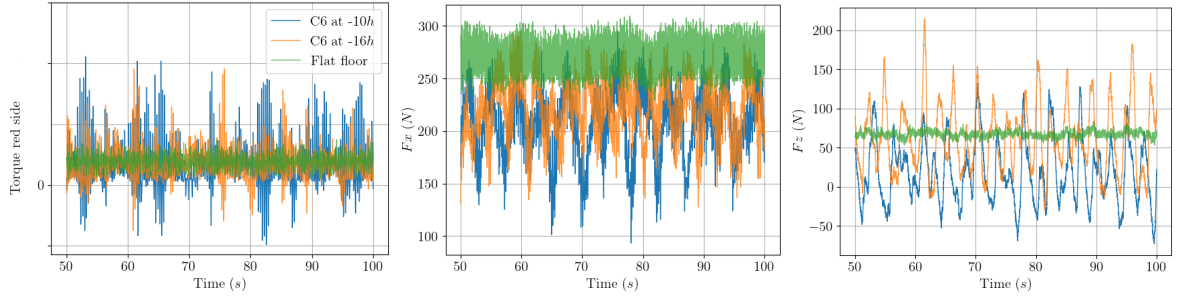


Figure A.7 – Temporal evolution of Q (left), F_x (middle) and F_z (right) at the best performance point. F_x and F_z come from the load cell located between the turbine and the base.

A.3.2 Load temporal analysis

Fig. A.7 presents a few examples of temporal signals in Flat floor and C6 configurations: the torque applied on the red column (Fig. A.1) and two forces measured by the load cell located between the turbine and the base. The massive increase of the fluctuations, observed in the previous section, is also noticeable here, for the torque and for the loads. The other forces and moments, as well as the C1C6 configuration, show the same behaviour, which is summarised in Tab. A.1 and A.2. Both tables show the impact induced by bathymetry variation on the fluctuations, represented by the standard deviation, and on the extreme values of the loads. Those quantities are of high interest for turbine makers when considering the structural design of their devices.

Between Flat floor and C6 configurations, the fluctuations of the forces rise in every direction and in the same proportion at $x = -10h$ and $x = -16h$. Indeed, the standard deviation is multiplied by approximately 1.7 for F_x , 3.1 for F_y and 10 for F_z . The massive increase of fluctuations in z is clearly visible in Fig. A.7 and can be explained by the vertical velocity component brought by the vortices and their rising trajectory behind C6 (Ikhennicheu et al., 2019b). The extreme values are much more widely spread behind the obstacle as the range is multiplied by more than 2 for F_x , around 4 for F_y and 7 for F_z , from Flat floor to C6. Those range increases are likely to have a great impact on the structural fatigue. F_x is usually monitored closely for turbines with gravity base because of the slippage risk. Here the maximum F_x value in C6 configuration does not exceed the one of Flat floor. Therefore, for the same inflow velocity, the presence of bathymetry variations does not increase the probability of slippage. However, for the two other components, the highest values can rise by up to a factor 2.5 between Flat floor and C6. This must be considered when looking at rupture issues. The load cell placed under the base shows mainly the same behaviour as the one between the base and the turbine. Yet, we observe a reduction of standard deviations and extreme ranges between 15 and 25 % for the three force components of all configurations presented in this section (except for F_z in Flat floor). The measurement range of the upper load cell is 1.5 kN while it is 20 kN for the lower one. In comparison, the measured forces do not exceed a few hundreds of newtons and the standard deviations a few tens. Therefore, we can assume the measurement range of the lower load cell to be too wide to measure every single variation, resulting in lower standard deviations.

Table A.1 – Forces standard deviation and extreme values at the best performance point. Load cell located between the turbine and the base. All values are in N.

Configuration	$\sigma(Fx)$	Fx range	$\sigma(Fy)$	Fy range	$\sigma(Fz)$	Fz range
Flat floor	17.8	228 / 313	10.2	0 / 58	4.0	50 / 84
C6 at x=-10h	32.1	80 / 300	32.5	-104 / 120	40.8	-73 / 166
C6 at x=-16h	28.9	111 / 303	31.2	-105 / 130	39.6	-32 / 215
C1C6 at x=-10h	20.8	142 / 287	32.4	-74 / 121	21.3	-40 / 121
C1C6 at x=-16h	22.5	126 / 280	28.2	-60 / 122	23.1	-32 / 148

In the tandem configuration, the global behaviour looks similar to the C6 configuration, with an increase of the standard deviation in comparison with the Flat floor case and extreme values more widely spread. However, the level of fluctuation is quite lower here than behind C6 for Fx and for Fz as their standard deviation is divided by 1.4 and 1.8 respectively from C6 to C1C6. The ranges between extreme values are quite smaller too. Their reduction from C6 to C1C6 stands between 13 and 35 % depending on the component and the distance considered. The wake maps of the section [A.2.3](#) show that the Reynolds shear stress (Fig. [A.4](#)) is lower behind C1C6 than behind C6. Therefore the overall turbulence level must be lower which leads to lower standard deviations and extreme ranges. Moreover, Magnier et al. (2020) showed that the turbulent structures shed by the C1C6 configuration are two times smaller than those shed by the isolated cylinder. As a consequence, the impact on the turbine is lower as well, leading to a lower risk of fatigue and failure issues.

The same analysis can be done for the moments (Tab. [A.2](#)) for which we observe a global increase of the fluctuations and extreme ranges behind C6 compared to Flat floor. This growth is slightly greater with the cylinder at $x = -16h$ than at $x = -10h$ for Mx but it is the other way around for My and Mz . The quantity of highest interest is My because of the turbine toppling risk. Here, we see that the maximum value in C6 cases is very close to the maximum in the Flat floor configuration. Hence, the turbine is unlikely to tip over due to bathymetric obstacles. However, with C6 upstream, Mx and Mz maxima rise by a factor between 2.6 and 5.1 depending on the moment and the distance, possibly leading to failure issues. The load cell located below the foundation shows the same influence of the bathymetry, but with higher values of σ and ranges for Mx and My for all cases. The average value of My is also always much greater (around 2.3 times) but that comes from a greater distance between the load cell and the application point of the force, assuming Fx to be the only force responsible for My . Indeed, previous measurements showed that half of the drag is due to the friction between the structure and the flow while the other half comes from the energy extraction by the rotors' rotation. Thus, the base has an influence only on the friction part and as it is in the boundary layer of the flow it only adds little friction. In Flat floor, \overline{Fx} rises by only 6 % between the upper and the lower load cell. Therefore, we can consider its point of application to be almost at the same location whether we consider the full machine or only the turbine part (excluding the base). We estimate that point of application to be located around the middle of the turbine, that is to say around 23 cm above the upper load cell. 26 cm separate the two load cells, therefore the distance between the point of application of the force and the sensor is more than doubled when we consider the lower load cell and so is the moment My . This explains the increase of My between the two load cells.

Table A.2 – Moments standard deviation and extreme values at the best performance point. Load cell located between the turbine and the base. All values are in Nm.

Configuration	$\sigma(Mx)$	Mx range	$\sigma(My)$	My range	$\sigma(Mz)$	Mz range
Flat floor	6.9	-18 / 23	5.3	39 / 64	2.6	-13 / 8
C6 at x=-10h	14.2	-47 / 48	6.9	13 / 63	9.3	-33 / 41
C6 at x=-16h	16.6	-62 / 61	5.8	18 / 65	7.4	-31 / 33
C1C6 at x=-10h	17.4	-43 / 49	5.9	24 / 69	5.9	-25 / 30
C1C6 at x=-16h	13.2	-37 / 46	5.0	24 / 59	6.4	-32 / 22

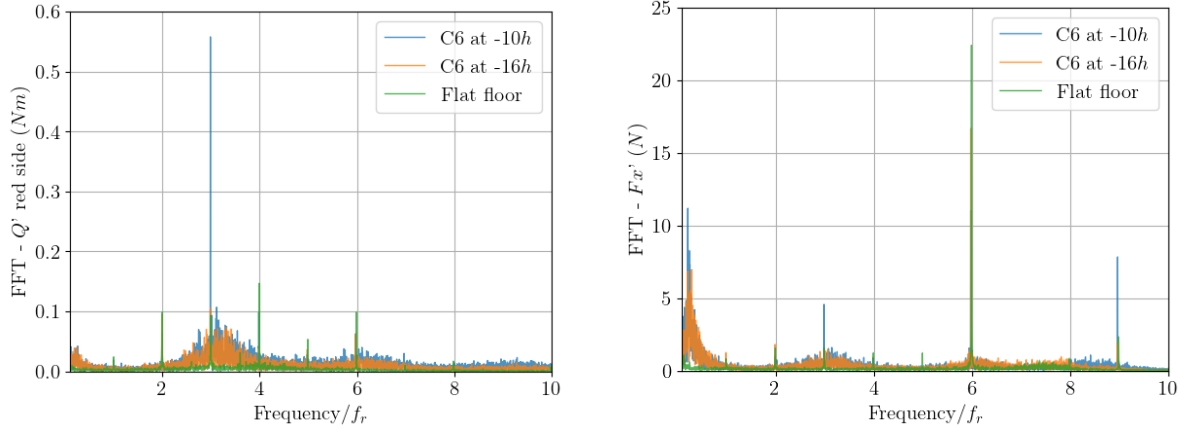


Figure A.8 – Fourier Transform of Q (left) and Fx (right) in FC at the best performance point, normalised by the rotation frequency.

In the same way as for the forces, we notice a smaller impact of C1C6 on the moments, particularly for My and Mz . Compared to C6, their standard deviations are divided respectively by 1.3 and 1.4 and their ranges reduction is between 10 and 26 % depending on the component and the distance with the obstacles. The load analysis corroborates what is found in the section A.3.1: a smaller impact when a cube is placed upstream of the cylinder than when the cylinder is isolated.

A.3.3 Load spectral analysis

Fig. A.8 presents the Fourier Transform of the torque on the red column and of Fx (load cell between the turbine and the base) for a large frequency range, between 0.1 and 10 Hz. It allows us to look at turbine related phenomena so frequencies are normalised by the rotation frequency (f_r). The other efforts behave the same way as Fx . Only the Flat floor and C6 configurations are displayed here but C1C6 exhibits the same features as C6.

First of all, looking at the Flat floor configuration, we notice sharp peaks at the harmonics of the rotation frequency. The torque is measured on one column, made of six blades. $6 * f_r$ is therefore the blades passing frequency and we expected to find an important peak there. The peak at $3 * f_r$ may reveal an asymmetry in the torque distribution between the top and bottom rotors while the other harmonics may come from the control system, geometry imperfections or flow asymmetry for instance. In

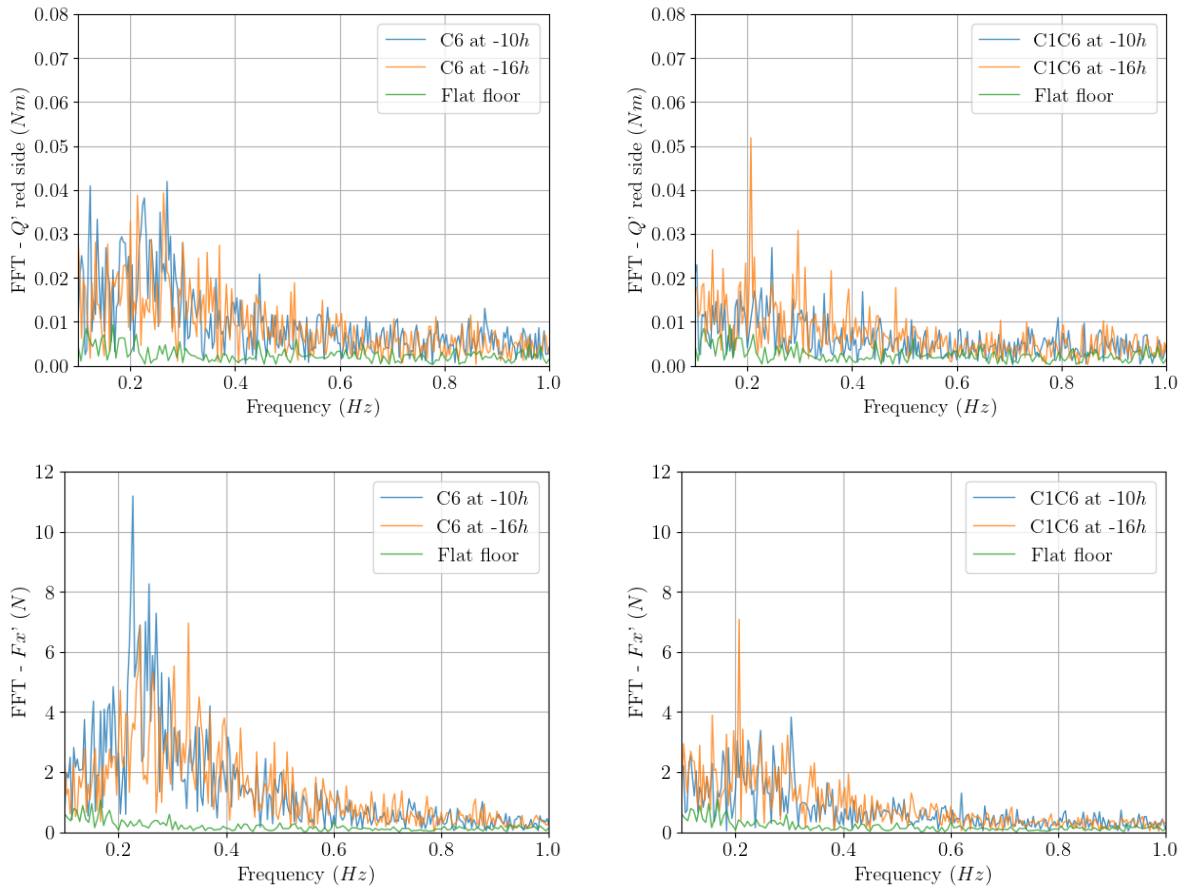


Figure A.9 – Fourier Transform of Q (top) and Fx (bottom) at the best performance point. Left: C6; right: C1C6

almost the whole frequency range, the behaviour is the same behind the obstacle than in the Flat floor case. The peaks are more widely spread though, the rotors' rotation being disturbed by the turbulence, which results in larger torque and rotational speed ranges as shown by the scatter plots in Fig. A.5. Fig. A.9 zooms in on low frequencies, between 0.1 and 1 Hz. It compares Flat floor with C6 on one side and with C1C6 on the other one. Fourier Transform of the torque on the red column and of Fx (load cell between the turbine and the base) are displayed. The Flat floor curves present no noticeable event whereas C6 and C1C6 cases have a strong frequency content. This time, the frequencies are not normalised by f_r as we are looking at a flow related phenomenon. For most of the load components, the strongest peaks are between 0.2 and 0.3 Hz. This frequency range corresponds to the large eddies detached from the cylinder at a frequency around 0.25 Hz brought to light in Ikhennicheu et al. (2019b). They seem to affect strongly the 2-VATT and might be responsible for structure failures should a turbine stand in their way. Looking in more details, differences appear when we compare C6 and C1C6. Firstly, the Fourier Transform levels are globally lower for C1C6 than for C6. It means that the energy of the large structures is lower in the tandem configuration, due to a lower turbulence level and smaller vortices as explained in the section A.3.2. Secondly, in C6 the phenomenon is stronger close to the obstacle ($x = -10h$) than far ($x = -16h$). (Ikhennicheu et al., 2019b) explains that high aspect ratio bathymetry variation leads

to energetic structures flowing downstream and towards the surface. Here the turbine is installed on the floor, therefore when the structures are ascending in the water column they are likely to avoid the turbine placed further downstream. Yet, in C1C6 the structures have a greater impact when the turbine is far from the obstacles ($x = -16h$) than when it is close ($x = -10h$). As shown in Magnier et al. (2020), a greater distance is needed for turbulent structures to aggregate behind C1C6 than behind C6 and they move horizontally in the wake. This is why the peak around 0.25 Hz is less noticeable at $x = -10h$ than at $x = -16h$.

A.4 Conclusion

This work reports on the response of a ducted twin vertical axis tidal turbine to bathymetry-induced turbulent flows. The experimental study used a bottom-mounted cube and a square cylinder to represent bathymetry variations. Their wakes, analysed in prior works, exhibit an important velocity reduction and large turbulent structures shedding at a frequency around 0.25 Hz. Those energetic vortices flow towards the surface in the wake of the large aspect ratio obstacle while they remain close to the floor in the tandem configuration. Consequently, the mean turbine's performance and loads are reduced compared to a smooth ocean floor, whereas their fluctuations and extreme ranges substantially increase. The mean values of the power and drag coefficients drop respectively by up to 41 % and 25 % while their standard deviations are multiplied respectively by up to 2.8 and 1.8. The configuration of the obstacles and their distance from the turbine play an important role in its behaviour. When the turbine is close to the bathymetry variation, a large aspect ratio obstacle has a greater impact than the same obstacle with a cube just ahead of it, because the former produces larger and more energetic vortices than the latter. Yet, when the turbine is placed further downstream, the tandem configuration becomes more impacting as its wake develops horizontally rather than rising towards the free surface. That comparison of two kinds of simplified bathymetries shows the complexity of the interaction between bathymetry variation and turbine behaviour. It is therefore necessary to consider each bathymetry specifically when choosing installation sites, for energetic performance assessment as much as for structural design.

Laser Doppler Velocimetry measurements in the turbine's induction zone will be used to better understand the impact of the obstacles wake on the turbine. On a reverse point of view, they could also help understand how the presence of the turbine modifies the obstacles wake, an interesting question when thinking about future arrays of tidal energy converters.

Influence of the velocity measurement location on the performance assessment

The average power and drag coefficient differences between the two measurement campaigns at sea (Fig. 2.8 and 2.18) question the influence of the velocity measurement location on the results due to the rough bathymetry of the test site (Fig. 2.2). Mercier et al. (2021a) and Mercier et al. (2022) showed that the seabed morphology is responsible for a high spatial variability of the average velocity field and of the turbulent kinetic energy production. The study of the ducted 2-VATT model response in the wake of a simplified bottom-mounted obstacle already showed that using either the far upstream velocity measurement or the measurement at the turbine location prior to its installation gives 20 to 30 % different average power and drag coefficients at the optimal operating point, with different optimal tip speed ratios (Fig. 4.23 and 4.24). To further discuss the influence of the reference velocity measurement location on the power and load assessments, we measure three vertical velocity profiles over the ducted 2-VATT height using the 3C-LDV at the cross-flow locations $y = \{0; -h; -2h\}$ ($h = 0.25$ m, the bathymetry obstacles height) and at $x = -6H$ ($H = 0.45$ m, the turbine height), between the C1C6 bottom-mounted obstacle combination placed at $x = -16h$ and the turbine operating at its optimal tip speed ratio (Fig. B.1 and B.2). For the recall, the position $x = -6H$ is the reference upstream position for the far upstream velocity measurement in our experiments as it is out of the ducted 2-VATT induction zone (Fig. 3.5). That distance gives 54 m at full-scale, which is roughly the distance between the ADCPs and the prototype locations at the Paimpol-Bréhat test site; and the distance between the downstream face of C6 and the 3C-LDV location would be 24 m at full-scale. Beyond our 3C-LDV measurements, the turbulent wake of the C1C6 bottom-mounted obstacle configuration alone (ie. without turbine downstream) was thoroughly analysed based on Particle Image Velocimetry (PIV) in Magnier et al. (2021).

Based on the 3C-LDV measurements, we compute the average of the streamwise velocity over the capture height (U_{cap}) at each of the three lateral positions. We compute the instantaneous velocity signals to the power 2 and 3 for the computation of the drag and power coefficients, respectively, before spatially averaging over the height and then

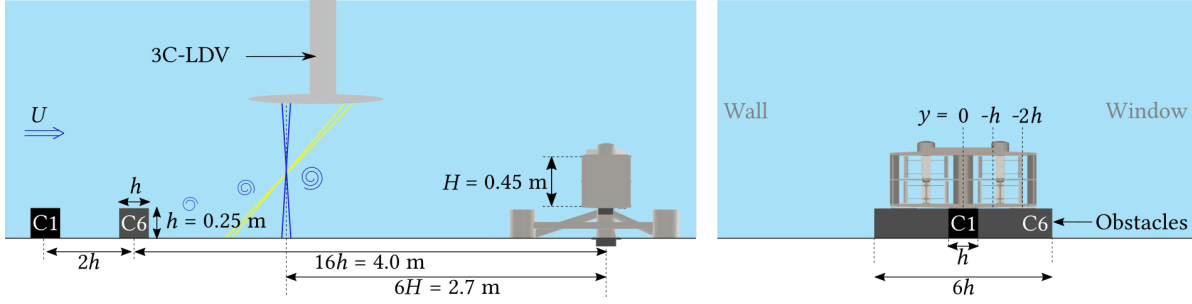


Figure B.1 – Schematic side view (left) and front view (right) of the experimental setup.

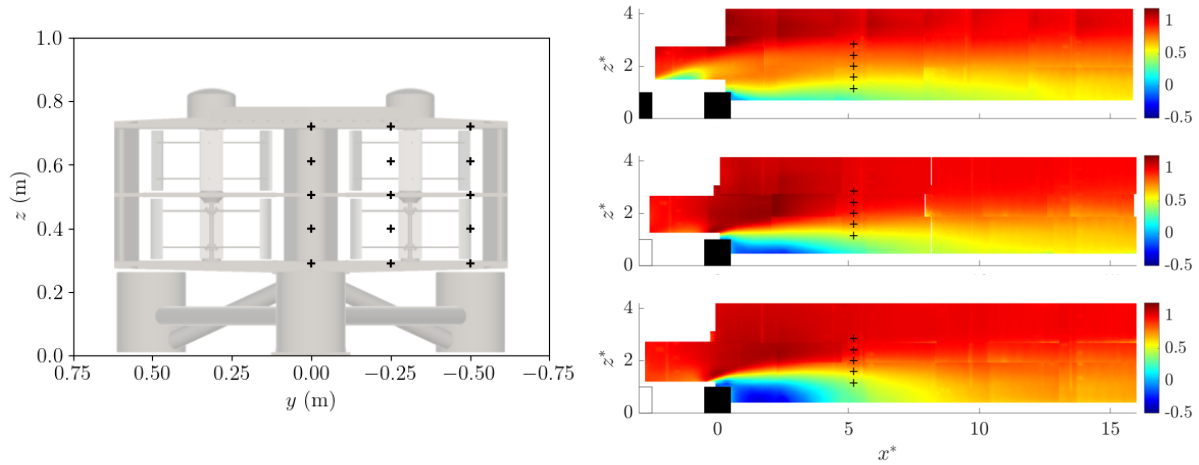


Figure B.2 – 3C-LDV measurement points location (crosses) displayed in front of the ducted 2-VATT model (left) and over streamwise average velocity contours (right) from PIV in the wake of C1C6 without turbine at $y = 0$ (top), $y = h$ (middle) and $y = 2h$ (bottom), with $x^* = x/h$ and $z^* = z/h$ (from Magnier et al. (2020)).

temporally over the 5 minute-long measurement, as it is required for the ADCP measurements in a power performance assessment following the TS 62600-200 (IEC, 2013). Due to the strong spatial variability of the average and turbulence flow characteristics downstream of this specific bottom-mounted obstacle configuration (Fig. A.3 and A.4), the maximal average power coefficient is more than 2 times higher when it is computed with $U_{cap}(y = 0)$ than with $U_{cap}(y = 2h)$ (Fig. B.3). The power 2 instead of 3 for the drag coefficient computation reduces the reference velocity difference between the lateral positions but we still observe almost 40 % difference between the average drag coefficient computed with $U_{cap}(y = 0)$ and with $U_{cap}(y = 2h)$.

By opposition to the LDV that measures locally the velocity in a ~ 0.01 cubic millimetre volume (Gaurier, 2020), an ADCP provides velocity measurements averaged over several cubic metre volumes (vertically over the cell-size height – 0.5 or 1 m in our measurements – and horizontally over the distance separating the slanted beams). For a Nortek Signature 500 ADCP with 25° slanted beams installed on the seabed, like those used during the in-situ measurement campaigns, the horizontal distance between two opposed beams is of the order of the ducted 2-VATT width at the bottom of the capture area and it is more than the double at the top. Therefore, the three 3C-LDV cross-flow measurement locations would be included in the horizontal averaging of an ADCP ve-

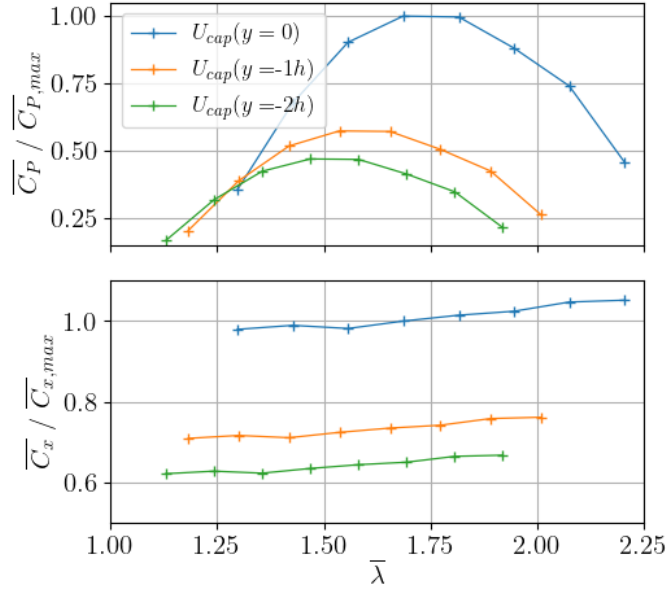


Figure B.3 – Average power (top) and drag (bottom) coefficients versus the tip speed ratio of the ducted 2-VATT model downstream of C1C6@16h, with three lateral positions of the upstream velocity measurements, normalised by the maximal value at the optimal operating point.

locity measurement at full-scale. In addition, we expect that using the measurements of an ADCP instead of the LDV at the same three cross-flow locations would have a more limited influence on the hydrodynamic coefficients due to the spatial averaging inherent to that measurement technique (Mercier et al., 2021b). Thus, the results presented here illustrate the sensitivity of the power and load coefficients to the cross-flow location of the velocity measurement in a specific spatially inhomogeneous flow configuration, but they cannot be directly transposed to in-situ measurements. The influence of the ADCP location, although in the footprint indicated by the TS 62600-200 (IEC, 2013), on the power and load coefficients assessment at sea still remains to be properly quantified.

Bibliography

- Achard, J.-L. and T. Maître (2006). *Hydraulic turbomachine*. URL: <https://hal.archives-ouvertes.fr/hal-00189351>.
- Ahmadi-Baloutaki, M., R. Carriveau, and D. S. Ting (2015). « Performance of a vertical axis wind turbine in grid generated turbulence ». In: *Sustainable Energy Technologies and Assessments* 11, pp. 178–185. DOI: [10.1016/j.seta.2014.12.007](https://doi.org/10.1016/j.seta.2014.12.007).
- Ahmadi, M. H. (2019). « Influence of upstream turbulence on the wake characteristics of a tidal stream turbine ». In: *Renewable Energy* 132, pp. 989–997. DOI: [10.1016/j.renene.2018.08.055](https://doi.org/10.1016/j.renene.2018.08.055).
- Bachant, P. and M. Wosnik (2011). « Experimental Investigation of Helical Cross-Flow Axis Hydrokinetic Turbines, Including Effects of Waves and Turbulence ». In: *ASME-JSME-KSME 2011 Joint Fluids Engineering Conference*. Shizuoka, Japan: ASMEDC, pp. 1895–1906. DOI: [10.1115/AJK2011-07020](https://doi.org/10.1115/AJK2011-07020).
- (2015). « Characterising the near-wake of a cross-flow turbine ». In: *Journal of Turbulence* 16.4, pp. 392–410. DOI: [10.1080/14685248.2014.1001852](https://doi.org/10.1080/14685248.2014.1001852).
- (2016). « Effects of Reynolds Number on the Energy Conversion and Near-Wake Dynamics of a High Solidity Vertical-Axis Cross-Flow Turbine ». In: *Energies* 9.2, p. 73. DOI: [10.3390/en9020073](https://doi.org/10.3390/en9020073).
- Bahaj, A., A. Molland, J. Chaplin, and W. Batten (2007). « Power and thrust measurements of marine current turbines under various hydrodynamic flow conditions in a cavitation tunnel and a towing tank ». In: *Renewable Energy* 32.3, pp. 407–426. DOI: [10.1016/j.renene.2006.01.012](https://doi.org/10.1016/j.renene.2006.01.012).
- Barltrop, N, K. S. Varyani, A Grant, D Clelland, and X. Pham (2006). « Wave-current interactions in marine current turbines ». In: *Proceedings of the Institution of Mechanical Engineers, Part M: Journal of Engineering for the Maritime Environment* 220.4, pp. 195–203. DOI: [10.1243/14750902JEME45](https://doi.org/10.1243/14750902JEME45).
- Beaudet, L. (2014). « Etude expérimentale et numérique du décrochage dynamique sur une éolienne à axe vertical de forte solidité ». PhD thesis. URL: <https://theses.hal.science/tel-01058929/>.
- Bennis, A.-C., L. Furgerot, P. Bailly Du Bois, E. Poizot, Y. Méar, and F. Dumas (2022). « A winter storm in Alderney Race: Impacts of 3D wave–current interactions on the hydrodynamic and tidal stream energy ». In: *Applied Ocean Research* 120.December 2021, p. 103009. DOI: [10.1016/j.apor.2021.103009](https://doi.org/10.1016/j.apor.2021.103009).
- Bertram, V. (2012). « Introduction ». In: *Practical Ship Hydrodynamics*. Elsevier, pp. 1–39. DOI: [10.1016/B978-0-08-097150-6.10001-6](https://doi.org/10.1016/B978-0-08-097150-6.10001-6).
- Black & Veatch (2020). *Lessons Learnt from MeyGen Phase 1A Final Summary Report*. Tech. rep. Black & Veatch Corporation, p. 30. URL: <https://h7g7q8k5>.

- stackpathcdn.com/cdn/ff/Yysz2k-kjIRKTcXlXt-xYQfAqKSp3t2ZYxpB4f17pTE/1593113924/public/2020-06/MeyGenLessonsLearntFullReport.pdf.
- Blackmore, T., L. E. Myers, and A. S. Bahaj (2016). « Effects of turbulence on tidal turbines: Implications to performance, blade loads, and condition monitoring ». In: *International Journal of Marine Energy* 14, pp. 1–26. DOI: [10.1016/j.ijome.2016.04.017](https://doi.org/10.1016/j.ijome.2016.04.017).
- Bloch, N., M. Moreau, G. Germain, and G. Maurice (2022). « Experimental study of bathymetry variation effects on a cross-flow water turbine ». In: *18èmes Journées de l’Hydrodynamique*. Poitiers, pp. 1–12. URL: <https://jh2022.sciencesconf.org/413851>.
- Bouferrouk, A., J. B. Saulnier, G. H. Smith, and L. Johanning (2016). « Field measurements of surface waves using a 5-beam ADCP ». In: *Ocean Engineering* 112, pp. 173–184. DOI: [10.1016/j.oceaneng.2015.12.025](https://doi.org/10.1016/j.oceaneng.2015.12.025).
- Boutier, A., ed. (2012). *Laser Velocimetry in Fluid Mechanics*. John Wiley & Sons.
- Brevik, I. and A. Bjørn (1979). « Flume experiment on waves and currents. I. Rippled bed ». In: *Coastal Engineering* 3.C, pp. 149–177. DOI: [10.1016/0378-3839\(79\)90019-X](https://doi.org/10.1016/0378-3839(79)90019-X).
- Chamorro, L. P., C. Hill, V. S. Neary, B. Gunawan, R. E. A. Arndt, and F. Sotiropoulos (2015). « Effects of energetic coherent motions on the power and wake of an axial-flow turbine ». In: *Physics of Fluids* 27.5, p. 055104. DOI: [10.1063/1.4921264](https://doi.org/10.1063/1.4921264).
- Chatellier, L, J Gorle, F Pons, and B Malick (2018). *Towing tank testing of a controlled-circulation Darrieus turbine*. Lisbon, Portugal: CRC Press, pp. 195–201. DOI: [10.1201/9780429505324](https://doi.org/10.1201/9780429505324).
- Coles, D., A. Angeloudis, D. Greaves, G. Hastie, M. Lewis, L. Mackie, J. McNaughton, J. Miles, S. Neill, M. Piggott, D. Risch, B. Scott, C. Sparling, T. Stallard, P. Thies, S. Walker, D. White, R. Willden, and B. Williamson (2021). « A review of the UK and British Channel Islands practical tidal stream energy resource ». In: *Proceedings of the Royal Society A: Mathematical, Physical and Engineering Sciences* 477.2255. DOI: [10.1098/rspa.2021.0469](https://doi.org/10.1098/rspa.2021.0469).
- Cossu, R., I. Penesis, J.-R. Nader, P. Marsh, L. Perez, C. Couzi, A. Grinham, and P. Osman (2021). « Tidal energy site characterisation in a large tidal channel in Banks Strait, Tasmania, Australia ». In: *Renewable Energy* 177, pp. 859–870. DOI: [10.1016/j.renene.2021.05.111](https://doi.org/10.1016/j.renene.2021.05.111).
- Darrieus, G. (1931). *Turbine Having its Rotating Shaft Transverse to the Flow of the Current*. URL: <https://patentimages.storage.googleapis.com/13/d6/3b/c8f2897a86ce96/US1835018.pdf>.
- Deskos, G., G. S. Payne, B. Gaurier, and M. Graham (2020). « On the spectral behaviour of the turbulence-driven power fluctuations of horizontal-axis turbines ». In: *Journal of Fluid Mechanics* 904, A13. DOI: [10.1017/jfm.2020.681](https://doi.org/10.1017/jfm.2020.681).
- Doman, D. A., R. E. Murray, M. J. Pegg, K. Gracie, C. M. Johnstone, and T. Nevalainen (2015). « Tow-tank testing of a 1/20th scale horizontal axis tidal turbine with uncertainty analysis ». In: *International Journal of Marine Energy* 11, pp. 105–119. DOI: [10.1016/j.ijome.2015.06.003](https://doi.org/10.1016/j.ijome.2015.06.003).
- Draycott, S., J. Steynor, A. Nambiar, B. Sellar, and V. Venugopal (2020). « Rotational sampling of waves by tidal turbine blades ». In: *Renewable Energy* 162, pp. 2197–2209. DOI: [10.1016/j.renene.2020.10.037](https://doi.org/10.1016/j.renene.2020.10.037).

- Draycott, S., A. Nambiar, B. Sellar, T. Davey, and V. Venugopal (2019). « Assessing extreme loads on a tidal turbine using focused wave groups in energetic currents ». In: *Renewable Energy* 135, pp. 1013–1024. DOI: [10.1016/j.renene.2018.12.075](https://doi.org/10.1016/j.renene.2018.12.075).
- Druault, P., B. Gaurier, and G. Germain (2022). « Spatial integration effect on velocity spectrum: Towards an interpretation of the $-11/3$ power law observed in the spectra of turbine outputs ». In: *Renewable Energy* 181, pp. 1062–1080. DOI: [10.1016/j.renene.2021.09.106](https://doi.org/10.1016/j.renene.2021.09.106).
- EDF and SEENEOH (2022). *Paimpol-Bréhat tidal turbine test site documentation v1.2*. Tech. rep. EDF, pp. 1–42. URL: <https://testsites.bretagneoceanpower.fr/en/technical-information>.
- Ebdon, T., M. J. Allmark, D. M. O’Doherty, A. Mason-Jones, T. O’Doherty, G. Germain, and B. Gaurier (2021). « The impact of turbulence and turbine operating condition on the wakes of tidal turbines ». In: *Renewable Energy* 165, pp. 96–116. DOI: [10.1016/j.renene.2020.11.065](https://doi.org/10.1016/j.renene.2020.11.065).
- Filipot, J.-F., M. Prevosto, C. Maisondieu, M. Le Boulluec, and J. Thomson (2015). « Wave and turbulence measurements at a tidal energy site ». In: *IEEE/OES 11th Current, Waves and Turbulence Measurement (CWTM)*, pp. 1–9. DOI: [10.1109/CWTM.2015.7098128](https://doi.org/10.1109/CWTM.2015.7098128).
- Frost, C., C. E. Morris, A. Mason-Jones, D. M. O’Doherty, and T. O’Doherty (2015). « The effect of tidal flow directionality on tidal turbine performance characteristics ». In: *Renewable Energy* 78, pp. 609–620. DOI: [10.1016/j.renene.2015.01.053](https://doi.org/10.1016/j.renene.2015.01.053).
- Frost, C. H., P. S. Evans, M. J. Harrold, A. Mason-Jones, T. O’Doherty, and D. M. O’Doherty (2017). « The impact of axial flow misalignment on a tidal turbine ». In: *Renewable Energy* 113, pp. 1333–1344. DOI: [10.1016/j.renene.2017.07.006](https://doi.org/10.1016/j.renene.2017.07.006).
- Furgerot, L., A. Sentchev, P. Bailly du Bois, G. Lopez, M. Morillon, E. Poizot, Y. Méar, and A. C. Bennis (2020). « One year of measurements in Alderney Race: preliminary results from database analysis ». In: *Philosophical transactions. Series A, Mathematical, physical, and engineering sciences* 378.2178, p. 20190625. DOI: [10.1098/rsta.2019.0625](https://doi.org/10.1098/rsta.2019.0625).
- Furgerot, L., P. B. Du Bois, Y. Méar, M. Morillon, E. Poizot, and A. C. Bennis (2018). « Velocity profile variability at a tidal-stream energy site (Alderney Race, France): From short (second) to yearly time scales ». In: *OCEANS and MTS/IEEE Kobe Techno-Oceans*. IEEE, pp. 2779–2789. DOI: [10.1109/OCEANSKobe.2018.8559326](https://doi.org/10.1109/OCEANSKobe.2018.8559326).
- Gaurier, B., P. Druault, M. Ikhennicheu, and G. Germain (2020a). « Experimental analysis of the shear flow effect on tidal turbine blade root force from three-dimensional mean flow reconstruction: Shear flow effect on tidal turbine blade ». In: *Philosophical Transactions of the Royal Society A: Mathematical, Physical and Engineering Sciences* 378.2178. DOI: [10.1098/rsta.2020.0001](https://doi.org/10.1098/rsta.2020.0001).
- Gaurier, B. (2020). « Etude expérimentale des performances d’une hydrolienne, soumise aux effets de la turbulence et de l’interaction houle-courant ». PhD thesis. Normandie Université. URL: <https://tel.archives-ouvertes.fr/tel-03030615>.
- Gaurier, B., C. Carlier, G. Germain, G. Pinon, and E. Rivoalen (2020b). « Three tidal turbines in interaction: An experimental study of turbulence intensity effects on wakes and turbine performance ». In: *Renewable Energy* 148, pp. 1150–1164. DOI: [10.1016/j.renene.2019.10.006](https://doi.org/10.1016/j.renene.2019.10.006).

- Gaurier, B., P. Davies, A. Deuff, and G. Germain (2013). « Flume tank characterization of marine current turbine blade behaviour under current and wave loading ». In: *Renewable Energy* 59, pp. 1–12. DOI: [10.1016/j.renene.2013.02.026](https://doi.org/10.1016/j.renene.2013.02.026).
- Gaurier, B., G. Germain, J.-V. Facq, and T. Bacchetti (2018). *Wave and current flume tank of IFREMER at Boulogne-sur-mer. Description of the facility and its equipment*. Tech. rep. IFREMER. DOI: [10.13155/58163](https://doi.org/10.13155/58163).
- Gaurier, B., M. Ikhennicheu, G. Germain, and P. Druault (2020c). « Experimental study of bathymetry generated turbulence on tidal turbine behaviour ». In: *Renewable Energy* 156, pp. 1158–1170. DOI: [10.1016/j.renene.2020.04.102](https://doi.org/10.1016/j.renene.2020.04.102).
- Gaurier, B., S. Ordonez-Sanchez, J.-V. Facq, G. Germain, C. Johnstone, R. Martinez, F. Salvatore, I. Santic, T. Davey, C. Old, and B. Sellar (2020d). « MaRINET2 Tidal Energy Round Robin Tests—Performance Comparison of a Horizontal Axis Turbine Subjected to Combined Wave and Current Conditions ». In: *Journal of Marine Science and Engineering* 8.6, p. 463. DOI: [10.3390/jmse8060463](https://doi.org/10.3390/jmse8060463).
- Goss, Z., D. Coles, and M. Piggott (2021). *Economic analysis of tidal stream turbine arrays: a review*. URL: <http://arxiv.org/abs/2105.04718>. arXiv: [2105.04718](https://arxiv.org/abs/2105.04718).
- Grondeau, M. and S. Guillou (2023). « High-fidelity modeling of a vertical axis tidal turbine model under realistic flow conditions ». In: *15th European Wave and Tidal Energy Conference*. September. Bilbao, pp. 218–1–7. DOI: <https://doi.org/10.36688/ewtec-2023-218>.
- Grondeau, M., S. Guillou, P. Mercier, and E. Poizot (2019). « Wake of a ducted vertical axis tidal turbine in turbulent flows, LBM actuator-line approach ». In: *Energies* 12.22, p. 4273. DOI: [10.3390/en12224273](https://doi.org/10.3390/en12224273).
- Guerra, M. and J. Thomson (2017). « Turbulence Measurements from Five-Beam Acoustic Doppler Current Profilers ». In: *Journal of Atmospheric and Oceanic Technology* 34.6, pp. 1267–1284. DOI: [10.1175/JTECH-D-16-0148.1](https://doi.org/10.1175/JTECH-D-16-0148.1).
- Guilbot, M. (2021). « Analyse et optimisation des performances de turbines à axe vertical et flux transverse par simulations numériques ». PhD thesis. Université Grenoble Alpes.
- Guillaud, N., G. Balarac, E. Goncalvès, and J. Zanette (2020). « Large eddy simulations on vertical axis hydrokinetic turbines - Power coefficient analysis for various solidities ». In: *Renewable Energy* 147, pp. 473–486. DOI: [10.1016/j.renene.2019.08.039](https://doi.org/10.1016/j.renene.2019.08.039).
- Guillaud, N. (2017). « Simulation et optimisation de forme d’hydroliennes à flux transverse ». PhD thesis. Université Grenoble Alpes.
- Guillou, N., G. Chapalain, and S. P. Neill (2016). « The influence of waves on the tidal kinetic energy resource at a tidal stream energy site ». In: *Applied Energy* 180, pp. 402–415. DOI: [10.1016/j.apenergy.2016.07.070](https://doi.org/10.1016/j.apenergy.2016.07.070).
- Guillou, N., S. P. Neill, and J. Thiébot (2020). « Spatio-temporal variability of tidal-stream energy in north-western Europe ». In: *Philosophical Transactions of the Royal Society A: Mathematical, Physical and Engineering Sciences* 378.2178, p. 20190493. DOI: [10.1098/rsta.2019.0493](https://doi.org/10.1098/rsta.2019.0493).
- Harrison, M., W. Batten, L. Myers, and A. Bahaj (2010). « Comparison between CFD simulations and experiments for predicting the far wake of horizontal axis tidal turbines ». In: *IET Renewable Power Generation* 4.6, p. 613. DOI: [10.1049/iet-rpg.2009.0193](https://doi.org/10.1049/iet-rpg.2009.0193).

- Harrold, M. and P. Ouro (2019). « Rotor Loading Characteristics of a Full-Scale Tidal Turbine ». In: *Energies* 12.6, p. 1035. DOI: [10.3390/en12061035](https://doi.org/10.3390/en12061035).
- Hasselmann, K., T. P. Barnett, E. Bouws, H. Carlson, D. E. Cartwright, K. Eake, J. A. Euring, A. Gicnapp, D. E. Hasselmann, P. Kruseman, A. Meerburg, P. Mullen, D. J. Olbers, K. Richren, W. Sell, and H. Walden (1973). « Measurements of wind-wave growth and swell decay during the joint North Sea wave project (JONSWAP) ». In: *Erganzungsheft zur Deutschen Hydrographischen Zeitschrift* A(8).12.
- Hill, C., V. S. Neary, B. Gunawan, M. Guala, and F. Sotiropoulos (2014). *U. S. Department of Energy Reference Model Program RM2 : Experimental Results*. Tech. rep. Albuquerque: Sandia National Laboratories, pp. 1–29. URL: <https://www.osti.gov/servlets/purl/1171458>.
- Hoerner, S., C. Bonamy, O. Cleynen, T. Maître, and D. Thévenin (2020). « Darrieus vertical-axis water turbines: deformation and force measurements on bioinspired highly flexible blade profiles ». In: *Experiments in Fluids* 61.6, pp. 1–17. DOI: [10.1007/s00348-020-02970-2](https://doi.org/10.1007/s00348-020-02970-2).
- Huchet, M., E. Droniou, L. Perez, F. Johnson, A. Baldock, B. Vermeulen, and C. Boake (2023). « Wake characterization of tidal turbines in the Pentland Firth using vessel-mounted ADCP measurements ». In: *15th European Wave and Tidal Energy Conference*. Bilbao.
- HydroQuest (2018a). *Démonstrateur de Paimpol - Chargements hydrodynamiques sur la turbine (HY-7152-NE-0209)*. Tech. rep. HydroQuest, pp. 1–61.
- (2018b). *Paimpol prototype - Basis of design (HY-7152-NE-0201)*. Tech. rep. HydroQuest, pp. 1–44.
- (2018c). *Paimpol prototype - Meteocean data analysis (HY-7152-NE-0200)*. Tech. rep. HydroQuest, pp. 1–46.
- (2021). *Démonstrateur de Paimpol - Analyse du comportement hydrodynamique et des performances (HY-7152-OM-514)*. Tech. rep. HydroQuest, pp. 1–105.
- (2022a). *Démonstrateur de Paimpol - Analyse du comportement mécanique (HY-7152-RE-516)*. Tech. rep. HydroQuest, pp. 1–127.
- (2022b). *Démonstrateur de Paimpol - Calibration finale des jauges de la fondation (HY-7154-RE-0540)*. Tech. rep. HydroQuest, pp. 1–35.
- IEA-OES (2022). *Annual report: An overview of ocean energy activities in 2022*. Tech. rep. International Energy Agency, pp. 1–228. URL: <https://www.ocean-energy-systems.org/publications/oes-annual-reports/>.
- (2023). *Tidal Current Energy: Developments highlights*. Tech. rep. International Energy Agency, pp. 1–11. URL: <https://www.ocean-energy-systems.org/publications/oes-brochures/>.
- IEA (2022). *Renewables 2022*. Tech. rep. Paris: International Energy Agency, p. 158. URL: <https://www.iea.org/data-and-statistics/data-tools/renewables-data-explorer>.
- IEC (2013). « Technical specification 62600-200: Electricity producing tidal energy converters – Power performance assessment ». In: *Marine energy – Wave, tidal and other water current converters*. International Electrotechnical Commission.
- IPCC (2023). « Summary for Policymakers ». In: *Climate change 2023: Synthesis report*. Ed. by Core Writing Team, H. Lee, and J. Romero. Report of. Geneva, Switzerland: International Panel on Climate Change, p. 36. URL: <https://www.ipcc.ch/report/sixth-assessment-report-cycle/>.

- Ikhennicheu, M., G. Germain, P. Druault, and B. Gaurier (2019a). « Experimental investigation of the turbulent wake past real seabed elements for velocity variations characterization in the water column. » In: *International Journal of Heat and Fluid Flow* 78. DOI: [10.1016/j.ijheatfluidflow.2019.108426](https://doi.org/10.1016/j.ijheatfluidflow.2019.108426).
- (2019b). « Experimental study of coherent flow structures past a wall-mounted square cylinder ». In: *Ocean Engineering* 182.May, pp. 137–146. DOI: [10.1016/j.oceaneng.2019.04.043](https://doi.org/10.1016/j.oceaneng.2019.04.043).
- Jaquier, T. (2011). « Hydroliennes à flux transverse : Développement d'un prototype HARVEST en canal ». PhD thesis. Université de Grenoble. URL: <https://theses.hal.science/tel-01424843>.
- Jeffcoate, P., R. Starzmann, B. Elsaesser, S. Scholl, and S. Bischoff (2015). « Field measurements of a full scale tidal turbine ». In: *International Journal of Marine Energy* 12.2015, pp. 3–20. DOI: [10.1016/j.ijome.2015.04.002](https://doi.org/10.1016/j.ijome.2015.04.002).
- Jégo, L. and S. Guillou (2021). « Study of a Bi-Vertical Axis Turbines Farm Using the Actuator Cylinder Method ». In: *Energies* 14.16, p. 5199. DOI: [10.3390/en14165199](https://doi.org/10.3390/en14165199).
- Jiang, Y., P. Zhao, T. Stoesser, K. Wang, and L. Zou (2020). « Experimental and numerical investigation of twin vertical axis wind turbines with a deflector ». In: *Energy Conversion and Management* 209.March, p. 112588. DOI: [10.1016/j.enconman.2020.112588](https://doi.org/10.1016/j.enconman.2020.112588).
- Lam, H. and H. Peng (2017). « Measurements of the wake characteristics of co- and counter-rotating twin H-rotor vertical axis wind turbines ». In: *Energy* 131, pp. 13–26. DOI: [10.1016/j.energy.2017.05.015](https://doi.org/10.1016/j.energy.2017.05.015).
- Laws, N. D. and B. P. Epps (2016). « Hydrokinetic energy conversion: Technology, research, and outlook ». In: *Renewable and Sustainable Energy Reviews* 57, pp. 1245–1259. DOI: [10.1016/j.rser.2015.12.189](https://doi.org/10.1016/j.rser.2015.12.189).
- Lewis, M., S. Neill, P. Robins, M. Hashemi, and S. Ward (2017). « Characteristics of the velocity profile at tidal-stream energy sites ». In: *Renewable Energy* 114, pp. 258–272. DOI: [10.1016/j.renene.2017.03.096](https://doi.org/10.1016/j.renene.2017.03.096).
- Lucas, N. S., M. J. Austin, T. P. Rippeth, B. Powell, and P. Wakonigg (2022). « Turbulence and coherent structure characterisation in a tidally energetic channel ». In: *Renewable Energy* 194, pp. 259–272. DOI: [10.1016/j.renene.2022.05.044](https://doi.org/10.1016/j.renene.2022.05.044).
- Lust, E. E., B. H. Bailin, and K. A. Flack (2021). « Performance characteristics of a cross-flow hydrokinetic turbine in current only and current and wave conditions ». In: *Ocean Engineering* 219, p. 108362. DOI: [10.1016/j.oceaneng.2020.108362](https://doi.org/10.1016/j.oceaneng.2020.108362).
- Magnier, M. (2023). « Étude expérimentale des courants de marée et de la houle sur la dynamique tourbillonnaire d'une variation bathymétrique et sur le comportement d'une hydrolienne ». PhD thesis. Université de Lille.
- Magnier, M., N. Delette, P. Druault, B. Gaurier, and G. Germain (2022). « Experimental study of the shear flow effect on tidal turbine blade loading variation ». In: *Renewable Energy*, p. 100061. DOI: [10.1016/j.renene.2022.05.042](https://doi.org/10.1016/j.renene.2022.05.042).
- Magnier, M., P. Druault, B. Gaurier, and G. Germain (2020). « Comparison of bathymetry variation effects on tidal turbine behaviour ». In: *17ème journées de l'hydrodynamique JH2020*, pp. 1–12. URL: <https://archimer.ifremer.fr/doc/00660/77243/78695.pdf>.
- Magnier, M., P. Druault, and G. Germain (2021). « Experimental investigation of upstream cube effects on the wake of a wall-mounted cylinder: Wake rising reduction,

- TKE budget and flow organization ». In: *European Journal of Mechanics - B/Fluids* 87.June, pp. 92–102. DOI: [10.1016/j.euromechflu.2021.01.004](https://doi.org/10.1016/j.euromechflu.2021.01.004).
- Martinez, R., S. Ordonez-Sanchez, M. Allmark, C. Lloyd, T. O'Doherty, G. Germain, B. Gaurier, and C. Johnstone (2020). « Analysis of the effects of control strategies and wave climates on the loading and performance of a laboratory scale horizontal axis tidal turbine ». In: *Ocean Engineering* 212.July, p. 107713. DOI: [10.1016/j.oceaneng.2020.107713](https://doi.org/10.1016/j.oceaneng.2020.107713).
- Martinez, R., G. S. Payne, and T. Bruce (2018). « The effects of oblique waves and currents on the loadings and performance of tidal turbines ». In: *Ocean Engineering* 164.June, pp. 55–64. DOI: [10.1016/j.oceaneng.2018.05.057](https://doi.org/10.1016/j.oceaneng.2018.05.057).
- Masters, I., R. Malki, A. J. Williams, and T. N. Croft (2013). « The influence of flow acceleration on tidal stream turbine wake dynamics: A numerical study using a coupled BEM–CFD model ». In: *Applied Mathematical Modelling* 37.16-17, pp. 7905–7918. DOI: [10.1016/j.apm.2013.06.004](https://doi.org/10.1016/j.apm.2013.06.004).
- McNaughton, J. (2014). *ReDAPT MC7.1: Initial operation power curve*. Tech. rep. Alstom Ocean Energy. URL: https://redapt.eng.ed.ac.uk/library/eti/reports/MC7.1InitialPowerCurve{_}A.pdf.
- Mendoza, V., A. Chaudhari, and A. Goude (2019). « Performance and wake comparison of horizontal and vertical axis wind turbines under varying surface roughness conditions ». In: *Wind Energy* 22.4, pp. 458–472. DOI: [10.1002/we.2299](https://doi.org/10.1002/we.2299).
- Mercier, P. and S. Guillou (2021a). « The impact of the seabed morphology on turbulence generation in a strong tidal stream ». In: *Physics of Fluids* 33.5, p. 055125. DOI: [10.1063/5.0047791](https://doi.org/10.1063/5.0047791).
- (2022). « Spatial and temporal variations of the flow characteristics at a tidal stream power site: A high-resolution numerical study ». In: *Energy Conversion and Management* 269.May, p. 116123. DOI: [10.1016/j.enconman.2022.116123](https://doi.org/10.1016/j.enconman.2022.116123).
- Mercier, P., M. Ikhennicheu, S. Guillou, G. Germain, E. Poizot, M. Grondeau, J. Thiébot, and P. Druault (2020). « The merging of Kelvin–Helmholtz vortices into large coherent flow structures in a high Reynolds number flow past a wall-mounted square cylinder ». In: *Ocean Engineering* 204.March, p. 107274. DOI: [10.1016/j.oceaneng.2020.107274](https://doi.org/10.1016/j.oceaneng.2020.107274).
- Mercier, P., M. Thiébaud, S. Guillou, C. Maisondieu, E. Poizot, A. Pieterse, J. Thiébot, J. F. Filipot, and M. Grondeau (2021b). « Turbulence measurements: An assessment of Acoustic Doppler Current Profiler accuracy in rough environment ». In: *Ocean Engineering* 226.December 2020, p. 108819. DOI: [10.1016/j.oceaneng.2021.108819](https://doi.org/10.1016/j.oceaneng.2021.108819).
- Michna, J. and K. Rogowski (2022). « Numerical Study of the Effect of the Reynolds Number and the Turbulence Intensity on the Performance of the NACA 0018 Airfoil at the Low Reynolds Number Regime ». In: *Processes* 10.5, p. 1004. DOI: [10.3390/pr10051004](https://doi.org/10.3390/pr10051004).
- Miller, M. A., S. Duvvuri, I. Brownstein, M. Lee, J. O. Dabiri, and M. Hultmark (2018). « Vertical-axis wind turbine experiments at full dynamic similarity ». In: *Journal of Fluid Mechanics* 844, pp. 707–720. DOI: [10.1017/jfm.2018.197](https://doi.org/10.1017/jfm.2018.197).
- Milne, I. A., R. N. Sharma, R. G. Flay, and S. Bickerton (2010). « The role of onset turbulence on tidal turbine blade loads ». In: *17th Australasian Fluid Mechanics Conference* December, pp. 444–447. URL: https://flair.monash.edu.au/intranet/proceedings/17afmc{_}proceedings/PDF/093{_}Paper.pdf.

- Modali, P. K., A. Vinod, and A. Banerjee (2021). « Towards a better understanding of yawed turbine wake for efficient wake steering in tidal arrays ». In: *Renewable Energy* 177, pp. 482–494. DOI: [10.1016/j.renene.2021.05.152](https://doi.org/10.1016/j.renene.2021.05.152).
- Molin, B. (2002). *Hydrodynamique des structures offshore*. Editions Technip.
- Möllerström, E., F. Ottermo, A. Goude, S. Eriksson, J. Hylander, and H. Bernhoff (2016). « Turbulence influence on wind energy extraction for a medium size vertical axis wind turbine ». In: *Wind Energy* 19.11, pp. 1963–1973. DOI: [10.1002/we.1962](https://doi.org/10.1002/we.1962).
- Moreau, M., N. Bloch, G. Maurice, and G. Germain (2023a). « Experimental study of the upstream bathymetry effects on a ducted twin vertical axis tidal turbine ». In: *Renewable Energy (Under review)*.
- Moreau, M., C. Derveaux, G. Maurice, J.-V. Facq, and G. Germain (2022a). « Experimental study of two opposed flow directions effect on a ducted twin vertical axis tidal turbine ». In: *Trends in Renewable Energies Offshore*. Ed. by C. Guedes Soares. London: CRC Press, pp. 161–167. DOI: [10.1201/9781003360773-19](https://doi.org/10.1201/9781003360773-19).
- Moreau, M., G. Germain, and G. Maurice (2023b). « Experimental Investigation of Surface Waves Effect on a Ducted Twin Vertical Axis Tidal Turbine ». In: *Journal of Marine Science and Engineering* 11.10, p. 1895. DOI: [10.3390/jmse11101895](https://doi.org/10.3390/jmse11101895).
- (2023c). « Experimental performance and wake study of a ducted twin vertical axis turbine in ebb and flood tide currents at a 1/20th scale ». In: *Renewable Energy* 214, pp. 318–333. DOI: [10.1016/j.renene.2023.05.125](https://doi.org/10.1016/j.renene.2023.05.125).
- (2023d). « Misaligned sheared flow effects on a ducted twin vertical axis tidal turbine ». In: *Applied Ocean Research* 138, p. 103626. DOI: [10.1016/j.apor.2023.103626](https://doi.org/10.1016/j.apor.2023.103626).
- Moreau, M., G. Germain, G. Maurice, and A. Richard (2022b). « Sea states influence on the behaviour of a bottom mounted full-scale twin vertical axis tidal turbine ». In: *Ocean Engineering* 265, p. 112582. DOI: [10.1016/j.oceaneng.2022.112582](https://doi.org/10.1016/j.oceaneng.2022.112582).
- Moreau, M., G. Germain, G. Maurice, A. Richard, and R. Coquet (2021). « HydroQuest : Feedback from Paimpol-Bréhat and validation of the design method ». In: *14th European Wave and Tidal Energy Conference*. Plymouth, pp. 2229–1–8.
- Morison, J., J. Johnson, and S. Schaaf (1950). « The Force Exerted by Surface Waves on Piles ». In: *Journal of Petroleum Technology* 2.05, pp. 149–154. DOI: [10.2118/950149-G](https://doi.org/10.2118/950149-G).
- Müller, S., V. Muhawenimana, C. A. Wilson, and P. Ouro (2021). « Experimental investigation of the wake characteristics behind twin vertical axis turbines ». In: *Energy Conversion and Management* 247, p. 114768. DOI: [10.1016/j.enconman.2021.114768](https://doi.org/10.1016/j.enconman.2021.114768).
- Murray, R (2016). « Passively adaptive tidal turbine blades: Design methodology and experimental testing ». PhD thesis. Dalhousie University. URL: <https://dalspace.library.dal.ca/handle/10222/72040>.
- Mycek, P., B. Gaurier, G. Germain, G. Pinon, and E. Rivoalen (2014). « Experimental study of the turbulence intensity effects on marine current turbines behaviour. Part I: One single turbine ». In: *Renewable Energy* 66, pp. 729–746. DOI: [10.1016/j.renene.2013.12.036](https://doi.org/10.1016/j.renene.2013.12.036).
- Myers, L. and A. Bahaj (2012). « An experimental investigation simulating flow effects in first generation marine current energy converter arrays ». In: *Renewable Energy* 37.1, pp. 28–36. DOI: [10.1016/j.renene.2011.03.043](https://doi.org/10.1016/j.renene.2011.03.043).

- Naberezhnykh, A., D. Ingram, and I. Ashton (2023). « Wavelet applications for turbulence characterisation of real tidal flows measured with an ADCP ». In: *Ocean Engineering* 270.January, p. 113616. DOI: [10.1016/j.oceaneng.2022.113616](https://doi.org/10.1016/j.oceaneng.2022.113616).
- Ordóñez-Sánchez, S., M. Allmark, K. Porter, R. Ellis, C. Lloyd, I. Santic, T. O'Doherty, and C. Johnstone (2019). « Analysis of a Horizontal-Axis Tidal Turbine Performance in the Presence of Regular and Irregular Waves Using Two Control Strategies ». In: *Energies* 12.3, p. 367. DOI: [10.3390/en12030367](https://doi.org/10.3390/en12030367).
- Ouro, P., P. Dené, P. Garcia-Novo, T. Stallard, Y. Kyojuda, and P. Stansby (2022). « Power density capacity of tidal stream turbine arrays with horizontal and vertical axis turbines ». In: *Journal of Ocean Engineering and Marine Energy*. DOI: [10.1007/s40722-022-00257-8](https://doi.org/10.1007/s40722-022-00257-8).
- Ouro, P. and T. Stoesser (2019). « Impact of Environmental Turbulence on the Performance and Loadings of a Tidal Stream Turbine ». In: *Flow, Turbulence and Combustion* 102.3, pp. 613–639. DOI: [10.1007/s10494-018-9975-6](https://doi.org/10.1007/s10494-018-9975-6).
- Payne, G. S., T. Stallard, R. Martinez, and T. Bruce (2018). « Variation of loads on a three-bladed horizontal axis tidal turbine with frequency and blade position ». In: *Journal of Fluids and Structures* 83.2018, pp. 156–170. DOI: [10.1016/j.jfluidstructs.2018.08.010](https://doi.org/10.1016/j.jfluidstructs.2018.08.010).
- Peng, H. and H. Lam (2016). « Turbulence effects on the wake characteristics and aerodynamic performance of a straight-bladed vertical axis wind turbine by wind tunnel tests and large eddy simulations ». In: *Energy* 109, pp. 557–568. DOI: [10.1016/j.energy.2016.04.100](https://doi.org/10.1016/j.energy.2016.04.100).
- Perez, L., R. Cossu, A. Grinham, and I. Peneisis (2022). « Tidal turbine performance and loads for various hub heights and wave conditions using high-frequency field measurements and Blade Element Momentum theory ». In: *Renewable Energy* 200.October, pp. 1548–1560. DOI: [10.1016/j.renene.2022.10.058](https://doi.org/10.1016/j.renene.2022.10.058).
- Pham, C.-T. and V. a. Martin (2009). « Tidal current turbine demonstration farm in Paimpol-Brehat (Brittany): tidal characterisation and energy yield evaluation with Telemac ». In: *Proceedings of the 8th European Wave and Tidal Energy Conference*, pp. 181–188.
- Pham, C.-T. and K Pinte (2010). « Paimpol-Bréhat tidal turbine demonstration farm (Brittany): optimisation of the layout, wake effects and energy yield evaluation using Telemac ». In: *International Conference on Ocean Energy*.
- Priegue, L. and T. Stoesser (2017). « The influence of blade roughness on the performance of a vertical axis tidal turbine ». In: *International Journal of Marine Energy* 17, pp. 136–146. DOI: [10.1016/j.ijome.2017.01.009](https://doi.org/10.1016/j.ijome.2017.01.009).
- Rathnayake, U., M. Folley, S. D. Gunawardane, and C. Frost (2020). « Investigation of the error of mean representative current velocity based on the method of bins for tidal turbines using ADP data ». In: *Journal of Marine Science and Engineering* 8.6, p. 390. DOI: [10.3390/JMSE8060390](https://doi.org/10.3390/JMSE8060390).
- Rolin, V. F. and F. Porté-Agel (2018). « Experimental investigation of vertical-axis wind-turbine wakes in boundary layer flow ». In: *Renewable Energy* 118, pp. 1–13. DOI: [10.1016/j.renene.2017.10.105](https://doi.org/10.1016/j.renene.2017.10.105).
- Ross, H. (2020). « Scaling Effects on the Hydrodynamics and Performance of Current Turbines ». PhD thesis. University of Washington. URL: <https://digital.lib.washington.edu/researchworks/handle/1773/46109>.

- Ross, H. and B. Polagye (2020a). « An experimental assessment of analytical blockage corrections for turbines ». In: *Renewable Energy* 152, pp. 1328–1341. DOI: [10.1016/j.renene.2020.01.135](https://doi.org/10.1016/j.renene.2020.01.135).
- (2020b). « An experimental evaluation of blockage effects on the wake of a cross-flow current turbine ». In: *Journal of Ocean Engineering and Marine Energy* 6.3, pp. 263–275. DOI: [10.1007/s40722-020-00172-w](https://doi.org/10.1007/s40722-020-00172-w).
- (2022). « Effects of dimensionless parameters on the performance of a cross-flow current turbine ». In: *Journal of Fluids and Structures* 114, p. 103726. DOI: [10.1016/j.jfluidstructs.2022.103726](https://doi.org/10.1016/j.jfluidstructs.2022.103726).
- Saouli, Y., M. Magnier, G. Germain, B. Gaurier, and P. Druault (2022). « Experimental characterisation of the waves propagating against current effects on the wake of a wide bathymetric obstacle ». In: *18ème Journées de l'Hydrodynamique*. 1. Poitiers, pp. 1–12. URL: <https://jh2022.sciencesconf.org/413878>.
- Scarlett, G. T., B. Sellar, T. van den Bremer, and I. M. Viola (2019). « Unsteady hydrodynamics of a full-scale tidal turbine operating in large wave conditions ». In: *Renewable Energy* 143.March 2020, pp. 199–213. DOI: [10.1016/j.renene.2019.04.123](https://doi.org/10.1016/j.renene.2019.04.123).
- Sentchev, A., T. D. Nguyen, L. Furgerot, and P. Bailly du Bois (2020). « Underway velocity measurements in the Alderney Race: towards a three-dimensional representation of tidal motions ». In: *Phil. Trans. R. Soc. A* 378.2178. DOI: [10.1098/rsta.2019.0491](https://doi.org/10.1098/rsta.2019.0491).
- Shahsavari, M. and E. L. Bibeau (2020). « Performance characteristics of shrouded horizontal axis hydrokinetic turbines in yawed conditions ». In: *Ocean Engineering* 197.January, p. 106916. DOI: [10.1016/j.oceaneng.2020.106916](https://doi.org/10.1016/j.oceaneng.2020.106916).
- Shamsoddin, S. and F. Porté-Agel (2016). « A Large-Eddy Simulation Study of Vertical Axis Wind Turbine Wakes in the Atmospheric Boundary Layer ». In: *Energies* 9.5, p. 366. DOI: [10.3390/en9050366](https://doi.org/10.3390/en9050366).
- Terme, L. and N. Gerard (2015). « Parc hydrolien EDF de Paimpol-Bréhat : premières réalisations et préparation du raccordement au réseau de la première ferme hydrolienne en France ». In: *La Houille Blanche* 101.1, pp. 22–26. DOI: [10.1051/lhb/2015003](https://doi.org/10.1051/lhb/2015003).
- Thiébaud, M., J.-F. Filipot, C. Maisondieu, G. Damblans, C. Jochum, L. F. Kilcher, and S. Guillou (2020). « Characterization of the vertical evolution of the three-dimensional turbulence for fatigue design of tidal turbines ». In: *Philosophical Transactions of the Royal Society A: Mathematical, Physical and Engineering Sciences* 378.2178, p. 20190495. DOI: [10.1098/rsta.2019.0495](https://doi.org/10.1098/rsta.2019.0495).
- Thomson, J., B. Polagye, M. Richmond, and V. Durgesh (2010). « Quantifying turbulence for tidal power applications ». In: *OCEANS 2010 MTS/IEEE SEATTLE*. 4. IEEE, pp. 1–8. DOI: [10.1109/OCEANS.2010.5664600](https://doi.org/10.1109/OCEANS.2010.5664600).
- Togneri, M., I. Masters, A. Williams, and I. Fairley (2021). « A spectral-statistical filter for decoupling wave and turbulence effects at tidal sites ». In: *Proceedings of the European Wave and Tidal Energy Conference*, pp. 1927–1–10.
- Vennell, R., S. W. Funke, S. Draper, C. Stevens, and T. Divett (2015). « Designing large arrays of tidal turbines: A synthesis and review ». In: *Renewable and Sustainable Energy Reviews* 41, pp. 454–472. DOI: [10.1016/j.rser.2014.08.022](https://doi.org/10.1016/j.rser.2014.08.022).
- Vergaerde, A., T. De Troyer, S. Muggiasca, I. Bayati, M. Belloli, J. Kluczevska-Bordier, N. Parneix, F. Silvert, and M. C. Runacres (2020a). « Experimental characterisation

- of the wake behind paired vertical-axis wind turbines ». In: *Journal of Wind Engineering and Industrial Aerodynamics* 206, p. 104353. DOI: [10.1016/j.jweia.2020.104353](https://doi.org/10.1016/j.jweia.2020.104353).
- Vergaerde, A., T. De Troyer, L. Standaert, J. Kluczevska-Bordier, D. Pitance, A. Immas, F. Silvert, and M. C. Runacres (2020b). « Experimental validation of the power enhancement of a pair of vertical-axis wind turbines ». In: *Renewable Energy* 146, pp. 181–187. DOI: [10.1016/j.renene.2019.06.115](https://doi.org/10.1016/j.renene.2019.06.115).
- Villeneuve, T., G. Winckelmans, and G. Dumas (2021). « Increasing the efficiency of vertical-axis turbines through improved blade support structures ». In: *Renewable Energy* 169, pp. 1386–1401. DOI: [10.1016/j.renene.2021.01.092](https://doi.org/10.1016/j.renene.2021.01.092).
- Vinod, A., C. Han, and A. Banerjee (2021). « Tidal turbine performance and near-wake characteristics in a sheared turbulent inflow ». In: *Renewable Energy* 175, pp. 840–852. DOI: [10.1016/j.renene.2021.05.026](https://doi.org/10.1016/j.renene.2021.05.026).
- Xin, Z., X. Li, and Y. Li (2023). « Coupled effects of wave and depth-dependent current interaction on loads on a bottom-fixed vertical slender cylinder ». In: *Coastal Engineering* 183, p. 104304. DOI: [10.1016/j.coastaleng.2023.104304](https://doi.org/10.1016/j.coastaleng.2023.104304).
- Zhang, X., R. Simons, J. Zheng, and C. Zhang (2022). « A review of the state of research on wave-current interaction in nearshore areas ». In: *Ocean Engineering* 243, June 2021, p. 110202. DOI: [10.1016/j.oceaneng.2021.110202](https://doi.org/10.1016/j.oceaneng.2021.110202).
- Zhang, X.-w., L. Zhang, F. Wang, D.-y. Zhao, and C.-y. Pang (2014). « Research on the unsteady hydrodynamic characteristics of vertical axis tidal turbine ». In: *China Ocean Engineering* 28.1, pp. 95–103. DOI: [10.1007/s13344-014-0007-6](https://doi.org/10.1007/s13344-014-0007-6).
- Zhou, Z., M. Benbouzid, J. F. Charpentier, F. Scuiller, and T. Tang (2017). « Developments in large marine current turbine technologies – A review ». In: *Renewable and Sustainable Energy Reviews* 71, pp. 852–858. DOI: [10.1016/j.rser.2016.12.113](https://doi.org/10.1016/j.rser.2016.12.113).